Proceedings of the 14th CEReS Int'l Symposium and SKYNET Workshop on

"Remote Sensing of the Atmosphere for Better Understanding of Climate Change"

November 13-14, 2008
Keyaki-Hall, Chiba University

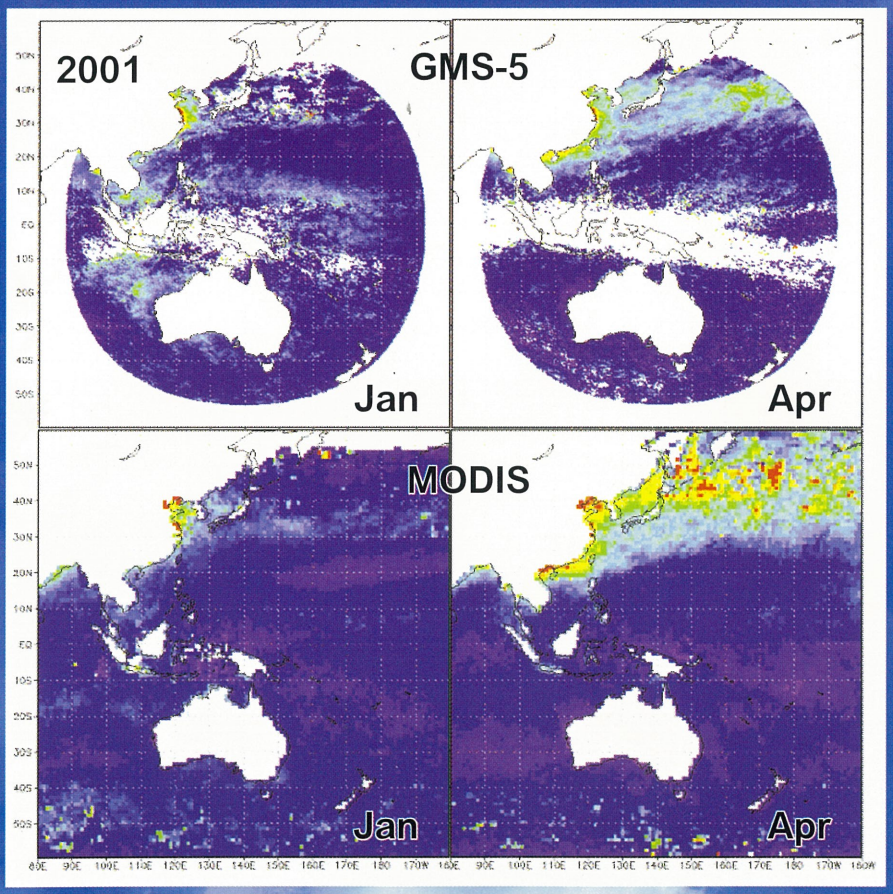

Aerosol retrieval by satellites [Fukuda et al.]

Center for Environmental Remote Sensing (CEReS)
Chiba University

The CEReS International Symposium and SKYNET Workshop has been supported and sponsored by the National University Corporation Chiba University and the activity**(climate change monitoring on aerosol effects through SKYNET observation)** of the MEXT(Ministry of Education, Science, Sports and Culture, Japan) – GEOSS plan.

Published by

Center for Environmental Remote Sensing(CEReS)

Chiba University, Japan

1-33 Yayoi-cho, Inage, Chiba, 263-8522 Japan

Proceedings of the 14th CEReS Int'l Symposium and SKYNET Workshop on "Remote Sensing of the Atmosphere for Better Understanding of Climate Change"

November 13-14, 2008

Organized by

Center for Environmental Remote Sensing(CEReS)

Chiba University, Japan

Edited by

H. Kuze and T. Takamura

CONTENTS

<aerosol observation and monitoring>

<atmospheric monitoring and its technique>

<radiative effects of aerosol and cloud (1) >

<satellite observation and its application>

The WMO/GAW Integrated Global Aerosol Observing and Analysis System

John A. Ogren[1]

[1]*National Oceanic and Atmospheric Administration, Earth System Research Laboratory, 325 Broadway, Boulder, CO, 80305, USA, John.A.Ogren@noaa.gov*

Abstract

Aerosol observations and analyses by the World Meteorological Organization's Global Atmosphere Watch (WMO GAW) are envisioned to play a central role in the evolving Earth observation system. The GAW aerosol program coordinates observations in three component networks measuring aerosol properties *in-situ*, vertical profiles, and optical depth. Integrated analyses and products derived from these observations are emerging, and more will follow as the networks mature.

Keywords **:** GAW, aerosol networks

1. Introduction

The mission of the WMO Global Atmosphere Watch, as summarized in the GAW Strategic Plan[i], is to reduce environmental risks to society and meet the requirements of environmental conventions; strengthen capabilities to predict climate, weather and air quality; and contribute to scientific assessments in support of environmental policy. This mission is accomplished through three primary activities: maintaining and applying global, long-term observations of the chemical composition and selected physical characteristics of the atmosphere; emphasizing quality assurance and quality control; and delivering integrated products and services of relevance to users. The aerosol component of GAW has emphasized the first two of these activities to date, and the state of the aerosol observing systems has advanced to where integrated products are beginning to emerge.

GAW aerosol observations fall into three categories: *in-situ* measurements of aerosol chemical, microphysical, and radiative properties; ground-based measurements of aerosol optical depth; and ground-based measurements of aerosol vertical profiles of backscattering and extinction with lidar. Coordination of the individual stations and networks within each of these categories is the responsibility of the GAW Science Advisory Group for Aerosols[ii] (SAG-Aerosol), and much work remains to integrate the measurements across the three different categories. The motivation to achieve this integration is considerable, however, as new products, such as the Sand and Dust Storm Warning Advisory and Assessment System, require a synthesis of observations and models in near real-time[iii].

2. GAW Observing Networks

In-situ measurement networks. Historically, the focus of SAG-Aerosol has been on *in-situ* measurements of aerosol chemical composition, radiative properties, and microphysical properties (number concentration, size distribution). This focus is largely a result of the research interests of the SAG members, which together represent the bulk of the GAW Global stations making these measurements. Emphasis has been on defining measurement priorities and sampling protocols[iv], improving measurements of aerosol physical properties, and archiving the data in World Data Center for Aerosols[v]. NOAA has been working closely with GAW stations in Canada, China, Hungary, Puerto Rico, and South Africa to deploy measurement systems that use identical hardware and software to measure aerosol light scattering, absorption, and number concentration. By using the same software, freely available from NOAA[vi], station operators can focus on measurements and quality assurance rather than software development and maintenance. The World Calibration Center for Aerosol Physics[vii] has been conducting 2-3 audits per year to help station operators identify and correct problems with sampling systems and their calibration, organizing workshops for characterization and intercomparison of field instruments, and conducting

Presented at the CEReS Symposium and SKYNET workshop on "Remote Sensing of the Atmosphere for Better Understanding of Climate Change", Center for Environmental Remote Sensing, Chiba University, Chiba, Japan, November 13-14, 2008.

training courses. A corresponding World Calibration Center for Aerosol Chemistry does not exist, and remains a major gap in the GAW aerosol program.

Aerosol optical depth networks. The GAW strategic objective is a long-term (multi-decadal) and global AOD network., with an eventual goal of providing data in near real-time for assimilation into global meteorological models. At present, there are numerous national and international networks monitoring aerosol optical depth using different instruments, measurement protocols, and analysis techniques. In an attempt to identify these networks and foster collaboration and integration, the WMO Secretariat and SAG-Aerosol organized a meeting of experts at the World Optical Depth Research and Calibration Center [viii] (WORCC) in 2004 to review the current state of long-term observational networks for aerosol optical depth.[ix] Ten independent networks, with a total of 90 stations, were identified as having a continuous record for the past 4 years (as of 2004) with a coverage of 50% of the available daylight observing opportunity. The identified international networks were AERONET (including AEROCAN, PHOTONS, AEROSIBNET, which together comprise about half of the identified stations), BSRN, GAW-PFR, and SKYNET, while national networks were identified in Australia, China, Finland, Germany, Japan, Netherlands (including Surinam), Russia, and USA. There were 13 sites where two or more of these networks overlap.

The primary conclusion of the 2004 meeting is that the international coordination of AOD networks is inadequate, and that a federation of the diverse networks should be coordinated under the WMO/GAW umbrella. A number of recommendations were made, and a standing sub-committee of SAG-Aerosol has been formed to oversee implementation of these recommendations. Highlights of these recommendations include:

- Development of common data policy agreements, technical standards, and strategy to fill spatial gaps in observations sites;
- Contributing networks should become traceable to WORCC through intercomparisons of representative instruments or co-location at specific GAW sites;
- All networks should maintain an internal calibration hierarchy that can provide an uncertainty of 0.015 optical depth at unit air mass, corresponding to a calibration accuracy and stability of 1.5%;
- A quality control and assurance manual should be prepared by a group of experts describing how the above data quality requirement is achieved;

A major benefit of a federated AOD network is in facilitating end-user access to multiple network archives. Current forecast models, addressing issues such as biomass burning, dust, and urban air quality, could use AOD as an input if the data were to be available on the order of three hours after measurement.

Lidar networks. The specific objective of the GAW Atmospheric Lidar Observation Network[x] (GALION) is to provide the vertical component of aerosol distributions through advanced laser remote sensing in a network of ground-based stations. The aerosol observed properties include the identification of aerosol layers, profiles of optical properties with known and specified precision (backscatter and extinction coefficients at selected wavelengths, lidar ratio, Ångström coefficients), aerosol type (e.g. dust, maritime, fire smoke, urban haze), and microphysical properties (e.g., volume and surface concentrations, size distribution parameters, refractive index). GALION is intended to provide sufficient coverage, resolution, and accuracy to establish comprehensive aerosol climatology, to evaluate model performance, to assist and complement space-borne observations, and to provide input to forecast models of "chemical weather".

Similar to the AOD network, GALION is conceived as a federation of seven regional lidar networks, totaling around 100 sites, which depends completely on voluntary contributions from the various existing networks (most of which, themselves, are based on voluntary cooperation) plus contributions from individual stations. These contributing networks have goals that may be independent of GAW, and a prerequisite for the success of GALION is that the contributing networks meet GAW's requirements for consistency of data, insured quality, and enhanced data distribution. To improve the coverage in areas with significant aerosol load, the networks will make efforts to accept new members operating at suitable locations and provide as much support as possible.

The observations within GALION serve different purposes requiring different operational characteristics. To establish a useful climatology it is necessary and sufficient to make regular measurements on a fixed schedule, thus avoiding a strong bias towards "blue sky" conditions. There is evidence that two measurements per week are sufficient for this purpose, so the minimum requirement for GALION is to perform measurements every Monday and Thursday. Because diurnal changes in the atmosphere require observations to be made at comparable local times,

and because some lidar systems are best operated at low levels of ambient light, it is suggested to perform these measurements in a time slot of a few hours around sunset.

3. Network Integration

Each of the three components of the GAW aerosol program (*in-situ*, AOD, lidar) have plans for integrating the measurements and data products from the contributing partners to that component. The focus in the near-term is to implement those plans, so that GAW becomes the source where users can turn for easy access to data of known, high quality. Looking beyond that near-term effort, issues of integration of the data across the component networks raise a different set of questions. While a handful of GAW stations make measurements of all three components, the more common case is that stations make measurements of only one, or perhaps two, of the components. This situation is unlikely to change anytime soon, as the goals and financial support of contributing stations place strong constraints on what can be measured. What is needed, then, is a strategy for merging data from stations in the same regions that are not co-located. A first step could be an analysis, using regional models like WRF-Chem [xi], of the auto-correlation scales of aerosol properties. Such an analysis can be used to determine the feasibility of combining, for example, climatologies of aerosol composition from in-situ stations, optical depth from other sites, and vertical profiles from yet other sites in the region, in order to attribute the derived aerosol radiative forcing to various types of aerosol sources.

Another aspect of network integration involves companion networks to GAW. An important example is the Baseline Surface Radiation Network[xii], which monitors the radiative fluxes that are strongly affected by the aerosols monitored in the GAW aerosol networks. Few BSRN stations are co-located with GAW stations, leading to network integration issues similar to those faced by the GAW component networks.

4. Integrated Analyses and Products

The ultimate success of GAW comes when the data that are so painstakingly acquired by the contributing stations are put to use. To date, the primary use of GAW aerosol data has been as the basis for research publications on aerosol properties and their spatial distributions, source, transformation, and removal processes, as well as for validation of aerosol products retrieved from satellite observations. GAW data are being used to evaluate model predictions of aerosol distributions, for example, by the "Aerosol Comparisons between Observations and Models (AEROCOM)" project[xiii]. For the most part, these applications rely on a data from individual stations or from just one of the component networks of GAW. Even greater benefits of GAW data will be realized when results from multiple component networks are integrated together, with satellite observations, and with global models.

Sand and dust storms. WMO is taking a lead with international partners to establish the Sand and Dust Storm Warning Advisory and Assessment System (SDS-WAS) to develop, refine and provide products to the global community useful in reducing the adverse impacts of sand and dust storms and to assess impacts of the SDS process on society and nature[xiv].

Model integration. As a consequence of the influence of aerosols on radiation, clouds, and precipitation, numerical models are evolving towards assimilation of aerosol observations in near real-time to improve their forecasts. An example of such an effort is the EU-funded "Global and regional Earth-system (Atmosphere) Monitoring using Satellite and in-situ data (GEMS)" project [xv], which is developing comprehensive data analysis and modelling systems for monitoring the global distributions of atmospheric constituents important for climate, air quality and UV radiation, with a focus on Europe. While the assimilation efforts have primarily used satellite observations, there is clearly an opportunity for GAW data to be used to improve models provided the data can be provided in near real-time.

5. Conclusion

GAW aerosol observations and analyses are envisioned to play a central role in the evolving Earth observation system. The intergovernmental *ad hoc* Group on Earth Observations (GEO), which has the goal of furthering the creation of a comprehensive, coordinated, and sustained Earth observing system, relies on the Global Climate Observing System (GCOS)[xvi] and the Integrated Global Atmospheric Chemistry Observation (IGACO) theme[xvii] to deliver measurements and integrated analyses of atmospheric

aerosols. The GAW aerosol program has a long way to go before this vision is realized. One of the first steps along the way will be for the component GAW aerosol networks to satisfy the ten GCOS Climate Monitoring Principles[xviii].

Acknowledgements

Sections of the above text were drawn verbatim, or nearly so, from the GAW Strategic Plan[i], AOD Workshop report[ix], GALION workshop report[x], and other sources cited below.

References

[i] http://www.wmo.int/pages/prog/arep/gaw/documents/gaw172-26sept07.pdf
[ii] http://gaw.tropos.de/
[iii] http://www.wmo.ch/pages/prog/arep/wwrp/new/Sand_and_Dust_Storm.html
[iv] http://www.wmo.int/pages/prog/arep/gaw/documents/gaw153.pdf
[v] http://wdca.jrc.it/
[vi] contact the author for further information
[vii] http://gaw.tropos.de/WCCPAP/index.html
[viii] http://www.pmodwrc.ch/worcc/
[ix] http://www.wmo.int/pages/prog/arep/gaw/documents/gaw162.pdf
[x] http://www.wmo.int/pages/prog/arep/gaw/documents/gaw178-galion-draft31July.pdf
[xi] http://ruc.fsl.noaa.gov/wrf/WG11/
[xii] http://www.gewex.org/bsrn.html
[xiii] http://nansen.ipsl.jussieu.fr/AEROCOM/
[xiv] http://www.wmo.ch/pages/prog/arep/wwrp/new/documents/sds_was_draft_implementation_plan.pdf
[xv] http://gems.ecmwf.int/about.jsp
[xvi] http://www.wmo.int/pages/prog/gcos/
[xvii] http://www.wmo.int/pages/prog/arep/gaw/documents/gaw159.pdf
[xviii] http://www.wmo.ch/pages/prog/gcos/Publications/gcos-92.pdf.

Observation Study of Dust Effect on Arid/Semi-Arid Climate

Jianping Huang[1]
[1]College of Atmospheric Sciences, Lanzhou University, Lanzhou, 730000

Abstract

Arid and semi-arid areas comprise about 30% of earth surface. Changes in climate and climate variability will likely have a significant impact on these regions. Due to the large spatial and temporal extent of desert dust in the atmosphere, the interactions of desert dust with clouds and land surface can have substantial climatic impacts. Dust storms may have contributed to the desertification of the Northwest China during recent decades. The objective of this extended abstract is to report the status of climate research group of Lanzhou University for observation study of dust aerosol effect on arid/semi-arid climate.

1. Introduction

Recently, special attention has been dedicated to cloud interactions with desert aerosol particles (*Huang et al, 2006a,b,c, 2007a,b, 2008b,c; Su et al., 2008*). Dust aerosols not only have direct effects on the climate through reflection and absorption of short and long wave radiation but also modify cloud properties, such as the number concentration and size of cloud droplets. This change in cloud properties, which could alter both cloud albedo and cloud lifetime if the total cloud water content remained unaffected constitutes the indirect effect on climate. Another important aspect of aerosols, especially absorbing aerosols, such as black carbon and mineral dust, is their semi-direct effect. Aerosol absorption at solar wavelengths could contribute to high diabatic heating in the atmosphere and enhance cloud evaporation. However, the knowledge of the indirect and semi-direct effects of Asian dust aerosols on climate is still very limited due to the lack of observations. The objective of this extend abstract is to review the progress in observation study of dust aerosol effect on arid/semi-arid climate(*Fu et al., 2008; Huang et al, 2006a,b,c, 2007a,b, 2008b,c; Su et al., 2008; Wang et al.; 2008*).

2. Satellite Measurements Analysis

2.1 Direct effect

The dust aerosol radiative forcing and heating rate over the Taklimakan Desert are estimated using the Fu-Liou radiative transfer model along with satellite observations (*Huang et al., 2008c*). The vertical distributions of the dust aerosol extinction coefficient are derived from the CALIPSO (Cloud-Aerosol Lidar and Infrared Pathfinder Satellite Observations) lidar measurements. The CERES (Cloud and the Earth's Energy Budget Scanner) measurements of reflected solar radiation are used to constrain the dust aerosol type in the radiative transfer model, which determines the dust aerosol single-scattering albedo and asymmetry factor as well as the aerosol optical properties' spectral dependencies. We find that the dust aerosol radiative heating and forcing have a significant impact on the energy budget over the Taklimakan desert. In the atmospheres containing light, moderate and heavy dust layers, the dust aerosols heat the atmosphere by up to 1, 2, and 3 K day^{-1}, respectively. The maximum daily mean radiative heating rate reaches 5.5 K day^{-1} at 5 km. The averaged daily mean net radiative forcings of the dust are 44.4, -41.9, and 86.3 W m^{-2}, respectively, at the top of the atmosphere (TOA), surface, and in the atmosphere. Among these forcings about two thirds of the warming effect at the TOA is related to the longwave radiation, while about 90% of the atmospheric warming is contributed by the solar radiation. At the surface, about one third of the dust solar radiative cooling effect is compensated by its longwave warming effect. The large modifications of radiative energy budget by the dust aerosols over Taklimakan

Desert should have important implications for the atmospheric circulation and regional climate.

2.2 Indirect effect

The indirect effects of dust aerosol on cloud properties and Radiative Forcing (RF) are analyzed over Northwestern China from April 2001 to June 2004 using data collected by the MODIS and CERES instruments on the Aqua and Terra satellites (Huang et al., 2006a, 2006b). On average, ice cloud effective particle diameter, optical depth and ice water path of cirrus clouds under dust polluted conditions are 11%, 32.8%, and 42% less, respectively, than those derived from ice clouds in dust-free atmospheric environments. Due to changes in cloud microphysics, the instantaneous net RF is increased from -161.6 W/m^2 for dust-free clouds to –118.6 W/m^2 for dust-contaminated clouds.

2.3 Semi-Direct effect

The semi-direct effects of dust aerosols are analyzed over eastern Asia using 2 years (June 2002 to June 2004) of data from the CERES)scanning radiometer and MODIS on the Aqua satellite, and 18 years (1984 to 2001) of International Satellite Cloud Climatology Project (ISCCP) data (Huang et al., 2006c). The results show that the water path of dust-contaminated clouds is considerably smaller than that of dust-free clouds. The mean ice water path (IWP) and liquid water path (LWP) of dusty clouds are less than their dust-free counterparts by 23.7% and 49.8%, respectively. The long-term statistical relationship derived from ISCCP also confirms that there is significant negative correlation between dust storm index and ISCCP cloud water path. These results suggest that dust aerosols warm clouds, increase the evaporation of cloud droplets and further reduce cloud water path, the so-called semi-direct effect. The semi-direct effect may play a role in cloud development over arid and semi-arid areas of East Asia and contribute to the reduction of precipitation.

Su et al. (2008) estimated the contribution to the cloud radiation forcing by dust direct, indirect and semi-direct effects using combined satellite observation and Fu-Liou model simulation. The four years mean value of combination of indirect and semi-direct shortwave radiative forcing is 82.2 Wm^{-2}, which is 78.4% of the total dust effect. The direct effect is only 22.7 Wm^{-2}, which is 21.6% of the total effect. Because both first and second indirect effects enhance cloud cooling effect, dusty cloud warming effect is mainly contributed by semi-direct effect of dust aerosol.

3. Surface Observation

To improve understanding and capture the direct evident of the impact of human activity on semi-arid climate over Loess Plateau, the Semi-Arid Climate & Environment Observatory of Lanzhou University (SACOL) has been established since 2005 (*Huang et al., 2008a*). SACOL consists of a large set of instruments and focuses on: 1) monitoring of long term tendencies in semi-arid climate changes; 2) monitoring of the aerosol effect on water cycle; 3) studies of interaction between land surface and atmosphere; 4) improving the land surface and climate model; and 5) validation of space-borne observations.

SACOL is about 48 km away from the centre of Lanzhou, situated at the southern bank of Yellow River in Gansu province, northwestern China. It situates on so called China-Loess Plateau is about 1965.8m above sea level. The topography around the site is characterized by loess plateau consisting of plain, ridge and mound, etc, with the elevation range of 1714~2089m. The soil parent material is mainly quaternary aeolian loess with the main soil types of sierozem. There is also some loess soil in the terrace, ridge and mound. The terrain where the measurements are carried out is flat, covered with short glass. The dominated species within the immediate area is stipa bungeana as well as artemisia frigida and leymus secalinus. Figure 1 shows the map of SACOL's location.

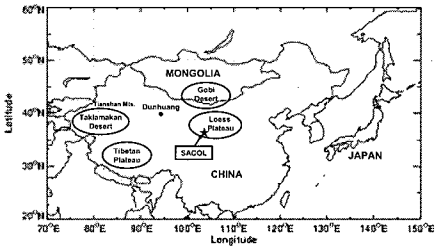

Fig. 1 Location of SACOL

SACOL consists of a large set of instruments and measure: 1) boundary layer meteorological parameters; 2) surface radiation; 3) surface fluxes; 4) soil heat and water moisture; 5) ambient air

quality; 6) aerosol optical properties; 7) temperature and water vapor profiles; 8) sky conditions. SACOL is a participating site in the Coordinated Enhanced Observing Period (CEOP) which was initiated as a major step towards bringing together the research activities in GHP/GEWEX and related projects in WCRP (CLIVAR; CLiC). An AERONET-Cimel sun photometer for spectral radiative and aerosol optical properties has been measured and archived at SACOL. Micro-Pulse Lidar Network (MPLnet) lidar is also operational at SACOL (*Huang et al., 2008d*). It provides real-time images of the vertical profile of backscatter. Figure 2 shows an example of MPL measurements. Figure 3 compares the MPL integrated aerosol optical depths with aerosol column optical depths obtained using CIMEL sun photometer (CE318) observations at 527 nm during daytime. The CIMEL optical depths are in good agreement (±10%) with the lidar-derived contribution of aerosol extinction, due to the dust layers.

The observational facilities of SACOL represent a unique resource for climate research and should allow the community to focus its effort on high priority problem of understanding semi-arid climate change. SACOL employs a multiplatform approach, with state-of-the-art instrumentation deployed on surface to provide a comprehensive description of atmosphere and land surface thermo-dynamic state, particulate composition, aerosol, cloud and radiative properties. This integrated dataset is being used to improving understanding of aerosol-climate interaction, test and improve climate model and satellite remote sensing techniques (*Huang et al., 2008a*). Results of the analyses performed to date, which have been summarized in this paper and are reported in more detail in other papers and elsewhere. SACOL's rich data can be accessed online through the SACOL home page at http://climate.lzu.edu.cn).

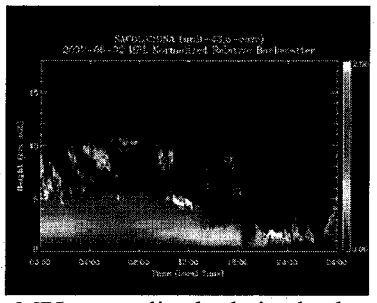

Figure 2. MPL normalized relative backscatter at SACOL for May 2, 2007.

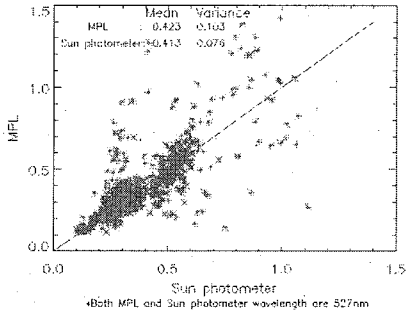

Figure 3. Comparison of MPL-derived aerosol optical depth (AOD) with sun photometer-derived AOD for the period April-May, 2007

4. Conclusions and Discussions

Aerosols are generally believed to exert a cooling influence on climate directly by scattering solar radiation and through their indirect effects on clouds. However, the semi-direct effect has the potential to offset this cooling by reducing low cloud cover and water path. Although the potential importance of the semi-direct effect has been addressed by model simulations, there are few reports discussing the semi-direct effect as seen from observational data. Our studies show some evidence of the semi-direct effect of Asian dust aerosols on cloud properties. Analysis of the satellite observations indicates that, on average, the water path of dusty clouds is considerably smaller than that from dust-free clouds in the same frontal systems. The key issue may be related to the dust aerosol warming effect through the absorption of solar radiation. The absorption or diabatic heating of Asian dusts can

cause the evaporation of cloud droplets and reduce cloud water path. The decrease of cloud optical depth and water path partially reduces cloud cooling effect. The semi-direct effect may be the dominating factor of dust aerosol-cloud interaction over arid and semi-arid areas in East Asia, and contribute to the reduction of precipitation via a significantly different mechanism as compared to that in Africa. Dust storms may have contributed to the desertification of the Northwest China during recent decades. The results presented here represent only a first step in better understanding the effect of Asian dust on climate. Further research should be focused on measurements of physical processes of aerosol-cloud interactions.

5. Acknowledgments
This research is supported by National Basic Research Program of China (2006CB400501).

6. References

Fu, P., J. Huang, C. Li, and S. Zhong, 2008: The properties of dust aerosol and reducing tendency of the dust storms in northwest China, *Atmos. Environ.*, ***42***, 5896-5904.

Huang, J., and co-auther. 2006a:, Possible influences of Asian dust aerosols on cloud properties and radiative forcing observed from MODIS and CERES, *Geophys Res. Lett.*, *33*, 2005GL024724.

Huang, J., and co-auther, 2006b: Dusty cloud radiative forcing derived from satellite data for middle latitude regions of East Asia, *Progress in Natural Science*. ***16***(10), 1084-1089.

Huang, J., and co-auther, 2006c:, Satellite based assessment of possible dust aerosols semidirect effect on cloud water path over East Asia, *Geophys. Res. Lett.*, 33,L19802, doi:10.1029/2006GL026561.

Huang, J., and co-auther, 2007a: Detection of Asia dust storms using multisensor satellite measurements, *Remote Sensing of Environment*, ***110***, 186-191.

Huang, J., and co-authers, 2007b:, Summer dust aerosols detected from CALIPSO over the Tibetan Plateau, *Geophys. Res. Lett.*, 34, L18805,doi:10.1029/2007GL029938.

Huang, J., and co-authors, 2008a:, An overview of the semi-arid climate and environment research observatory over Loess Plateau, *Advance in Atmospheric Sciences,* ***25***(6), 1-16.

Huang, J., and co-authors, 2008b: Long-range transport and vertical structure of Asian dust from CALIPSO satellite and surface measurements during PACDEX, *J. Geophys. Res*, in press.

Huang, J. and co-auther, 2008c, Taklimakan dust aerosol radiative heating derived from CALIPSO observations using the Fu-Liou radiation model with CERES constraints, submitted to *J. Geophys. Res.*

Huang, J. and co-auther, 2008d, Micro-Pulse lidar measurements of aerosol vertical structure over Loess Plateau, *Atmospheric and Oceanic Science Letters, in press.*

Liu, Z., D. Liu, J. Huang, and co-auther, 2008: Airborne dust distributions over the Tibetan Plateau and surrounding areas derived from the first year of CALIPSO lidar observations, *Atmos. Chem. Phys.*, ***8***, 5045-5060.

Su, J., J. Huang, Q. Fu, P. Minnis, J. Ge, and J. Bi, 2008: Estimation of Asian dust aerosol effect on cloud radiation forcing using Fu-Liou radiative model and CERES measurements, *Atmos. Chem. Phys.* ***8***, 2763-2771.

Wang, X., J. Huang, M. Ji, and K. Higuchi, 2008: Variability of East Asia dust events and their long-term trend, *Atmos. Environ.*, ***42***, 3156-3165.

Aerosol optical characteristics in SKYNET/GEOSS site from measurements of sky radiometers.

*Kazuma Aoki (University of Toyama), Tadahiro Hayasaka (Tohoku University), and SKYNET/GEOSS members

*kazuma @ sci.u-toyama.ac.jp

Abstract

Aerosol and cloud optical properties are studied using data from sky radiometer measurements. We started the long-term monitoring of aerosols and cloud by using a sky radiometer on SKYNET project since 1994. We are seeking in this data information on the aerosol optical characteristics at each site. The observation site of SKYNET/GEOSS is located mainly in Cape Hedo, Fukue-jima, Miyako-jima, Japan, and some Asian site. The Sky radiometer is a portable instrument that takes measurements of aerosols only during daytime under clear sky condition. It observes both direct solar irradiance and diffuse sky radiation at every 10 minutes. We present the temporal and spatial variation of the aerosol optical properties in each site using sky radiometer. The aerosol optical properties have a clearly spatial variability in Japan site and short period of time (e.g. Asian dust event). Alpha is low and AOD(0.5) are high during spring by Asian dust events.

Optical properties of aerosol in Seoul using skyradiometer measurements

Yeonjin Jung[1] · Jhoon Kim[1] · Ja-Ho Koo[2]

[1]Global Environment Lab./Dep. of Atmos. Sci., Yonsei University, Seoul, Korea, clover529@yonsei.ac.kr
[2]School of Earth and Atmos. Sci.,, Georgia Institute of Technology, Atlanta, Georgia, USA, zach45@yonsei.ac.kr

Abstract

Aerosols can have significant effects on global climate change through direct effects and indirect effects. In spite of the significance of such aerosol effects on climate, the accurate evaluation of aerosol radiative forcing have not been achieved due to our poor knowledge of aerosol properties and the mechanism of aerosol-cloud interaction on climate change. Since aerosols are rapidly increasing during the last decades, East Asia is expected to be important to see such anthropogenic aerosol effects. Among the East Asia, Seoul represents well about the characteristics of both anthropogenic and natural aerosols due to the influence of urbanization and dust from China.

In this study, aerosol optical properties over Seoul were examined to study representative properties of aerosol in East Asia using skyradiometer measurements during 2007. To investigate these properties, the temporal characteristics and the optical properties of aerosols in Seoul for Asian dust are analyzed. Aerosol optical depth shows a peak in July, and single scattering albedo and Ångström exponent show the lowest values in spring when Asian dust dominates. Size distribution is bimodal shape with one peak over 0.11 ㎛ in fine mode and the other peak over 11 ㎛ of coarse mode. The height of peak in coarse mode is relatively high in winter and spring, while the height of peak in fine mode is higher in autumn. In addition, backward trajectory analysis using HYSPLIT (Hybrid Single Particle Lagrangian Integrated Trajectory) is also executed to analyze the properties of aerosols according to characteristics of trajectory. Fast north-westerly from northern China flows into Seoul from December to April and slows as it approaches to May. Easterly generated from May continued to late autumn. These ground-based results compared with satellite are expected to contribute to understand the optical characteristics of aerosols over Seoul, Korea. This study would be informative to study the aerosol effects on global climate change in more detail.

Keywords: Aerosol optical depth, Single scattering albedo, Skyradiometer

1. Introduction

Atmospheric aerosols influence the climate directly by scattering and absorbing incoming solar radiation (Charlson *et al.*, 1992) and indirectly by acting as cloud condensation nuclei, therefore modifying the microphysics, radiative properties, and life time of clouds (Twomey *et al.*, 1984). There have been numerous previous studies to understand the radiative forcing by aerosols, but it has still large uncertainty. Analysis of the optical properties and temporal and spatial variability of aerosols are necessary to understanding the effects of aerosols. Long-term monitoring of aerosols using ground-base measurements is important in terms of that.

Many studies have examined aerosols optical properties in different regions using the data of AERONET (Aerosols RObotic NETwork) or SKYNET (SKYradiometer NETwork), which integrate the data measured by sunphotometers and Skyradiometers. Kim *et al.* (2004) examined the optical properties of aerosols with different regions such as desert and industrialized region. Eck *et al.* (2005) investigated the property of monthly average and wavelength dependency of optical parameters over the East Asia and Pacific region. They concluded that the peak of aerosol optical depth (AOD) and Ångström exponent (AE) appear from March to May when the Asian dust dominates over the East Asia. In addition, recent studies have shown that aerosols are transported from East Asia to the North Pacific. Higurashi *et al.* (2000) showed that both aerosol optical thickness

and Ångström exponent are large between 40°N and 60°N in April and July because of gas –to-particle conversion process in which are sources of anthropogenic aerosols in industrial areas.

In this study, we investigate various optical properties of aerosols in Seoul using the data measured by skyradiometer. There are many previous studies over Seoul, which presents the characteristics of not only anthropogenic aerosols due to the influence of urbanization and industrial activity but also natural aerosols such as Asian dust from China (Kim *et al.*, 2006). This study would be informative to understand the effects of aerosols on global climate in more detail.

2. Data

The ground-based Skyradiometer (PREDE, Model POM-02) is the instrument which measures the direct and diffuse solar irradiance to retrieve the aerosol optical parameters, and it produces initial data with the electronic value per 10 minutes at 11 channels (315, 340, 380, 400, 500, 675, 870, 940, 1020, 1600, 2200 nm). The raw data, as a input of Skyrad.pack,, are used to retrieve physical parameters of aerosol optical properties such as aerosol optical depth (AOD), single scattering albedo (SSA) and volume size distribution (Nakajima *et al.*, 1996). The data at Yonsei University is registered SKYNET since December 2005.

In our analysis, we used only seven wavelengths (340, 380, 400, 500, 675, 870, 020 m) to monitor aerosols. The other two wavelengths (315 and 940 nm) can be used to estimate total ozone and precipitable water (Shiobara *et al.*, 1996), topics beyond the scope of this study. Therefore, we have been examined the optical properties of aerosols from January to December in 2007.

3. Results

3.1. Aerosol Optical Depth (AOD)

Monthly mean AOD at 7 channels are shown in Figure 1. Due to different extinction efficiency in accordance with the size parameter as a function of wavelength and particle radius, AOD is different at each wavelength. Monthly mean AOD in Seoul increase after February to present the maximum value in July. After then, AOD decrease due to wet deposition by recipitatio in rainy season and low in autumn with low relative humidity. Seasonal AOD shows the highest values in spring and the lowest values in autumn. It seems that AOD is high in spring due to the inflow of dust particle and also in summer due to the growth of particle.

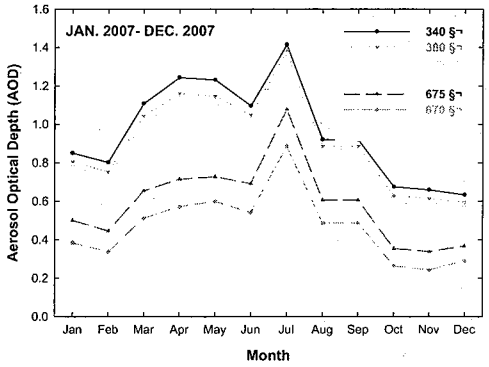

Figure 1. Monthly mean AOD for 7 wavelengths in 2007.

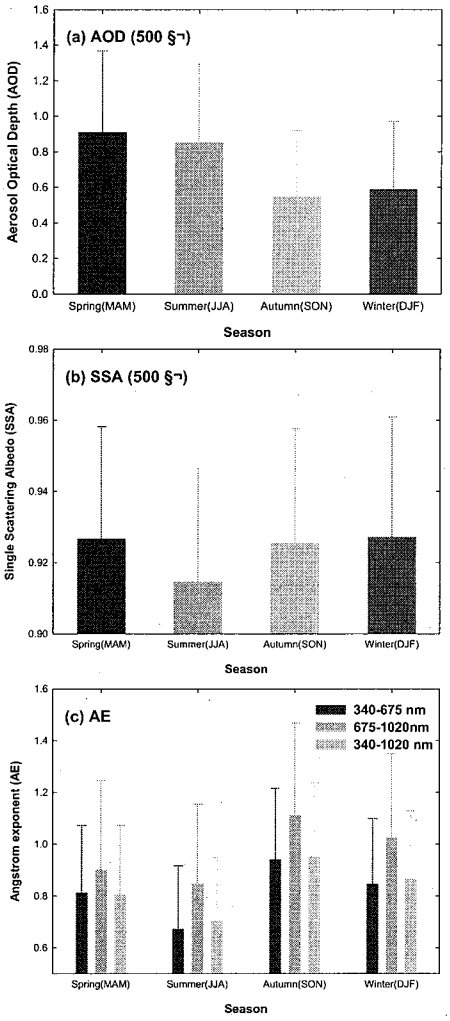

Figure 2. Seasonal mean value of (a) AOD at 500 nm, (b) SSA at 500 nm, and (c) AE at 340-675, 675-1020 and 340-1020 nm. The vertical error bars show the standard deviation, respectively.

3.2. Single Scattering Albedo (SSA)

Single scattering albedo describes the scattering properties of particles out of extinction. As it closes to 1, the particles have scattering more than absorption in their optical properties. Figure 3 shows the monthly mean SSA for 7 wavelengths. As seen in this Figure, SSA represents the lowest value of 0.91 in April when the Asian dust flows into Seoul from China in spring. After spring, SSA increase to 0.94 representing high characteristics of scattering. It is interested that there are difference in wavelengths, which shows the difference trends between shorter wavelength (340, 380 and 400 nm) and longer wavelength 9500, 675, 870, 1020 nm). It can be seen that radiation is absorbed in the wavelength at 202-422 nm for photo-dissociation under the clear-sky condition.

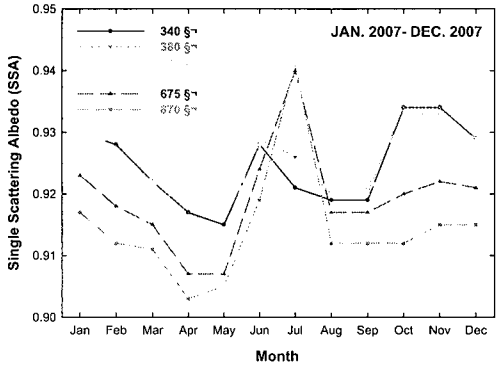

Figure 3. Monthly mean SSA for 7 wavelengths in 2007.

3.3. Ångström exponent (AE)

Ångström exponent (AE) is inversely related to the average size of the particles in the aerosols. The smaller the value shows, the larger the particle is. Figure 4 shows monthly mean of AE at three wavelength pairs of 340-675, 675-1020 and 340-1020 nm. AE for 340-1020 nm shows 1.0 in January and after then, it decrease to 0.4 in July due to the Asian dust. Low peak in July seems to be due to the influence of precipitation. As seen in Figure 2c, seasonal average in AE showed that the lowest value in spring because of Asian dust and the highest value in autumn because the air is clean after rainy season.

3.4. Volume size distribution

Volume size distribution according to the radius of particle characteristics the distribution of aerosol volume as a function of particle size. Generally bimodal distribution, which has one peak at fine mode and the other peak at coarse mode, is dominant in urban. Figure 5 shows the seasonal pattern of volume size distribution. These are analyzed for the clear-sky condition (51 days) that when cloud amount is less than 1.0 tenth. Volume size distribution over Seoul has the bimodal distribution with one peak of 0.11 ㎛ of fine mode and the other peak of 1 ㎛ of coarse mode. Seasonally the height of peak in coarse mode is relatively high in winter and spring, while the height of peak in fine mode is higher in autumn.

4. Summary

Measurements of the optical properties of aerosols from skyradiometers over Seoul are analyzed in 2007. Monthly mean aerosol optical depth (AOD) has a peak in July because of weak ventilation. When the Asian dust dominants in spring, single scattering albedo (SSA) and Ångström exponent (AE) show the lowest value. Volume size distribution have the peak of 0.11 ㎛ and 11 ㎛.

Because the properties of aerosols are related to the characteristics of transported aerosols, back trajectory analysis is also necessary to inform the origin. Using the HYSPLIT4 (Hybrid Single – Particle Lagrangian Integrated Trajectory 4), we would be analyzed the difference of characteristics of aerosols depending source region, path and direction of trajectory. In addition, these ground-based measurements compared with satellite data would be provided to accumulate the knowledge of aerosols.

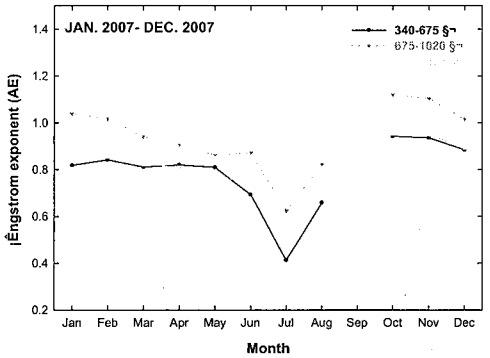

Figure 4. Monthly mean AE for 3 wavelength pairs (340-675 nm, and 675-1020 nm and 340-1020 nm) in 2007.

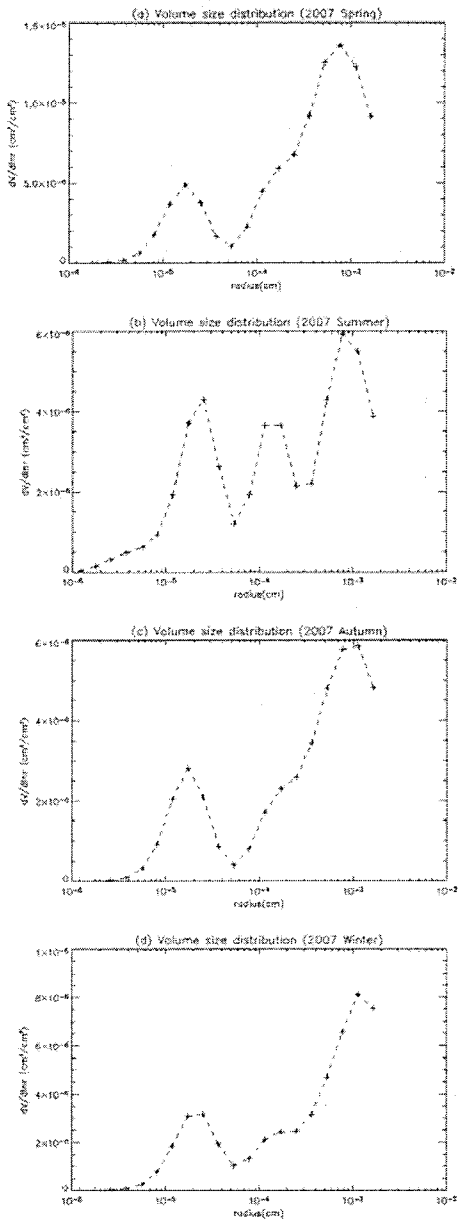

Figure 5. The seasonal pattern of volume distributions. These are retrieved for clear-sky conditions (cloud amount less than 1.0 tenth) in (a) spring, (b) summer, (c) autumn and (d) winter.

Acknowledgements

This work is supported by NIER (National Institute of Environment Research) research grant project 'On the foundation of Asian dust chemistry modeling (Development of satellite remote sensing algorithm)'.

References

1) Charson, R. J., S. E. Schwarts, J. M. Hales, R. D. Cess, J. A. Coakley, Jr., J. E. Hansen, D. J. Hofmann, 1992: Climate forcing by anthropogenic aerosols. *Science*, **255**, 423-430.

2) Eck, T. F., B. N. Holben, O. Dubovik, A. Smirnov, P. Goloub, H. B. Chen, B. Chatenet, L. Gomes, X.-Y. Zhang, S.-C. Tsay, Q. Ji, D. Giles, and I. Slutsker, 2005: Columnar aerosol optical properties at AERONET sites in central eastern Asia and aerosol transport to the tropical mid-Pacific. *J. Geophys. Res.*, **110**, D06202, doi:10.1029/2004JD005274.

3) Higurashi, A., T. Nakajima, B. N. Holben, A. Simrnov, R. Frouin and B. Chatenet, 2000: A study of global aerosol optical climatology with two channel AVHRR remote sensing. *J. Climate*, **13**, 2011-2027.

4) Kim, D.-H., B.-J. Sohn, T. Nakajima, T. Takemura, T. Takemura, B.-C. Choi, and S.-C. Yoon, 2004: Aerosol optical properties over East Asia determined from ground-based sky radiation measurements. *J. Geophys. Res.*, **109**, D02209, doi:10,1029/2003JD003387.

5) Kim, S. W., S. –C. Yoon, J. Kim, and S.-Y. Kim, 2006: Seasonal and monthly variations of columnar aerosol optical properties over East Asia determined from multi-year MODIS, LIDAR and AERONET Sun/sky Radiometer Measurements. *Atmos. Environ.*, **41**, 1634-1651.

6) Nakajima, T., G. Tonna, R. Rao, P. Boi, Y. Kaufman and B. Holben, 1996: Use of sky brightness measurements from ground for remote sensing of particulate polydispersions. *Appl. Opt.*, **35**, 2672–2686.

7) Shiobara, M., J. D. Spinhirne, A. Uchiyama and S. Asano, 1996: Optical depth measurements of aerosol, cloud, and water vapor using sun photometer during FIRE cirrus IFO II. *J. Appl. Meteor.*, **35**, 36–46.

8) Twomey, S. A., M. Piepgrass and T. L. Wolfe, 1984: An assessment of the impact of pollution on global cloud albedo. *Tellus*, **36**, 356-366.

Recent decade variations of aerosol optical properties and radiative forcing inferred from ground-based broadband radiometers at Tsukuba

Rei Kudo[1], Akihiro Uchiyama[1], Akihiro Yamazaki[1], Eriko Kobayashi[1]

[1]*The Third Research Laboratory, Climate Research Department, Meteorological Research Institute, Japan Meteorological Research Agency, 1-1 Nagamine, Tsukuba-shi, Ibaraki-ken, 305-0052, Japan,reikudo@mri-jma.go.jp*

Abstract

Global average trend in solar radiative flux at the Earth's surface increases since the mid 1980's ("global brightening"). This is seen under both the cloudy and cloudless conditions. The aerosol change is one of the most important factors for the radiative flux change at the surface. The aerosol optical thickness is related to the magnitude of the surface radiative forcing, and the aerosol single scattering albedo influences the slope of the aerosol radiative forcing. Therefore, the optical thickness and single scattering albedo are important parameters for the understanding of the aerosol radiative forcing change. We have developed a new method to estimate the aerosol optical parameters from the ground-based broadband radiometers. The method assumes the 4 aerosol components, and estimates the aerosol optical thickness, single scattering albedo, and asymmetry factor from the direct and diffuse fluxes in VIS and NIR regions. We applied this method to the recent decade observations (April 1998 to May 2008) at Tsukuba, Japan. The daily mean global flux in cloudless condition increased by 0.47 Wm^{-2} per year. The daily mean aerosol radiative forcing decreased by 0.55 Wm^{-2} per year. The aerosol radiative forcing tends to decrease, and the radiative flux tends to increase at Tsukuba during 1998－2008. On the other hands, the aerosol optical thickness had no tendency, but the aerosol single scattering albedo and asymmetry factor increased by 0.011 and 0.003 per year. The recent decadal decrease of the aerosol radiative forcing was caused by the aerosol absorptive and forward scattering characters.

Keywords : CEReS, 14 th International symposium

1. Introduction

Global average trend in solar radiative flux at the Earth's surface increases since the mid 1980's ("global brightening"). This is seen under both the cloudy and cloud-free conditions[1)]. The aerosol change is one of the most important factors for the radiative flux change at the surface.

The aerosol particles strongly affect the solar radiative flux at the surface by scattering and absorption. In particular, the absorbing aerosols have larger negative surface radiative forcing than other primally scattering aerosols and greenhouse gases by factors of 3 to 10[2)]. Therefore, not only aerosol loading but also aerosol absorptive character is needed to evaluate the surface radiative effect of aerosols.

In general, the aerosol optical thickness (loading) is related to the magnitude of the surface radiative forcing, and the aerosol single scattering albedo (ratio of scattering to scattering + absorption) influences the slope of the aerosol surface radiative forcing. Therefore, the long-term variations of the optical thickness and single scattering albedo are important for the understanding of global brightening.

For the estimating the long-term variations of aerosol optical properties, the broadband radiometers are useful. The instruments have been working in long period. In this study, we have developed a new method to estimate the aerosol optical parameters from ground-based broadband radiometers. We applied this method to the recent 10 years observation at Tsukuba, Japan, and studied the tendencies of aerosol surface radiative forcing and their optical properties changes.

2. Methods

2-1. Observation

We have observed the broadband fluxes with some broadband radiometers since 1997. The instruments are calibrated regularly in JMA Meteorological Instrument Calibration Center in Tsukuba. The observation items are the global, direct and diffuse fluxes in total and NIR bands. In this study, we used the global fluxes as the sum of the direct and diffuse fluxes, and calculated VIS-fluxes as the differences between total- and NIR-fluxes. The analysis period is April 1998 to May 2008.

2-2. Estimation of daily mean aerosol radiative forcing

For the climate effect of aerosols, the daily mean surface

radiative forcing under the cloudless condition is used in many papers. These papers estimated the daily mean global flux by the polynomial or power law fit to the instantaneous fluxes the under cloudless condition. We tested some fits, and selected the most stable second-order polynomial fit.

$$F = a(\cos\theta)^2 + b(\cos\theta),$$

F is an instantaneous global flux. θ is the solar zenith angle. We assumed the global flux is zero at $\theta = 0$.

The daily mean radiative forcing is calculated as the difference between the daily mean observed global flux and the daily mean global flux calculated without aerosols. The fluxes without aerosols are calculated by the modified computational scheme of Nishizawa et al. 2004[3].

2-3. Estimation of aerosol optical properties

Aerosol optical thickness, single scattering albedo and asymmetry factor are estimated from observed the direct and diffuse fluxes in VIS and NIR regions. Our method assumes an external mixture of 4 types of aerosol components, and searches their optimum combination for the observed fluxes. The assumed aerosols are water soluble, soot, sea salt, and mineral dust of OPAC[4]. Water soluble and soot are small particles, and sea salt and mineral dust are large particles. Water soluble and sea salt are less absorptive than soot and mineral dust. Fig. 1 shows the dependencies of these assumed aerosols to the direct and diffuse fluxes in VIS and NIR regions. The upper figure shows the direct flux differences (VIS − NIR), and the under figure shows the diffuse flux differences (VIS − NIR). The small particles are more sensitive to the direct flux differences than the small particles. The sizes of aerosols are divided by the direct flux differences. The non-absorptive aerosols increase the diffuse flux differences, but the absorptive aerosols decrease them. The absorptive characters of the aerosols are divided by the diffuse flux differences.

We tested this method for some aerosol models of OPAC. The retrieval results are shown in Table 1. The estimated optical properties are good agreement with the truth. The estimated accuracies are less than 0.05 for less than 1.025 μ m.

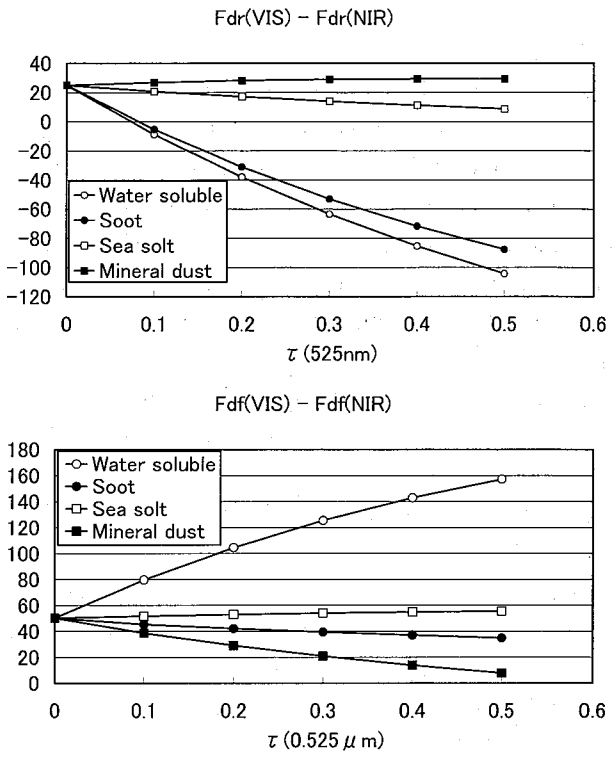

Fig. 1 Flux differences between VIS and NIR direct fluxes (upper) and between VIS and NIR diffuse fluxes (under) as functions of the optical thickness of 4 aeorosls.

Table 1 The errors of estimated aerosol optical properties (525nm) in simulation.

	Optical thickness	Single scattering albedo	Asymmetry factor
Continental clean	0.000	-0.002	-0.003
Continental average	0.000	0.001	-0.003
Continental polluted	0.000	0.000	-0.002
Urban	0.001	0.000	-0.002
Desert	0.000	-0.010	0.024
Maritime clean	0.001	-0.005	0.000
Maritime polluted	0.000	0.003	0.001

3. Results

3-1. Tendency of daily mean aerosol radiative forcing

Fig. 2 show the monthly means of the daily mean global flux and the daily mean aerosol radiative forcing. Since the seasonal variations are very large, it is difficult to estimate the decadal tendencies. Therefore, we excluded the seasonal variations. Fig. 3 shows the yearly mean seasonal variations calculated from the monthly means (Fig. 3). Using the deviations from the seasonal variations, the recent decade tendencies were calculated (Fig. 4). The daily mean global flux in cloudless condition increased by 0.47 Wm^{-2} per year (0.26 for VIS, 0.22 for NIR). The daily mean aerosol radiative forcing decreased by 0.55 Wm^{-2} per year (0.33 for VIS, 0.22 for NIR).

We also calculated the tendencies for the daily mean fluxes and cloud + aerosol radiative forcings under all conditions (cloudy and cloudless skies). The daily mean global flux in all conditions increased by 1.28 Wm^{-2} per year (0.84 for VIS, 0.44 for NIR). The daily mean cloud + aerosol radiative forcing decreased by 1.13 Wm^{-2} per year (0.77 for VIS, 0.37 for NIR).

The cloud and aerosol radiative forcing tends to decrease, and the radiative flux tends to increase at Tsukuba during 1998−2008.

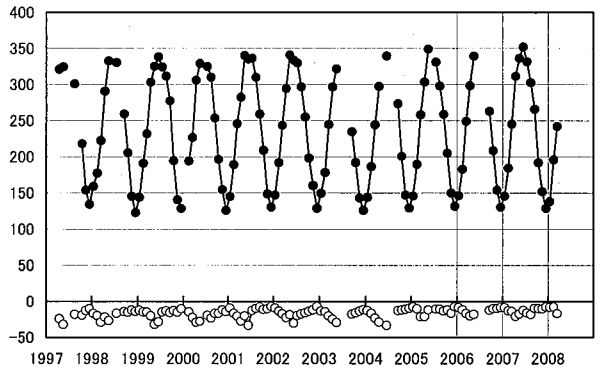

Fig. 2 Monthly means of daily mean global flux [W/m^2] (closed circles) and daily mean aerosol radiative forcing [W/m^2] (open circles).

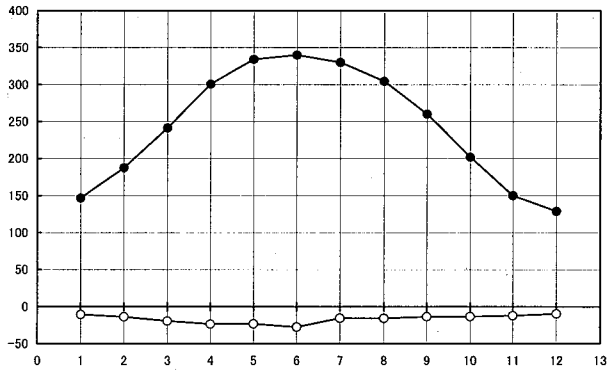

Fig. 3 Yearly mean seasonal variations of daily mean global flux [W/m^2] (closed circles) and daily mean aerosol radiative forcing [W/m^2] (open circles).

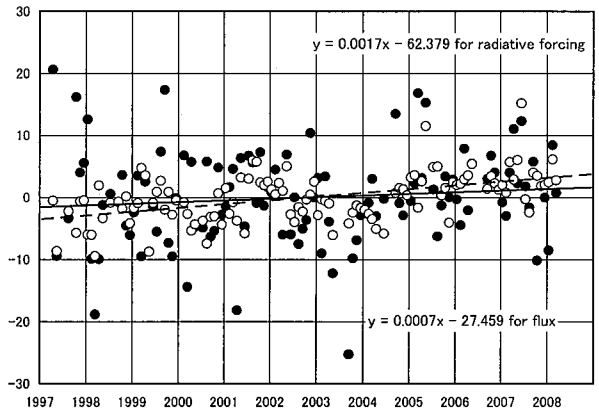

Fig. 4 Deviations from the yearly mean seasonal variations. Global flux [W/m^2] (filled circles). Aerosol radiative forcing [W/m^2] (open circles). Regression lines for global flux (solid line) and radiative forcing (dashed line).

3-2. Tendencies of aerosol optical properties

Fig. 5 shows the monthly means of the daily mean optical thickness, single scattering albedo, and asymmetry factor. They are the values at 525nm. Optical thickness is seen to decrease slightly. On the other hands, single scattering albedo and asymmetry factor increase clearly. Fig. 6 shows the tendencies of deviations from normal values. The deviations are calculated by the same way as the radiative forcing. The optical thickness has no tendency, but the single scattering albedo and asymmetry factor increase by 0.011 and 0.003 per year. In the recent ten decade, the aerosol loading was almost constant, but the absorptive character decreased clearly, and the forward scattering character increased. This result indicates the surface flux changes by aerosols are caused by not the aerosol loadings but the

aerosol absorption and forward scattering characters.

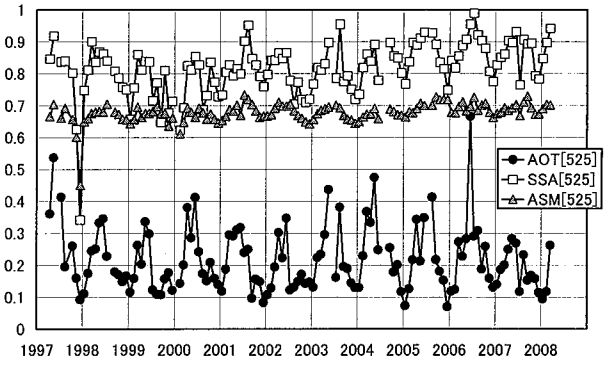

Fig. 5 Same as Fig. 2, but for optical thickness (closed circle), single scattering albedo (open square), and asymmetry factor (closed triangle).

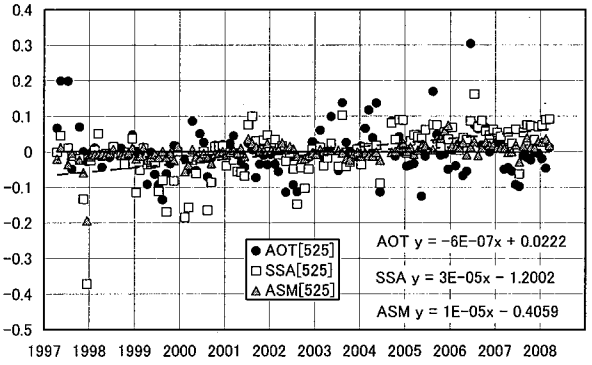

Fig. 6 Same as Fig. 4, but for optical thickness (closed circle), single scattering albedo (open square), and asymmetry factor (closed triangle). Regression lines for optical thickness (solid line), single scattering albedo (long dashed line), and asymmetry factor (short dashed line).

4. Summary

The recent decade tendencies of the aerosol radiative forcing and the aerosol optical properties were studied. The aerosol radiative forcing decreased, and the surface flux increased in the recent decade. These tendencies were caused by not the aerosol optical thickness but the aerosol single scattering albedo and asymmetry factor.

References

1) Wild et al. From Dimming to Brightening: Decadal Changes in Solar Radiation at Earth's Surface. Science 308, doi:10.1126/science.1103215 (2005).

2) Ramanathan et al. Indian Ocean Experiment: An integrated analysis of the climate forcing and effects of the great Indo-Asian haze. J. Geophs. Res. 106, 28271-28398 (2001).

3) Nishizawa et al. SEASONAL VARIATION OF AEROSOL DIRECT RADIATIVE FORCING AND OPTICAL PROPERTIES ESTIMATED FROM GOUND-BASED SOLAR RADIATION MEASUREMENTS. J.Atmos. Sci. 61, 57-72 (2004).

4) Hess et al. Optical Properties of Aerosols and Clouds: The Software Package OPAC. Bull. Ame. Met. Soc. 79, 831-844 (1998).

Characterization of Asian aerosols at Fukue-jima island using in-situ observation and remote sensing data

Mayumi Hibino[1], Yoko Inoue[1], Makoto Kuji[1], Sachiko Hayashida[1], Tadahiro Hayasaka[2]

[1]*Faculty of Science, Nara Women's University, Kita-uoya Nishimachi, Nara 630-8506, Japan*

[2]*Center for Atmospheric and Oceanic Studies, Tohoku University, 6-3 Aoba, Aramaki, Aoba, Sendai 980-8578, Japan*

Corresponding: Makoto Kuji (makato@ics.nara-wu.ac.jp)

Abstract

We investigated particle size and shapes using in-situ observation and ground-based remote sensing data to characterize the Asian aerosols during Kosa events in particular. In this study, we analyzed the data observed in Fukue-jima island (32.6 ° N, 128.8 ° E) from 2003 to 2004. We estimated the particle size and sphericity using OPC and LIDAR observation data, respectively. We made a detailed match-up analysis based on the report of Kosa event at Fukue-jima by Japan Meteorological Agency. As a result, we have a linear relationship between particle size and sphericity in Kosa events, which is clearly different from the other seasons statistically. We further confirmed that larger and nonspherical particles were not exclusively dominated in Kosa events, compared to the other seasons. This also suggests that smaller and spherical particles, such as sea salts from the surrounding ocean or air pollution materials from mega cities, were mixed with Kosa aerosols statistically. We will further discuss the results with other match-up analyses using skyradiometry, and will compare the results to regional transport model simulations so as to identify the Asian aerosols around this region in detail.

Keywords **:** Aerosol, Asian dust, OPC, LIDAR, Skyradiometer

1. Introduction

Aerosol has a crucial role in earth radiation budget on a global scale as well as in a source of air pollution on a regional scale. We have Yellow Sand (Kosa) events over East Asia in springtime every year. Kosa aerosol usually consists of mineral dusts, which originates in Gobi or Taklimakan desert. Recently, several studies suggest that Kosa aerosol is mixed with smaller polluted materials after the air mass travels over mega cities in East Asia. [1)]

Aerosol has many aspects to be considered, such as amount, size, sphericity, composition, spatiotemporal distribution, and so forth. Consequently, it is better to combine several observation data to investigate the characteristics of Asian aerosols, such as mixture state of several component s in the atmosphere.

In this study, we investigate Asian aerosol characteristics through analyses of direct sampling data at surface and ground-based remotely sensed ones at Fukue-jima island from 2003 to 2004.

2. Analyses of data

Fukue-jima is considered as one of the best sites to observe the aerosol all through the year because it is located between Korean Peninsula and western Japan where we can observe the Asian aerosol including Kosa aerosol with little influence of local air pollution.

We have several kinds of in-situ observation data and remotely sensed data at Fukue-jima, such as Optical Particle Counter (OPC), LIDAR, skyradiometer, and so on.

We describe parameters from each sensors used in this study as follows.

a) Aerosol amount and size from OPC data at surface

From OPC data, we can define a parameter "Vtotal" as follows:

$$V_{total} = \sum_{j=1}^{5} \frac{4}{3} \pi \left(\frac{d_j}{2} \right)^3 n_j . \qquad (1)$$

This Vtotal is a sphere-equivalent total aerosol volume in the unit of μm^3. We use this paramter as an index of aerosol amount at surface in this study.

We can also define a parameter "gamma" as follows:

$$\gamma = \frac{\log_{10}(\sum_j n_j \mid d_j \geq 2.0\mu m)}{\log_{10}(\sum_j n_j \mid d_j \geq 0.3\mu m)} . \qquad (2)$$

This gamma is a logarithmic number fraction of coarse mode particles whose diameter is larger than and equal to 2.0 μm, to total particles whose diameter larger than and equal to 0.3 μm. the range of gamma value is from 0 to 1. the value 0 corresponds to no coarse mode aerosol and the value 1 to no fine mode particles. We use this gamma is an index for coarse mode particles on a number basis at surface.

Aerosol number is one of the important parameters for Aerosol indirect effect study for example. Nakajima et al. [2] studied the relationship between cloud droplet number and aerosol columnar number. Recently, NASA MODIS provides Fine Mode Fraction (FMF), which is defined as the optical thickness fraction of fine mode particles (radius less than 1.0 μm) to total particles. [3]

b) Aerosol sphericity from LIDAR data of the lower atmosphere

From LIDAR data, we can define a parameter "eta" as follows:

$$\eta = \frac{\tau_{lidar(dust)}}{\tau_{lidar(dust)} + \tau_{lidar(sphere)}}. \qquad (3)$$

This eta is an optical thickness fraction of "dust" (non-spherical) particles to total optical thickness, which is consisted of both dust and "sphere "(spherical) particles. The aerosol extinction profiles for both dust (non-spherical particles) and sphere (spherical particles) are derived assuming S1 parameter 50. [4] The eta is an index for non-spherical particles on an optical measurement basis. It is also a proxy parameter as a depolarization for a lower atmosphere. The parameter is estimated based on extinction profiles for both dust and sphere particles. The integration of extinction profiles is carried out only from surface to the top height more than or equal to 3km, for which the non-negative extinction values of the lower atmosphere. The range of the value eta is from 0 to 1. The value 0 corresponds to the situation all aerosols consist of sphere particles only, while the value 1 do non-sphere (dust) particles only.

c) Aerosol optical thickness and size from skyradiometer data over Fukue-jima island

From skyradiometer data, we have aerosol optical thickness ("tau_a") and Angstrom exponent ("alpha") defined as follows:

$$\tau = \tau_{0.5}\left(\frac{\lambda}{0.5}\right)^{-\alpha}, \qquad (4)$$

where tau_0.5 is aerosol optical thickness at wavelength 0.5μm and lambda is a wavelength in μm. [2] The alpha is an index for a columnar aerosol size.

In the following section, we show the results from match-up analysis that the three measurements with OPC, LIDAR and skyradiometer, are coincident within five minutes.

3. Results and discussion

We compare three parameters (gamma, eta, and alpha) in the cases of Kosa events defined by Japan Meteorological Agency (JMA) and in all match-up cases from 2003 to 2004 at Fukue-jima island. As a result, we have five match-up cases coincident to the JMA-defined Kosa events (9:00 and 15:00 JST April 3, 9:00 and 15:00 JST April 22, and 9:00 JST May 7, 2004).

a) Comparison between OPC and LIDAR

Figure 1 illustrates the relationship between gamma and eta for Kosa events defined by Japan Meteorological Agency at Fukue-jima island.

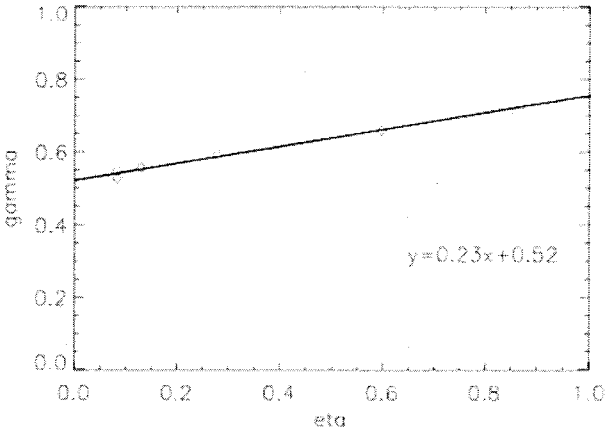

Fig. 1. A scatter diagram between gamma vs. eta, only for Kosa events defined by Japan Meteorological Agency. A linear regression line is overlaid.

From Fig. 1, we have linear relationship between gamma and eta, which suggests the more non-spherical particles, the larger particles size, even for only five events' case study. Figure 1 also suggests that larger and non-spherical particles necessarily dominate and there exist smaller and spherical

aerosol particles while eye observer at surface reports Kosa events.

Figure 2 illustrates the relationship between gamma and eta for all match-up data at Fukue-jima island from 2003 to 2004. We have plots with three colors such as red, blue, and green, which correspond to the Vtotal value of more than and equal to 10^4.5 (μm^3), between more than 10^4.0 and lower than 10^4.5, and less than 10^4.0, respectively. The red means larger amount of aerosols which includes the Kosa events in Fig. 1.

Fig. 2. Same as Fig. 1, except for all cases that are available in match-up analyses among OPC, LIDAR, and skyradiometer from 2003 to 2004. A regression line (solid) is overlaid for all match-up plots as well as the regression line (dashed) for the Kosa events in Fig. 1.

From Fig. 2, we find that the logarithmic number ratio of coarse mode particles are almost constant, while the linear regression line for Kosa events has some positive slope, which means larger variation in size with Kosa events. Comparing Figs. 1 and 2, non-sphericity, i.e., eta has the maximum value 1.0 in non Kosa events while it does up to 0.6 even in Kosa events, which suggests smaller and spherical particles are also increased in the Kosa events.

b) Comparison between skyradiometer and LIDAR

Figure 3 illustrates the relationship between alpha and eta for Kosa events defined by Japan Meteorological Agency at Fukue-jima island.

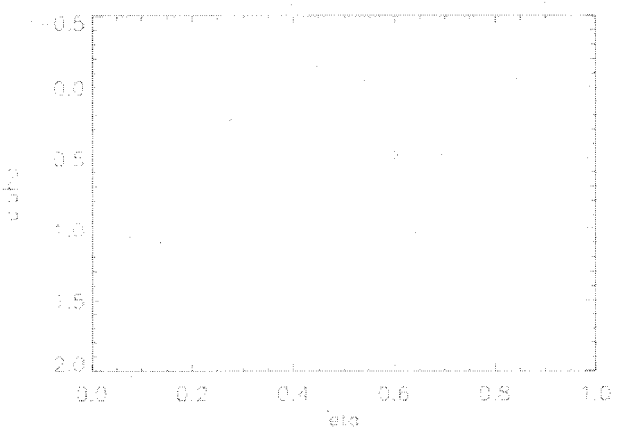

Fig. 3. Same as Fig. 1, except for relationship between alpha vs. eta. Note that the ordinate alpha is plotted in reverse order corresponding to particle size.

From Fig. 3, we have a positive correlation qualitatively, but it is not so clear as the relationship between gamma and eta in Fig. 1. One of the possible reasons is that skyradiometer has information of upper troposphere where OPC and LIDAR are not sensitive.

Figure 4 illustrates the relationship between alpha and eta for all match-up data at Fukue-jima island from 2003 to 2004.

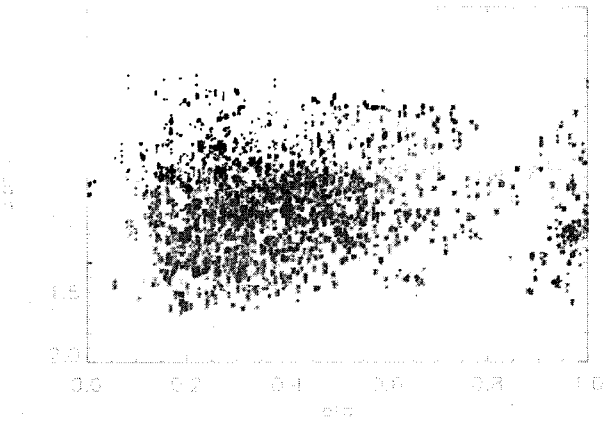

Fig. 4. Same as Fig. 2, except for relationship between alpha vs. eta.

From Fig. 4, we do not have clear relationship between alpha and eta at present. But, such comparison among OPC, LIDAR, and skyradiometer has a possibility to provide us a vertical aerosol microphysics distribution in future.

4. Concluding remarks

We analyze the data of optical particle counter (OPC), LIDAR, and skyradiometer so as to investigate aerosol

characteristics observed at Fukue-jima island from 2003 to 2004.

We found that spherical and smaller particles are mixed with non-spherical and larger particles even in Kosa events defined by Japan Meteorology Agency. The comparison between OPC and LIDAR data analyses, also suggests that eye observer at surface has some specific sensitivity in terms of aerosol particle amount, size and sphericity of the lower-atmosphere.

It is necessary to investigate detailed processes for each specific event as well as wide area picture with regional model results and satellite remote sensing data.

Acknowledgements

The authors are grateful to Dr. A. Shimizu of NIES, Dr. K. Aoki of University of Toyama, Dr. N. Kikuchi of NIES, and Prof. T. Takamura of CEReS for their valuable comments. The OPC, LIDAR, and skyradiometer data used in this study were provided by NIES / CCSR / CEReS / RIHN.

References

1) Y. Hara, K. Yumimoto, I. Uno, A. Shimizu, N. Sugimoto, Z. Liu, and D. M. Winker, Asian dust outflow in the PBL and free atmosphere retrieved by NASA CALIPSO and an assimilated dust transport model. ACPD, 8, 8715-8742, 2008.

2) Nakajima, T., A. Higurashi, K. Kawamoto, and J. E. Penner (2001), A possible correlation between satellite-derived cloud and aerosol microphysical parameters, Geophys. Res. Lett., 28, 1171– 1174.

3) Remer, L. A., et al. (2008), Global aerosol climatology from the MODIS satellite sensors, J. Geophys. Res., 113, D14S07, doi:10.1029/2007JD009661.

4) Shimizu, A., N. Sugimoto, I. Matsui, K. Arao, I. Uno, T. Murayama, N. Kagawa, K. Aoki, A. Uchiyama, and A. Yamazaki (2004), Continuous observations of Asian dust and other aerosols by polarization lidars in China and Japan during ACE-Asia, J. Geophys. Res., 109, D19S17, doi:10.1029/2002JD003253.

Characterization of atmospheric aerosols at the Observatory for Atmospheric Research at Phimai, Thailand, a station of SKYNET

Haruo Tsuruta[1], Jinchula Chotpitayasunon[2], Boossarasiri Thana[2], Pradeep Khatri[3] Tamio Takamura[3], Tadahiro Hayasaka[4], Teruyuki Nakajima[1]

[1]*Center for Climate System Research, The University of Tokyo, 5-1-5 Kashiwanoha, Kashiwa, Chiba, JAPAN: haru2004@ccsr.u-tokyo.ac.jp, teruyuki@ccsr.u-tokyo.ac.jp*

[2]*Department of Geology, Chulalongkorn University, Phayathai road, Bangkok 10330, Thailand: share7@hotmail.com, boossara@geo.sc.chula.ac.th*

[3]*Center for Environmental Remote Sensing (CEReS), Chiba University, 1-33 Yayoi-cho, Inage-ku, Chiba 263-8522, JAPAN, pradeep.nep@gmail.com, takamura@faculty.chiba-u.jp*

[4]*Center for Atmospheric and Oceanic Studies, Tohoku University, 6-3, Aoba, Aramaki, Aoba-ku, Sendai 980-8578, JAPAN, tadahiro@m.tains.tohoku.ac.jp*

Abstract

Atmospheric aerosols were measured at the Observatory of Atmospheric Research, in Phimai, Thailand, during 2006-2008, which is one of the stations of SKYNET. The major chemical components of aerosols were much higher in the dry seasons than in the wet seasons. In fine particles, ammonium sulfate, and elementary and organic carbons were major components. The concentration ratio of elementary carbon to sulfate in the dry seasons was much higher than that at Amami-Oshima in southwest Japan, where the anthropogenic aerosols from fossil-fuel combustion were transported from the urban-industrial area of the east coast of China. Single scattering albedo measured by sky radiometer was >0.95 in the wet seasons, and much higher than in the dry seasons. According to the MODIS fire maps, many fires possibly due to the biomass burning of agricultural residues were detected in the dry seasons almost all over Thailand. These results clearly indicate that the aerosols emitted from biomass burning could affect on atmospheric environment, and radiation budget in southeast Asia.

Keywords: aerosols, Asian monsoon, biomass burning, chemical composition, single scattering albedo

1. Introduction

Chemical and optical properties of atmospheric aerosols in a regional scale are expected to be much different because there are many different sources of aerosols in natural and anthropogenic origins. As one of the APEX-E3 field campaign program, atmospheric aerosols were measured at Amami-Oshima (28.44°N, 129.70°E) located in the southwestern part of Japan, in the 2003 spring season[1)], and chemical characterization of aerosols indicate that ammonium sulfate, EC and OC was the major components in fine particles ($PM_{2.5}$), and soil dusts and sea salt particles were dominant in coarse particles. Single scattering albedo was estimated independently by chemical composition (SSAc) and direct optical measurement (SSAo) at the surface (Fig. 1). The SSAc was in a range of 0.88-0.97, and the SSAo was a little bit lower than the SSAc, although the time series variation was almost similar between SSAc and SSAo.

In contrast, atmospheric aerosols in Southeast Asia are frequently affected by the aerosols emitted by biomass burning of crop residues and/or forest fires in regional scale. It suggests that chemical and optical properties of atmospheric aerosols are also different from those at Amami-Oshima, in East Asia. The purpose of this study is to introduce the preliminary results from the aerosol measurements at Phimai, Thailand, in Southeast Asia.

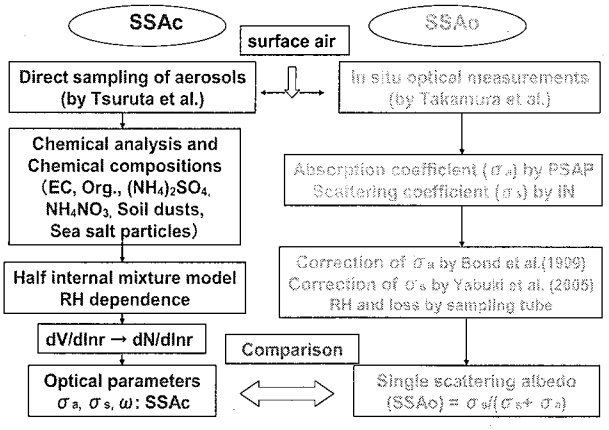

Fig. 1 Methodology to calculate single scattering albedo from chemical compositions (SSAc) and optical measurements (SSAo)

2. Methods

Atmospheric aerosols were measured at the Observatory of Atmospheric Research (OAR) in Phimai (15.18°N, 102.57°E), one of the stations of SKYNET, located in northeastern Thailand. The first and second sampling period was from June 2006 to February 2007, and from July 2007 to August 2008, respectively. A series of half-day samplings in the daytime and nighttime for three days was made twice in almost every month. Atmospheric aerosols were collected on the filters of 47 mm in diameter (d) by using multi-nozzle cascade impact (MCI) samplers. These samplers were stored in a shelter fixed on the roof of the station house, to directly collect atmospheric aerosols with no use of any sampling tube. The four-size range of atmospheric aerosols was d<1.0μm, 1.0μm<d< 2.5 μm, 2.5μm <d< 10 μm, and 10 μm<d. Chemical analysis was made for OC and EC by optical thermal OC/EC analyzer, water soluble ions by IC, and trace elements by PIXE. Single scattering albedo was analysed by using the original data measured by sky radiometer at the OAR. Meteorological data and the concentration of atmospheric CO and O_3 were also used, which were also measured at the OAR.

The air masses arrived at Phimai was estimated by using the backward trajectory analysis of NOAA ARL HYSPLIT MODEL[2] (http://www.arl.noaa.gov/ready/hysplit4.html/). Biomass burning over Thailand was estimated by using the MODIS fire maps[3] (http://rapidfire.sci.gsfc.nasa.gov/). Some chemical components of atmospheric aerosols[4] was also used, which was measured during August-December 2002, at the Thana Rata station in Cameron Highlands, Peninsular Malaysia, one of the air quality monitoring stations by Malaysia Meteorological Department.

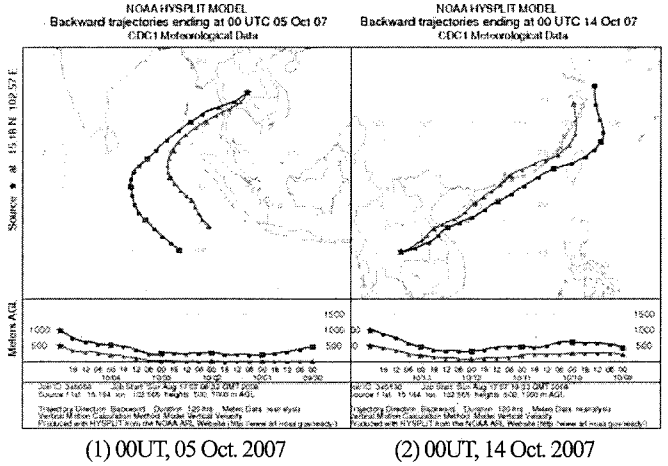

(1) 00UT, 05 Oct. 2007 (2) 00UT, 14 Oct. 2007

Fig. 2 A five-day backward trajectory of air masses arrived at Phimai by NOAA HYSPLIT MODEL

3. Results and Discussion

It is well known that the wind patterns at the site in Thailand are controlled by the Asian monsoon. The surface wind direction measured at the OAR in 2007 showed that a wet season when the southwesterly wind from the Indian Ocean prevailed, finished around on 10 October, 2007. After that, the wind direction gradually shifted to east or northeast, and a dry season started. The backward trajectory analysis clearly showed that the air masses arrived at Phimai, were transported from the Indian Ocean in the wet season, while in the dry season, they were transported from Laos and Vietnum/ the East China Sea (Fig. 2).

3.1. Time series of major chemical components

Time series of the daily mean EC and OC concentration was much higher in the dry season than in the wet season (Fig. 3), and the mean total concentration of OC was 3.5 times higher than that of EC in all the period. The mean EC in $PM_{2.5}$ had about 90 and 95 % of the mean total concentration in the wet and dry season, respectively, while the mean OC in $PM_{2.5}$ had about 65 and 80 % of the total in the wet and dry season, respectively. It suggests that the gas phase organic carbon might be absorbed in the coarse particle in the wet season, or the major sources of EC and OC might be different between the wet and dry season.

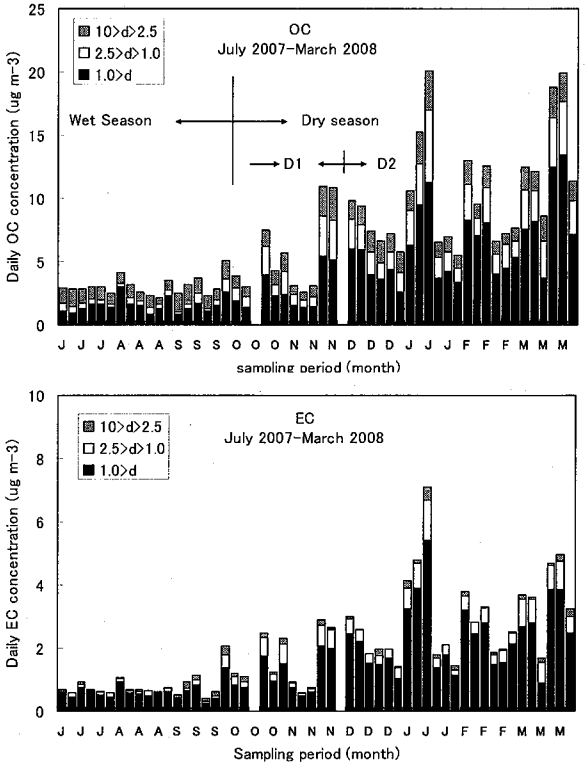

Fig. 3 Time series of daily mean OC and EC concentrations in $PM_{2.5}$ at Phimai (July 2007- March 2008)

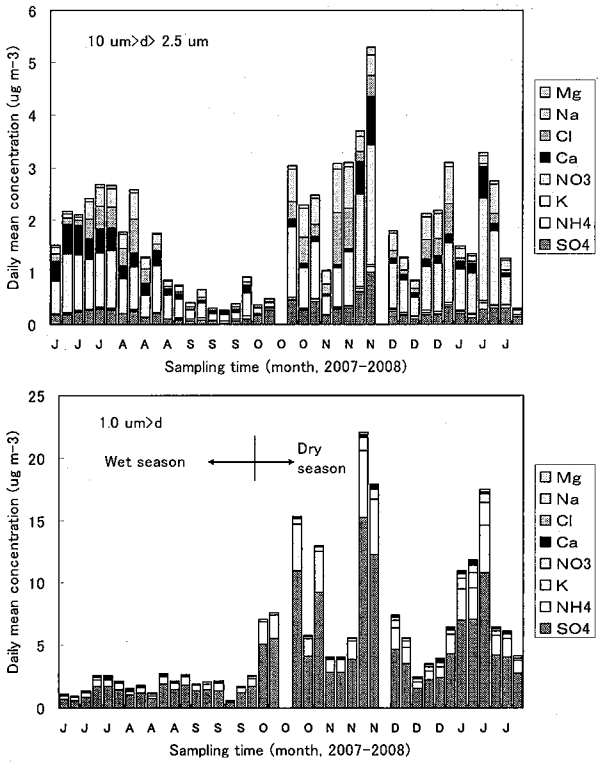

Fig. 4 Time series of daily mean concentrations of major ions in coarse (2.5μm <d< 10 μm) and fine (d<1.0μm) particles (July 2007 – March 2008)

The scatter diagram between OC and EC concentration in $PM_{2.5}$ clearly shows a linear relationship with a slope of 3.0 with no difference between wet and dry seasons, and which was a little bit higher than that measured at Amami-Oshima. The major water soluble chemical composition was $(NH_4)_2SO_4$ and $Ca(NO_3)_2$ in fine and coarse particles, respectively, and these concentrations were also much higher in the dry season than in the wet season (Fig. 4). In addition, the surface CO concentration measured at the OAR, an indicator of air pollutants, was much higher in the dry season than in the wet season. On the contrary, soil dust particles and sea salt particles in coarse particles were much lower in the wet and dry seasons, than at Amami in the spring season.

3.2. Effects of biomass burning on the atmospheric aerosols

A scatter diagram between EC and sulfate in $PM_{2.5}$ (Fig. 5) showed the three groups; the one was a dataset for the wet season (W) and, the other two groups were for the dry season (D1 and D2). The second one (D1) was in a period of October to November 2007, and very similar to the dataset measured at Amami-Oshima in the 2003 spring season. For the third one (D2) was, however, the slope of a linear regression equation between EC and sulfate was much

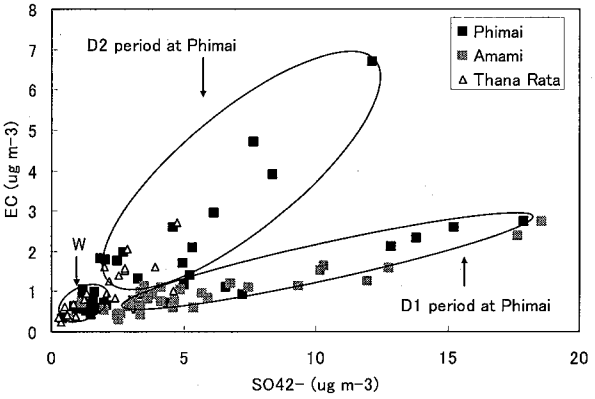

Fig. 5 Scatter diagram between EC and sulfate at Phimai, Amami-Oshima, and Thana Rata

higher than that for the second one, and almost equal to that measured at Thana Rata in central Peninsular Malaysia during July-October 2002. In that period, the polluted air masses were transported to Thana Rata from a region where biomass burning in central Sumatra, Indonesia was active due to the El Nino event. According to the MODIS fire map, many fires were detected almost all over Thailand from December 2007 to April 2008, although even in the dry season, very few fires were observed in the period of D1 from October to November 2007.

These results strongly suggest that the possible major source of enhanced aerosols in the D2 period was the biomass burning in Southeast Asia including Thailand, while the major source in the D1 period might be the fossil fuel combustion.

3.3. Single scattering albedo over Phimai

A preliminary analysis from the dataset measured by the sky radiometer indicate that a mean single scattering albedo (SSA) in the daytime over Phimai was >0.95 in the wet season of July and August 2007, when the aerosol concentration was very low and many dataset were not available for the SSA analysis due to many cloudy or rainy days. In contrast, most of the mean SSA in the D2 period of January and February was in a range of 0.80-0.90, much lower than in the wet season. It suggests that optical properties over Phimai might be significantly affected by aerosols emitted from biomass burning in southeast Asia.

Acknowledgements

We would like to express our great thanks to many staffs in Department of Geology, Chulalongkorn University, Thailand for management and maintenance of the

Observatory of Atmospheric Research at Phimai. We are also thankful to Yuichiro Shirasuna, Yokohama Environmental Science Research Institute, Japan, for precise weighting of the filters before and after aerosol sampling. This field study was supported by the University of Tokyo, under an international cooperative project for Alliance for Global Sustainability (AGS).

References

1) Tsuruta, H. and M. Yabuki (2008): Chemical Characterization and Single Scattering Albedo of Atmospheric Aerosols measured at Amami-Oshima, Southwest Japan, during Spring Seasons under the APEX and ABC-EAREX2005 Field Campaign Programs, Meteorological Research Note, 218, 80-100. (in Japanese)

2) NOAA: NOAA ARL HYSPLIT MODEL (http://www.arl.noaa.gov/ready/hysplit4.html)

3) NASA/GSFC: MODIS fire maps (http://rapidfire.sci.gsfc.nasa.gov/)

4) Tsuruta, H., S. Sudo, L.C. Peng, K.N. Ibrahim, I.E.S. Neo, and S. Urban (2003): The effect of biomass burning on atmospheric aerosols measured at Tanah Rata station in Cameron Highland, Peninsular Malaysia, during Jul.-Dec. 2002, a poster presentation at the ABC Workshop, Tokyo, 17-18 November 2003.

Atmospheric Environment Change Monitoring by Active and Passive Optical Methods

Young J. Kim, Young Min Noh, Hanlim Lee
Advanced Environmental Monitoring Research Center (ADEMRC)
Department of Environmental Science and Engineering
Gwangju Institute of Science and Technology (GIST)
1 Oryong-dong, Buk-gu, Gwangju 500-712, Republic of Korea
Tel: +82-62-970-3401 Fax: +82-62-970-3404 Email: yjkim@gist.ac.kr

Abstract

Integrated approach has been adopted at the ADvanced Environmental Research Center (ADEMRC), Gwangju Institute of Science and Technology (GIST), Korea for effective monitoring of atmospheric environment. Various active and passive optical remote sensing techniques such as multi-wavelength (3β + 2α) Raman LIDAR, sun-photometry, MAX-DOAS, and satellite monitoring have been utilized. This integrated monitoring system approach combined with in-situ surface measurement is to allow better characterization of physical and optical properties of atmospheric aerosol. Atmospheric environmental change monitoring has been conducted by measuring trace gases and aerosol in urban areas including Seoul, Gwangju, and Beijing as well as in remote areas such as volcanic sites and coastal areas.

Keywords : Raman lidar, Sunphotometry, DOAS, atmospheric aerosol, satellite monitoring

1. Introduction

The Korean peninsular located downwind of major emission source regions is vulnerable to not only its local emission but also largely to long-range transported air pollutants. Though air pollutants including aerosol causes adverse effects on human heath and climate change, our scientific understanding of radiative effects of those atmospheric species are still low and need be further investigated. Therefore characterization of physical, chemical, and optical properties of atmospheric aerosols and air pollutants over Korean peninsula and their effects on regional air quality and climate change is of scientific importance. Integrated approach has been adopted at the ADvanced Environmental Research Center (ADEMRC), Gwangju Institute of Science and Technology (GIST), Korea for effective monitoring of atmospheric environment. Various active and passive optical remote sensing techniques such as multi-wavelength (3β + 2α) Raman LIDAR, sun-photometry, MAX-DOAS, and satellite monitoring have been utilized. This integrated monitoring system approach combined with in-situ surface measurement is to allow better characterization of physical and optical properties of atmospheric aerosol. Atmospheric environmental change monitoring has been conducted by measuring trace gases and aerosol in urban areas including Seoul, Gwangju, and Beijing as well as in remote areas such as volcanic sites and coastal areas. MAX-DOAS and Imaging-DOAS measurements of ClO and BrO emitted from Sakurajima volcano and Anmyeon Island located off the coastal area in Korea were also conducted. Development of AMAX-DOAS is now underway for airborne trace gas measurement by scanning the relatively larger areas. The results obtained from active and passive optical methods can be used for validation of and improvements of atmospheric chemical transport models. ADEMRC has also participated in various international field studies such as ACE-Asia, ABC, APN, PRD, CareBeijing, and IGAC Mega-Cities. The results obtained from those campaigns can be used to monitor and predict the atmospheric environmental change by integrating with a 3-D chemical transport model, and provide scientific basis for formulation of control policy for air quality improvement and climate change mitigation

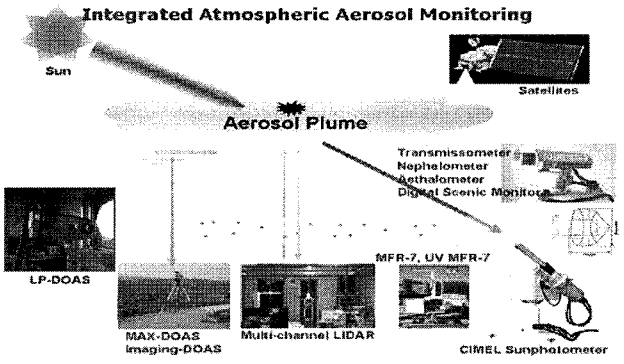

Fig. 1. An Integrated Monitoring System at GIST/ADEMRC

Table 1. Average values of the lidar ratio, Ångström exponent, depolarization ratio, and relative humidity for different types of aerosol observed in spring.

	S_a, sr		å	δ	RH (%)
	355 nm	532 nm	355 – 532 nm		
Dust	56.3 ± 9.9	51.3 ± 5.9	0.98 ± 0.27	0.20 ± 0.04	36.5 ± 17.3
Non-dust	57.5 ± 8.9	60.0 ± 10.1	1.41 ± 0.67	0.09 ± 0.04	41.7 ± 19.6
Smoke	45.5 ± 7.0	64.7 ± 7.7	0.93 ± 0.26	0.08 ± 0.01	46.6 ± 18.9
non-categorized aerosol	54.1 ± 8.6	48.6 ± 5.0	1.23 ± 0.57	-	27.2 ± 25.9

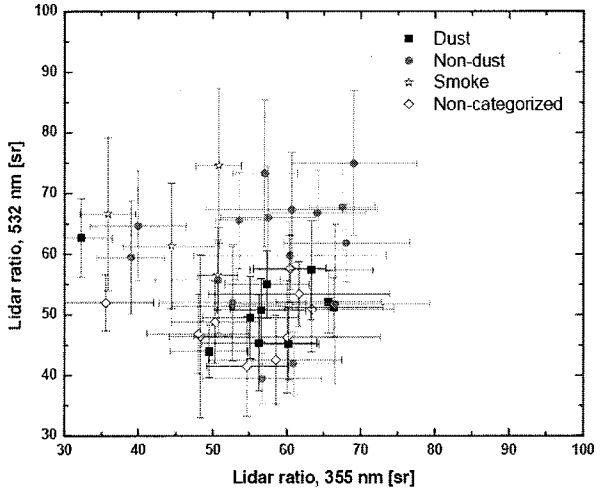

Fig. 2. Lidar ratio at 355 nm vs. 532 nm for different aerosol types obtained in spring [Noh et al., 2008]

2. Integrated Monitoring system

An integrated monitoring system used in this research is composed of various optical sensing techniques such as multi-wavelength LIDAR system, Sun-photometry, MAX-DOAS and satellite monitoring as shown in Figure 1. A multi-wavelength LIDAR system which use the Nd-YAG laser as a light source has been used to retrieve the vertical profiles of the backscatter coefficients, extinction coefficients and lidar ratios of atmospheric aerosols from the simultaneous detection of three elastic-backscatter signals (1064, 532, and 355 nm) and two Raman signals (607 and 387 nm) backscattered by nitrogen molecules[1]. The aerosol backscatter coefficient, extinction coefficient, and lidar ratio at 355 and 532 nm were determined from the elastic and inelastic return signals according to the method described by Ansmann et al.(1990)[2] and Whiteman et al. (1992)[3]. Radiosonde data collected about 5 km from the lidar site provided information on the vertical profiles of pressure, temperature and relative humidity, which allowed an accurate correction of the Rayleigh scattering effects on the signals. Based on the 'Error propagation equation'[4], typical statistical errors for the determination of the aerosol backscattering coefficient, extinction coefficient and lidar ratio in the middle part of the observed aerosol layers were 5~15%, 5~15% and 15~30%, respectively.

The column aerosol optical depth (AOD) and size distribution are obtained through the ground observation from sunphotometry. Total column-integrated volume size distributions, effective radius (r_{eff}), single-scattering albedo (ω_o), spectral aerosol optical depth (AOD), and Angstrom exponent (å) between 440 and 870 nm were determined by the AERONET retrieval algorithm[5),6)].

The sequential MAX-DOAS system mainly consists of a small aluminium box containing a miniature spectrograph and a telescope. The miniature spectrograph (Ocean-Optics USB2000, cross Czerny-Turner type, 1/f = 2.2) consists of a grating (2,400 grooves mm^{-1}) yielding a spectral coverage of 289 to 431 nm (at 0.7 nm FWHM spectral resolution) and a CCD detector (2,048 pixels at 14 mm center-to-center spacing), which was coupled to a 12-bit ADC connected to a laptop computer via USB interface. The spectrometer was kept at ~ 10° C by thermoelectric cooling to reduce the thermal noise. The MAX-DOAS box was attached directly to a stepper motor, allowing sequential measurement of scattered sunlight at various elevation angles between 10° and 90° above the horizon. The Imaging-DOAS instrument employs pushbroom imaging to acquire a spectrum of scattered sunlight in one spatial direction simultaneously with a 2D CCD detector, which corresponds to one column of the scene. The spectrum is acquired in the second spatial direction by scanning the field of view with a motorized scanning mirror. Details of the measurement principles for I-DOAS are described elsewhere[7].

3. Results

Optical characteristics of atmospheric aerosols were measured with the GIST/ADEMRC multi-wavelength

Raman lidar system at Gwangju, Korea (35.10°N, 126.53°E) during several observation periods between February 2004 and May 2005. Seasonal variation of the lidar ratio S_a at 355 and 532 nm showed lower values in spring (55.0 ± 9.5 and 55.6 ± 9.0 sr) than in the fall (61.4 ± 7.5 and 63.1 ± 12.8 sr). A low mean value of 51 sr at 532 nm was observed for Asian dust particles in spring, and was clearly distinguishable from values for non-dust (60 sr) and smoke (65 sr) aerosol[8].

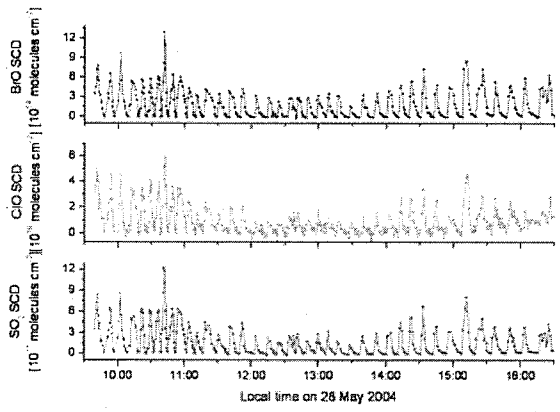

Fig. 4. Slant column densities of BrO, ClO and SO2, measured by a series of scans through the Sakurajima volcanic plume on 28 May 2004 [Lee, C. K. et al., 2005]

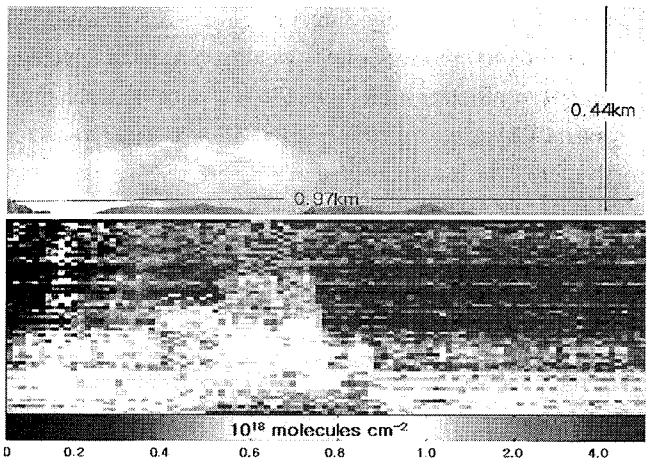

Fig. 5. 2D distributions of SO_2 retrieved using the GIST Imaging-DOAS for the Sakurajima volcanic plume on 14 November 2005

Very high lidar ratios were observed above the planetary boundary layer in the fall, and are believed to have largely resulted from an increased amount of light-absorbing particles in the fine mode of the particle size distribution, generated by coal combustion and agricultural biomass burning. Fig. 2 and Table 1 shows the optical properties and lidar ratio distribution of categorized aerosol at wavelengths of 355 and 532 nm[8]. Dust and smoke aerosols can be clearly distinguished. Non-dust aerosol shows a higher lidar ratio at both wavelengths compared to other aerosol forms. The non-categorized aerosols show a distribution similar to one of the dust aerosols. The high lidar ratio in comparison to pure Asian dust must have been affected by this mixing with fine pollution aerosols.

Successful remote measurement of significant amount of ClO (as well as BrO and SO2) in a volcanic plume from the Sakurajima volcano in Japan was made using ground-based multi-axis differential absorption spectroscopy[9]. BrO, ClO and SO2 were detected in each scan through the plume (Fig. 4) . The cross-sectional distribution of slant column densities was characterized by maximum SCDs in the viewing direction (elevation angle) toward the center of the plume at any other elevation angle, as shown in Fig. 4. SCDs measured during the measurement period ranged up to 1.4×10^{15}, 5.9×10^{16}, 1.3×10^{18} molecules cm^{-2} in the center of the plume for BrO, ClO and SO_2, respectively. The SCDs of BrO and ClO are highly correlated with that of SO2, with a Pearson's correlation coefficient of 0.89 for BrO and 0.91 for ClO. The BrO/SO2 and ClO/SO_2 molecular ratios measured were 1.0×10^{-3} and 4.9×10^{-2} which correspond to the mass ratios of 1.5×10^{-3} and 3.9×10^{-2}, respectively. 2D distributions of SO_2 have been successfully retrieved using the GIST Imaging-DOAS (Fig. 5) for the Sakurajima volcanic plume. It was found that BrO emission from the crater at Sakurajima volcano was negligible during the measurement period. SO_2 SCD from the crater were successfully measured to be $0.2 \sim 4.5 \times 10^{18}$ molecules cm^{-2}.

During the CAREBEIJING campaign in 2006, imaging-DOAS measurements were made from 08:00 until 16:00 on September 9 and 10 over Beijing, China[10]. Detailed images of the near-surface NO_2 Slant Column Density (SCD) distribution over Beijing were obtained. Images with less than a 30-min temporal resolution showed both horizontal and vertical variations in NO_2 distributions. For SCD to mixing ratio conversion light path length along the lines of I-DOAS sight was estimated using the light-extinction coefficient and Ångstrom exponent data obtained by a transmissometer and a sunphotometer, respectively. Mixing ratios measured by an in-situ NO_2 analyzer were compared with those estimated by the I-DOAS instrument. The obtained temporal and spatial variations in NO2 distributions

measured by I-DOAS for the two days are interpreted with consideration of the locations of the major NO_x sources and local wind conditions. I-DOAS measurement has been applied in this study for estimating NO_2 distribution over an urban area with multiple and distributed emission sources[10].

The six-year (2000~2005) record of aerosol optical thickness (AOT or τ) data from the Moderate Resolution Imaging Spectroradiometer (MODIS) was analyzed over the Northeast Asia. The MODIS AOT standard products (MOD04_L2) over both ocean and land were collected to evaluate the spatial and temporal variability of the atmospheric aerosols over the study region (32°N~42°N and 115°E~133°E). The monthly averaged AOT result revealed slight changes, which was almost unchangeable over Korea. In contrast, the large AOT values (> 0.6) and a significant AOT increase (> 0.004 τ/month) over East China were observed[11].

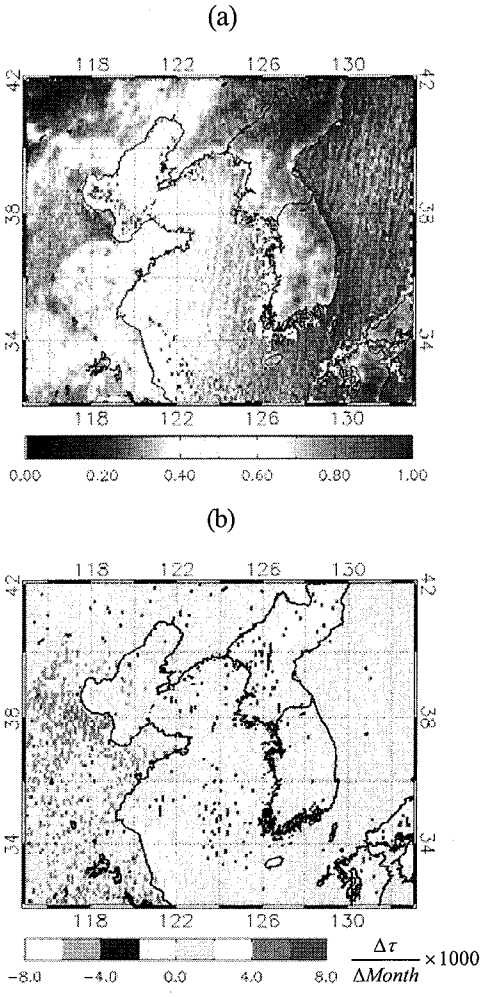

Fig. 6. (a) Average AOT distribution for 6 years during 2000 to 2005 over Northeast Asia. Each pixel has 0.1° x 0.1° resolution retrieved with latitude of 32°N to 42°N and longitude of 115° E to 133°E. (b) Average monthly AOT change rate at each pixel over the observed area by TERRA/MODIS from 2000 to 2005(Lee, D. H. et al., 2006).

Aerosol optical depth has been retrieved from satellite data using the modified BARE algorithm at GIST/ADEMRC. Fig. 7. shows MODIS-retrieved AOD on 20 May 2003 as the smoke aerosol plume originated from Russian Siberian forest fires transported toward Korea. Very high AOD (> 2.0) with a maximum exceeding 3.0 was observed over Korean peninsula[12].

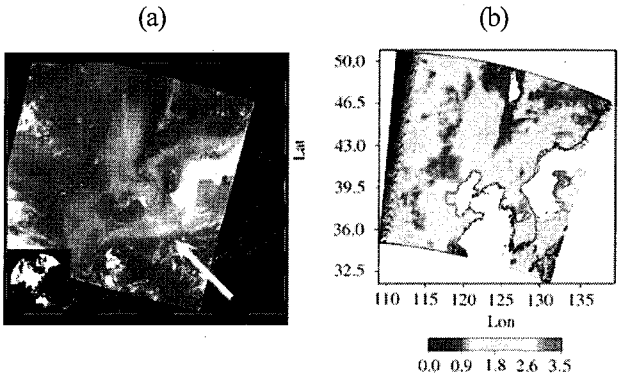

Fig. 7. (a) MODIS RGB image and (b) MODIS retrieved AOD at 555 nm on 20 May 2003(Lee, K. H. et al., 2005).

4. Conclusions

Vertical profile variation of optical properties such as aerosol extinction coefficient, depolarization ratio and size distribution are calculated using simultaneous observation data by multi-wavelength Raman LIDAR system. And these results can be compared with sunphotometer measurements. Also satellite data analysis results can utilize to detect horizontal distribution and transportation of aerosol in wide range and increase the accuracy and confidence of data through comparing analysis with LIDAR and sunphotometer observation data on the ground. An integrated atmosphere monitoring system of GIST/ADEMRC can monitor origin and pathway of atmospheric aerosols in 3-D and be expect to offer essential information to predict the fine particle concentration through the data assimilation with atmospheric chemistry transfer model (CTM). The applications of passive DOAS techniques are introduced for remote sensing of trace gases. Those passive and active optical methods have demonstrated the enhanced capability to investigate the atmospheric environment change.

Acknowledgements

This symposium is sponsored by the Ministry of Education, Science, Sports and Culture, Japan (MEXT), and National University Corporation Chiba University. This work was supported by the Korea Science and Engineering Foundation (KOSEF) grant funded by the government (MEST) (No. R17-2008-042-01001-0)

References

1) Noh, Y. M., Kim, Y. J., Choi, B. C., Murayama, T., 2007. Aerosol Lidar Ratio Characteristics Measured by a Multi-Wavelength Raman Lidar System at Anmyeon Island, Korea, *Atmospheric Research*, 86, 76-87

2) Ansmann, A., Wandinger, U., Riebesell, M., Weitkamp, C., Michaelis, W., 1990. Measurement of atmospheric aerosol extinction profiles with a Raman lidar. *Optics Letters* 15, 746–748.

3) Whiteman D. N., Melfi, S. H., Ferrare, R. A., 1992. Raman lidar system for the measurement of water vapor and aerosols in the Earth's atmosphere, *Applied Optics*, 31(16), 3068-3082.

4) Bevington, R. P., Robinson, D. K., 1992. Data reduction and error analysis for the physical sciences. *McGraw-Hill*, Inc., Nework, 38-51.

5) Dubovik, O., Holben, B. N., Lapyonok, T., Sinyuk, A., Mishchenko, M. I., Yang, P., Slutsker, I., 2002. Non-spherical aerosol retrieval method employing light scattering by spheriods, *Geophysical Research Letter,* 29, 54-1 - 54-4.

6) Ogunjobi, K. O., Z. He, K. W. Kim, and Y. J. Kim, 2004. Aerosol optical depth during episodes of Asian dust storms and biomass burning at Kwangju, South Korea, *Atmospheric Environment*, 38 (9) 1313-1323

7) Lee, H., Y. J. Kim, and C. Lee, 2008. Estimation of the rate of increase in nitrogen dioxide concentration from power plant stacks using an Imaging-DOAS, *Environmental Monitoring and Assessment*, in press

8) Noh, Y. M., Y. J. Kim, and D. Muller, 2008. Seasonal characteristics of lidar ratio measured with a Raman Lidar at Gwangju, Korea in spring and autumn, *Atmospheric Environment*, 42(9), 2208-2224

9) Lee C.K., Kim Y.J., Tanimoto H., Bobrowski N., Platt U., Mori T., Yamamoto K., and Hong C.S., 2005. High ClO and ozone depletion observed in the plume of Sakurajima volcano, Japan. *Geophysical Research Letters,* 32 L21809

10) Lee, H., Y. J. Kim, J. Jung, C. Lee, K.-P. Heue, and U. Platt, 2008. Spatial and temporal variations in NO_2 distributions over Beijing, China measured by imaging differential optical absorption spectroscopy, *Journal of Environmental Management*, submitted manuscript

11) Lee, D. H., Lee, K. H. Kim, J. E., Kim Y. J., 2006. Characteristics of Atmospheric Aerosol Optical Thickness over the Northeast Asia Using TERRA/MODIS Data during the Year 2000~2005, Atmosphere (in Korean), 16(2), 85-96

12) Lee, K. H., J. E. Kim, Y. J. Kim, J. Kim, and W. von Hoyningen-Huene, 2005. Impact of the Smoke Aerosol from Russian Forest Fires on the Atmospheric Environment over Korea during May 2003, *Atmospheric Environment*, 39 (1) 85-99

Atmospheric Features over a tropical station Gadanki, India – Lidar Observations from Troposphere to Mesopause region

Musali Krishnaiah*

CEReS, Chiba University

profkrishnaiah@restaff.chiba-u.jp

Abstract

The vertical structure of the atmosphere particularly over tropics is essential for various applications in weather forecasting and space meteorology and it has been studied at NARL, Indian tropical station, Gadanki, with MST Radar, and other collocated facilities. Of them, the lidar technique has been found to be a potential remote sensing method for probing the earth's atmosphere from troposphere to mesopause region. The portable lidar nocturnal observations over Gadanki, usually showed a thick aerosol layer in the lowermost atmosphere, which corresponds to the local mixing layer. However, on several occasions during winter 2005, a thin aerosol layer was observed above the local boundary layer, in the free troposphere, between 3 and 4 km heights

Using Mie and Rayleigh backscattering lidar system, regular observations of upper tropospheric clouds, aerosols at stratospheric heights and atmospheric temperatures in the range from 30 to 80 km have been made. Several tropical cirrus cloud structures having low to moderate ice content and occasionally, thin sub-visible cirrus in the vicinity of the tropical tropopause have also been detected. Rayleigh-scattering lidar observations revealed the temperature inversions at mesospheric heights, significant warming in the lower mesosphere associated with a consistent cooling in the upper stratospheric heights particularly in the winter season, during the events of sudden stratospheric warming (SSW).The formation and decay of the sporadic sodium layer at mesospheric heights is studied using newly augmented Resonance lidar. Many interesting features such as temperature climatology, Gravity wave activity etc are studied using long data base and results are compared with other centers corresponding values .

*JSPS fellow. Permanent address: Department of Physics, Sri Venkateswara University, Tirupati, India

1. Introduction

The study of the vertical structure of the atmosphere is one of the prerequisites for understanding of the various processes taking in it ,particularly over tropics where the high solar irradiance is responsible for atmospheric processes of different spatial scales such as the development of deep convective systems which transport energy and momentum from the low to the high altitudes ,higher production rate of ozone molecules in the stratosphere and the formation of the equatorial electron jet in the ionosphere. Systematic exploration of the vertical structure of the atmosphere is essential for various applications of meteorology and space. Several measurement techniques have extensively been used for better understanding of global atmosphere. Of them, Laser radar more popularly known as LIDAR (Light Detection And Ranging) has become the excellent tool for mentoring the atmosphere in a relatively short period of time (few seconds to minutes). The laser radiation interacts with various constituents of the atmosphere in different

types of optical processes related to different types of light scatterings (Measures 1984).Both continuous wave and pulsed laser systems have been extensively used notably in different parts of the globe to study aerosols/clouds (Mie Scattering), atmospheric density and temperature (Rayleigh Scattering), metallic ion species (Resonance Scattering), minor constituents and trace gases (Differential absorption), composition (Raman Scattering) and winds (Doppler LIDAR).

In India a major advance has been made in vertical probing of the atmosphere with establishment of a high power Mesosphere-Stratosphere-Troposphere (MST) Radar, Rayleigh, Mie, Sodium and Boundary layer lidars, sodar, lower atmospheric wind profiler etc. at National Atmospheric Research Laboratory (NARL),Gadanki (13.5 N;79.2 E; dip 12.5 N,6-3 magnetic latitude;~370m MSL) is a rural tropical site in south India It is aimed here to present the salient features of the atmosphere observed using the lidar systems from troposphere to mesopause region.

2. Lidar systems used

The BLL system at NARL- employs a diode pumped Nd:YAG laser that operates at its 532 nm wavelength with 10 μJ and 2500 Hz. The laser beam divergence was reduced to less than 200 μrad using an external beam expander. The monoaxial configuration is employed with 150 mm diameter classical cassegrainin telescope for collecting the laser backscattered returns from the atmosphere. The design focal length of the telescope is 1350 mm. A pin-hole of 0.5 mm was used to obtain a receive FOV of about 400 μrad. A narrowband optical Interference filter is used to reduce background light. The BLL system employs photon counting electronics using a high gain PMT.

The Rayleigh and Mie lidar system was installed at NARL in 1998 by CRL, Japan. The complete description and operation are discussed elsewhere (Bhavani Kumar, 2006) Indo-Japanese lidar (IJL) system, a monostatic system augmented with Raman capability to obtain the height profiles of water vapor mixing ratio and further augmented with a tunable pulsed dye laser pumped by a frequency-doubled Nd: YAG laser as Resonance lidar and tuned to sodium D2 line at 589 nm as transmitter to observe the aeronomy of the mesopause region.

3. Lidar Experimental Results.

3.1 Boundary layer lidar observations of Aerosols and Clouds.

A portable back scatter lidar developed at NARL has been used to monitor the boundary layer aerosol dynamics and high altitude clouds during the night time. Figure 1(a) shows the altitude profile of aerosol scattering coefficient derived from the lidar data on 4 January 2005 and an elevated thin aerosol layer above the local boundary layer between 2 and 3 km. It is considered that these layers represent long-range transport of aerosols. Figure 1(b) shows the typical photon count profile obtained from the BLL system during the nocturnal observation period. It is presented in logarithmic scale and shown up to 20 km height. The data was collected during midnight hours between 02:13 and 02:23 Hrs LT on 6 January 2005. The photon count profile corresponds to a time integration of 10 minutes. A layer of strong scattering is clearly seen in the upper troposphere at heights between 12 and 14 km, which corresponds to the occurrence of high altitude cloud over the lidar site during the period of observation. Fig 1(c) is an

example of boundary layer dynamics over the lidar site.(Bhavani Kumar,2006)

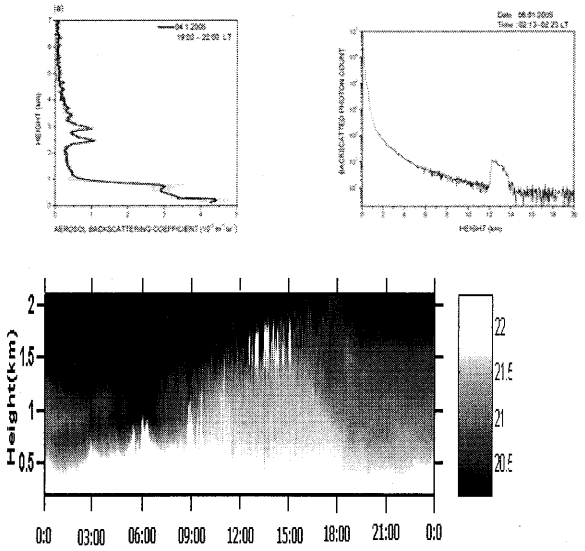

Fig1.BLL observation of elevated aerosol layer, occurrence of high altitude cloud and the time series of range-squared signal can interpret the ABL dynamics over lidar site

3.2 Indo-Japanese lidar (IJL) observations of high altitude clouds and aerosols

The (IJL) system, equipped with polarization diversity, has detected several different structures of tropical cirrus in the altitude ranging from 10 -17 km with derived peak volume depolarization in the range of 0.1 to 0.32. In Figure 2(a), a single cirrus layer in the height range of 14-16 km is detected and observation shows that cloud appeared for a period of about an hour and later it decayed in its strength and becomes too week to detect. After two hours, that is from 00:12 Hrs of IST, cloud starts building up in strength (more scattering) and formed a significant spatial structure as shown. Figure 2(b) shows, the observation on 11-12 November 1998, two different layers of cirrus structures observed during their passage over the lidar site. A thin cirrus layer occurred in the altitude range of 16 to 16.5 km, which appeared to be very close to the tropical tropopause, and persisted for about 5 hrs. These thin cirrus layers contribute significantly to the radiation budget and thereby to the warming of atmosphere The other cirrus layer is identified in the altitude range of 12 to 14 km altitudes is shown in Figure 2(b) as patchy type of cirrus bands

Typical height profiles of aerosol backscatter ratio integrated over two hour period, as observed by Indo-Japanese lidar, on the nights of 16th March, 16th October, 28 December1998 and 19th January 1999 is shown in Figure 2(c). Each lidar profile is shown with a corresponding radiosonde temperature profile that is obtained from the nearest meteorological station, Chennai for identification of the local tropopause altitude. The horizontal arrows indicate the altitude of cold-point tropopause obtained from these temperature measurements. A significant observation from these height profiles is the extended vertical distribution of stratospheric aerosol. There are no noticeable sharp enhancements in aerosol backscatter observed at the stratospheric heights. This confirms that during the time of our observations the tropical upper troposphere and stratosphere over Gadanki appears free from volcanic aerosols and what we observe now is the background variable aerosol (Barnes and Hofmann 1997, 2001; Jaeger 1998). Another significant observation in the backscatter profiles is a noticeable minimum in BSR at the height marked as the local tropopause. A sharp gradient in the temperature accompanied by the tropical tropopause may be the probable reason for such minimum in the aerosol concentration. (Bhavani Kumar, et al., 2006).

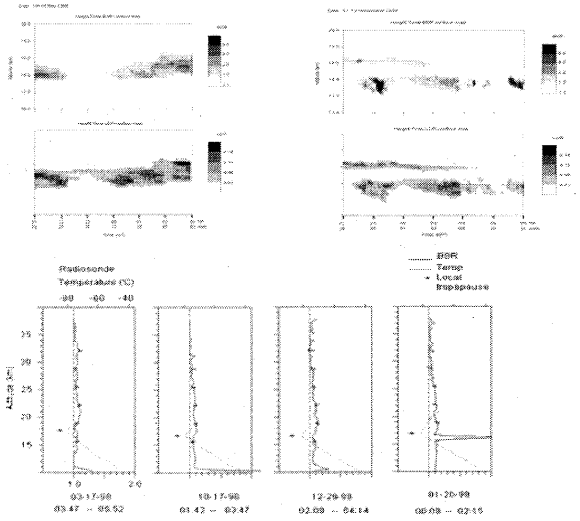

Fig 2. Different structures of tropical cirrus and height profiles of aerosol backscatter ratio integrated over two hours.

3.3 Measurement of Upper stratospheric and Lower Mesospheric temperatures

Absolute temperatures are derived from the density measurements by assuming that the atmosphere is in hydrostatic equilibrium and integrating the Ideal Gas Law from the greatest altitude downward. Figure 3(a) and (b) show the profiles of temperature and standard error derived from Rayleigh-scatter lidar data integrated over a period of two hours. Figure 3(c) shows the sequences of half-hour integrated temperature profiles for the nights of 21-22 October, 21-22 May and 07-08 February 1999 representing the periods of equinoctial, summer and winter. For October, a localized warming near stratopause with maximum temperature is found to be around 275 K. For May, a clear wave perturbation at lower stratospheric heights with quite broad stratopause. For February, a clear wave perturbed temperature profile causing lower mesosphere warming followed by upper stratospheric cooling.

The temperature profiles obtained by Rayleigh-scatter lidar frequently exhibit a strong temperature inversion with 20-40 K at mesospheric heights. The observed inversion was explained by the heating of the turbulent layers generated by the continuous breaking of the upward propagating internal gravity waves. The Indo-Japanese lidar observation of gravity wave activity in neutral temperatures is shown in Figure 4(a).Another unusual feature was observed in the profiles of temperature during the winter period of 1998 and 1999. A substantial cooling in the height profiles of temperatures has been noticed on 23 December 1998 and 28 February 1999 as shown in Figure 4(b). This is about 15 to 20 K lower than the corresponding temperature of the COSPAR International Reference Atmosphere (CIRA) 1986, which represents a monthly zonal mean for December and February at 15°N (Bhavani Kumar et al., 2006)

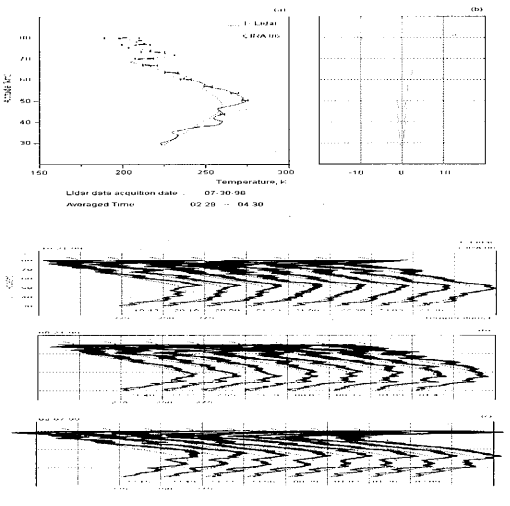

Fig. 3(a) and (b) show the profiles of temperature and standard error 3(c) shows the sequences of half-hour integrated temperature profiles for the nights of 21-22 October, 21-22 May and 07-08 February 1999.

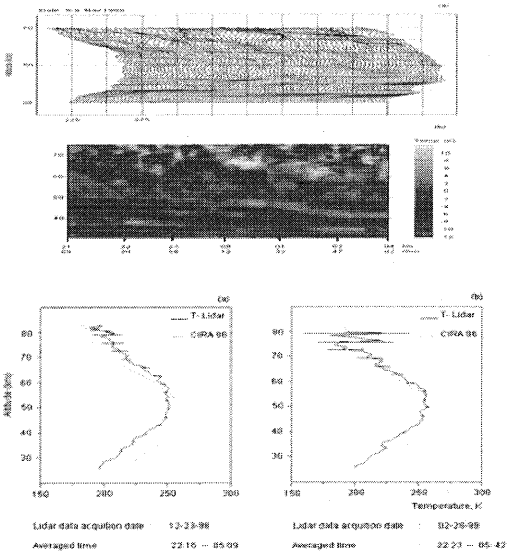

Fig 4(a) Sequences of successive basic temperature profiles to indicate the wave like structures and (b)substantial cooling in the height profiles of Temperatures

3.4 Resonance Lidar observations of sporadic Na layers

The photon count profile collected on 12 January 2005 (Bhavani Kumar et al. 2007) and two examples of sporadic sodium layer (SSL) profiles on 12 February 2005 (solid) and on 2 January 2006 (dashed curve) are shown in Fig5(a &b). A special SSL event is identified on 12 February 2005 (solid curve).with the greatest peak density occurs at an altitude of 92 km with a peak width (FWHM) of 2.1 km. These profiles show that the occurrence of SSL events is highly variable in altitude, density and peak width. In order to show the formation and decay of the sodium layers, two examples are shown in Fig 5(c&d) in which the durations of the SSL events are different. In the figure, the sodium density profiles are plotted in steps every 20 min for 11 January 2005 (3rd panel) and in steps every 6 min for 15 January 2005 (last panel). It can be observed in the 3rd panel that a thin dense Na layer is superposed on the normal Na layer during 02:32–05:34 IST (Indian Standard Time, which is ahead of Local Time (LT) by 13.2 min). The duration of the event is around 3 h. The thickness of this layer (FWHM) is about 1.62 km. The duration of the event shown in the3rd panel is relatively shorter (about 70 min), as the dense Na layer appears during 21:22.22 IST. In both the cases, the evolution and decay of the SSL events can be observed (Vishnu Prasanth, 2007).

4. Conclusions

A new portable micro pulse lidar system developed at the National Atmospheric Research Laboratory, Gadanki, India, has indicated the presence of thick aerosol layer in the lower most troposphere, which was considered as the local mixing layer. The lidar system has also detected the elevated aerosol layer, above mixing layer and also high altitude clouds.

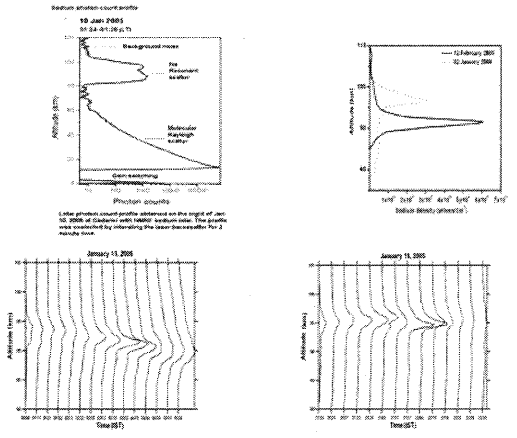

Fig. 5. Photon count profile collected on 12 January and Two examples of SSL profiles on 12 February 2005 (solid) and 2 January 2006 (dashed) and . Successive profiles of sodium density showing evolution and decay of an SSL event on 11 January 2005(center) and 15January 2005 (last panel).

Indo-Japanese lidar has been used for the detection of high altitude clouds, stratospheric aerosols, and derive the temperatures in the height range of 30 to 80 km. Thin cirrus clouds are occasionally detected near the tropical tropopause. The measurement of stratospheric aerosols by the lidar system confirms that during the times of present observation, the tropical upper troposphere and lower stratosphere over Gadanki site appears free from volcanic aerosols what we observe now is the background variable aerosols. Rayleigh-scatter lidar observations of temperatures in the upper stratosphere and the lower mesosphere were found to show prominent wave activity. Interesting features such as temperature inversions at mesospheric heights and noticeable cooling in stratosphere temperatures during stratwarm period were observed over the tropical site Gadanki. Resonance lidar has been used to observe the formation and decay of the intense sporadic sodium layer at mesospheric heights.

Acknowlegements: M. Krishnaiah gratefully acknowledge the Japan Society for Promotion of science(JSPS) for awarding the invitaion fellowship 2008 and to Prof Hiroaki Kuze, Center for Environmental Remote Sensing,Chiba University, Japan for providing the facilities.

References

1 Bhavani Kumar.Y, 2006, Portable lidar system for atmospheric boumdary layer measurements, 2006, Optical engineering 45(7), 076201.

2..Bhavani Kumar. Y,C.Nageswara Raju and M.Krishnaiah, 2006, Indo-Japanese Lidar Observations of the Tropical Middle atmosphere During 1998 and 1999, Advances in Atmospheric sciences, Vol 23, No,5, 711-725.

3. Measures, R.M.,1984, Laser Remote Sensing, Fundamentals and Applicatoons, J. Willey and Sons, Newyork, 510pp.

4.Vishnu Prasanth. P,S.Sridharan, Y Bhavani Kumar and D. Narayana Rao, 2007, Ann. Geophys., 25, 1759-1766.

LIDAR TECHNIQUE AND MONITORING AT AIOFM, CHINA

Jun Zhou Shungxing Hu Dongsong Sun Huanling Hu
Anhui Institute of Optics and Fine mechanics, Chinese Academy of Sciences
Hefei 230031, People's Republic of China jzhou@aiofm.ac.cn

Abstract

This paper introduces a number of lidar systems, which are developed by Anhui Institute of Optics and Fine Mechanics, Chinese Academy of Sciences (AIOFM, CAS). It also presents jointed national projects and international cooperation programs on lidar monitoring for atmosphere at the AIOFM .

Keywords: Lidar, Atmospheric monitoring, Laser remote sensing

1. Introduction

Detection of the spatial and temporal distribution of greenhouse gases, aerosols, clouds is required for climate change and environmental assessment. Lidar can provide the vertical component of this distribution through advanced laser remote sensing.

In recent years, under supporting by Chinese Academy of Sciences, Ministry of Science and Technology of the People's Republic of China, and Ministry of Environmental Protection of the People's Republic of China, Anhui Institute of Optics and Fine Mechanics, Chinese Academy of Sciences (AIOFM, CAS) has developed many kinds of Lidar systems. These include Multiple-wavelength Mie scattering lidar, Polarization lidar, Micro Pulse Lidar, Raman lidar, Differential absorption lidar, Doppler lidar and Rayleigh-LIFluorescence lidar etc. By using these lidar systems, long-term, or field campaign, observations of aerosol, cloud, water vapor, O_3 ,SO_2, CO_2, wind and temperature have been made.

AIOFM has also actively jointed in national and international cooperation projects on lidar monitoring for atmosphere. These are National Basic Research Program of China: Aerosol in China and its Climate Effect, Basic Scientific and Technical Data Sets: Measurements of Important Atmospheric Parameters with High Vertical Resolution in East China, SKYNET, AD-Net, CALIPSO validation program, and GALION .

This paper will introduce a number of these lidar systems and also present the lidar observed results in the above-mentioned projects.

2. Lidar systems

2.1 Two-wavelength lidar [1]

The lidar system is mainly composed of a two-wavelength Nd:YAG laser transmitter, a receiving optics, a signal receiver and a data-acquisition. Fig. 1 shows the schematic diagram of the lidar system.

AIOFM is one of the validation team members of the CALIPSO. The lidar system is used in the CALIPSO Quid Pro Quo (QPQ) validation program. Fig.2 presents Comparison of attenuated backscatter profiles at both 532nm (left figure) and 1064nm (right figure) wavelengths measured by this lidar and CALIPSO lidar nighttime at 02:11 Beijing time on Nov.24, 2007.

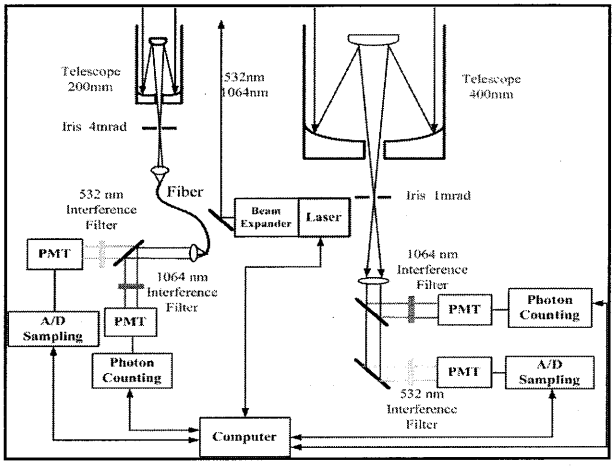

Fig.1. schematic diagram of the two-wavelength lidar.

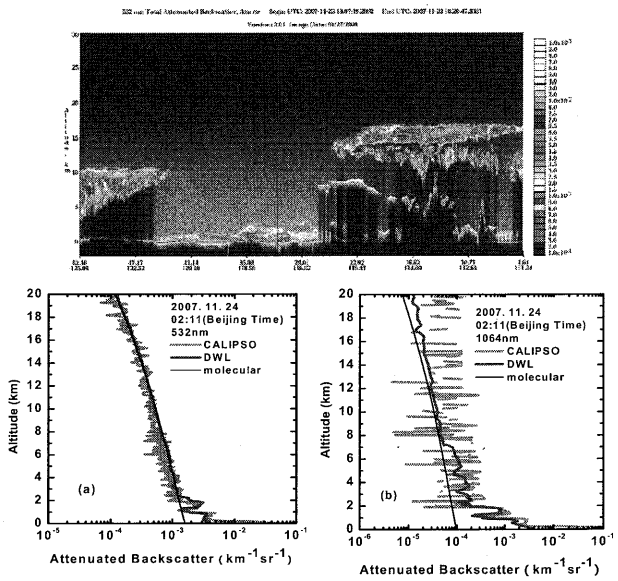

Fig. 2. Comparison of attenuated backscatter profiles during nighttime at 02:11Beijing time on Nov. 24, 2007.

Fig.3 presents the Comparison results just for 532 nm wavelength during the daytime at 13:30 Beijing time on Nov.29, 2007 and at 13:32 Beijing time on March 20, 2008, respectively.

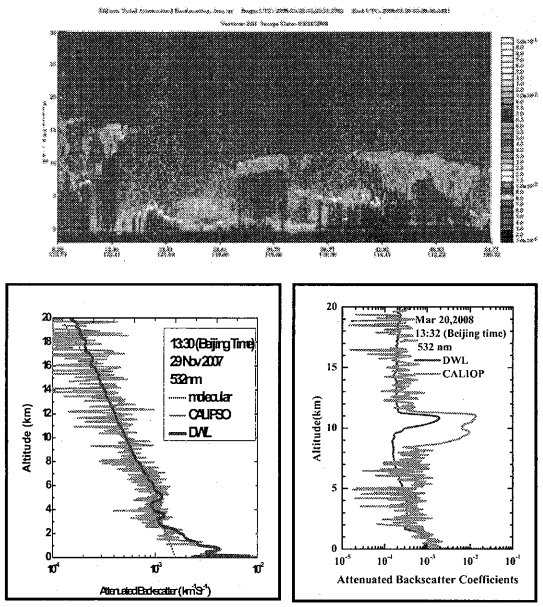

Fig.3. Daytime Comparison results at 532nm wavelength between CALIPSO and this lidar.

These Comparison results indicate that for both wavelengths the attenuated backscatter profiles measured by CALIPSO lidar generally agree well with the ones by our ground-based two-wavelength lidar during nighttime and daytime. The mixed layer was apparent by the CALIPSO lidar measurements.

However, the CALIPSO's attenuated backscatter profile at 1064 nm wavelength appeared large fluctuation in the upper troposphere because of lower signal- to -noise ratio.

2.2 Transportable Raman lidar [2]

The transportable Raman lidar system is used for measuring the vertical profiles of water vapor mixing ratio by Raman scattering. Fig. 4 shows the schematic diagram of the lidar system.

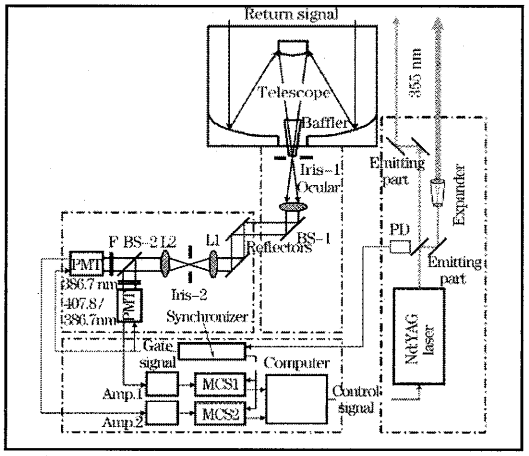

Fig.4. Schematic diagram of the Raman lidar system.

Fig. 5 (a) (b) presents the vertical profiles of water vapor mixing ratio measured by the Raman lidar at night on sep.12 (a) and Oct.9, 2004 in Hefei, respectively.

The radiosonde and another Raman lidar (L625) measuremental results are also shown in the figure for comparison.

The figure indicates that during the nighttime the Raman lidar can measure the water vapor mixing ratio from ground to about 8 km altitude.

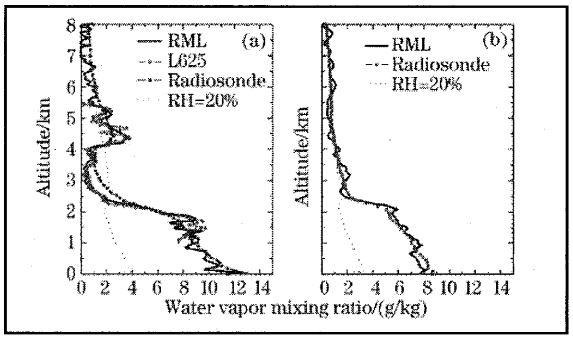

Fig. 5. Vertical profiles of water vapor mixing ratio at night on sep.12 (a), Oct.9 (b), 2004 in Hefei.

2.3 Mobile DIAL[3]

The Mobile DIAL is used for measurements of SO_2 and O_3 and NO_2 in the low troposphere. Fig. 6 shows photograph of the Mobile DIAL. Fig. 7 presents its schematic diagram.

Fig.6. Photograph of the Mobile DIAL.

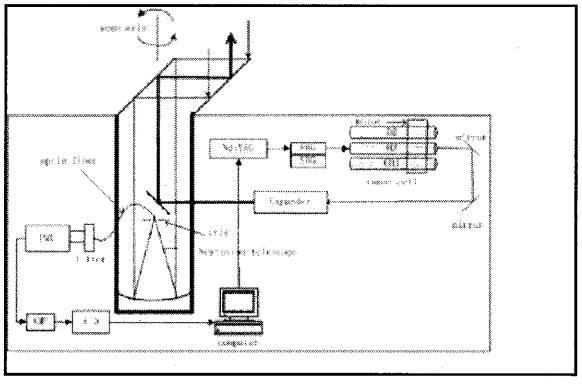

Fig. 7. Schematic diagram of the DIAL.

Fig. 8 presents the comparison results of vertical profiles of O_3 measured by this lidar with ozonesonde in Beijing on Nov. 5, 2004. Good agreement between them is apparent.

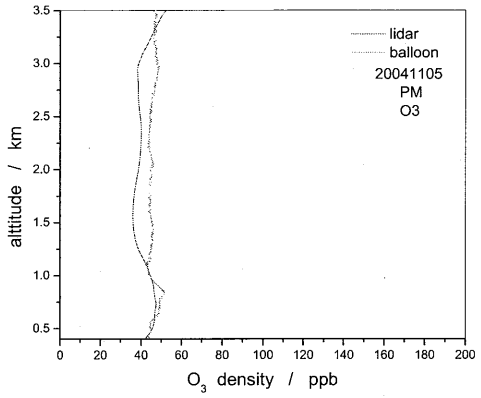

Fig. 8. Comparison results of vertical profiles of O_3 measured by the DIAL with ozonesonde in Beijing on Nov. 5, 2004.

2.4 Doppler wind lidar[4]

The 1064nm aerosol Doppler wind lidar (DWL) system based on the double edge technique is capable of measuring three-dimensional wind profiles in the low troposphere. Fig. 9 presents its schematic diagram.

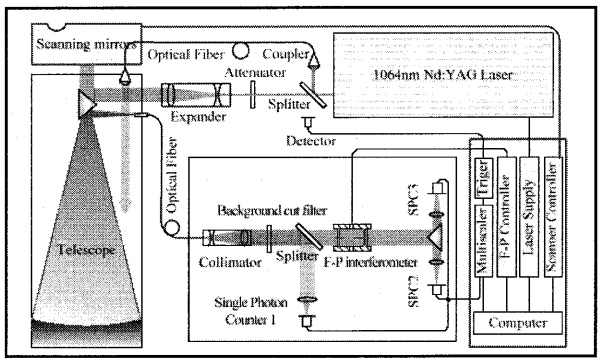

Fig. 9. Schematic diagram of the DWL.

A two axis mirror scanning system allows the lidar to achieve full sky coverage. Backscattered light is collected by a 30 cm diameter Cassegrain telescope. A dual Fabry-Perot etalon with a narrowband (0.5nm) interference filter is used to cut sky background radiation and provide a high spectral resolving element to measure the Doppler shift. A feedback circuit is developed and locks the laser frequency to the reference frequency.

The receiver for the frequency measurement is calibrated by the known line-of-sight Doppler shift produced from a rotating disk, and the calibration accuracy in velocity is less than 1% in the range of ±40m/s.

This system has line-of-sight wind speed dynamic range of 84m/s (±42m/s) and can measure wind profiles up to 10km altitude.

Comparison observations of the lidar wind profile were performed with CINRAD/SA Doppler weather radar, Airda16000 microwave radar and Vaisala balloon. Fig. 10 presents one of these observed results.

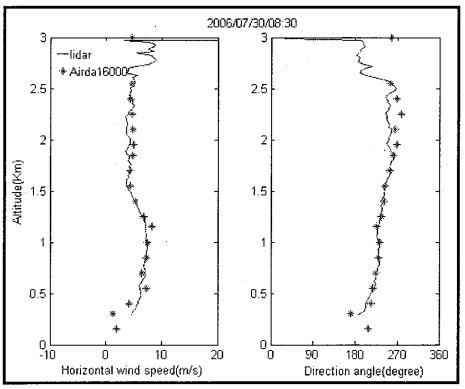

Fig.10. Profiles of wind speed and direction measured by DWL compared with data measured from Airda16000 Radar on July 30, 2006.

The Figure shows that in the altitude from 0.2km to 3 km, accuracies of wind vectors were better than 2m/s with 21.2m vertical resolution and 10 minute temporal resolution. Moreover, the accuracy, vertical resolution and temporal resolution can be improved with the current parameters of this lidar system.

Routine measurements have proved that DWL system is stable and reliable and has the capability of unattended automated measurements. Fig. 11 gives an example of continuing two-day observations by the lidar system.

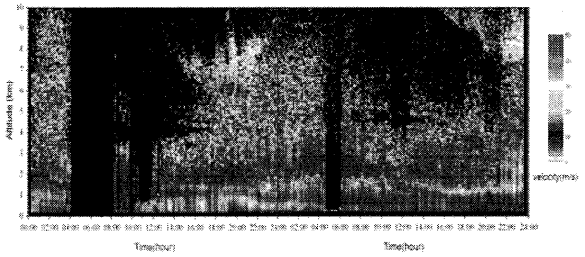

Fig.11 A color plot of two-day wind profiles measured by Doppler wind lidar from 00:00 of Apr.23 to 24:00 of Apr.24, 2006.

3. Lidar monitoring for atmosphere[5-10]

Anhui Institute of Optics and Fine Mechanics has actively jointed in national and international projects on lidar monitoring for atmosphere.

These projects are:

National Basic Research program of China: Aerosol in China and its Climate Effect.

Basic Scientific and Technical Data Sets: Measurements of Important Atmospheric Parameters

with High Vertical Resolution in East China

SKYNET (SKY radiation observation NETwork)

AD-Net (Asian Dust lidar observation NETwork)

CALIPSO Quid Pro Quo (QPQ) validation program, and

GALION (GAW Aerosol Lidar Observation Network).

Here give an example. For the program of Aerosol in China and its Climate Effect, seasonal average aerosol backscatter coefficient profiles in Hefei have been obtained from the lidar measurements. They are shown in Fig. 12. It should be noted that the days with cirrus clouds and Asian dusts have been removed from the statistics. The figure clearly indicates that larger aerosol backscatter coefficients were observed from 3 km to about 12km altitude range in the springtime rather than any other season.

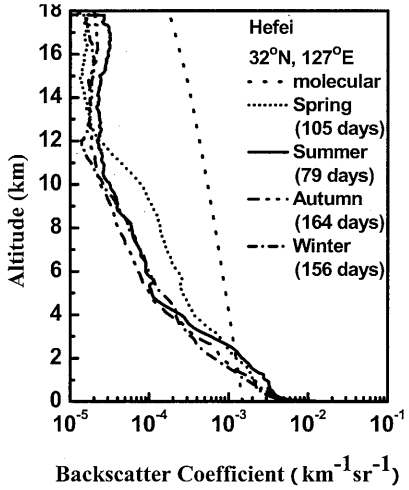

Fig.12. Seasonal average aerosol backscatter coefficient profiles from 1998 to 2008.

The fitting to the above profiles for spring, summer, autumn and winter can be expressed in the following form:

$$\beta_a(z) = 3.92\times10^{-3}\exp(-\frac{z}{1.76}) + 1.00\times10^{-4}\exp[-(\frac{z-7.61}{3.39})^2] + 1.60\times10^{-5}\exp[-(\frac{z-16.7}{4.78})^2]$$

$$\beta_a(z) = 6.16\times10^{-3}\exp(-\frac{z}{1.32}) + 4.16\times10^{-5}\exp[-(\frac{z-8.56}{3.37})^2] + 2.89\times10^{-5}\exp[-(\frac{z-16.5}{4.30})^2]$$

$$\beta_a(z) = 4.36\times10^{-3}\exp(-\frac{z}{1.26}) + 3.36\times10^{-5}\exp[-(\frac{z-7.43}{4.99})^2] + 1.96\times10^{-5}\exp[-(\frac{z-16.9}{3.99})^2]$$

$$\beta_a(z) = 4.77\times10^{-3}\exp(-\frac{z}{1.04}) + 1.01\times10^{-4}\exp[-(\frac{z-4.18}{5.08})^2] + 1.94\times10^{-5}\exp[-(\frac{z-15.6}{3.51})^2]$$

Selected publications related to these projects are presented in the References 5 through 10.

REFERENCES

1. Bo Liu, Zhiqing Zhong and Jun Zhou, Development of a Mie scattering lidar system for measuring whole tropospheric aerosols, *Journal of Optics A: Pure and Applied Optics*, 9, 828-832, 2007.
2. Chenbo Xie, Jun Zhou, Guming Yue et. al., New Mobile Raman Lidar for Measurement of Tropospheric Water Vapor, *Acta Optica Sinica*, Vol.26, No.10. 2006 (in Chinese).
3. X. Liu, Y. Zhang , H. Hu , K. Tan, Z.Tao, S. Shao, K. Cao, G. Zhang Gaixia and S. Yu, Mobile lidar for measurements of SO_2 and O_3 in the low troposphere, *Optical Technologies for Atmospheric, Ocean, and Environmental Studies,* Daren Lu, Gennadii G. Matvienko; Eds. Proc. SPIE Vol. 5832, 156-163, May 2005.
4. D. Sun, Z. Zhong, J. Zhou, H. Hu, T. Kobayashi, Accuracy analysis of the Fabry-Perot etalon based Doppler wind lidar, *Optical Review* , Vol.12, No.5, 409-414, 2005.
5. J. Zhou, G. Yu, C. Jin, F. Qi, D. Liu, H. Hu, Z. Gong, G. Shi, T. Nakajima and T. Takamura, Lidar Observations of Asian Dust over Hefei, China in the Spring of 2000, *JGR*, 107, D15, AAC51-58, 2002.
6. J. Zhou, X. Qiu, G. Yu, C.Jin, F. Qi, Lidar Observations of Asian Dust over Eastern China (31.90° N, 117.16o°E) from 1998 to 2001, *Lidar Remote Sensing In Atmosphere and Earth Sciences, reviewed and revised papers Presented at 21th ILRC, Quebec, Canada,* 273-276,8-12 July, 2002.
7. D. Liu, F. Qi, C. Jin, G. Yue and J. Zhou, Polarization lidar observations of cirrus and Asian dust aerosols over Hefei, *Chinese Journal of Atmosphere Sciences,* Vol. 27, 1093-1100, 2003 (in Chinese).
8. S. Yuan, X.Yu, and J. Zhou, Lidar observations of the lower atmospheric layer in Hefei, *Chinese Journal of Atmosphere Sciences,* No.3, Vol. 29, 387-395, 2005(in Chinese).
9. J. Zhou, D. Liu, G. Yu, F. Qi, A. Fan, H. Hu, Z. Gong, G. Shi, T. Nakajima, T. Takamura, Seven years of Asian dust lidar observations over southeastern China, *Optical Technologies for Atmospheric, Ocean, and Environmental Studies,* Daren Lu, Gennadii G. Matvienko; Eds. Proc. SPIE Vol. 5832, 122-130, May 2005.
10. J. Zhou, D. Liu, G. Yue, F. Qi, A. Fan, H. Hu, Z. Gong, G. Shi: Vertical Distribution and Temporal Variation of Asian Dust Observed by Lidar over Hefei, China, *Journal of Korean Physical Society*, No.1,Vol. 49, 320-326, 2006.

Role of aerosol and cloud in the Earth's climate

Teruyuki Nakajima[1]

[1]*Center for Climate System Research, The University of Tokyo*

Abstract

In this article I like to overview several important climate effects of aerosol and cloud that can change the earth's radiation budget and hence the earth's climate. There are still large uncertainties in evaluation of these effects by models and observation. Therefore, surface networks of skyradiometers and other instruments are indispensable for improving the evaluation. I like to propose recommendations for future works to reduce the large uncertainties.

Keywords **:** aerosol, cloud, climate

1. Introduction

Anthropogenic short-lived atmospheric constituents such as aerosols can make significant effects on the earth's climate, especially in the Asian region with large aerosol emission sources, of which forcing is comparable to that of long-lived greenhouse gases (LGHG) but with opposite sign and different geographical distributions (e.g., Forster et al., 2007). Recent studies have found that various climate effects of aerosols are possible. The aerosol direct effect is that aerosols directly scatter and absorb/emit radiation, through which the earth's radiation budget can be modified. There are several evidences that the solar radiation at the earth's surface undergoes a significant long-term trend in the last several decades, indicating a surface dimming effect in the polluted areas. At the same time, aerosols are found to cause various indirect effects to change the radiation budget, temperature, cloudiness, precipitation etc. A well known indirect effect is called the first indirect effects or Twomey effect (Twomey et al., 1984) that causes an increase in the cloud optical thickness (COT) when aerosols act as cloud condensation nuclei (CCN) to increase the cloud droplet number and hence to decrease the effective cloud droplet radius (CDR) when the total liquid water path (LWP) of the cloud does not change. The secondary indirect effect or Albrecht effect (Albrecht, 1989) is also recognized as important because this effect significantly increases LWP and hence increases COT when aerosols reduce CDR to lower the precipitation efficiency of the cloud layer. Recent studies also show significant cloud and precipitation changes can be produced by aerosol indirect effects of various kinds (e.g., Rosenfeld, 2000; Chung and Ramanathan, 2007; Mukai et al., 2008)

Figure 1 shows estimates of the radiative forcing at the top of the atmosphere (TOA) and the bottom of the atmosphere (BOA) since 1750 from IPCC (Forester et al., 2007) and from MIROC model (Takemura et al., 2005). The figure shows that the total forcing of aerosol direct and first indirect effects at TOA from IPCC is about -1.2 Wm^{-2} (Forster et al. 2007) to cancel about 40% of the positive GHG forcing. It is found, however, each contribution is different among studies and uncertainty is as large as about ±0.5 Wm^{-2}. The total BOA forcing of aerosol is -2.1 Wm-2 according to MIROC model simulation and dominates over the positive forcing of GHGs.

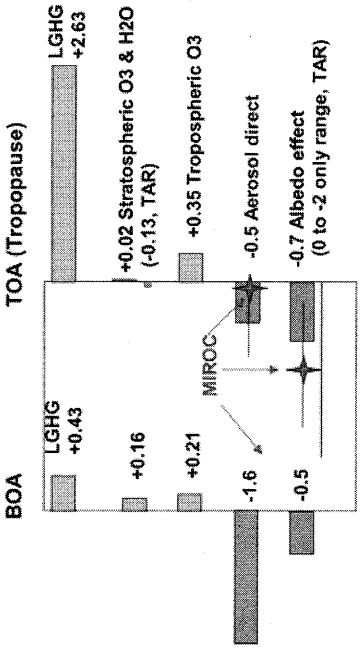

Fig. 1. Radiative forcings at TOA and BOA since 1750. TOA values are from IPCC TAR and AR4. Star symbols and BOA values show values from the MIRC model.

2. Aerosol characteristics and direct radiative forcing

Global dimming and brightening phenomena have been studied using data of surface radiation networks (Wild et al., 2005; Che et al., 2005; Qian et al., 2006). These studies showed that the surface solar radiation is increasing in the

European region, while the Asian region still suffers a decrease in the surface solar radiation due to increasing anthropogenic aerosols. Future trend of anthropogenic aerosol change depends on the future economical growth and actions for reducing air pollution in this region. Surface pyranometer and pyrheliometer networks of GEWEX/BSRN and of each country, especially that of Chinese Meteorological Administration covering a large area, are useful for long-term monitoring of the surface radiation flux and equivalent aerosol optical thickness (AOT) for several decades.

One of important parameters for determining surface and TOA radiation budget is the single scattering albedo, SSA, defined as the ratio between scattering and extinction cross sections. The SSA value is strongly controlled by the black carbon content of aerosols. Also mineral dust particles are predominant in the springtime to affect the value of SSA in the East Asian region. Hence the aerosol optical properties in this region are very complicated (Clarke et al., 2004; (Moteki et al., 2007). In order to elucidate the optical and radiative properties of Asian aerosols, large scale comprehensive regional experiments have been performed: INDOEX, ACE-Asia, APEX, ABC-EAREX & APMEX, EAST-AIRE, Pearl River Delta Experiment, and others. Nakajima et al. (2007) showed that the radiative efficiency factor, defined as $\beta = -\Delta F/\Delta\tau_{500}$ where ΔF is the 24 hour solar radiative forcing of aerosol and $\Delta\tau_{500}$ is the AOT at wavelength of 500nm, can reach a value as large as 100 in the case of Asian dust events, which is very large compared with a mean value around 70 as reported by many other studies (Nakajima et al., 2007) as shown by Fig. 2. They showed such large forcing efficiency can be produced when soot particles adhere on the surface of coarse mineral dust particles. Another possibility for such a large β value is that mineral dust particles themselves are highly absorbing as suggested by several past studies (Sokolik and Toon, 1999; Aoki et al., 2005).

3. Cloud field perturbation and possible climate effects

It has been a common recognition that direct and indirect effects of aerosols at TOA reduce the available solar energy and significantly offset the global warming by increasing greenhouse gas concentration. On the other hand, it is still needed to study how the regional climate is perturbed by aerosols. Past studies have shown that there is a long-term trend in the cloud amount over China (Kaiser et al., 2002). Several reasons are possible for this regional cloud change. Global warming phenomenon can cause a change in the global circulation and land-ocean temperature gradient causing a change in Monsoon circulation. Change in the land use and vegetation distribution can cause perturbation to the soil moisture and vertical atmospheric stability. From these mechanisms a significant change in the cloud amount is expected.

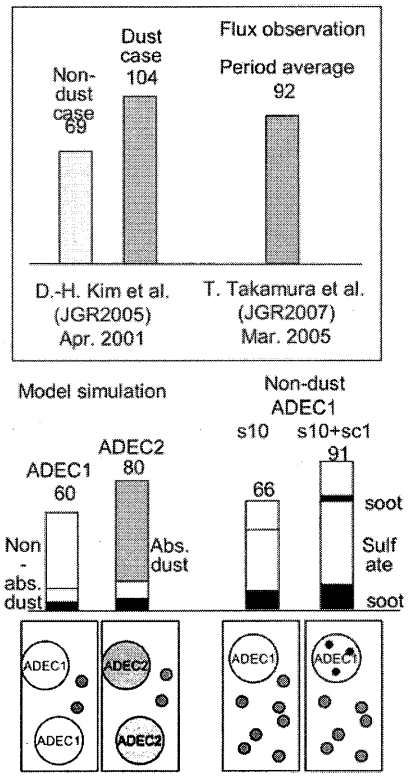

Fig. 2. Radiative forcing efficiencies from observation and models. Model values are from one dimentiona

Along with these effects, anthropogenic aerosols can generate a large scale circulation change and hence cloud amount change as discussed by Mukai et al. (2007). They found observed trend of cloud amount change over China can be explained by competing effects of greenhouse gas effect and aerosol effect. The latter effect can be further divided into two mechanisms: One is a change of local cloudiness by regional direct and indirect aerosol forcing. Direct forcing cools the surface of the region and hence the atmospheric stability is changed. At the same time aerosols act as CCN to increase the cloud amount through the secondary indirect effect which increases the cloud lifetime. The second effect is that the large scale general circulation is changed when the surface of the region is cooled by aerosols through direct and indirect surface forcing. Simulations by a general circulation model, which is coupled with a mixed-layer ocean model, suggested that cloud and precipitation can be changed even over tropical region (Takemura et al., 2005; Mukai et al., 2007). And the

simulation results also showed that the dominant mechanism for the change in China is different in northern part, eastern part, and southern part of China. So the interpretation of the observed change of cloud amounts for low, middle, and high level clouds is very complicated and we need more validation study.

Useful data for validation are distributions of AOT, COT, CDR, and LWP from satellite remote sensing (e.g., Kawamoto et al., 2004). There is the following relation,

$$b(\log \mathrm{LWP}) = b(\log \mathrm{CDR}) + b(\log \mathrm{COT}),$$

where the sensitivity is defined as $b(\log y) = d\log(y)/d\log(N_a)$ with the column aerosol number N_a. Figure 3 shows various estimates of the sensitivities from satellite remote sensing and models. The figure indicates that the existing satellite data analyses showed a large variety in the dependence of the cloud parameters on the aerosol index (Nakajima and Schultz, 2008). Remote sensing and model results have different tendencies especially over land. It is, therefore, we also need more elaboration of satellite data analysis.

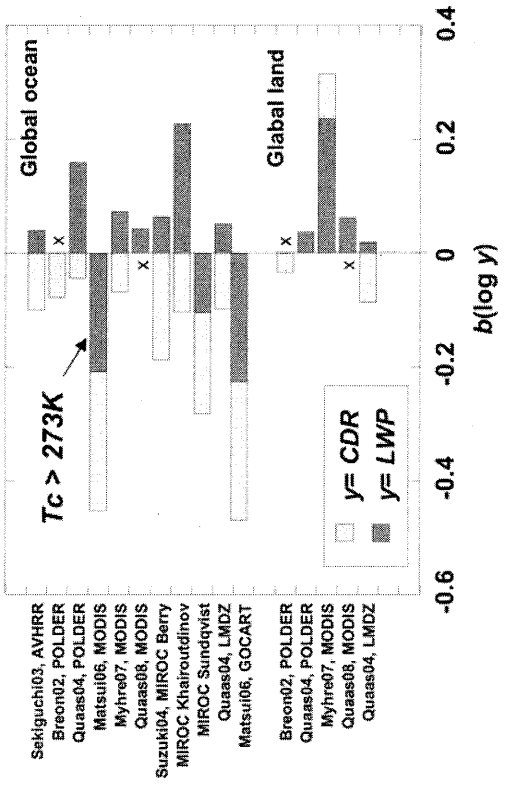

Fig. 3. Various estimates of slopes of COT and LWP sensitivities on the aerosol number.

4. Conclusions and Recommendation for future tasks

The following conclusions and recommendations are drawn from this study:

(1) Aerosols have many pathways to change the regional climate. Our understanding level of each process is not high.

(2) One of important aerosol effects is an indirect effect through change in the earth's surface temperature and general circulation.

(3) Observed long-term trend of regional geophysical parameters (cloud amount, cloud properties, precipitation, and so on) needs to be interpreted as the total effect of global warming, aerosol effect and others. It is, therefore, we need comprehensive and careful model simulations and data analysis to understand the change.

In order to overcome the above-listed problems, the following works have to be done:

(a) Physical and chemical modeling of aerosol properties and radiative effect must be improved. Such improvements should be supported by more surface measurements and laboratory experiments.

(b) Regional and global simulations making use of non-hydrostatic meso-scale models are needed to understand the mechanism of the regional climate change. In this regard, models have to be improved for better simulation of cloud formation process and aerosol-cloud interaction process. Especially deep cloud modeling is important.

(c) Collaboration and coordinated effort are needed for improving Asian networks of aerosol, cloud, and radiation measurements. Data exchange and collaboration for data analyses are very important, because comprehensive analyses need efforts by researchers in different fields, i.e., atmospheric dynamics, physics, and chemistry.

References

Albrecht, B. A., 1989: Aerosols, cloud microphysics, and fractional cloudiness, Science, 245, 1227_1230.

Aoki, T., T. Y. Tanaka, A. Uchiyama, M. Chiba, M. Mikami, and S. Yabuki, 2005: Sensitivity experiments of direct radiative forcing caused by mineral dust simulated with a chemical transport model, J. Meteorol. Soc. Japan, 83A, 315_331.

Che, H. Z., G. Y. Shi, X. Y. Zhang, R. Arimoto, J. Q. Zhao, L. Xu, B. Wang, and Z. H. Chen, 2005: Analysis of 40 years of solar radiation data from China, 1961 _ 2000, Geophys. Res. Lett., 32, L06803, doi:10.1029/2004GL022322.

Chung, C. E., and V. Ramanathan, 2007: Relationship

between trends in land precipitation and tropical SST gradient, Geophys. Res. Lett., 34, L16809, doi:10.1029/2007GL030491.

Clarke, A. D., et al., 2004: Size distributions and mixtures of dust and black carbon aerosol in Asian outflow: Physiochemistry and optical properties, J. Geophys. Res., 109, D15S09, doi:10.1029/2003JD004378.

Forster, P., V. Ramaswamy, P. Artaxo, T. Berntsen, R. Betts, D.W. Fahey, J. Haywood, J. Lean, D.C. Lowe, G. Myhre, J. Nganga, R. Prinn, G. Raga, M. Schulz, and R.V. Dorland, 2007: Changes in Atmospheric Constituents and in Radiative Forcing, in Climate Change 2007: The Physical Science Basis. Contribution of Working Group I to the Fourth Assessment Report of the Intergovernmental Panel on Climate Change, edited by S. Solomon, D. Qin, M. Manning, Z. Chen, M. Marquis, K.B. Averyt, M.Tignor, and H.L. Miller, Cambridge University Press, United Kingdom and New York, NY, USA.

Kaiser, D. P., and Y. Qian, 2002: Decreasing trends in sunshine duration over China for 1954 _ 1998: Indication of increased haze pollution?, Geophys. Res. Lett., 29, 2042, doi:10.1029/2002GL016057.

Kawamoto, K., T. Hayasaka, T. Nakajima, D. Streets, and J.-H. Woo, 2004: Examining the aerosol indirect effect using SO2 emission inventory over China using SO2 emission inventory. Atmos. Res.,72, 353-363.

Moteki, N., Y. Kondo, Y. Miyazaki, N. Takegawa, Y. Komazaki, G. Kurata, T. Shirai, D.R. Blake, T. Miyakawa, and M. Koike, 2007: Evolution of mixing state of black carbon particles: Aircraft measurements over the western Pacific in March 2004, Geophys. Res. Lett., 34, L11803, doi:10.1029/2006GL028943.

Mukai, M., T. Nakajima, and T. Takemura, 2008: A study of anthropogenic impacts of the radiation budget and the cloud field in East Asia based on model simulations with GCM, J. Geophys. Res., 113, D12211, doi:10.1029/2007/JD009325.

Nakajima, T., and M. Schulz, 2008: What do we know about large-scale changes of aerosols, clouds, and the radiation budget?, in Perturbed Clouds in the Climate System, Eds. J. Heintzenberg and R.J. Charlson, FIAS Forum, to be published.

Nakajima, T., S.-C. Yoon, V. Ramanathan, G-Y. Shi, T. Takemura, A. Higurashi, T. Takamura, K. Aoki, B.-J. Sohn, S.-W. Kim, H. Tsuruta1, N. Sugimoto, A. Shimizu, H. Tanimoto, Y. Sawa, N.-H. Lin, C.-T. Lee, D. Goto, and N. Schutgens1, 2007: Overview of the Atmospheric Brown Cloud East Asian Regional Experiment 2005 and a study of the aerosol direct radiative forcing in east Asia, J. Geophys. Res., 112, D24S91, doi:10.1029/2007JD009009.

Qian, Y., D.P. Kaiser, L.R. Leung, and M. Xu, 2006: More frequent cloud-free sky and less surface solar radiation in China from 1955 to 2000.

Rosenfeld, D., 2000: Suppression of rain and snow by urban and industrial air pollution, Science, 287, 1793_1796.

Sokolik I.N., and O.B. Toon, 1999: Incorporation of mineralogical composition into models of the radiative properties of mineral aerosol from UV to IR wavelengths, J. Geophys. Res., 104, 9423-9444.

Takemura, T., T. Nozawa, S. Emori, T.Y. Nakajima, and T. Nakajima, 2005: Simulation of climate response to aerosol direct and indirect effects with aerosol transport-radiation model. J. Geophys. Res., doi:10.1029/2004JD005029.

Twomey, S., M. Piepgrass and T. L. Wolfe, 1984: An assessment of the impact of pollution on global cloud albedo. Tellus, 36B, 356-366.

Wild, M., H. Gilgen, A. Roesch, A. Ohmura, C. N. Long, E. G. Dutton, B. Forgan, A. Kallis, V. Russak, and A. Tsvetkov, 2005: From dimming to brightening: Decadal changes in solar radiation at earth's surface, Science, 308, 847-850, doi: 10.1126/science.1103215.

Progress in Satellite Radiation Budget Research: Application to Climate Issues

R. T. Pinker
Department of Atmospheric and Oceanic Science, University of Maryland, College Park, MD, USA
pinker@atmos.umd.edu

Abstract
In this presentation discussed will be recent applications of satellite estimates of radiative fluxes in climate research as well as some new products of particular interest for hydrological modeling. The examples will be drawn from work based on information developed at the University of Maryland (UMD/SRB). Covered will be applications to climate issues as related to the Tropical Pacific and Atlantic oceans (Rodriguez-Puebla et al., 2008; Grodsky et al., 2008), issues of relevance to the Coordinated Energy and Water Cycle Observations Project (CEOP) such as diurnal variability in clouds and convection over the Indian Monsoon region (Wonsick et al., 2008), the effect of aerosols in the framework of the Elevated Heat Pump Hypothesis (Lau et al., 2006; Wonsick et al., 2008), possible improvements in modeling net primary productivity (Pinker et al., 2008), and hydrological modeling at basin scale (Wood et al., 2008)
Keywords: Shortwave Radiation Budgets

1. Introduction

Radiative fluxes are the driving force of the climate system and as such, there is a need for information on their spatial and temporal distribution and variability. For several years now, work has been in progress on the utilization of satellite observations for estimating such fluxes and more recently, on their use in climate research. Applications include: modeling of the hydrological cycle, representation of interactions and feedbacks between the atmosphere and the surface, and validation of climate and numerical weather prediction models. Steering has been provided by the World Climate Research Programme (WCRP)/World Meteorological Organization (WMO) and by several national and international projects, such as the Global Energy and Water Budget Experiment (*GEWEX*), the International Biosphere/Geosphere Program *(IGBP*), and the Coordinated Energy and Water Cycle Observations Project *(CEOP)* which coordinates scientific issues related to the development and implementation of Regional Hydroclimate Projects. Progress has also been made to derive spectral components of radiative fluxes such as Photosynthetically Active Radiation (PAR) and UV radiation. To meet the user's needs for information on the quality of various available products, under the support of WCRP a *Radiative Flux Assessment* activity is underway to provide a framework for estimating accuracy of such products. Evaluation results by individual investigators, either data producers or users, are quite encouraging. As a result, numerous studies have been undertaken where such data are used to address a wide range of climate issues.

2. Methods

There is a trade-off in the quality of the satellite data of high spatial and temporal resolution and the extent of their spatial coverage. Most global data sets (e.g., ISCCP D1) are of low spatial and temporal resolution while the higher resolution data cover smaller regions. Examples to be discussed are based on data of different scales. The objective is to illustrate the usefulness of each scale and the need for compatibility between scales and issues at hand. In this abstract provided will be selected examples and a reference list of work completed and in progress from which the examples are drawn.

Case 1: Evaluation of radiative fluxes from NWP models

The models selected for comparison with satellite estimates are from the AMIP II runs: CCSM3 (USA) (Collins et al., 2006), UKMO-HadGEM1 (UK) (Gordon et al., 2000) and CNRM-CM3 (France) (Deque et al., 1994). The data used cover the period from July 1983 to June 2000 and include the notable El Ni˜no and La Ni˜na events. The period used is limited by the availability of shortwave (SW)↓ surface fluxes from model simulations, satellites, and sea surface temperature (SST) data from the National Oceanic Atmospheric Administration (NOAA) (Reynolds et al., 2002). The comparison is performed over the tropical Pacific where a strong signal of inter-annual variability occurs. As seen in Figure 1, the best agreement between the satellite estimates and model output is for the UKMO-HadGEM1 model (these three models were the best in terms of correlation with satellite estimates from all those that participated in AMIP II). In Figure 2 illustrated are anomalies or departures from the mean in the Hovm¨oller representation for SST and SW↓surface corresponding to UMD/SRB and the HadGEM1 AMIP II run. The shaded

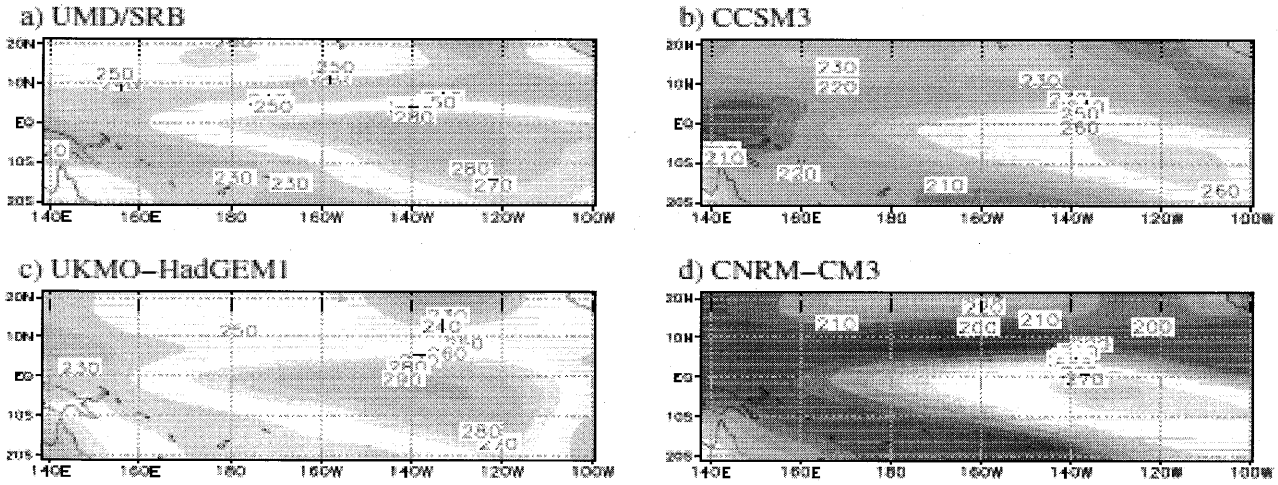

Figure 1. SW↓ surface radiative fluxes over the tropical Pacific in Wm^{-2} for: (a) UMD/SRB estimates; (b) CCSM3; (c) UKMOHadGEM1; (d) CNRM-CM3 AMIP II runs.

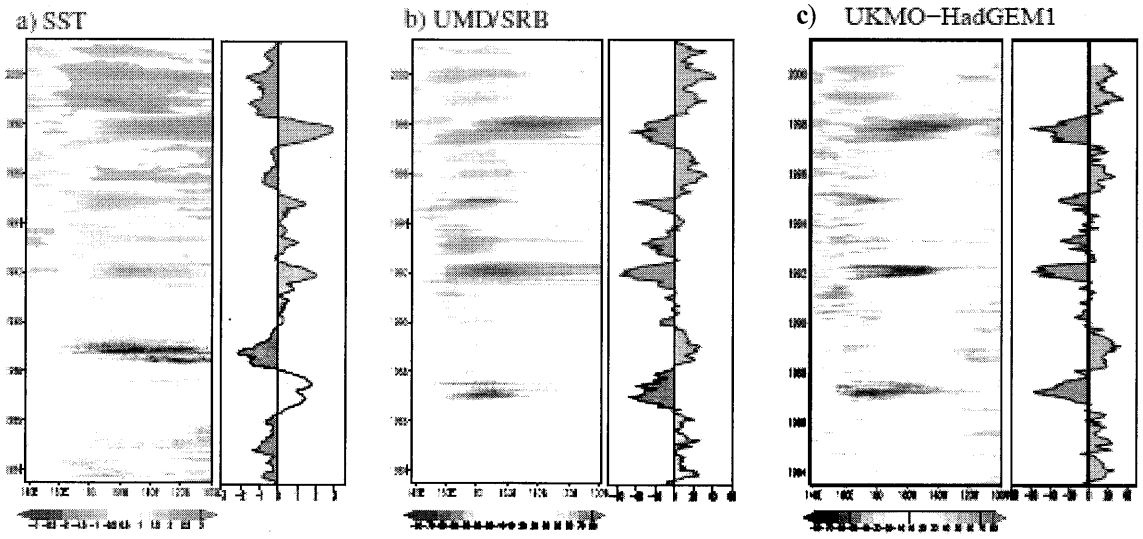

Figure 2. Time-longitude plot (Hovm¨oller representation) for the departures of the mean averaged over 5°S to 5°N corresponding to: (a) SST (°C), (b) SW↓ surface UMD/SRB; (d) UKMO-HadGEM1, in Wm^{-2}. The right figure of each Hovm¨oller representation is the time series averaged over El Ni˜no 3.4 region for SST and over El Ni˜no 4 region for SW↓ surface

contours show the time-longitude evolution for the equatorial Pacific (5° S to 5°N). To the right of each Hovm¨oller figure, the time series evolution averaged over the above referenced boxes is represented. As expected, the positive (negative) phase of SST in the eastern Pacfic is related to negative (positive) SW↓surface anomalies in the central Pacific. There is a clear correspondence between amplification and dissipation of the anomalies, which is indicative of a forcing that affects both atmosphere and ocean almost simultaneously. These results agree with Ramanathan and Collins (1991) and Yu and Boer (2002).

Case 2: Asian Monsoon region

In support of the Indian Ocean Experiment (INDOEX) *Meteosat-5* was moved to cover the Indian continent in 1998 and replaced by *Meteosat-7 in 2007*. These data provide a unique opportunity to study in detail the diurnal variability of cloud amounts, cloud types, and various components of the radiation budget over that region. The objective as discussed in (Wonsick et al., 2008) is to use the derived cloud products to address questions about the Indian Monsoon, to characterize clouds and convection during its various phases, and to demonstrate how this product can be used for evaluation of numerical model cloud products. In Figure 3 illustrated is the SW↓ surface radiation at 0.125^0 resolution as derived from *Meteosat-5*.

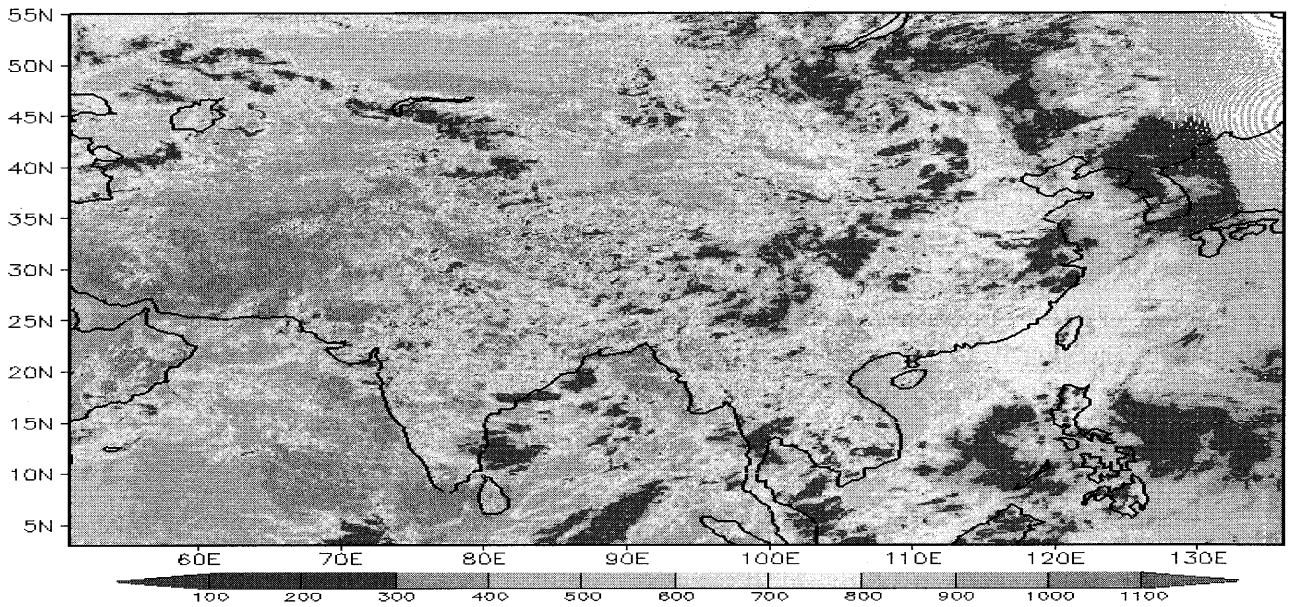

Figure 3. Instantaneous values of SW↓surf for 1 August 1998 at 07 UTC using *Meteosat-5* observation at 5 km gridded to 0.125^0 resolution.

Recently it has been postulated that aerosol-induced anomalous mid- and upper-tropospheric warming above the Tibetan Plateau leads to early onset and a northwestward shift in monsoon rainfall—the so-called "Elevated Heat Pump" effect (Lau et al. 2006). In particular, black carbon emissions from sources in Northern India and dust from western China, Afghanistan, Pakistan, and Southwest Asia, are the driving forces behind the anomaly. This concept is based on results from runs of the NASA finite-volume general circulation model with and without radiative forcing from different types of aerosols. Cloud and radiation data from *Meteosat-5* observations are used to take an observational approach to detect signatures of the "Elevated Heat Pump" effect in the cloud cover and cloud type distributions over the Asian Monsoon region, supplemented with surface temperature data from the NCEP/NCAR Reanalysis and precipitation data from the Global Precipitation Climatology Project. Features are compared for the highest- and lowest-aerosol content years of the current decade. Not all the elements of the hypothesis have been verified in the observations. In the presentation discussed will be additional applications of radiative fluxes to current climate issues.

Acknowledgements

This symposium is sponsored by the Ministry of Education, Science, Sports and Culture, Japan (MEXT), and National University Corporation Chiba University.

The author wishes to acknowledge the contribution of all co-authors in the list of ""References for Talk" and the sponsoring agencies acknowledged in these papers.

References Related to Talk

1) Gadhavi, H., R. T. Pinker, and I. Laszlo, 2008. Estimates of Surface Ultraviolet (UV) Radiation over North America using GOES observations, J. Geophys. Res., doi:10.1029/2007JD009308.
2) Grodsky, Semyon. A., Abderrahim Bentamy, James A. Carton, and Rachel T. Pinker, 2008. Intraseasonal latent heat flux based on satellite Observations. JOURNAL OF CLIMATE, submitted.
3) Karnieli, A., Nurit Agam, Rachel T. Pinker, Martha Anderson, Mark L. Imhoff, Garik G Gutman, Natalya Panov, Alexander Goldberg., 2008. Use of NDVI and LST for Drought Assessment: Merits and Limitations. JOURNAL OF CLIMATE, submitted.
4) Kun Yang, Rachel T. Pinker, Yaoming Ma, Toshio Koike, Margaret M. Wonsick, Stephen J. Cox, Yuanchong Zhang, and Paul Stackhouse, 2008. Evaluation of Satellite Estimates of Downward Shortwave Radiation over the Tibetan Plateau JOURNAL OF GEOPHYSICAL RESEARCH, VOL. 113, doi:10.1029/2007JD009736, 2008
5) Liu, H. Q.; Pinker, R. T., 2008. Radiative fluxes from satellites: Focus on aerosols JOURNAL OF

GEOPHYSICAL RESEARCH-ATMOSPHERES Volume: 113 Issue: D8 Article Number: D08208.

6) Liu, H. Q.; Pinker, R. T.; Chin, M., and L. Remer, 2008. Synthesis of information on aerosol optical properties. JOURNAL OF GEOPHYSICAL RESEARCH-ATMOSPHERES, Volume: 113 Issue: D7, D07206.

7) Pinker, R. T., H. Wang, Maosheng Zhao, and E. F. Wood' 2008. Evaluating the Impact of Photosynthetically Active Radiation (PAR) on Estimates of Net Primary Productivity. GLOBAL BIOGEOCHEMICAL CYCLES, submitted.

8) Rodriguez-Puebla, C., Pinker, R. T.; Nigam, S., 2008. Relationship between downwelling surface shortwave radiative fluxes and sea surface temperature over the tropical Pacific: AMIP II models versus satellite estimates, ANNALES GEOPHYSICAE, Volume: 26 Issue: 4, 785-794.

9) Wang, H., and R. T. Pinker, 2008. Radiative Fluxes from MODIS. JOURNAL OF GEOPHYSICAL RESEARCH, submitted.

10) Wang, H. and R. T. Pinker, 2008. How good are buoy observations of radiative fluxes? GEOPHYSICAL RESEARCH LETTERS, submitted.

11) Wonsick, M.. M.., Rachel T. Pinker and Yves Govaerts, 2008. Cloud Variability over the Indian Monsoon Region as Observed from Satellites. JOURNAL OF APPLIED METEOROLOGY, in revision.

General References

1) Collins, W. D., Bitz, C. M., Blackmon, M. L., Bonan, G. B., Bretherton, C. S., Carton, J. A., Chang, P., Doney, S. C., Hack, J. J., Henderson, T. B., Kiehl, J. T., Large, W. G., McKenna, D. S., Santer, B. D., and Smith, R. D.: The Community Climate System Model version 3 (CCSM3), Journal of Climate, 19, 2122–2143,

2) Deque, M., Dreveton, C., Braun, A., and Cariolle, D.: The Arpege/ifs atmosphere model -a contribution to the French Community Climate Modeling, Climate Dynamics, 10, 249–266, 1994.

3) Gordon, C., Cooper, C., Senior, C. A., Banks, H., Gregory, J. M., Johns, T. C., Mitchell, J. F. B., and Wood, R. A.: The simulation of SST, sea ice extents and ocean heat transports in a version of the Hadley Centre coupled model without flux adjustments, Climate Dynamics, 16, 147–168, 2000.

4) Lau, K.-M., M. K. Kim, and K. M. Kim, 2006: Asian summer monsoon anomalies induced by aerosol direct forcing: the role of the Tibetan Plateau. *Clim. Dyn.*, **26**, 855-864, doi:10.1007/s00382-006-0114-z.

5) Ramanathan, V. and Collins, W.: Thermodynamic regulation of ocean warming by cirrus clouds deduced from observations of the 1987 El-Ni˜no, Nature, 351, 27–32, 1991.

6) Reynolds, R. W., Rayner, N. A., Smith, T. M., Stokes, D. C., and Wang, W. Q.: An improved in situ and satellite SST analysis for climate, Journal of Climate, 15, 1609–1625, 2002.

7) Yu, B. and Boer, G. J.: The roles of radiation and dynamical processes in the El Nino-like response to global warming, Climate Dynamics, 19, 539–553, 2002

Evaluation of Cloud Observation with MMCR FALCON-I from Hedo Campaign 2008

Jun Yamaguchi[1], Toshiaki Takano[1], Youhei Kawamura[1], Hideji Abe[1]
Tamio Takamura[2], G. Pandithurai[23] Atsushi Shimizu[4], Ichiro Matsui[4]
[1]*Chiba University Graduate School of Engineering, 1-33 Yayoichou Inage Chiba Chiba Japan,*
junyamaguchi0728@graduate.chiba-u.jp
[2]*Chiba University The Center for Environmental Remote Sensing, 1-33 Yayoichou Inage Chiba Chiba Japan*
[3]*Indian Institute of Toropical Meteorology, Pune India*
[4]*National Institute for Environmental Studies, 16-2 Onogawa Tsukuba-City Ibaraki 305-8506 Japan*

Abstract

The Millimeter-Wave Cloud Radar (MMCR) is an effective tool to detect clouds. , Chiba University developed the Frequency Modulated Continous-Wave (FMCW) MMCR, named FALCON-I, at 95GHz, which provides cloud top, base height, reflectivity, and doppler velocity. Although it has provided clear and detailed radar reflectivity from many observations, the technics of MMCR still have some uncertainties which must be take into consideration for correction of radar reflectivity. This paper examines the differences between FALCON-I data and data from other meteorological tools observed during the 2008 Hedo Campaign (organized by the National Institute for Environmental Studies) and evaluate those differences to figure out what is able to be observed by FALCON-I.

1. Introduction

Chiba University Shimakura Lab. has developed a FMCW Millimeter-Wave Cloud Radar named FALCON-I at 94.79GHz with 10MHz modulated in sawtooth wave, shown in Fig.1, for measurements of radar reflectivity and cloud droplets doppler velocity. This radar has two cassegrain antennas (transmitting antenn and receiving antenna), and the main characteristics of the radar are listed in Table 1.(1)

Table 1 : Main Characteristics of FALCON-I

Center Frequency	94.79GHz (W-band)
Modulation Range	∓10MHz
Transmitting Power	0.5W (27dBm)
Range	500m – 20000m
Spatial Resolution	15m (variable)
Temporal Resolution	1sec (minimum)
Anttena Diameter	1m
Antenna Gain	57dBi
Antenna Distance	1.4m

FALCON-I has joined several observation projects which had been organized by Japan Agency for Marine-Earth Science and Technology (JAMSTEC) and National Institute for Environmental Studies (NIES). Radar reflectivity calibration was done by simultaneous observation with MMCR "SPIDER" developed by National Institute of Information and Communications Technology(2).

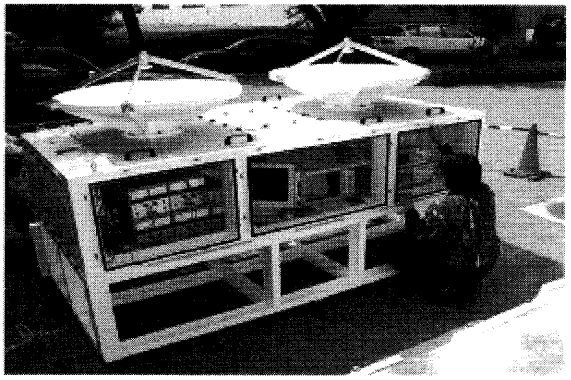

Fig.1 : Outlook of FALCON-I

FALCON-I provides cloud top height, cloud base height, radar reflectivity and doppler velocity. Radar reflectivity is calculated from radar equation (equ.1) from receiving power at receiving antenna.

$$P_r = \frac{\pi^3 P_t G \theta_h^2 \Delta r |K_w|^2}{2^9 (\ln 2) \lambda^2 r^2} \frac{Z_e}{A_a A_c A_r F_p} \quad \bullet \bullet \bullet \text{(equ.1)}$$

Parameters
P_r :Receiving Power (W) P_t :Transmitting Power (W) G :Antenna Gain
θ_h :Half-Power Beamwidth (rad) Δr :Range Resolution (m)
K_w :Complex Permittivity Factor of Water λ :Wavelength (m) r :Distance (m)
Z_e :Equivalent Radar Reflectivity Factor (mm^6/m^3) A_a : Atmospheric Attenuation
A_c : Cloud Attenuation A_r : Rain Attenuation F_p : Parallax Correction Factor

Although most of the parameters in radar equation are constant, the parameters of attenuation are not yet to be corrected. The attenuations which must be considered include atmospheric attenuation caused by water vapor and oxygen in the atmosphere, cloud attenuation caused by the

absorption of radio waves in the clouds, and parallax attenuation that results when the radar has two antennas on different antenna axes. The parameters of these attenuations at equation 1 are expressed in Aa, Ac, Ar and Fp.

The main object of this study is to evaluate the observed data of FALCON-I by comparing with the cloud base height from LIDAR of NIES and relative humidity from the Radio-Zonde at Naha of Japan Meteorological Agency, comparing with the calculated cloud top height from brightness temperature of MODIS (MODerate Resolution Imaging Spectroradiometer) developed by NASA (National Aeronautics and Space Administration), and comparing with LWP (Liquid Water Path) observed and calibrated from Micro Radiometer.

2. Methods

2.1 Cloud Base Height

FALCON-I provides cloud base height which is decided from radar reflectivity. The cloud base height of LIDAR is used to evaluate the ability of FALCON-I to determine cloud base height. Fig.2 shows zenith radar reflectivity on April 26 in 2008 at Cape Hedo Site of NIES. High density cloud were detected until 6:00 (UTC), and weak reflectivity was constantly detected below 1km all day.

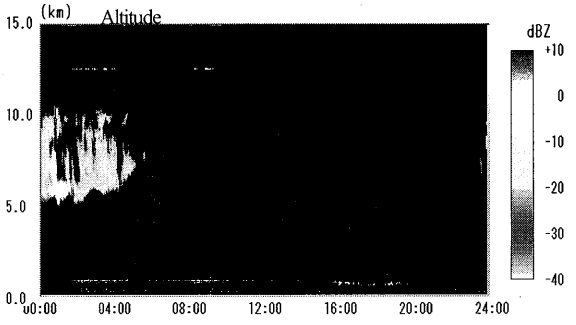

Fig. 2 : Time/Height Plot of Radar Reflectivity on April 26 in 2008

Fig.3 Shows Time/Altitude cloud base height plot of LIDAR and FALCON-I. Red-round plots are LIDAR cloud base height. Time resolution is 15 minutes. Blue-cross plots are the lowest cloud layer's base height of FALCON-I, and light blue-triangle plots are the second lowest cloud layer's base height of FALCON-I. Time resolution of FALCON-I is 1 minute. As shown in Fig.2, the observed cloud before 6:00 was thick, which leads to good matching between FALCON-I and LIDAR aroud 5-8km in Fig.3. There are also some good matching below 1km around 9:00 and 18:00 in Fig.3.

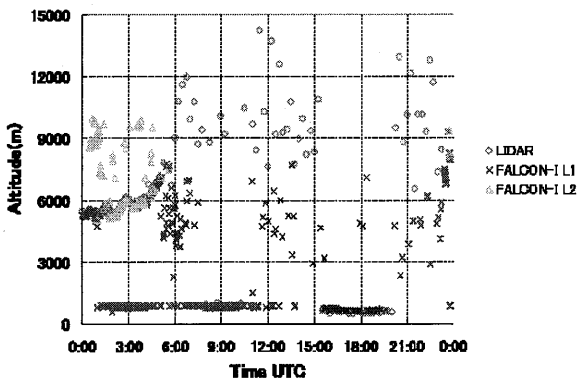

Fig.3 :Cloud Base Height Plot of LIDAR and FALCON-I on April 26 in 2008

Some plots of FALCON-I over 3000m after 9:00 do not seem reflectivity from clouds, comparing with radar reflectivity of Fig.2 and cloud base height of Fig.3. Although the resource of this reflectivity has yet to be revealed, atmospheric emission, clear-air-echo or temporary system noise of FALCON-I are one of the possibilities.

Cloud base height below 1km were never detected before 8:00 by LIDAR. On the other hand, FALCON-I detected cloud base height under 1km before 8:00. It is apparently that non-cloud echo like the echo or noise mentioned above are counted in cloud base height calculation algorithm. To avoid this confusion, the threshold of reflectivity is needed. It depends on the situation what kinds of clouds are targeted, but -30dBZ is proposed to be the threshold for many cases. It was reported that more than 80% of clouds which influences thermal emission and absorption at middle latitude areas in the north hemisphere are over -30dBZ[2].

Not only comparing base height, but also comparing LIDAR cloud base height and FALCON-I's radar reflectivity at cloud base height is needed to evaluate FALCON-I's sensitivity.

2.2 Cloud Top Height

FALCON-I also provides cloud top height which is determined from radar reflectivity. MODIS is one of the other useful observation instruments to evaluate cloud top height of FALCON-I. The MODIS contains several instruments which is operating on the two spacecrafts named "Terra" and "Aqua". It scans the entire surface of the earth every one to two days with measuring 36 spectral bands between 0.405 amd 14.385um, and its spatial resolutions are selectable from 250m, 500m and 1000m [3].

Cloud top height is to be guessed from cloud top temparture. MODIS observes around 2am over Cape Hedo almost everyday. Statistic correlation of cloud top height between FALCON-I and MODIS will be done during FALCON-I's

observation period from February 17th until May 4th, 2008.

2.3 Liquid Water Path

There are several reports and methods about radar reflectivity - liquid water content (Z-LWC) relationship. Not only value are important, but also classification of clouds influences this relationship[4]. The micro radiometer of Chiba Univercity CEReS (Center for Environmental Remote Sensing) set at the Hedo site provides LWP (Liquid Water Path) every three minutes. In this paper, integrated radar reflecivity from could bottom to top and liquid water path from the micro radiometer are compared in several cloud cases to evaluate correlation between FALCON-I and micro radiometer.

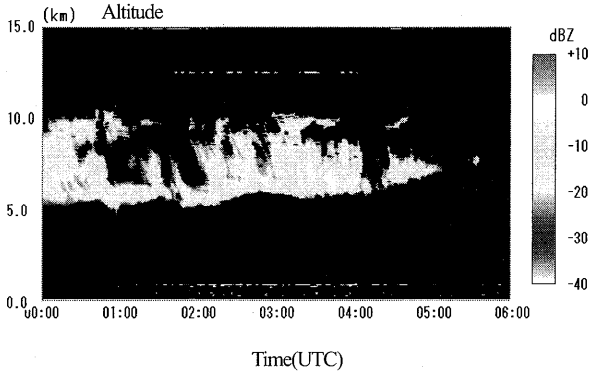

Fig. 4 : Radar Reflectivity from 0:00 to 6:00

Fig.4 shows Time/Height plot of radar reflectivity (Z) on April 26, 2008 in Universal Time. Precipitation was not detected, but thick and relatively high density clouds were observed during 0am – 6am.

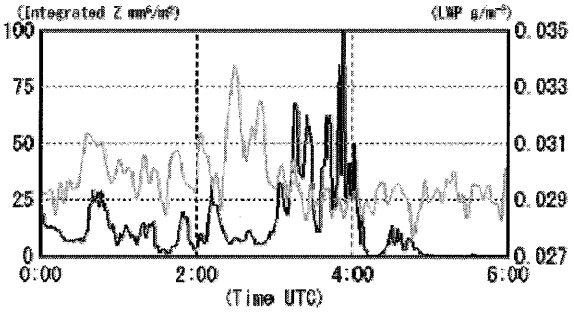

Fig.5 : Integrated Radar Reflectivity and LWP

Black line is the integrated radar reflectivity of FALCON-I and grey line is the liquid water path observed by micro radiometer.

Fig.5 shows the integrated radar reflectivity of FALCON-I and the LWP of the micro radiometer. The peaks of the both lines mitches well until 2am, but the highest peak of micro radiometer is around 2:30 and the peak of FALCON-I is around 3:50. The most important point when radar reflectivity and LWP are compared is removing the influence of ice clouds. Micro radiometer does not detect the frequencies which are emitted by ice clouds, and strong ice clouds have large reflectivity. It is guessed that most of the clouds observed before 2am are liquid water clouds and the clouds observed after 2am contained high density ice clouds. Other methods are needed to evaluate this hypothesis. Radio-Zonde data is one of the method to separate liquid region and ice region of clouds. Radio- Zonde observation was closed at March 31st, 2008 at Naha where is 100km apart from Hedo, but there might be several cases that this method can evaluate the correlation of Z and LWP.

2.4 Cloud Appearance Frequency

The several methods of evaluating FALCON-I, comparing with other meteorological observation instruments, were discussed the above. It is also needed for FALCON-I to be evaluated by meteorological common sense.

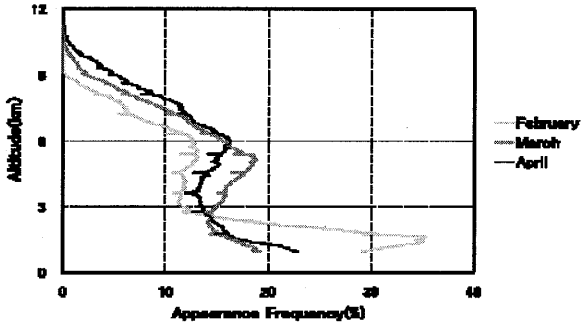

Fig. 6 : Cloud and Precipitation Appearance Frequency by Month during Observation Period.

Fig.6 shows Cloud and Precipitation Apperance Frequency by each month (Feburuary, March and April) / Height plot. Data below 1km was ignored to prevent unprecipitation or non-cloud echo from influencing the result. It is clearly seen that the highest height goes up as month goes by. Another unique point is February line has the peak at 2km, although March and April lines have the peak at the lowest height. This implies that stratus cloud or stratocumulus cloud appear more often in February in Okinawa, which strongly influence global climate because of their high albedo[5]. Annual observation of MMCR might give more hints about thermal emission change of the each seasons.

3. Conclusion

There were some unique results mentioned above from FLACON-I observation. There are also useful data to evaluate FALCON-I's results. Although evaluation has just began, it is expected that new characteristics of clouds are

found and some results would give hints for correction of radar equation to estimate the real radar reflectivity.

Acknowledgements

This symposium is sponsored by the Ministry of Education, Science, Sports and Culture, Japan (MEXT), and National University Corporation Chiba University.

The author would like to thank Dr. Shimizu and Dr. Matsui of NIES for providing LIDAR data and giving some guidance, Prof. Ishizaka of Aichi Gakuin University to evaluate assumed CCN (Cloud Condensation Nuclei).

References

1) Toshiaki Takano, Jun Yamaguchi, Hideji Abe, Kenichi Futaba, Shinichi Yokote, Youhei Kawamura, Tamio Takamura, Hiroshi Kumagai, Yuichi Ohno, Yuji Nakanishi, Teruyuki Nakajima : "Development and Performance of the Millimeter-wave Cloud Profiling Radar at 95GHz", IEEJ Trans, FM Vol.128, No.4 pp.258-262 (2008)

2) H. Horie, H. Kuroiwa, Y. Ohno: "Cloud Observation with CRL Airborne Cloud Radar", CRL Japan, Vol.48, No.2, pp.71-80 (2002) (in Japanese)

3) MODIS Web at homepage of National Aeronutics and Space Administration "http://modis.gsfc.nasa.gov/about/"

4) Neil I. Fox, Anthony J. Illingworth : "The Retrieval of Stratocumulus Cloud Properties by Ground-Based Cloud Radar", American Meteorological Society, Journal of Applied Meteorology Volume 36, Issue 5 (May 1997)

5) Virendra P. Ghate, Ieng Jo, Efthymios Serpetzoglou and Bruce A. Albrecht: "High Resolution Observations of Drizzle From Stratocumulus Using a 95 GHz FMCW Radar", Extented abstract at 32nd conference on radar meteorology (October 2005)

Aerosol Indirect Effect Studies at Cape Hedo during Spring Campaign-2008

G. Pandithurai[1,2], J. Yamaguchi[3], T. Takano[3], Y. Ishizaka[4] , A. Shimizu[5] and T. Takamura[1]

[1]*CEReS, Chiba University, 1-33, Yayoi-cho, Inage-ku, Chiba 263-8522, Japan*
[2]*Permanent Affiliation: Indian Institute of Tropical Meteorology, Pune 411 008, India*
[3]*Faculty of Engineering, Chiba University, 1-33 Yayoi-cho, Inage-ku, Chiba 263-8522, Japan*
[4]*Aichi Gakuin University, Japan*
[5] *National Institute for Environmental Studies, Tsukuba, Japan*
Email: pandi@restaff.chiba-u.jp

1. Introduction

The effect of aerosols on the microphysics of clouds has been the subject of intense scrutiny for decades. For a constant amount of condensed water, an increase in the number of cloud condensation nuclei (CCN) will generate a cloud that consists of smaller drops and reflects more energy to space, which is commonly referred to as the "first aerosol indirect effect". However, because the droplets are smaller they may inhibit collision-coalescence in the cloud, suppressing droplet growth that stops drizzle and other precipitation and extends cloud lifetime. Cloud cover can both decrease and increase with increasing aerosol loading. Recently, satellite remote sensors have been employed to provide a regional and even global view of aerosol effects on clouds. Current estimates of global average aerosol indirect forcing based on satellite data, range from –0.6 to –1.7 Wm^{-2}. More recently, surface-based remote sensing has also been applied to address aerosol effects on cloud microphysics, as these surface stations yield high temporal resolution data and because they sample aerosol below, rather than adjacent to clouds they do not suffer from "cloud contamination". The motivation of this study is to investigate the effect of aerosols on cloud microphysics using collocated surface remote sensing observations over Cape Hedo in Spring 2008.

2. Data and Methodology

Experimental facilities that operated during the spring 2008 observational campaign conducted at Cape Hedo (26.87 N, 128.25 E), Okinawa Island includes cloud radar, microwave radiometer, lidar, CCN counter, whole sky imager, nephelometer and radiation instruments. Cloud droplet effective radius profiles were retrieved using a 95 GHz Doppler radar reflectivity and microwave radiometer derived liquid water path for non-precipitating, ice-free clouds. Collocated measurements of aerosol scattering coefficients, and CCN using a nephelometer and CCN counters were analyzed to quantify the response of drop sizes to changes in CCN. The microwave radiometer made it possible to sort the cloud data according to liquid water path (LWP), consistent with Twomey's conceptual view of the aerosol impact on cloud microphysics.

3. Results

Single layer homogeneous, ice free stratocumulus cloud cases were selected for the analysis. Figure 1 shows diurnal variation of CCN at supersaturation of 0.5% and aerosol scattering coefficient (β_{sca}) measured at the surface on March 30, 2008. Covariation between CCN and β_{sca} agree very well with good correlation (R=0.96). It can be noted from Figure 1 that CCN increases from 16 UTC onwards and reached maximum around 20 UTC. Average CCN concentrations are 69 and 303

cm^{-3} for the periods, 12-16 UTC and 16-20 UTC, respectively. Figure 2 shows cloud droplet effective radius (R_{eff}) for the period in which drastic increase in CCN is observed. It can be noted that R_{eff} decreased from 3.2 to 2.4 μm, in agreement with Twomey effect.

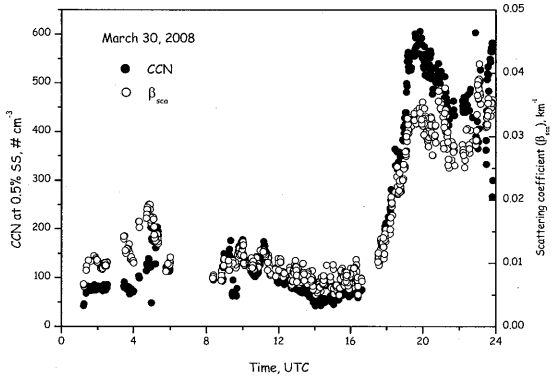

Figure 1. Diurnal variation of CCN at 0.5% supersaturation and aerosol scattering coefficient on March 30, 2008.

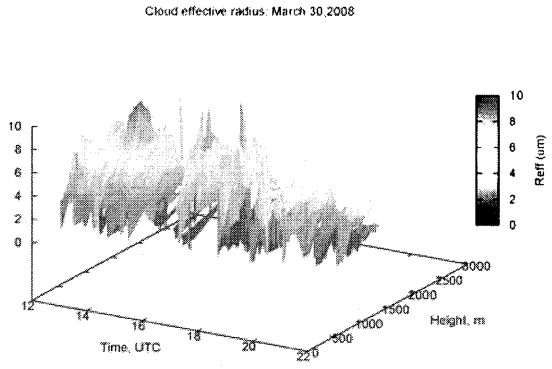

Figure 2. Cloud effective radius retrieved using radar reflectivity and microwave radiometer LWP on March 30, 2008.

3.1 Retrieval of cloud droplet effective radius using FALCON cloud radar and its comparison with i-skyradiometer

Cloud droplet effective radius profiles are retrieved from reflectivity of bistatic frequency modulated continuous wave (FMCW, FALCON) cloud radar operating at a frequency of 95 GHz using methodology proposed by *Frisch et al.* (2002). Technical details of the FALCON system and its comparison with SPIDER system can be found elsewhere (*Takano et al.* 2005). First method, which uses only the radar reflectivity with an assumption of constant cloud droplet number concentration (N_d=200 cm^{-3}) and droplet spread (σ=0.34). The second method, which uses radar reflectivity and microwave radiometer (MWR)-derived liquid water path (LWP), eliminates the assumption of droplet number concentration. Figure 2 shows the time-height cross-section of R_{eff} during the period from 1200 to 2200 hours where in the CCN has increased about a factor of 4. It can also be noted that R_{eff} values increases from cloud base to cloud top. Cloud effective radius is also retrieved from ground-based measurements of the transmitted solar radiation by a multi-spectral radiometer (Prede POM-02) called as i-skyradiometer. The retrieval procedure compares measurements of the cloud transmittance from the ground at water-absorbing and non-absorbing wavelengths with lookup tables of the transmittance pre-computed for plane-parallel, vertically homogeneous clouds (*Kikuchi et al.,* 2006). Three near-infrared wavelengths at 1.02, 1.6, and 2.2 μm correspond to spectral channels 9, 10, and 11 of a sun-sky radiometer. Among these wavelengths, 1.02 μm has been adopted as a non-absorbing wavelength, while the other two are water-absorbing wavelengths. At water absorbing wavelengths, water droplets absorb more solar radiation as the particles increase in size, whereas at non-absorbing wavelength, water droplets absorb little solar radiation. Figure 3 shows the Reff retrieved from radar, radar-MWR and POM-02 (channels 9& 10 and 9 & 11).

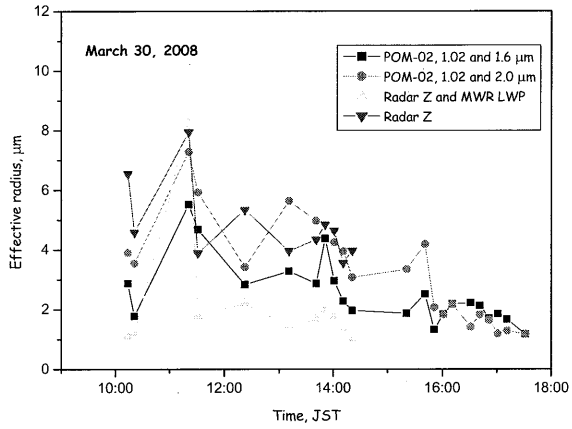

Figure 3. Comparison of retrieved cloud effective radius retrieved from Radar and i-skyradiometer.

Overall, they agree with similar temporal variation. The values are lower for the method, which uses Z and LWP. The error in retrieved LWP by statistical approach can induce an error in Reff. An attempt has been made to retrieve LWP using a physical approach, which uses surface meteorological observations, lidar & radar derived cloud base and top heights to estimate LWP iteratively by minimizing the observed and estimated brightness temperatures. The comparison between retrieved LWP using site-dependent and physical approach are shown in Figure 4 showing over all that an underestimate of site dependent approach. If this underestimation is taken into account the LWP values should be higher and this in turn will lead to slightly higher R_{eff} values, which will be closer to i-skyradiometer-derived R_{eff} values. However, the advantage of remote measurements for estimating aerosol indirect effect is less reliability on absolute measure as we will be looking at the relative changes in cloud effective radius for relative changes in aerosol proxies such as CCN or aerosol scattering coefficient.

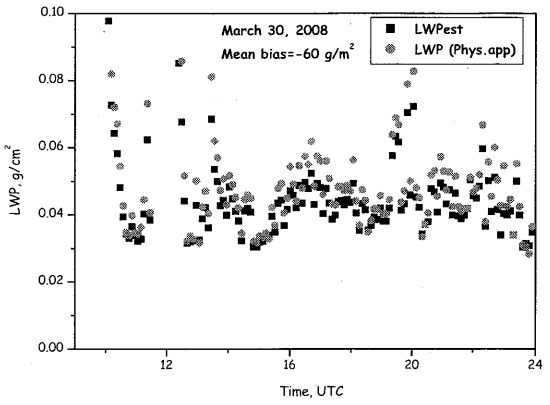

Figure 4. LWP retrieved with site-dependent and physical approaches.

3.2 Aerosol Indirect effect

To investigate the effect of aerosols on cloud droplet effective radius, collocated measurements of different experimental systems were analyzed. Figure 5 shows the covariation between R_{eff}, aerosol particle >0.5 um number concentration and scattering coefficient as observed on April 10, 2008.

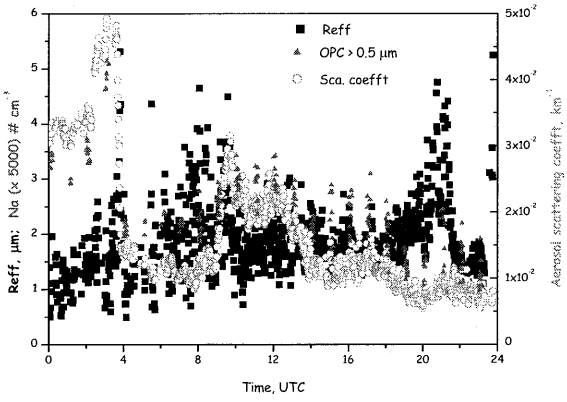

Figure 5. Covariation between R_{eff}, Na>0.5 μm and scattering coefficient (β_{sca}) as observed on April 10, 2008.

It can be noted from the figure that there is a overall negative correlation between cloud droplet R_{eff} and aerosols. Higher aerosol concentration in the beginning of the day

(00-03 hrs UTC) and 0900-1200 hrs UTC associated with a decrease in R_{eff} clearly demonstrate Twomey effect.
The sensitivity of R_{eff} to aerosols can be described by

$$IE=-d \ln re / d \ln \propto$$

Where re is the cloud droplet effective radius and $\propto$ is the proxy for aerosol concentration. The scatter plot between R_{eff} and CCN or β_{sca} shown in Figure 6 on April 10 and March 20, 2008 show Twomey effect and indirect effect of 0.154 and 0.1, respectively.

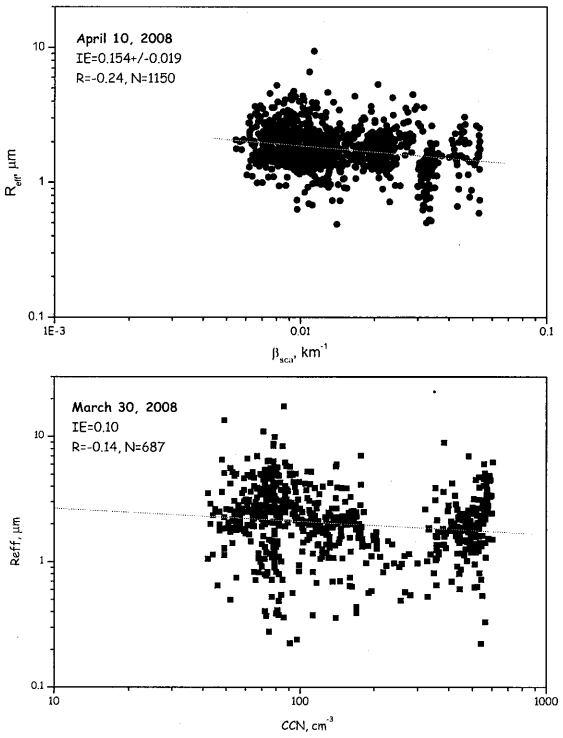

Figure 6. Scatter plot between R_{eff} and aerosol proxy (CCN or β_{sca}) on April 10 and March 30, 2008.

It is proposed to integrate observations (ground-based and satellite) in a cloud-resolving model at the range of relevant temporal/spatial scales so as to separate meteorological effects from aerosol effects on clouds.

References

Feingold, G., W. Eberhard, D.E. Lane, and M. Previdi (2003), First measurements of the Twomey effect using ground-based remote sensors, *Geophys. Res. Lett., 30(6), 1287, doi:10.1029/2002GL016633.*

Frisch, A.S., M. Shupe, I. Djalalova, G. Feingold, and M. Poellot (2002), The retrieval of stratus cloud droplet effective radius with cloud radars, *J. Atmos. Ocean Tech., 19*, 835-842.

Kikuchi, N., T. Nakajima, H. Kumagai, H. Kuroiwa, A. Kamei, R. Nakamura, and T. Y. Nakajima (2006), Cloud optical thickness and effective particle radius derived from transmitted solar radiation measurements: Comparison with cloud radar observations, *J. Geophys. Res., 111, D07205, doi:10.1029/2005JD006363.*

Takano, T., K. –I. Akita, H. Kubo, Y. Kawamura, H. Kumagai, T. Takamura, Y. Nakanishi, T. Nakajima (2005), Observations of clouds with the newly developed cloud profiling FM-CW radar at 95 GHz, *Proc. SPIE 5979 art no 597907.*

Acknowledgements

Primary author (GP) sincerely thanks JSPS for invitation fellowship and also thank IITM Director for deputing him to work in CEReS, Chiba University. We thank SKYNET and CHAMMPS, Cape Hedo for maintaining the experimental facilities at the site. We also thank Global Earth Observation System of Systems (GEOSS), Ministry of Education, Culture, Sports, Science and Technology (MEXT), Japan.

Long term camera records of Asian dust events in eastern Asia during 2005-2008

K. Kinoshita[1]*, T. Nagamatsu[1], N. Iino[2], N. Wang[3], G. Zhang[3], D. Jugder[4] and N. Otgonjargal[4]

[1] *Kagoshima University, Kagoshima 890-0065, Japan,* [2] *Kumamoto University, Kumamoto 860-8555, Japan*
[3] *Northeast Normal University, Changchun 130024, China,* [4] *Institute of Meteorology and Hydrology, Ulaanbaatar 210646, Mongolia, * E-mail: kisei@izm.bbiq.jp*

Abstract

Automatic interval recordings of sky images by digital cameras have been made at three locations in eastern Asia, i.e., Changchun in northeast China, Ulaanbaatar in Mongolia, and Kagoshima in southwest Japan, so as to see the arrival of Asian dust through the changes in the sky color and the decreases in visibility. The results in the springtime during 2005-2008 are compared with the images of meteorological satellites NOAA, MTSAT and Terra,Aqua/MODIS, and other information on dusty air. Many heavy dust events are clearly seen in the series of the images lasting for a day or two, while light or dispersed events are difficult to distinguish from cloudy scenes.

Keywords **:** air turbidity, digital camera, interval recording, paranomic view, RGB analysis, visibility

1. Introduction

Digital camera with the function of interval mode may be regarded as an apparatus to record air turbidity automatically for a few months or longer. In order to obtain long-term visual records of Asian dust phenomena, digital cameras have been set in Changchun, Jilin Province, China, since March 2003 [1], and in Ulaanbaatar and other places in Mongolia since March 2004 [2-4]. In Kagoshima, Japan, the web-camera recording has been working since the end of 2000 [1], and digital camera recordings including near-infrared modes and panoramic views have been added since the end of 2005. In this report, a brief review of the results in 2005-2008 is given, in connection with the satellite imagery to detect the transport of the dusty air, and other meteorological information. The onset of dusty air is clearly detected in camera images as the change of the sky color and the decrease of the visibility distance, in accordance with satellite images of Asian dust events and other reports on dusty air.

2. Camera settings

At Northeast Normal University in Changchun, a digital camera Casio QV-R4 has been operating in the springtime since 2003, while at Institute of Meteorology and Hydrology in Ulaanbaatar, a camera Ricoh Caplio G4wide has been operating since 2004. With one our interval, both cameras can record JPEG images of the VGA size (640x480) in a SD memory of 512 MB for a few months. The latter type is also operating at the point B near Kamoike port in Kagoshima all throughout the year since the end of 2005, by changing the memory twice a year. In such operations, initial proper setup is of vital importance, including the interval time, the white balance as daylight mode, and so on. Unexpected power shortage that stop the recording should also be monitored, so as to restart the recording. At the locations in Changchun and Ulaanbaatar, the video cameras SONY DCR-TRV40E and TRV900 respectively have been operating with ten-minute interval and half sec. record mode to take three months records in a cassette tape for the backup of the digital still camera recordings.

At the Faculty of Education, Kagoshima University (the point A), a web-camera directed to eastern sky started in the end of 2000, so as to monitor the eruption clouds of Sakurajima Volcano in real time, and to record with five-minute interval all throughout the year in the daytime. The interval time has been shortened into one minute since June 22, 2006. Another web-camera with near-infrared mode also started on Aug. 20, 2007 at the point B, 9.8 km WSW from the crater of the volcano, with ten sec. interval to see quick changes of eruption clouds. Though these web-camera images are useful to see the air turbidity, selected scenes with longer time intervals are enough for slow phenomena such as Asian dust.

In taking sky images, wide field of view with the horizon in lower side is adopted, so as to see the change of the sky color with the vertical angle. At the point B in Kagoshima, multi-directional photographs were taken temporarily and manually covering eastern half directions by three or four images with conventional color and near-infrared (NIR) modes of a camera SONY DSC-V1 or V3, where night-shot mode with IR-filter shielding 840 nm was used to obtain NIR images [5]. In a panoramic set of images, one may find

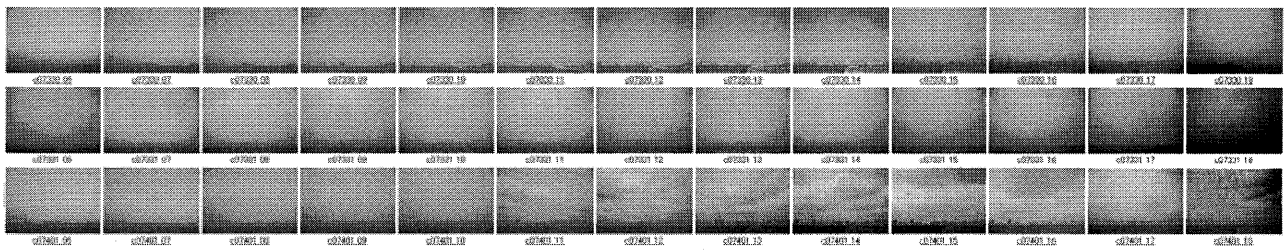

Fig. 1. Changchun sky during March 30 - April 1, 2007, exhibiting dusty air on March 31.

many targets with various distances to estimate the visibility distance, which is expected to be longer in NIR mode.

3. Edition and analysis of camera images

In order to find out dusty air scenes by scanning many sky images, it is convenient to rename them to indicate the date and time with an initial of the place, and separate out night scenes. All of the daylight scenes are edited via html, with the thumbnails of a day in one line, such as shown in Fig. 1. The raw data thus edited are exchanged among collaborating members, and main part of them are shown in http://arist.edu.kagoshima-u.ac.jp/adust/kosa-e/kosa-e.htm

We may identify dusty days from camera images by the difference in color, the lack of the brightness change with vertical angle, and the decrease of the contrast between far away objects and the sky. Quantitative study can be done by taking the RGB (Red, Green and Blue) profiles in 8 bit [1-4], along a common vertical line in the sky in different images. In the case of clear sky, the relationship B > G > R holds among three color-components, and the difference of each is significantly large especially in the sky far away from the horizon. For cloudy sky, the differences become small, especially between G and R, but the relation never changes. For dusty sky, the relationship is reversed as B < G < R, and the differences increase with dusty levels. A scatter diagram of the values B/G and R/G is useful to classify the cases according to the air turbidity. The RGB values along a line near the horizon are useful to study the decrease of the visibility in dusty air.

The satellite images of NOAA, MTSAT and Terra,Aqua/MODIS are useful to study the transport and dispersion of the dusts in eastern Asia. Visible and NIR band images of them are useful to detect thick dusts in daytime, while the Aerosol Vapor Index (AVI) images, given by the difference of thermal infrared bands at 12 and 11 μm, may give the dust distributions in the day and night [6]. We may compare camera images with the satellite data and other reports of dusty air, such as the dust chart of eastern Asia summarized by Japan Meteorological Agency (JMA) and communications in Asian Dust Network.

4. Results during 2005-2008

Spring 2005

Digital camera Sharp MD-PS1 was set at Dalanzadgad meteorological station in southern Gobi, Mongolia, in addition to three cities as shown in Fig. 2. Interval recording data during March 14-28 was obtained, with a sand storm in the afternoon on 15, snowfall on 16, and fine days after that. Mechanical trouble prevented the continuation of the automatic recording there. In Ulaanbaatar, the recording was successful during March 6 and June 6, in which heavy dust events were not found.

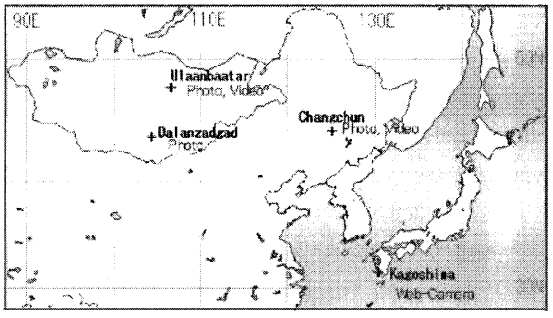

Fig. 2. Location map of observation stations in the spring of 2005

In Changchun, interval records during March 8 - June 17 were obtained, with many dust events starting from heavy one on March 9. Fig. 3 shows a decrease of the visibility on March 21 compared with fine and rainy days.

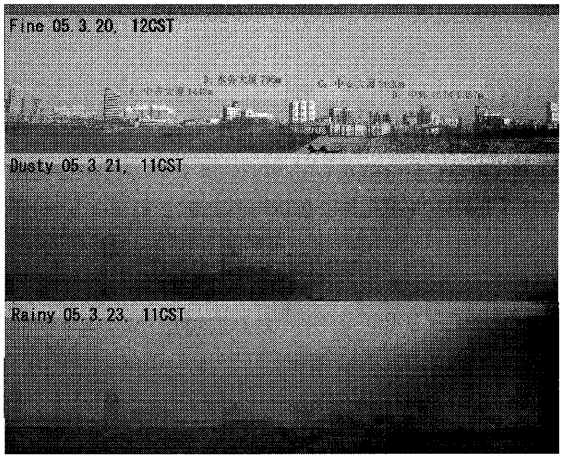

Fig. 3. Comparison of views near the horizon on fine, dusty and rainy days on March 20, 21 and 23, respectively.

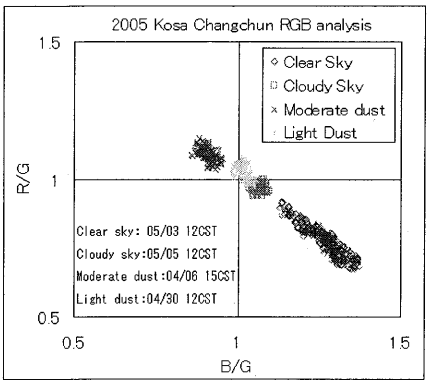

Fig. 4 A scatter plot of B/G and R/G at 350 pixels from the top along a vertical line in the center on clear and cloudy skies on 3 and 5 May, and moderate and light dust skies on 6 and 30 April, 2005.

Fig. 4 shows a scatter plot of B/G and R/G, where moderate dust on April 6 is clearly separated from clear and cloudy skies, while light dust on April 30 is difficult to distinguish from cloudy case. As the RGB values are at the points from the top along a vertical line, the plot for fine day scatters exhibiting vertical dependence of the sky color.

In NOAA AVI images received at Kagoshima University, many dust events were found, in accordance with the Changchun camera and the dust reports in eastern Asia. Especially, the event on April 21 was overwhelming over Korea and Japan. The spring 2005 results are reported in [7]. Remarkable dust was also observed on November 7 over Korea and Japan, originating from inner Mongolia on November 5. Such an autumn dust had been also seen in 2002 [1].

Spring 2006

Changchun sky was recorded from Feb. 27 to June 20, with many dust events travelling to Korea and Japan in the following days. In Kagoshima, three hours interval records were obtained during Mar.12- May 15. March-April events are briefly summarized as follows [8], with the notation m.dd for m= month and dd=date.

3.10 Heavy dust in Changchun -> 3.11-13 Korea, not much to Japan

3.27 Dust in Changchun -> 3.28 S. Korea & Kyushu, Kagoshima

4.7 Dust in Changchun -> 4.8-9 Korea & Japan, Kagoshima

4.17 Heavy dust over Shangdong -> 4.18-19 Korea & Japan (Changchun: cloudy or rainy, Kagoshima : rather clear)

4.23 Dusty in Changchun -> 4.23-25 Korea, 24-25 Japan, Kagoshima

4.30 Korea, W-Japan (4.28-29 Not so dusty in Changchun)

Fig. 5 shows visible and NIR images of NOAA/AVHRR-1 and 2 in late afternoon on April 8, exhibiting thick dust band over Korean peninsula and west Japan. Particle image velocimetry analysis of dust transport of this event was done, using one hour interval AVI images of geostationary satellite MTSAT [9].

As for Ulaanbaatar, the captured images at 9, 12 and 15 Mongolian standard time (= CST = JST-1) during March 10 - June 4 of video records is used for the analysis, as the digital still camera records were unsuccessful. In this year, the correlation between dusty skies in and dust storms in Mongolia were found, while the correlation with Changchun images were not so clear.

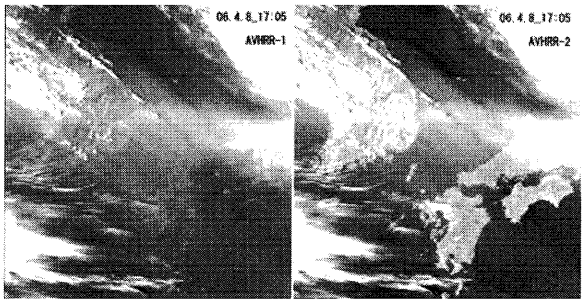

Fig. 5. NOAA/AVHRR-1 and 2 images of Korea and west Japan at 17:05 JST on April 8, 2006.

Spring 2007

Changchun sky was recorded for five months during March 5 - August 7. Most prominent dust event was on March 31 as shown in Fig. 1. This is due to strong low pressure system with a vortex structure consisting of cloudy area and dry dusty slot in MTSAT AVI image such as shown in Fig. 6. A time series of AVI images show how the bright AVI area covers Changchun, and goes over Korea and Japan in the next day gradually dispersing. Other dust events in 2007 were moderate or light in Changchun. The observation in Ulaanbaatar was unsuccessful due to a failure at initial setup.

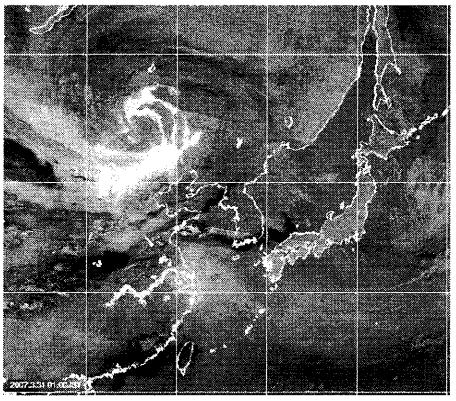

Fig. 6. MTSAT/AVI image at 1:00 JST on March 31, 2007.

In Kagoshima, the visibility often decreased not only with the arrival of dispersed dust, but also due to polluted air masses from the continent and other meteorological conditions. Estimation of the visibility length from the photographs may be useful to study the air quality. As a reference, a view of three-hour interval recording on fine day is shown in Fig. 7. In order to increase targets with various distances, four directional photographs were taken manually to obtain panoramic view covering north-east-south directions from the point B as shown in Fig. 8. Close-up images to indicate the targets in both sides are shown in Fig. 9. Temporal panoramic photography started in 2006, and the format was established in 2007. Springtime results are displayed in the homepage of the collaboration.

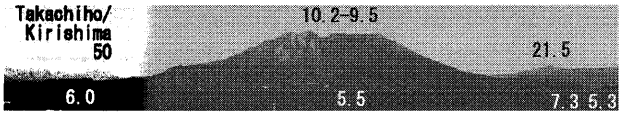

Fig. 7. The fixed view near the horizon of the camera with 3 hr. interval at the point B, with the distance of the targets in km.

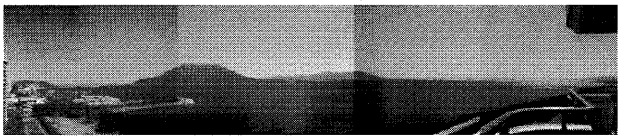

Fig. 8. A mosaic of four photographs at noon on March 11, 2007, covering north-east-south directions from the point B.

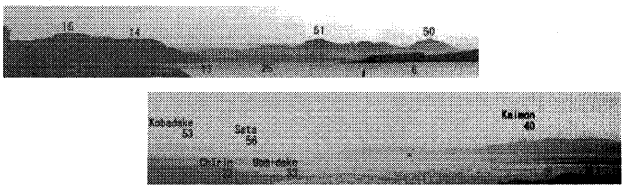

Fig. 9. Close-up images to indicate the targets in north-northeast and southeast-south sides, with the distance of the targets in km. The upper one is a part of image at the sunrise in a different day, while the lower is a part of Fig. 8.

Spring 2008

The camera records were obtained in Ulaanbaatar during 25 March - 20 May with 30 minutes interval. The sky was rather clear during most of the spring time, with an exception of a dusty event in the afternoon on April 17 shown in Fig. 10, where one hour interval images for 16-18 in April are listed. A dusty color lasted only two hours, indicating the dust storm to be local one.

The first arrival of Asian dust in Japan was on March 2-3 over wide area from west to east. In Kagoshima, visibility decreased to 5 km. There were not many heavy dust events after that. At JMA stations this year, days of dust observation were only 11, which is the minimum number since 2000. Changchun data are to be studied later.

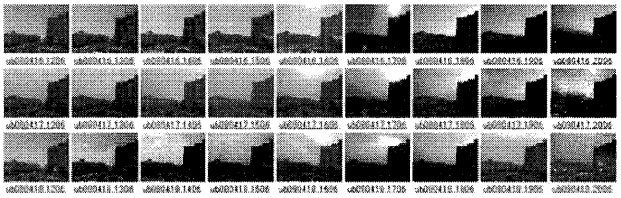

Fig. 10. One hour interval images of April 16-18, 2008 in Ulaanbaatar.

5. Concluding remarks

Long term automatic recording by digital cameras is useful for the study of Asian dust, in conjunction with satellite imagery and other related data. Manual photography to obtain panoramic view is helpful for the visibility studies.

References

[1] K. Kinoshita et al., Long-term observation of Asian dust in Changchun and Kagoshima, Water, Air and Soil Pollution : Focus 5, pp. 89-100, 2005.

[2] K. Kinoshita et al., Properties of long-time digital camera records in Changchun and Ulaanbaatar, Proc. CEReS International Symposium on Radiation Budget and Atmospheric Parameters Studied by Satellite and Ground Observation Data, Chiba, Japan, 2005, pp.136-141.

[3] K. Kinoshita et al., Interval Camera Recordings of 2004 Asian Dusts in Mongolia, Northeast China and Southwest Japan, Proc. 4th ADEC Workshop. Nagasaki, Japan, 2005, pp.349-352.

[4] K. Kinoshita et al., Automatic image recording network of sand storm and dusty airs in northern Asia, International Radiation Symposium: Current Problems in Atmospheric Radiation, 2004, Busan, Korea, Deepak Pub., pp. 319-322, 2006.

[5] K. Kinoshita et al., Ground and Satellite Monitoring of Volcanic Aerosols in Visible and Infrared Bands, Proc. CEReS Int. Symp. Remote Sensing, Chiba, Japan, Dec. 2003, pp.187-196

[6] Kagoshima Kosa Analysis Group, Satellite Imagery of Asian Dust Events, Kagoshima University, 159 pp., 2001; N.Iino et al., NOAA and GMS observations of Asian dust events during 2000-2002, Proc. SPIE Vol. 4895, pp. 18-27, 2003.

[7] N. Wang et al., Automatic camera observation of Asian dusts in Changchun, Ulaanbaatar and Kagoshima in the spring of 2005, 3rd. Int. Workshop on Dust Storms and Associated Dust-fall, Huhhot, China, 2005.

[8] D. Jugder et al., Fixed-point camera observation of Asian dust in Northeast Asia and satellite imagery, 4th Int. Workshop on Dust/Sand Storms, Ulaanbaatar, Mongolia, 2007.

[9] A. Nishimachi et al., Analysis of the transport of yellow sand by satellite remote sensing data, Proc. 41th Rem. Sens. Soc. Japan, pp.103-104, 2006 (in Japanese with English abstract).

Remote sensing of tropical high altitude clouds and aerosols using ground based lidar and MODIS

Y. Padmavati Kulkarni[1], Bhavani Kumar[1],Bannu[2], M. Krishnaiah[2]* and H.Kuze[2]
C. Sujathamma[2]*and A. Kondoh[2]
[1]National Atmospheric Research Laboratory (NARL), Gadanki, India
[2]Center for Environmental Remote Sensing (CEReS), Chiba University, Chiba 263-8522, Japan.

Abstract

Indo-Japanese lidar system established over a tropical station, Gadanki (13.5 N,79.2 E), India is in operation since 1998.Using this system regular observations of upper troposphere clouds, and aerosols at stratospheric heights were made. The Moderate Resolution Imaging Spectroradiometer (MODIS) measurements on the Terra spacecraft are also used for remote sensing of high altitude clouds aerosols from space. Data collected using the polarization lidar during the period 1998-2004 are selected for systematic investigation and presentation. Several tropical cirrus cloud structures have been identified with low to moderate ice content. Occasionally thin sub visible clouds in the vicinity of tropical tropopause have been identified. Lidar observations clearly show occurrence of cirrus clouds over this station with varying thickness. The interseasonal variation of cirrus occurrence frequencies shows much of the occurrences during the monsoon season.

The aerosol measurements in the upper troposphere and lower stratosphere show low aerosol content with vertical distribution upto 35km altitude. Scattering ratio (SR) and aerosol extinction are found to exhibit seasonal and interannual variations in upper troposphere (UT) and lower stratosphere(LS).SR in UT in 2001 and 2004 during winter is lower than that of summer, while LS winter profiles are found to have higher SR values apparently experience a shift in altitude corresponding to the seasonal change in tropapause indicating a relation between the two. The correlation observations made using MODIS satellite are compared with lidar data for systematic statistical study.

1. Introduction

Over the past two decades the lidar technique has been found to be a potential remote sensing method for probing the earth's atmosphere. Depending on the design of the lidar, a variety of atmospheric parameters may be measured, including aerosol and cloud properties, temperatures and species concentration. Lidar has the capability to delineate the position and spatial structure of clouds in the atmosphere. Because of its high spatial resolution, it can be used to locate cloud base and its top with a good precision that is not possible with any other remote sensing technique. Another thrust area where the backscatter lidar has the prospective application in the atmospheric research is the spatial and temporal evolution of dust particles or aerosols. As the aerosols and clouds in higher altitude play an important role in the Earth's radiation budget and its climate (Ackerman and Chung 1992)., it is of interest in this paper to study their properties using the monostatic Nd: YAG lidar, measurements and compare with MODIS data for the observations made over a tropical station located at National Atmospheric Research Laboratory (NARL), Gadanki

2. Lidar site and observations

2.1 Lidar site

Gadanki (13.5°N, 79.2° E) is a tropical rural site located at an altitude of about 375 meters above mean sea level and about 80 km from the Bay of Bengal coast, in southern India.. In summer at Gadanki the minimum and maximum surface temperatures range from about 22°C to 43°C; while in winter the temperature varies

from about 13°C to 32°C.

The Indo-Japanese Lidar (IJL) system installed at NARL by NICT (CRL) has been measuring upper-tropospheric clouds and the stratospheric aerosol backscatter at 532nm wavelength with dual polarization since March 1998. The basic lidar signal represents the total backscatter that contains returns from both molecules and particle part of the atmosphere. The particulate part of the atmosphere represents either aerosol or clouds composed of ice crystals or hydrometeors. The strength of aerosol or cloud backscatter is usually represented in terms of the backscatter ratio. The noise-corrected lidar signal is subjected to range normalization and inversion (Fernald 1984) to derive the backscatter ratio profile and details are reported (Bhavani Kuamr etal 2006).

The Moderate resolution Imaging Spectro-radiometer (MODIS) is the primary imager on the Earth Observing Systems Terra platform. The MODIS data are generally processed into different levels from level 1 (radiances or brightness temperature) level 2 (derived geographical data products) and level 3,with the integration of the level 2 products the level 3 daily, eight- day, and monthly mean products are generated globally at a 1°x1°Latitude-longitude grid resolution. The MODIS Cloud Product combines infrared and visible techniques to determine cirrus reflectance. Atmospheric monthly mean and annual mean high cloud reflectance are used in this study.

2.2 Observations of high altitude clouds and stratospheric aerosol

The appearance of deep cumulus clouds during convective periods is a common phenomenon at tropical latitudes. The formation of high altitude clouds such as cirrus in the tropics plays a particularly important role in the Earth-atmosphere radiation budget. Tropical cirrus develops in a variety of forms, ranging from optically thick anvil cirrus that is closely associated with deep convection (Houze 1993) to optically thin cirrus layers frequently observed near the tropopause (Boehm et al. 1999).The Indo-Japanese lidar (IJL) system, equipped with polarization diversity, has detected several different structures of tropical cirrus in the altitude ranging from 10 to 17 km with derived peak volume depolarisation in the range of 0.1 to 0.32.. Figure 1 show the two different nights of cirrus detection with single layer and multiple layers. Single layer cirrus shows the observation of cloud at 21:04 LT and after some time the cloud was not observed and again appeared. Other night figure shows two-layered cirrus cloud where one layer appeared at an altitude of 12 km and another layer at 15 km.

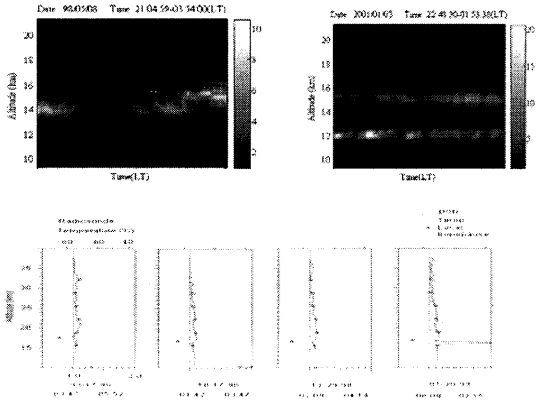

Fig 1. Case studies of LIDAR observed single and multiple layers of cirrus cloud. and Height profiles of aerosol back scattering ratio integrated over 2- hour period as seen by lidar on 16-17 march,16-17 October,28-29 December 1998 and 19-20 January 1999.

Typical height profiles of aerosol backscatter ratio integrated over two hour period, as observed by Indo-Japanese lidar, on the nights of 16th March, 16th October, 28 December1998 and 19th January 1999 is shown in Figure 1 Each lidar height profile of aerosol is shown with a corresponding radiosonde temperature profile that is obtained from the nearest meteorological station, Chennai for identification of the local

tropopause altitude. The horizontal arrows indicate the altitude of cold-point tropopause obtained from these temperature measurements. A significant observation from these height profiles is the extended vertical distribution of stratospheric aerosol. There are no noticeable sharp enhancements in aerosol backscatter observed at the stratospheric heights. This confirms that during the time of our observations the tropical upper troposphere and stratosphere over Gadanki appears free from volcanic aerosols and what we observe now is the background variable aerosol (Barnes and Hofmann 1997, 2001; Jaeger 1998). The horizontal bars show standard error dR in the measurements of R for a few sample heights for clarity.

3. Results and discussion

3.1 Interannual and interseasonal occurrence statistics

The variability of cirrus cloud interannually and interseasonally has been studied using ground based LIDAR set Measurements taken only during 1998-2004 cloud free nights. In figure3, LIDAR observed interannual observations showed significant enhancement in percentage of occurrence of cirrus during 2001 and less occurrences during 2002. The cloud variation can be understood with reference to monsoon conditions and the year is accordingly divided into four seasons viz., Winter (December, January and February), Pre-monsoon (March, April and May), Monsoon (June, July and August) and Post-monsoon season (September, October and November).The LIDAR observed interseasonal statistics show higher occurrence during monsoon period. Similar interannual statistics are obtained with the recently available MODIS terra data set and are shown in Fig. 3.

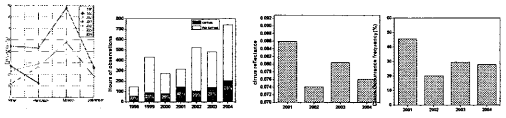

Fig. 2 (a) Interseasonal and interannual frequency statistics derived from lidar and MODIS Terra

3.2 Seasonal variation in vertical profiles of aerosols

To understand the further seasonal variations in aerosol characteristics SR values are plotted from10 to 30 km for winter and summer seasons for the year the years 2001,2004 and 2005 as shown in fig 4.Horizontal bars represent $\pm 1\,\sigma$ and are plotted at 2 km interval for purposes of clarity and illustration. The winter and summer variation in SR is found to exhibit a relation with tropopause altitudes. The mean tropopause altitude for summer (77days) and winter (51 days) were found

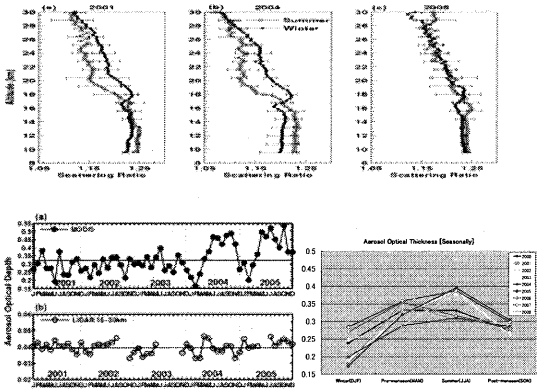

Fig 3 Winter and Summer scattering ratio profiles and 550 nm derived aerosol optical depth from MODIS Terra satellite compared with 532 nm integrated aerosol extinction in the 10-30 km region over Gadanki during 2001-2005

to be 17 km.(temperature 193.71K) and 17.3 km (temperature 191.89K) respectively.

3.3 Aerosol optical depth and integrated extinction

Winter and summer scattering ratio profiles and Monthly mean AODs for Gadanki during 2001-2005 with the integrated aerosol extinction from 10 - 30 km

derived from 532 nm lidar are plotted in fig 3. 5 year mean 550 nm AOD is found to be 0.32 while 5 year 10-30 km integrated extinction at 532 nm from lidar is estimated to be 0.04.This value indicates that on an average about 12% of AOD is contributed from 10-30 km while the rest comes from the lower altitudes of the troposphere. AODs derived from MODIS are found to be higher than 0.4 during March-November 2004 and 2005 respectively. Both the columnar AOD and the 10-30 km integrated extinction are found to be exhibit seasonal variations. It should also be noted that AODs over Gadanki on an average are higher during 2004 and 2005 when compare to the previous years. The monthly mean AODs and integrated extinction from 10-30 km during 2001-2005 yielded a positive correlation coefficient of 0.62,suggesting that aerosols in the lower troposphere could contribute to UT and LS aerosols over Gadanki The increasing trends in UT and LS aerosols, the yearly increase in AOD during 2001-2005 and the lower – upper troposphere coupling over Gadanki are relevant in terms of climate change over the Indian sub continents the increasing aerosol abundance over India any be impacting the monsoon.

4. Summary and conclusions

By using Mie-backscattering lidar, we have observed high altitude clouds, stratospheric aerosols, The tropical cirrus clouds have been detected in the altitude range of 10-17 km. Thin cirrus clouds are occasionally detected near the tropical tropopause. The interannual study shows an enhancement in the cirrus occurrence frequencies during 2001 and fewer amount of occurrence during 2002.The intra seasonal variation of cirrus occurrence frequencies shows much of the occurrences during monsoon. The measurement of stratospheric aerosols by the lidar system confirms that during the times of present observation, the tropical upper troposphere and lower stratosphere over Gadanki site appears free from volcanic aerosols what we observe now is the background variable aerosols. SR in UT in 2001 and 2004 during winter is lower than that of summer, while in LS winter profiles are found to have higher SR values. In 2001 and 2004 the mean SR values are higher than in summer in LS. In 2005 no significant winter – summer differences in SR are seen in UT and LS which could be due to minor volcanic eruption that took place in 2005.

Acknowlegements:

M. Krishnaiah thanks JSPS, Japan for the Invitation Fellowship 2008. The authors would like to acknowledge with thanks the numerous contributions by their colleagues at the NARL India and (NICT), Japan in successfully operating the lidar facility under an Indo-Japanese collaboration

"The MODIS Level 3 images used in this study were acquired using the GES-DISC Interactive Online Visualization and Analysis Infrastructure (Giovanni) as part of the NASA's Goddard Earth Sciences (GES) Data and Information Services Center (DISC)."

References

Ackerman, F., and H. Chung, 1992: *J.Appl.Met*, **31**, 223-233.

Barnes, J.E., and David J. Hofmann, 1997: *Geophys. Res. Lett.*, **24**, 1923-1926.

Barnes, J.E., and D. J. Hofmann, 2001: *Geophys. Res. Lett.*, 2859-2863.

Bhavani Kumar,et al 2006,Inod-,Adv,Atm.Sci **23,** 5, 711-725

Fernald, F. G., 1984:. *Appl. Opt.*, **23**, 652–653.

Jaeger, H., and Homburg F., 1998: *19th ILRC, NASA/CP-1998-207671/PT1*, pp 335-338.

Studies on net long-wave radiation on clear days in Hefei region

Zhen-zhu Wang[1], Jun Zhou[1], Chao Li[1], Tamio Takamura[2], Nobuo Sugimoto[3]

[1]*Anhui Institute of Optics and Fine Mechanics, Hefei 230031, China, zzwang@aiofm.ac.cn*

[2]*Center for Environmental Remote Sensing, Chiba University, Japan*

[3]*National Institute of Environmental Studies, Japan*

Abstract

Net long-wave radiation is an important component of radiation budget. The knowledge of induced factors (such as water vapor, aerosol) of radiation budget provides an opportunity for understanding the impact of environmental changes on climate. Utilizing the radiation data observed by pyrgeometer at definite times every day from 2003 to 2007 at SKYNET Hefei site in East China, the characteristic of net long-wave radiation over grassy land is discussed on 293 clear days. Meanwhile, based on these five years observations of integrated water vapor by microwave radiometer WVR-1100, variability of the atmospheric water vapor on sunny days has been statistically analyzed. And the aerosol optical property in the corresponding period is also obtained by an automated two wavelength (1064nm, 532nm) polarization (532nm) lidar. For the value of integrated water vapor, validation is given by a local radiosonde and good agreement is shown. As to the lidar dataset, we apply the Fernald's method to derive the extinction coefficient. The profile of aerosol extinction coefficient is compared with anther lidar system PML and indicates great agreement. Then the AOD under the height of 3 km is calculated by layer-integrated extinction coefficient. This study mainly addresses the daily and seasonal variations of net long-wave radiation, integrated water vapor and AOD as well. We attempt to characterize the optical property of aerosol and the value of integrated water vapor and their effects on the net long-wave radiation over Hefei. The results show that some certain negative correlations are considered to occur between the latter two kinds of factors and the net long-wave radiation. And especially in summer the effects of water vapor and the aerosol on net long-wave radiation are very obvious. Large water vapor and aerosol loading lead to a very low net long-wave radiative effect.

Keywords: net long-wave radiation; integrated water vapor; AOD

1. Introduction

The radiation balance of the Earth system is an accounting of the incoming and outgoing components of radiation. Net long-wave radiation is an important component of radiation budget. And it is a measure of the difference between outgoing long-wave radiation from the earth surface and incident atmospheric long-wave counter-radiation. Many factors determine the value of net long-wave radiation[1)]. In this paper, we analyze the seasonal variation of net long-wave radiation, integrated water vapor and aerosol optical depth as well using the observed data on clear day from 2003 to 2007 at SKYNET Hefei site (31.90N, 117.16E) in East China. Some relationships are found among the three foregoing parameters. Besides, in order to validate these data, good agreements are acquired by blind validations.

2. Instruments and validation

The measurement site is located at Anhui Institute of Optics and Fine Mechanics, 15 km west of Hefei city. The institute is surrounded by farmland, lake and villages. The factory district is centered in the eastern suburbs of the city. Therefore, influence of urban plume

and industrial emission on the observed data is less important. Data obtained from two pyrgeometers, a microwave radiometer, and a NIES Lidar is analyzed in this paper. The instruments were placed at a height of 1.5 m over short non-irrigated grass and they are operated continuously.

The pyrgeometers (model PIR), manufactured by the EPPLEY LAB.INC., were calibrated by Precision Infrared Radiometer in Eppley's Blackbody Calibration System. Downward and upward long-wave radiation was measured by them in continuous operation. Thus, they were inspected several times per week and an alternate method of calibration was also been done each year to compare the PIR against another calibrated working standard PIR in a cloudless night sky.

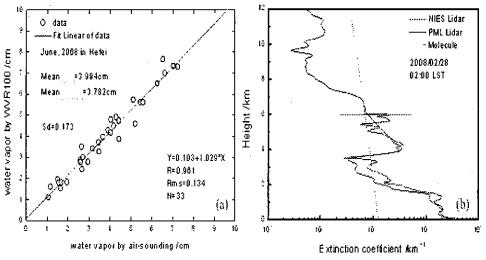

Fig. 1(a) Scatter plot of water vapor retrieved from microwave radiometer data vs. that measured by radiosonde; (b) Comparison extinction profiles at 532nm measured by PML Lidar with NIES Lidar

The Radiometrics WVR-1100 portable water vapor radiometer receives microwave radiation from the sky at 23.8 GHz and 31.4 GHz for total Integrated Water Vapor and Cloud Liquid Water. This instrument does not need to be always calibrated if no change shows in the plot of noise diode injection temperature (i.e. the instrument is sufficiently calibrated.). In this paper, we compared the value of integrated water vapor retrieved from microwave radiometer data and that measured by radiosonde. Figure 1(a) shows the results. It was found from the retrieval results of the microwave radiometer data taken at Hefei in June, 2008 that on average, the retrieved value of water vapor was 0.212 cm greater than that measured by radiosonde and the standard deviation was 0.173 cm; the linear correlation coefficient between the two value is 0.961, and the Rms error was 0.134 cm. In general, good agreement was shown except small difference because of certain non-comparable fact[2].

The NIES Lidar[3] employs 1064-nm fundamental and 532-nm second harmonic of a flash-lamp pumped Nd:YAG laser and the direction of measurement is vertical. The scattered light is received with a 20-cm Schmidt-Cassegrain telescope. The received light is collimated to 1064-nm channel and two 532-nm polarization channel. It is operated automatically, and the 5-minute averaged lidar profiles are recorded every 15 minutes in the continuous observation mode. We apply the Fernald's method iteratively with non-zero boundary value at 6 km to derive the extinction coefficient for the data without clouds. And the aerosol optical depth (i.e. AOD) under the height of 3 km is calculated by layer integrated extinction coefficient. In order to check the reliability of observed data by this Lidar, the profile of aerosol extinction coefficient is compared with anther lidar system PML[4]. The results are shown in the Figure 1(b). The Figure clearly indicates that aerosol extinction profiles for 532 nm measured by the two lidars agree very well. During these 5 years, the number of clear days in every month is shown in Table 1.

Table 1 Number of clear days in every month in Hefei region during 2003-2007

Season	Winter			Spring			Summer			Autumn		
Month	12	1	2	3	4	5	6	7	8	9	10	11
Number	36	29	26	30	30	24	14	7	13	20	30	34	293

3. Results and discussion

3.1. Typical daily variation

Net long-wave radiation was determined from measured upward and downward long-wave radiation by the flux difference between them. This section gave a typical example of the daily variation of long-wave radiation, aerosol optical depth and integrated water vapor. Meanwhile the relationships between net long-wave radiation and anther two parameters were shown.

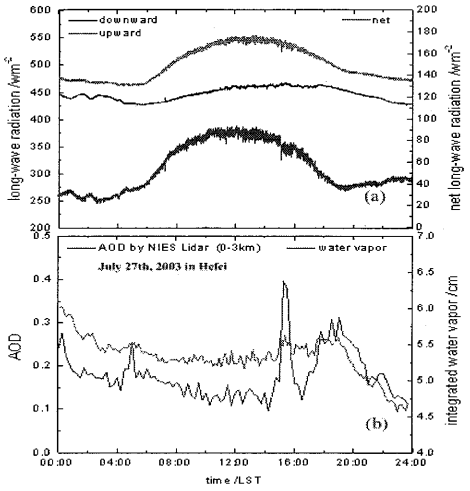

Fig. 2 the diurnal variation of long-wave radiation, AOD and water vapor observed in Hefei on July 27th, 2003

Figure 2 shows that the 24 hours variations of long-wave radiation, AOD and water vapor were observed in Hefei on July 27th, 2003. It was a sunny day except for the occurrence of low cloud at a height of 2-3km occasionally. From figure 2 (a), we can see the downward, upward and net long-wave radiation experience an obvious variation with big value in the daytime and small at night. Figure 2 (b) gives us that the diurnal variation of AOD and integrated water vapor has similar trend. We can also find the value of AOD rises quickly due to clouds (e.g. at about 15:00 pm). Furthermore, the results on figure 2 show that some certain negative correlations are considered to occur among these three parameters (i.e. the relative variation of net long-wave radiation is effected by whether aerosol and water vapor rise or fall at a certain degree). Because the mass of water vapor and aerosol in the air increase, the downward long-wave radiation will enhance. Accordingly, the net long-wave radiation will decrease to some extent.

Besides, many other factors, such as the existence of cloud and the temperature of air or surface, can cause changing of the net long-wave radiation. We do not discuss them in this essay.

3.2. Statistical seasonal variation

In order to investigate the net long-wave radiation under the influence of aerosol and water vapor furthermore, the seasonal variation of long-wave radiation, integrated water vapor and AOD were presented and discussed in detail. The results obtained in figure 3: the value of long-wave radiation and integrated water vapor is monthly mean daily one and the value of AOD (0.03-3.0 km) is derived from lidar by averaging every one in correspondence month. According to the measurements, the downward and upward long-wave radiation have same trend in every month during these 5-year. The lowest monthly mean daily value of them is in January and the maximum long-wave radiation flux occurred in the summer season (see figure 3(a)). But the seasonal variation of net long-wave radiation is widely different marked by summer the lowest and spring the highest value, and the discrepancy between winter and fall is feeble (see the red line in figure 3(b)). And a maximum monthly mean daily net long-wave radiation equals to 96.85 Wm^{-2} on May and a minimum one occurs to 53.04 Wm^{-2} on August.

Interestingly, the seasonal variation of water vapor has the similar tendency with down/upward long-wave radiation, and the minimum monthly mean daily value of integrated water vapor is only 0.29 cm in

winter and the maximum is 5.20 cm in July to August with a big leap (see the blue line in figure 3(b)). From figure 3(c), the lidar derived monthly average AOD (0.03-3.0 km) shows no great fluctuant. But it still appears much larger average value in spring and summer and a relative small one in July. That's because the dust weather sometimes happen in spring and increase the value of AOD. And the summer rainfall in July makes the air in Hefei cleanly and decreases the value of AOD.

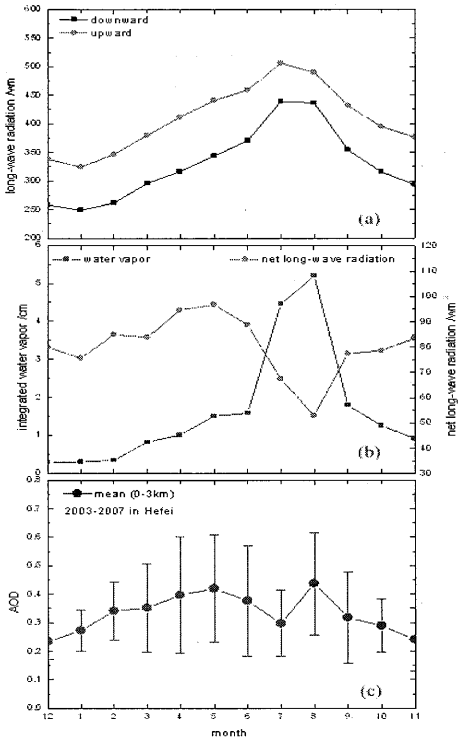

Fig. 3(a) the monthly mean daily value of long-wave radiation; 3(b) the monthly mean daily value of net long-wave radiation (red line) and integrated water vapor (blue line); 3(c) the lidar derived monthly average AOD (0.03-3.0 km) over Hefei from 2003 to 2007 on clear days

Well, in figure 3 we can conclude that in summer the effects of water vapor and the aerosol on net long-wave radiation are obvious. To some extent, negative correlations are considered to come up like the daily variation. Large water vapor and aerosol loading lead to a very low net long-wave radiative effect. However, in other seasons these relationships are not very evident. In my opinion, many other factors, such as the existence of cloud and the temperature of air or surface, maybe play an important role in the net long-wave radiation and we will discuss them in the near future work.

4. Summary

Net long-wave radiation is of major importance for all radiative balance studies. Under different weather/climate, many factors affected on net long-wave radiation must be discussed. We have primarily analyzed the changing of water vapor and aerosol could lead to variation of net long-wave radiation over Hefei in clear days. In some cases, the two parameters are playing a great role in net long-wave radiation (e.g. in summer) and maybe the other factors should be required for more detailed analyses.

Reference

1) Xiquan Dong, Baike Xi, Patrick Minnis, Observational Evidence of Changes in Water Vapor, Clouds, and Radiation at the ARM SGP site, Submitted to Science as a report (May 25, 2006).

2) LIU Chaoshun, LV Daren, DU Bingyu, A study on Ground-Based Remote Sensing of Atmospheric Integrated Water Vapor and Cloud Liquid Water, J. of Nanjing Institute of Meteorolog, 29(5), 606-612, 2006.

3) N. Sugimoto, A. Shimizu, I. Matsui, et al. Study of Dust Transport Using a Network of Continuously Operated Polarization Lidars, Water, Air, and Soil Pollution: Focus 5, 145-157, 2005.

4) Z. Z. Wang, R. L. Chi, B. Liu, et al. Depolarization properties of cirrus clouds from Polarization Lidar measurements over Hefei in Spring. CHINESE OPTICS LETTERS, Vol. 6(4): 235-237, 2008.

Retrieval of atmospheric water vapor amount over land using ADEOS-II / GLI near infrared data

Makoto Kuji[1], Nobuyuki Kikuchi[2], Akihiro Uchiyama[3], Tamio Takamura[4]

[1]*Faculty of Science, Nara Women's University, Kita-uoya Nishimachi, Nara 630-8506, Japan*

[2]*Center for Global Environmental Research, National Institute for Environmental Studies, 16-2 Onogawa, Tsukuba 305-8506, Japan*

[3]*Meteorological Research Institute, Japan Meteorological Agency, 1-1 Nagamine, Tsukuba 305-0052, Japan*

[4]*Center for Environmental Remote Sensing, Chiba University, 1-33 Yayoicho, Inage, Chiba 263-8522, Japan*

Corresponding: Makoto Kuji (makato@ics.nara-wu.ac.jp)

Abstract

A retrieval algorithm of vertically integrated water vapor amount (precipitable water) over land was applied to the near infrared data of Global Imager onboard Advanced Earth Observing Satellite-II (GLI / ADEOS-II). Comparing the retrieved precipitable water with radiosonde observation, we had some underestimation with some systematic bias for larger water vapor amounts in a preliminary analysis. Accordingly, we re-evaluated a relationship between radiance to be observed with GLI and water vapor amount, carrying out more detailed radiative transfer simulations. The retrieved water vapor amount with the coefficients was compared to radiosonde observation and ground-based microwave radiometer measurements. As a result of the validation, we have a relative error of about 30% and 10%, respectively. It also turns out that the linearity is quite good between the precipitable water with GLI and that with the radiosonde or microwave radiometer observation. Further, it is necessary to compare the satellite-retrieved results with the skyradiometry on a local basis as well as other satellite products on a global basis.

Keywords **:** Water vapor, ADEOS-II, GLI, AMSR, Radiosonde, Microwave Radiometer

1. Introduction

Water vapor is one of typical gas species governing the greenhouse effect as well as aerosol modulator through the humidity effect. Investigation of water vapor distribution is a clue to understand the radiation budget of earth atmosphere system as well as the global energy and hydrological circulation. Although water vapor is mostly distributed in the lower atmosphere (planetary boundary layer from surface to a few kilometers), the water vapor amount often increases in the middle and upper troposphere accompanying horizontal advection of humid air mass. Thus, precipitable water, (i.e. the vertically integrated water vapor amount) is considered to be the most representative quantity of water vapor amount in the atmosphere.

Historically, TIROS-N Operational Vertical Sounder (TOVS) data have often been used to estimate water vapor amount at lower, middle, and upper regions of the troposphere. [1)] Although TOVS is a splendid vertical sounder with a number of channels sensitive to water vapor absorption, their footprints are about several tens kilometers, rather larger than those of environmental sensors onboard earth-observing satellites. Better spatial resolutions of several hundred meters to several kilometers are available with MODIS / EOS sensors, wavelengths and bandwidths of which are very similar to those of TOVS. Combining the near infrared data of water vapor absorbing and non-absorbing channels with the thermal infrared data, precipitable water is derived from the MODIS mission with a relatively high spatial resolution along with information of clouds and aerosols. [2)]

In contrast to TOVS and MODIS, GLI onboard ADEOS-II is designed to obtain data of both the surface properties (vegetation, ocean color, and snow and ice, etc.) and atmospheric properties (cloud, aerosol, and radiation budget, etc.). In general, atmospheric correction is indispensable when surface geophysical properties are retrieved from satellite remote sensing data. Correction of atmospheric ozone, aerosol, and in particular, water vapor is important for precise retrieval of vegetation conditions and ocean color. In the GLI mission, the water vapor information is incorporated from the quasi-real-time objective analysis data. Nevertheless, it is desirable to use the water vapor information concurrently obtained with the same spatial resolution as other channels. In this context, we developed a retrieval algorithm of precipitable water with near infrared channels of GLI. The outline of the retrieval

algorithm is described in Sec. 2 together with an initial result of a global map. In Sec. 3, results of the validation are analyzed and discussed. Section 4 presents the summary and related future works.

2. Analysis of Data

We developed retrieval algorithm for water vapor amount (vertically integrated water vapor amount i.e., precipitable water) using GLI near infrared channel (1135nm) based upon the MODIS algorithm. With a sensitivity study, this algorithm is more sensitive to water vapor amount over land (higher albedo region) than over ocean (lower one). [3)]

The relationship between radiance ratio RR and precipitable water W (mm) is as follows:

$$RR = a + b\exp\left(-c\sqrt{W\left(\frac{1}{\cos\theta}+\frac{1}{\cos\theta_0}\right)}\right), \quad (1)$$

where the coefficients a, b, and c are 0.0690, 1.23, and 0.209 ($mm^{-1/2}$), respectively over land. Using Eq. (1), we can retrieve precipitable water from radiance ratio estimated from GLI observation.

This method was applied to GLI data over land on a monthly basis. Figure 1 shows a monthly precipitable water maps retrieved with ADEOS-II / GLI over land, in addition to those over ocean retrieved with Advanced Microwave Scanning Radiometer (AMSR) onboard ADEOS-II, and discuss a seasonal contrast of precipitable water on a global basis. From Fig. 1, you could see a good seasonal variation of columnar water vapor amount between spring and summer over both land and ocean.

We made a validation using radiosonde observation. We confirmed the retrieved results are comparable to the radiosonde observation at some observation sites over a northern America continent. But there existed some underestimation of satellite-derived precipitable water.

After this initial validation study, we re-evaluated the coefficients in Eq. (1) with more detailed radiative transfer calculations. The new coefficients are 0.0930, 1.183, and 0.192 ($mm^{-1/2}$) for a, b, and c, respectively.

We have two combinations to estimate the radiance ratio between water vapor absorbing and non-absorbing channels: one is two channel method using 1135nm and 1240nm for water vapor absorbing and non-absorbing channels, respectively; The other is three channel method using 1050nm as well as 1240nm for non-absorbing channel. As a result of the validation study over northern American continent, we found some irregular feature in the retrieved water vapor amount on a histogram basis. The reason of the irregular feature is still open question, but we discuss the results based on the two channel method in this article.

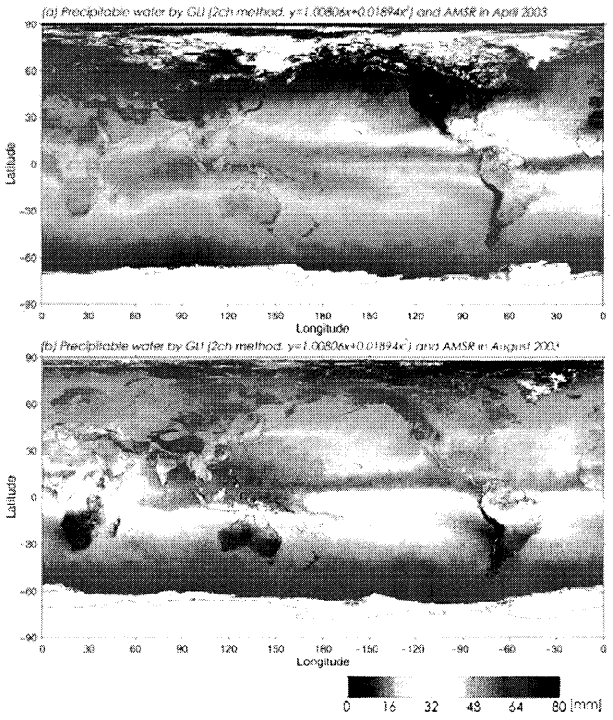

Fig. 1. A global map of monthly average columnar water vapor amount (precipitable water) retrieved with GLI and AMSR onboard ADEOS-II. Upper panel: April, lower panel: August (by courtesy of JAXA / EORC).

3. Validations and discussion

In this section, we describe validation results with radiosonde and microwave radiometry based on the new coefficients described in previous section.

In this validation study, we prepared GLI match-up data set that is small segment of 11 x 11 pixels around the radiosonde or microwave observation sites. Cloud screening is a critical issue in this validation. We adopted the following conditions as cloudy: average reflectance and standard deviation of the match-up segment is more than and equal to 25% and 0.03, respectively. We did not use the cloudy match-up segment in this validation study. We also constrain scan geometries. The condition is adopted that solar and satellite zenith angles is less than and equal to 60 and 30 degrees, respectively. As a result, we prepared the clear (non-cloudy) segments.

Next we prepared radiosonde match-up data out of the world sites over 750 sites of DCDF. The date of the

collected data expands from April 2 to October 24, 2003 and we used the data when the observation was carried out within ADEOS-II overpass. We also adopted the following cloud screening condition: if the relative humidity in some atmospheric layer is over 80%, the layer is possibly cloudy, and then the data were not used in this validation.

Figure 2 illustrates the comparison of integrated water vapor amount derived from GLI and radiosonde observation. As a result, GLI retrieved precipitable water has relative error of as much as 30 %.

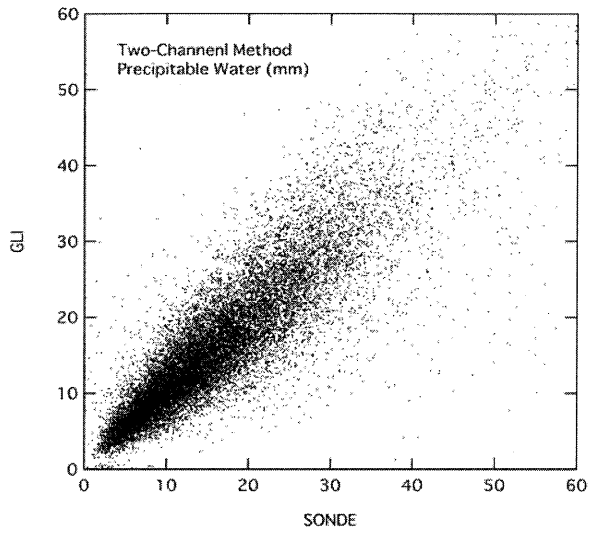

Fig. 2. Comparison of precipitable water between GLI and radiosonde observation.

However, water vapor is one of the most variable gaseous components in the atmosphere spatiotemporally. It is necessary therefore to make a more coincident comparison since radiosonde observation has time lag around several hours from satellite overpasses and it possibly has some departure from the site location due to strong wind in the free troposphere.

We further tried to compare the GLI retrieved water vapor amount to the ground-based microwave radiometer observation coincident within 10 minutes to GLI overpass since the microwave radiometer makes observation continuously.

Figure 3 illustrates the comparison of integrated water vapor amount derived from GLI and ground-based microwave radiometer for Hefei in China where is one of the SKYNET observatory. The microwave radiometer is a model WV-1100 manufactured by Radiometrics Corporation. It has two channels at 23.8 GHz near the water vapor absorption band and 31.4 GHz in the window region. The error bars illustrated in Fig. 3 are sufficiently small, which indicates the standard deviation of GLI water vapor amount for 11x11 pixels. The error of the difference between GLI and microwave radiometer measurements is almost 10 % that is smaller than result of comparison between GLI and radiosonde measurements.

This decrease of the error results from no time lag between microwave radiometer continuous observations and GLI observation as opposed to a time lag between GLI and radiosonde observation for maximum 6 hours. The results show that the water vapor amounts derived from GLI are close to ones derived from microwave radiometer. The other reason of the better estimation with the microwave radiometer than with the radiosonde are ascribed to that microwave radiometry is little sensitive to aerosol loading which is a potential error source in principle.

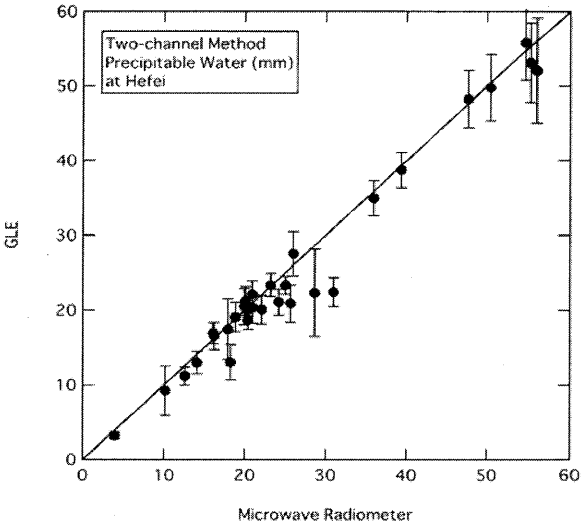

Fig. 3. Comparison of precipitable water between GLI and microwave radiometer at Hefei, China.

4. Concluding remarks

In this study, we applied a retrieval algorithm to ADEOS-II / GLI near infrared data over land. The validation study with radiosonde and ground-based microwave radiometer observation resulted in the relative error of 30 and 10 %, respectively. It is found that such a simple retrieval algorithm is useful to estimate water vapor over land. Water vapor has large spatial variation, so it is further feasible to compare the GLI retrieved precipitable water to the ground-based skyradiometry as well as the other satellite-derived water vapor amounts.

Acknowledgements

The authors are grateful to Dr. Hiroshi Murakami of JAXA / EORC for his provision of GLI and AMSR

precipitable water map. The authors are also grateful to Prof. Teruyuki Nakajima of CCSR, University of Tokyo for his useful suggestions.

References

1) B. J. Soden and F. P. Bretherton: Interpretation of TOVS water vapor radiances in terms of layer-average relative humidities: Method and climatology for the upper, middle, and lower troposphere. J. Geophys. Res., 101, pp. 9333-9343, 1996.
2) M. D. King, Y. J. Kaufman, W. P. Menzel, and D. Tanre: Remote sensing of cloud, aerosol, and water vapor properties from the moderate resolution imaging spectrometer (MODIS). IEEE Trans. Geoscience and Remote Sensing, 30, pp. 2-27, 1992.
3) M. Kuji and A. Uchiyama, Retrieval of Precipitable Water Using Near Infrared Channels of Global Imager / Advanced Earth Observing Satellite-II (GLI / ADEOS-II), Journal of Remote Sensing Society of Japan, 2000.

Estimation of radiation budget using ADEOS-II/GLI

Hideaki Takenaka[1], Satoru Fukuda[2], Cui Yu[1], Takashi Y. Nakajima[3], Akiko Higurashi[4],

Tamio Takamura[1], Teruyuki Nakajima[2], and Rachel T. Pinker[5]

1. Center for Environmental Remote Sensing, Chiba University, Japan
2. Center for Climate System Research, The University of Tokyo, Japan
3. Department of Network and Computer Engineering, Tokai University
4. National Institute for Environmental Studies, Japan
5. Department of Atmospheric and Oceanic Science, University of Maryland

Abstract

The Global Imager (GLI) observed data provides the particle product including detailed optical properties. This products promotes radiation budget studies for better understanding of Earth system. In this study, analysis of seven months in 2003 (April to October) was carried out. The GLI land and ocean aerosol and cloud particle products are included by Neural Network (NN) algorithm in Shortwave (SW) fluxes analysis. The downward SW fluxes at the surface is discussed for the influence of cloud with the direct and the diffuse components. On the equator, the global SW flux is weakened by a influence of clouds over the intertropical convergence zone (ITCZ). And, the diffuse component is predominant in the northern hemisphere side in April and May that is a remarkably seen in the Pacific and the Atlantic Oceans. This diffuse component trends may have a close relation between the activity of the cloud and the aerosol of the northern hemisphere. The North Pacific Ocean in middle latitude has been kept bright by scattering of clouds, and the blocking of the direct component is distinctive trend.

Keywords **:** ADEOS-II/GLI, Solar radiation, Radiation budget

1. Introduction

The Global Imager (GLI) is equipped the Advanced Earth Observation Satellite - II (ADEOS-II), it observes the land, ocean, and atmosphere with 36 channels [Nakajima, 1999][1]. It retrieves detailed particle optical characteristics in the atmosphere for a better understanding of global climate and Earth system. Clouds have enormous influence in Earth's radiation budget that is closely relates to Earth's energy budget. Clouds cool Earth by reflecting solar radiation, while it keep Earth warm by absorbing the terrestrial radiation and emitting to Earth surface. Because cloud modeling is not optimized well, these effect is uncertainty in General Circulation Model (GCM) [Tsushima and Manabe, 2001]. It perturbs the long term analysis for climate change of global warming. Aerosols have the effects of reflection and absorption on the solar radiation, and relates to cloud activities. Some particles cause the complex change of nominal particle optical characteristics by internal or external mixing. Because it changes the absorbing and the scattering characteristics of atmosphere, it has influence on the atmospheric radiation. In addition, because aerosols which become cloud nucleus, also influence cloud activities. Therefore, it become the uncertainty of radiation budget in the direct and the indirect effect. It is necessary to evaluate the influence of particles for radiation budget. Thus, accurate estimation of Solar fluxes are first step of them. In this study, downward and upward SW fluxes at the surface and TOA are estimated using ADEOS-II/ GLI particles product and surface albedo product. The ADEOS-II has once a day sampling because of a polar orbit (Sun-synchronous Sub-recurrent Orbit). However, the

estimation of the solar fluxes including a strict optical characteristics has an effective meaning. These products of the ADEOS-II/GLI is used to discuss the influence of detailed optical characteristics of atmospheric particles. The estimated solar fluxes of the direct and the diffuse components indicate regional characteristics.

2. GLI products

The ADEOS-II/GLI standard products are used to estimate the solar fluxes in this study. Particles optical characteristics and surface albedo retrieval algorithm utilizes the ADEOS-II/GLI observation data to the maximum. The latest land and ocean aerosols, water and ice clouds, and surface albedo products are used that is a test version. Ocean surface aerosols are retrieved by Retrieval of Aerosol Optical Properties (REAP) [Higurashi and Nakajima, 2002][2]. The four-channel method for the aerosol retrieval is effective based on aerosol type classification. Water and ice clouds are analyzed by Comprehensive Analysis Program for Cloud Optical Measurement (CAPCOM) [Nakajima and Nakajima, 1997][3] based on the solar reflection method. It estimated optical properties and spatial distribution of cloud. Moreover, a land surface aerosol is added new product. New algorithm for land surface aerosols covered from dark to bright target, that proposes the desert, the forest area aerosols and other various surface aerosols [Fukuda and Nakajima, 2008][4]. In addition, land surface albedo is updated by using Bidirectional Reflectance Distribution Function (BRDF) model. Analysis of the surface albedo based on the geometrical conditions correct to the surface Bidirectional Reflectance Factor (BRF) [Yu, 2008][5]. These are included estimation of solar radiation at the surface and the TOA.

3. Algorithm

Solar fluxes at the surface and the TOA are estimated by Neural Network algorithm. We developed an algorithm based on NN and applied to ADEOS- II/GLI for estimation of radiation budget. The NN approach is one of the solution to following problems. In general, satellite based estimate methods often use a Look-up Tables (LUT). Since pre-calculated values are used, the LUT methods are effective for large amount of data processing. However, if the effects of absorbing gasses and the particle optical characteristics are

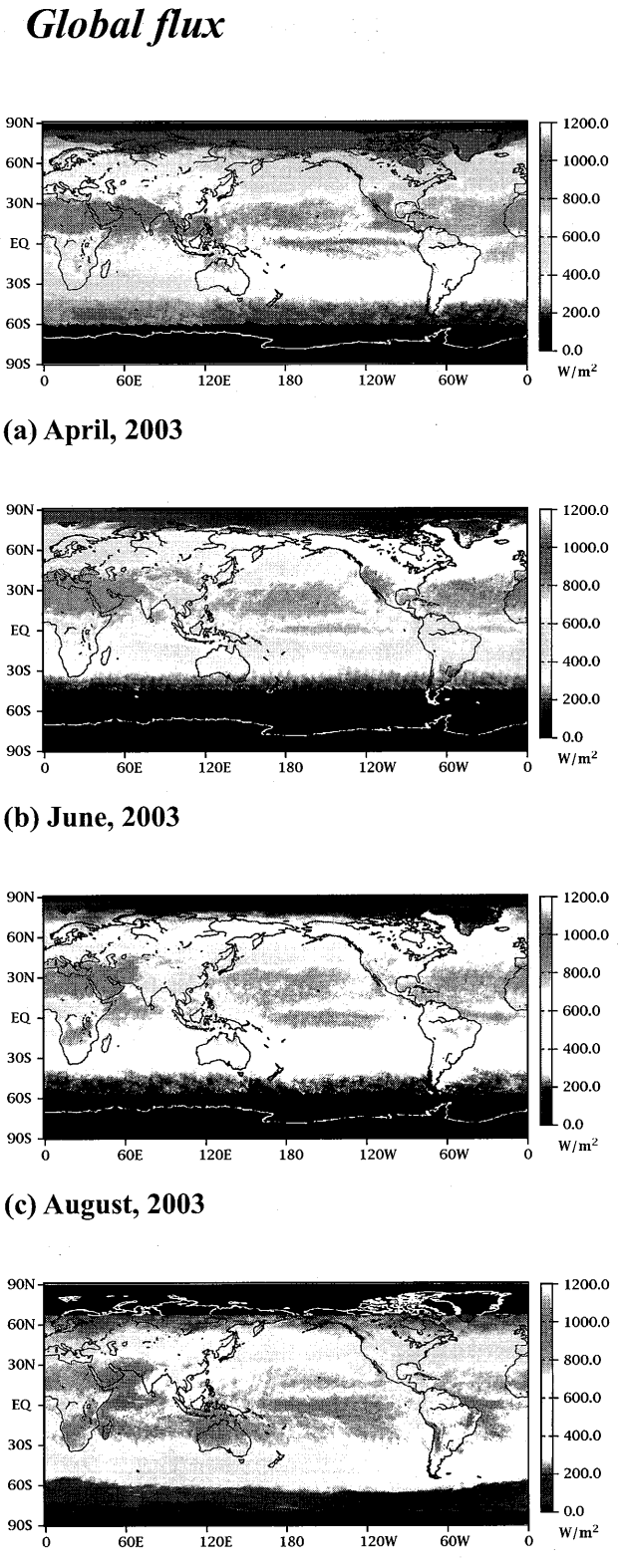

Figure 1: Monthly averaged downward shortwave flux at the surface that include the GLI particle product (land and ocean aerosols, water and ice cloud, land surface albedo). (a) April, 2003 (b) June, 2003 (c) August, 2003 (d) October, 2003

Direct component

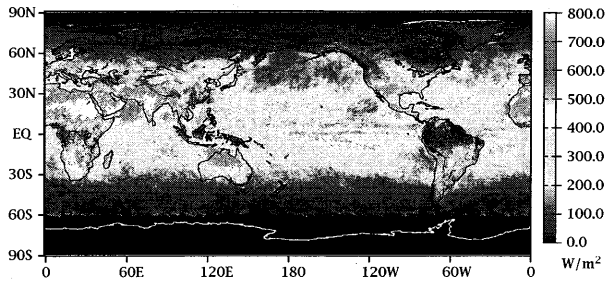

(a) April, 2003

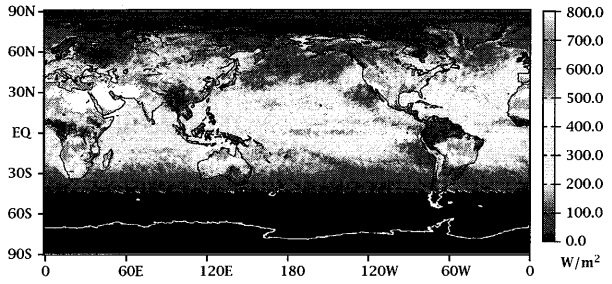

(b) June, 2003

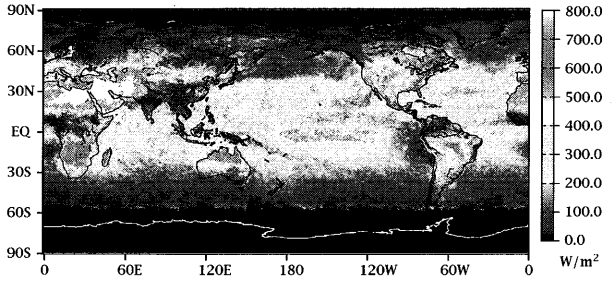

(c) August, 2003

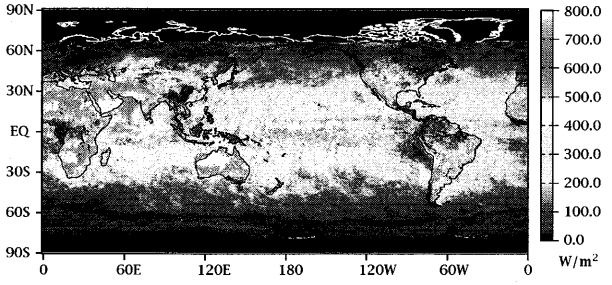

(d) October, 2003

Figure 2: Same as Figure 1, but for direct component. (Monthly averaged downward shortwave flux at the surface, direct component)

Diffuse component

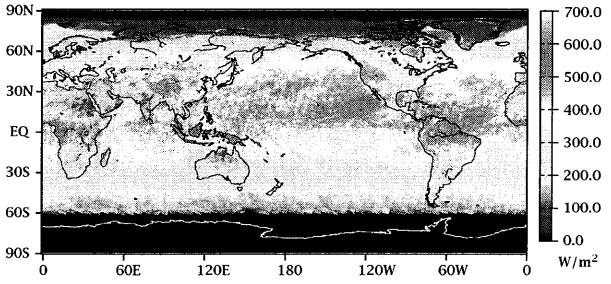

(a) April, 2003

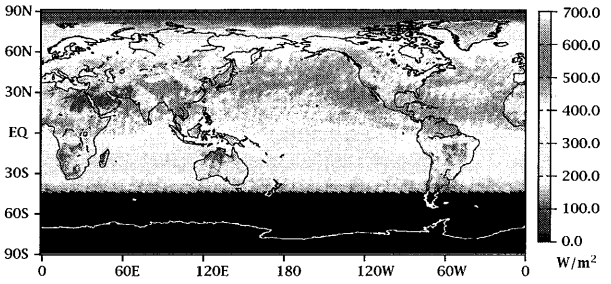

(b) June, 2003

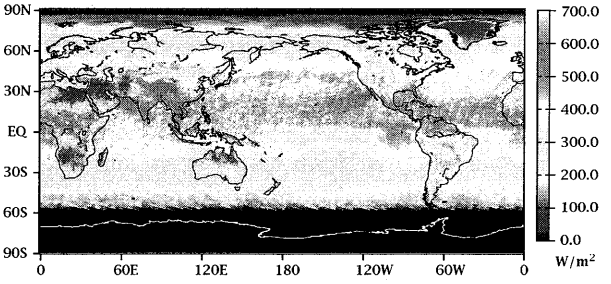

(c) August, 2003

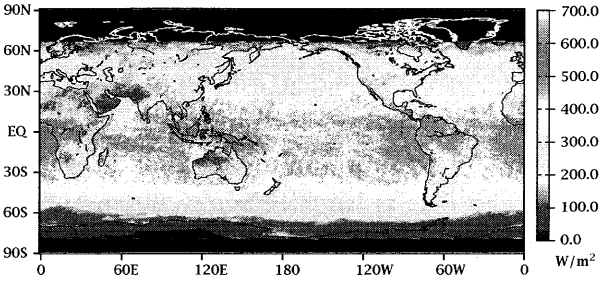

(d) October, 2003

Figure 3: Same as Figure 1, but for diffuse component. (Monthly averaged downward shortwave flux at the surface, diffuse component)

incorporated precisely, LUT becomes huge volume. An increase in parameter needs not only the increase of LUT volume but also complex interpolation of LUT. We apply the Extreme speed and Approximation module Multiple drive System (EXAM SYSTEM) for estimation of solar fluxes with the GLI products. The EXAM SYSTEM integrated these parameters of atmospheric radiation into the solar fluxes. Neuro-link Network solver (NN solver) for estimation are built by improved learning algorithm "Distortion-BP" [Takenaka et al., 2008][6]. It estimated the solar fluxes at the surface and the TOA.

4. Result and discussion

Figure 1 indicates the downward SW flux at the surface. It is strongly distributed in low latitudes (around equator) through the period. Because, equator has the influence of clouds of intertropical convergence zone (ITCZ), it indicates the weakened line of the global flux. Figures 2 and 3 are direct and diffuse components of downward SW flux at the surface, respectively. Contrast of rainy and dry season are clearly in India. Direct component is predominant in April (Fig. 2a), but it has very low value in August(Fig. 2c). While the diffuse component has a reverse trend. It was brought by the cloud. This trend indicates rainy season from June to September. For the other regions, such as North Africa to Middle East has the strong global flux, very strong direct component is predominant due to few clouds. Northern Australia shows the same trend for the same reason. The most important effects of clouds are the blocking of direct component and strong diffuse component caused by thin clouds (Fig. 4). In North Pacific Ocean, a strong scattering was caused by a thin cloud. Therefore it has been kept bright by scattering, and the blocking of the direct component is distinctive trend. This trend close relation with the activity of the cloud and the aerosol of from East Asia to North Pacific Ocean. Its a trend remarkably seen in the North Pacific Ocean and the North Atlantic Ocean. And, the West coast of north side of South America has the same trend. Especially, blocking of direct component is indicated ADEOS-II/ GLI observation period (April to October, 2003).

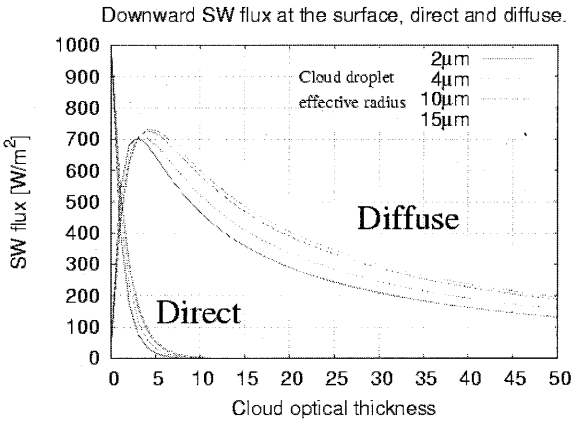

Figure 4 : Influence of cloud on downward SW flux at the surface, based on classification of cloud droplet effective radius. The kind of lines indicates the difference of a cloud droplet effective radius. (Solar zenith angle =20.0 degree. US standard atmosphere, surface albedo is 0.03.

References

1) Nakajima, T., T. Y. Nakajima, M. Nakajima, and the GLI Algorithm Integration Team (GAIT) (1999), Development of ADEOS-II/GLI operational algorithm for earth observation, SPIE, 3870, 314-322.
2) Higurashi, A., and T. Nakajima (2002), Detection of aerosol types over the East China Sea near Japan from four-channel satellite data., Geophys. Res. Lett., 29(17), 1836, doi:10.1029/2002GL015357.
3) Nakajima, T. Y., and T. Nakajima (1995), Wide-area determination of cloud microphysical properties from NOAA AVHRR measurements for FIRE and ASTEX regions, J. Atmos. Sci., 52, 4043-4059.
4) Fukuda, S., T. Nakajima1, A. Higurashi, N. Kikuchi, and T. Y. Nakajima (2008), Aerosol retrieval from GLI over land and its comparison with ground observation, CEReS symposium 2008.
5) Cui, Y., et al., (2008) An empirical anisotropy correction model for estimating land surface albedo for radiation budget studies, Remote Sensing of Environment, doi:10.1016/j.rse
6) Takenaka, H., T. Y. Nakajima, A. Higurashi, A. Higuchi, T. Takamura, R. T. Pinker, Estimation of Solar radiation by Neural Network, J. Geophys. Res. (submitted).

Assessment of surface urban heat island using land surface temperature derived from MTSAT-1R over East Asia

Ki-Ok Hong[1], Myoung-Seok Suh[1*], Jeon-Ho Kang[1], Chong-Heum Kwak[1], Maeng-Ki Kim[1]

[1] Department of Atmospheric Science, Kongju National University,
182 Shinkwan-dong, Gongju-city 314-701, ChungCheongnam-do, Korea
[1*] e-mail: sms416@kongju.ac.kr

Abstract

To evaluate the seasonal and diurnal variations of surface urban heat island (SUHI) according to the geographic locations, we used the land surface temperature (LST) derived from MTSAT-1R data. We developed split-window type LST retrieval algorithm to estimate the LST over East Asian region from MTSAT-1R data. The coefficients of split-window algorithm were obtained by means of a statistical regression analysis from the radiative transfer simulations using MODTRAN 4.0 for wide range of atmospheric profiles, satellite zenith angle and lapse rate conditions including the surface inversions. The accuracy of the LST retrieval algorithm has been evaluated with the MODIS LST data. The discrimination between urban and rural area is performed using normalized vegetation difference index (NDVI) and land cover map. The seasonal and diurnal variations of SUHI are assessed according to the geographic location, season, and NDVI. Preliminary results over South Korea showed that SUHI is generally greater during summer and day time than during other seasons and night time. And the seasonal and diurnal variations of SUHI are found only at day time and during summer without regard to the urban size and geographic location, respectively.

Keywords **:** land surface temperature, surface urban heat island, MTSAT-1R

1. Introduction

Urban heat island (UHI) is one of the most well known forms of anthropogenic climate modification. Modification of land-cover and artificial addition of heat in urban areas can cause the local air and surface temperatures to rise several degrees higher than the simultaneous temperatures of the surrounding rural areas. So the UHI (Surface UHI) is defined by air (surface) temperature difference between urban area and surrounding rural area. As in the UHI, SUHI is the combined results of various factors and affected by many conditions, such as the population number, city function, environment and weather conditions. In general, it is one of the most difficult surface variables to observe due to the strong spatio-temporal variations.

Therefore, numerous works have been made to retrieve the LST from the satellite data, especially polar orbit satellite (NOAA/AVHRR, Terra/MODIS, Landsat/TM (e.g., Kerr et al., 1992; Ulivieri et al., 1994; Wan and Dozier, 1996). In recent years, many works on the UHI (or SUHI) have been performed using these polar orbit satellite data (e.g., Hung et al., 2006). Reviews on the thermal remote sensing of urban climates are well documented in Voogta and Oke (2003).

And the quality of geostationary satellite (e.g., MSG/SEVIRI, MTSAT-1R) has been greatly improved recently (e.g., quantization: 8 bits ➔ 10 bits, spatial resolution: 5~10 km ➔ 4 km, observation frequency: 1H ➔ ~ 15 min, navigation accuracy, SNR). As a result, the quality of LST retrieved from geostationary satellite data, such as MSG/SEVIRI, has been significantly improved. As in the MODIS LST group, the LST over Africa and Europe retrieved operationally by the EUMETSAT LSA SAF (Land Surface Analysis Science Application Facility). So, temporal variations of SUHI using the LST derived from geostationary meteorological satellite data can be possible.

The goal of this study is to investigate the temporal variations of SUHI over East Asia using

the LST retrieved from MTSAT-1R. For this goal, we have developed split-window type LST retrieval algorithm using the simulated data and validated with MODIS LST

2. Methods

The radiances of infrared bands measured by the satellite sensor are mainly affected by surface conditions (e.g., emissivity, LST), atmospheric conditions (water vapor, aerosol) and target-sensor geometry. We developed split-window type LST retrieval algorithm to estimate the LST over East Asian region from MTSAT-1R data. Fig. 1 shows a flow chart of this study. The coefficients of split-window algorithm were obtained by means of a statistical regression analysis from the radiative transfer simulations using MODTRAN 4.0 for wide range of atmospheric profiles, satellite zenith angle and lapse rate conditions including the surface inversions. Because match-up data base of the observed LST for the LST retrieval algorithm is not available in this region. The detailed conditions used in the RTM simulations are as follows:

- RTM: MODTRAN 4
- Atmospheric profiles: 535 TIGR data (see Fig. 2)
- LST = Ta – 6K ~ Ta + 14K (Δt = 2K.)
- SZA : 0.~ 60. ($\Delta\theta$ = 5.)
- Band emissivity
  - IR1: 0.9576 ~ 0.9890 ($\Delta\varepsilon$: 0.00314)
  - IR2: IR1–3$\Delta\varepsilon$ ~ IR1+3$\Delta\varepsilon$(7steps), $\Delta\varepsilon$ = 0.004525

To derive the spectral emissivity over East Asian region, vegetation cover method (VCM, Caselles et al., 1997) is used. The effective emissivity of each channel is defined as the sum of the components from the vegetated area and the remaining ground area within pixel.

$$\varepsilon_i = \varepsilon_{i,g} \times (1 - FVC) + \varepsilon_{i,v} \times FVC$$

Where, $\varepsilon_{i,g}$, and $\varepsilon_{i,v}$, are the vegetation and ground emissivity corresponding to the land cover types. Emissivities of vegetation and ground according to the land cover types were obtained from Peres and DaCamara (2002). FVC is the fraction of vegetation and calculated using the normalized difference vegetation index (NDVI).

$$FVC = \frac{NDVI - NDVI_{\min}}{NDVI_{\max} - NDVI_{\min}}$$

$NDVI_{max}$ and $NDVI_{min}$ are the NDVI when the pixel is completely covered with vegetation and ground, respectively.

Cloud is a critical obstacle in retrieving the surface parameters using satellite data. In this study, the least clouded scenes of MTSAT-1R were selected through a visual inspection using visible and infrared imagery.

3. Results

The LST retrieval equation has been derived.

$$LST = -1.5418 + 1.00333T_{IR1} + 2.78769\Delta T + 0.31635\Delta T^2 + 1.1552(\sec\theta - 1) + 89.9499(1 - \varepsilon)$$

To validate the LST estimated in this study, collocated MODIS LST is used. Fig. 3 shows the spatial distribution LST derived from MODIS, MTSAT-1R and their differences for the day and night time. And the validation results are shown in Table 1 for the 4 selected cases. The LST estimated in this study is very similar to the MODIS LST, especially at night time. In general, the LST algorithm overestimates and underestimates the LST during day time and night time, respectively. However, the correlation coefficients, bias and RMSE showed that the LST retrieval algorithm developed in this study can be used for the LST retrieval in this region.

Fig. 4 shows a spatial distribution of LST over South Korea derived from MTSAT-1R at the daytime in summer and autumn cases. The LST over the urban area, especially for the large cities such as Seoul, Daegu, and Busan, is much higher than that over the surrounding rural areas.

Diurnal variation of SUHI in Seoul according to the season is shown in Fig. 5. Unlike the UHI, the diurnal variation is only significant with strong maximum at noon time during summer. However, the SUHI is very consistent with time during other seasons although their magnitudes are slightly

different. The magnitude of SUHI are ranged from 0 to 15 C and clearly affected by the season and time, urban size, geographic locations and weather conditions. The patterns of diurnal variation of SUHI over other cities are very similar (not shown).

SUHI shows a different seasonal variation according to the day and night (Fig. 6). In general, the seasonal variation of SUHI at daytime is much greater than that of nighttime without regard to the urban size and geographic location. The strong SUHI during summer is related with the two factors: One is the small thermal heat capacity and less available soil moisture of urban surface due to the paved surface, and the other is strong solar heating during daytime in this region.

4. Summary

In this study, temporal variations of SUHI over East Asia have been examined using the LST retrieved from MTSAT-1R. For the analysis of SUHI, LST retrieval algorithm have been developed using the synthetic data derived from radiative transfer simulations using MODTRAN 4.0 and TIGR data. The quality of LST derived from MTSAT-1R comparable to the MODIS LST regardless of the day and night.

Although MTSAT-1R has a relatively low spatial resolution (4 ~ km) compared to the MODIS or AVHRR, it can detect SUHI and its spatio-temporal variations. The magnitude of SUHI are ranged from 0 to 15 C and clearly affected by the season and time, urban size, geographic locations and weather conditions. The selected cases showed that seasonal variation of SUHI is found only at day time with maximum during summer. And diurnal variation is most significant during summer with the maximum at noon but no distinct diurnal variation is found during other seasons. The spatial magnitude of SUHI is greater at inland area than coastal area.

More works should be performed to assess the temporal variations of SUHI quantitatively under the various weather conditions using satellite data and ground data with the precise cloud masking algorithm.

Acknowledgements

This work is partly sponsored by the STAR project of Kongju National University.

References

1) Caselles V., C. Coll, and E. Valor, 1997, Land surface emissivity and temperature determination in the whole HAPEX-Sahel area from AVHRR data. *Int. J. Remote Sens.*, 18, 1009–1027.

2) Kerr Y. H., J. P. Lagouarde, and J. Imbernon, 1992. Accurate land surface temperature retrieval from AVHRR data with use of an improved split window. *Remote Sens. Env.*, 41, 197-209.

3) Hunga,T., D. Uchihama, S. Ochi, Y. Yasuoka , 2006: Assessment with satellite data of the urban heat island effects in Asian mega cities, *Int. J. of Appl. Earth Obs. and Geoinfo.*, 8, 34-48.

4) Peres L., and C. C. DaCamara, 2002, An emissivity look-up table for LST estimations from MSG data. *SAF on land Surface Analysis Training Workshop, Lisbon, Portugal, July 8-10.*

5) Ulivieri C., M. M. Castronouvo, R. Francioni and A. Cardillo, 1994. A split-window algorithm for estimating land surface temperature from satellites. *Adv. Space Res.*, 14(3), 59-65.

6) Voogta, J.-A., and T.-R. Oke, 2003, Thermal remote sensing of urban climates, *Remote Sens. Env.*, 86, 370-384.

7) Wan Z, and J. Dozier, 1996. A generalized split-window algorithm for retrieval of land surface temperature from space. *IEEE Trans. Geosci. Remote Sens.*, 34, 892-905.

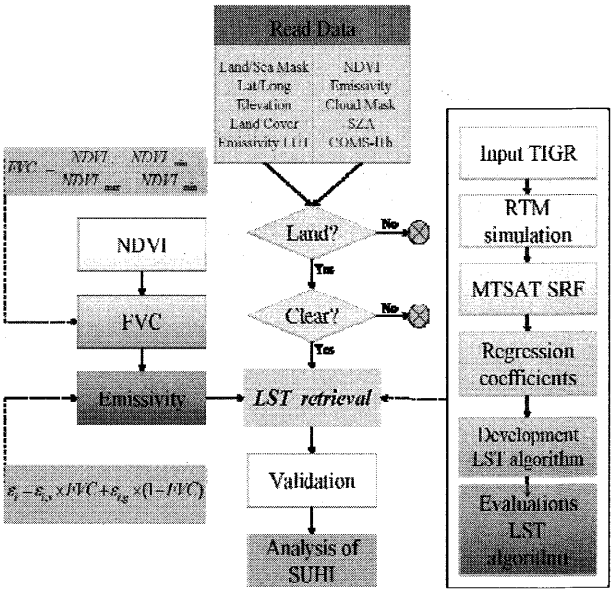

Fig. 1. Flow chart of LST retrieval and SUHI analysis.

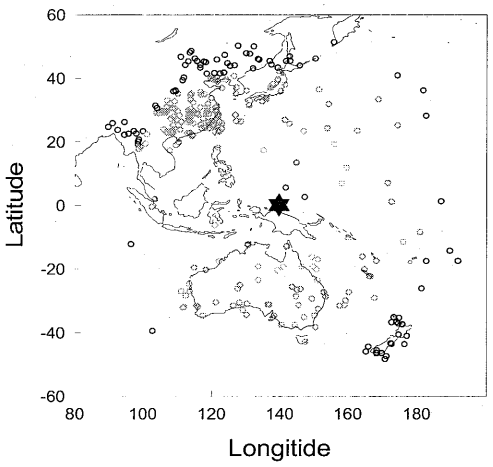

Fig. 2. Spatial distribution of TIGR data used in this study

.

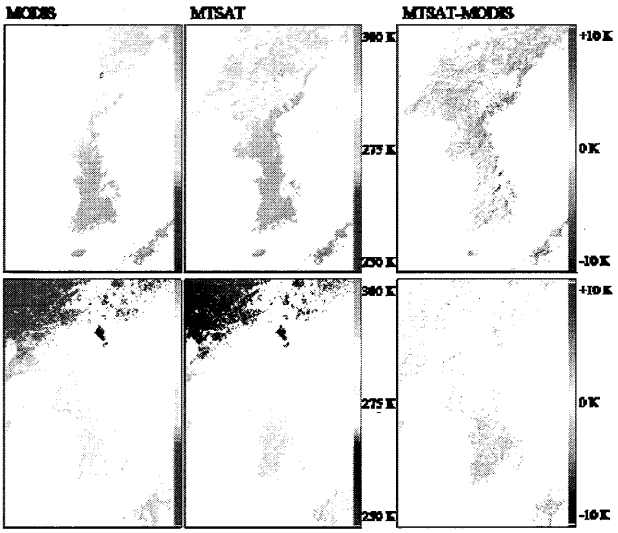

Fig. 3. Spatial distribution of LST derived from MODIS, MTSAT-1R and their differences for the day and night time.

Table 1. Validation results of LST estimated from MTSAT-1R data for the 4 selected cases.

	MTSAT time	MODIS time	R	Bias	RMSE	Val_P_Num
Case1 /day	0200	0210 0215	0.939	+1.507	2.701	14057
Case2 /day	0400	0350 0355	0.832	+1.976	4.062	23915
Case3 /night	1333	1315 1320	0.989	-0.364	1.389	14729
Case4 /night	1500	1455 1500	0.889	-1.017	1.895	33973

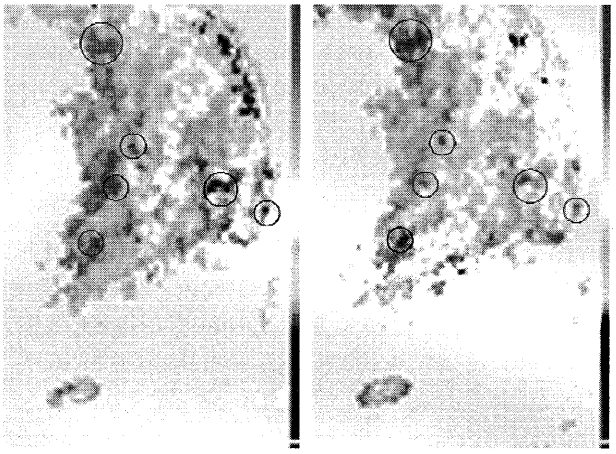

Fig. 4. Spatial distribution of LST estimated from MTSAT-1R during summer (left: 0400UTC 11 June 2006) and autumn (right: 0400UTC 06 October 2006)

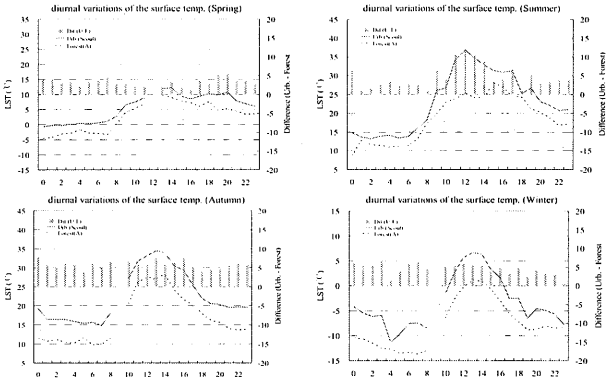

Fig. 5. Diurnal variation of SUHI in Seoul according to the season.

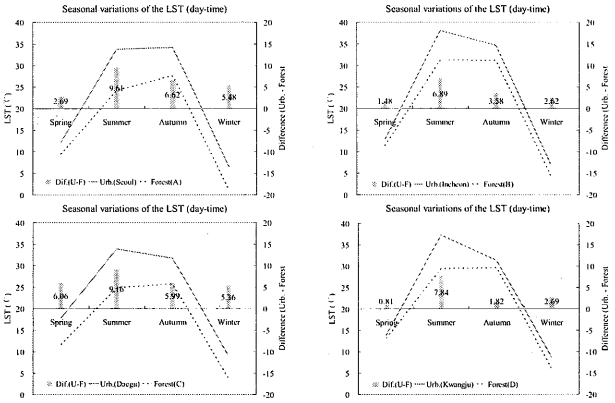

Fig. 6. Seasonal variation of SUHI at daytime for the selected major cities over South Korea.

Aerosol characteristics of two urban cities

Nobuo TAKEUCHI [1], Nofel LAGROSAS[2], Suekazu NAITO[3], Masanori YABUKI[1], Naohiro MANAGO[1], and Hiroaki KUZE[1]

[1] *CEReS, Chiba University, 1-33 Yayoi-cho, Inage-ku, Chiba 263-8522, Japan*
E-mail:takeuchi@faculty.chiba-u.jpan

[2] *Ateneo de Manila Univ., Katipunan Ave., Loyola Heights, Quezon City, 1108 Philippines , E-mail: nofel@observatory.ph*

[3] *Chiba Pref. Environmental Research Center, 1-8-8 Iwasaki-nishi, Ichihara, Chiba 290-0046, Japan E-mail: s.nitu3@mc.pref.chiba.jp*

Abstract

Chiba and Manila (Quezon) Cities are two typical coastal cities in east Asia. Aerosol properties of two cities were compared by sampling around the same period (dry season) and analyzed at the same instruments. Aerosol were sampled using two sets of NILU-type samplers for EC/OC analysis (quartz fiber filter) and for ion-chromatography analysis (PTFE filter). Particle size were classified into 3 stages (giant particle; d(diameter) > 10 μm, coarse particle; 10 μm > d > 2.5 μm, fine particle; d< 2.5 μm). In dry season, the wind direction was north to east in Manila, west to north in Chiba. In both sites, the soil components were most abundant; however there are some differences. In Manila, in all sizes, the soil shows the largest, but in Chiba, in the fine particle it showed small fraction; $(NH_4)_2SO_4$ showed the largest in fine particle in Chiba, but not in Manila. EC/OC were the main components of fine particle in both cities. Sea salt showed larger fraction in larger size. The fraction of giant particle is constantly around 15μg/m^3 in Manila, but varies 5 to 20 μg/m^3 in Chiba, especially large in April with larger concentration of soil, probably due to Asian dust.

1. Introduction

Aerosol is an important factor of global radiation budget. The optical properties of aerosol is important to derive radiation budget. One of the methods to estimate the optical properties is to calculate based on the chemical component of the aerosol. For the purpose of obtaining the component data, Chiba University has continued once-a-month sampling since 1998[1,2]. Recently we had a chance to sample simultaneously at two sites in Chiba and Manila (Quezon). In this paper, we showed the properties of aerosol sampling at two cities.

2. Features of two cities

Both Chiba and Manila cities are coastal cities, and sampling were done in the dry season. Chiba is located in 36 deg N, while Manila is located in 25 deg N. So the average temperature is ten to twenty degrees higher in Manila city. Dry season is similar both November to February. Annual precipitation is higher in Manila. Sampling is done at Chiba University (on the roof floor at 45 m ASL) and at Ateneo de Manila University (50 m ASL). Both samples are analyzed at Chiba Prefectual Environment Center in Ichihara city, Chiba for the measurement of EC/OC and cation and anion concentration..

Table. 1 Comparison of two cities.

	Chiba City (Chiba Univ.)	Quezon City (Ateneo de Manila U.)
Population	930,000	2,660,000
Area	272 km^2	166 km^2
Average temp.	5～25℃	23～36℃
Dry season	Nov.～March	Nov.～Feb.
Wet season	(June～Oct.)	June～Oct.
Precipitation	1600 mm	2000 mm
Sampling point		
latitude	35.63° N	14.64° N
longitutde	140.10° E	121.07° E
elevation	19m (45m)	50m

3. Sampling and Analysis

The data of period in January, 2007 to April (June) 2007 are compared in two cities. In this season, in Philippine the wind flows from north in winter and rotates to east, then swirls in early summer. In Japan, in winter the wind prevails westerly or north-westerly, then often changes the direction,

depending the location of high and low pressures.

Wind direction is an important information on the aerosol characteristics. Wind trajectory is obtained using NOAA HYSPLIT4[3].

Aerosol was sampled at the flowing speed of 20ℓ/min for 4 days. The aerosol sample was collected by two sets of NILU-type Cascade impactors (Tokyo Dylec) : One sampler installs quarttz fiber filter (Tokyo Dylec) for EC/OC analysis by thermal method. The other installs PTFE (Teflon) fiber filter (Advantec) for ion-chromatography.

This time, the filters sampled in Manila were transported to Japan. Both samples in Chiba and Manila were analyzed at Chiba Environmental Research Center using CHN-coder (Yanaco MT-6) and ion- chromatograph (Dionex DX-120).

4. Analytical method

Aerosol samples analyzed by CHN-coder and ion-chromatograph are classified into 6 aerosol categories : EC (elemental carbon), Org (organic carbon), NaCl (Sea salt), Soil, NH_4NO_3 (AN: ammonium nitrate), and $(NH_4)_2SO_4$ (AS: Ammonium sulfate), using the following formula[2].

EC : measured value [EC] of the CHN-coder.

Org : 1.2 × measured value [OC] of the CHN-coder.

NaCl : $1.195\times[Na^+]+[Cl^-]+[Na^+]\times0.252$

Soil : $(100/6.422)\times[N.S.S.Ca^{++}]$

$[N.S.S.Ca^{++}]=[Ca^{++}]-(0.4/10.556)\times[Na^+]$

AN (NH_4NO_3) : $[NO_3^-]+[NH_4^+]\times(([NO_3^-]/62)/(2\times[N.S.S.SO_4^{--}]/96+[NO_3^-]/62))$

AS ($(NH_4)_2SO_4$) : $[N.S.S.SO_4^{--}]+[NH_4^+]\times([N.S.S.SO_4^{--}]/96)/(2\times[N.S.S.SO_4^{--}]/96+[NO_3^-]/62))$

$[N.S.S.SO_4^{--}]=[SO_4^{--}]-0.252\times[Na^+]$

5. Analysis and Further Discussion

The analyzed results are shown in the following.

Each component of sampled aerosol is shown, separated in fine particle (d<2.5 μm), coarse particle (2.5 μm < d < 10μm), and giant particle (d>10 μm) in Fig. 1 and Fig. 2 for Manila and Chiba, respectively.

In Manila, soil component shows large concentration through all sizes. But in Chiba, the concentration of soil is not so high in fine particle. Comparing to the soil, the ratio of EC, Org, and ammonium sulfate are high. The fraction of giant particle is around 15μg/m^3 in Manila, but in Chiba it varies between 5 to 15 μg/m^3. Especially in the season of Asian dust (March and April), concentration of fine particle is high

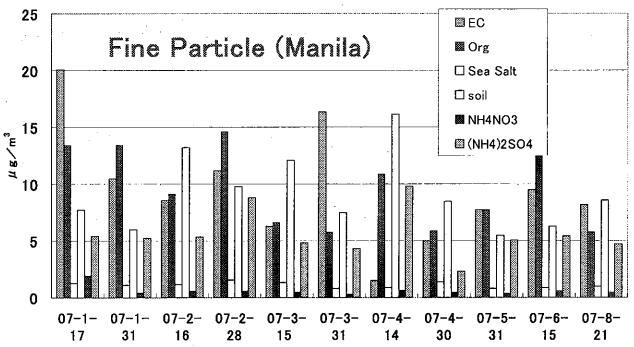

Fig. 1a) Fine particle concentration of Manila aerosol in early 2007.

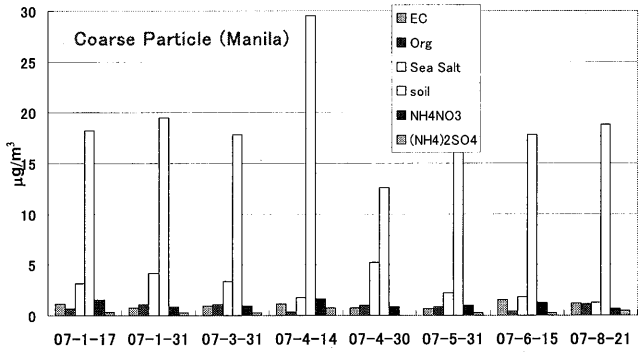

Fig. 1b) Coarse particle concentration of Manila aerosol in early 2007. Soil is predominant.

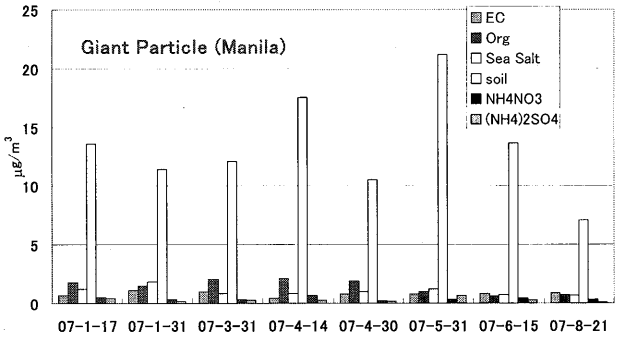

Fig. 1c) Giant particle concentration of Manila aerosol in early 2007. Soil is also predominant.

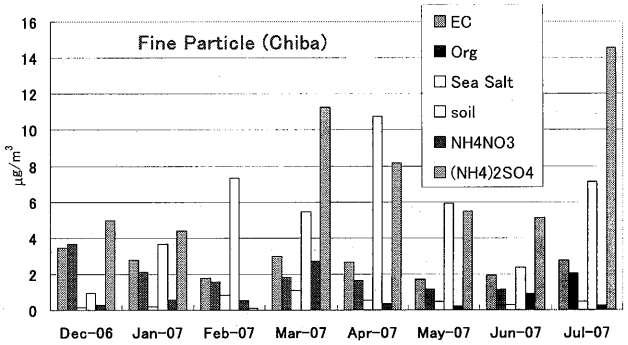

Fig. 2a) Fine particle concentration of Chiba aerosol in early 2007.

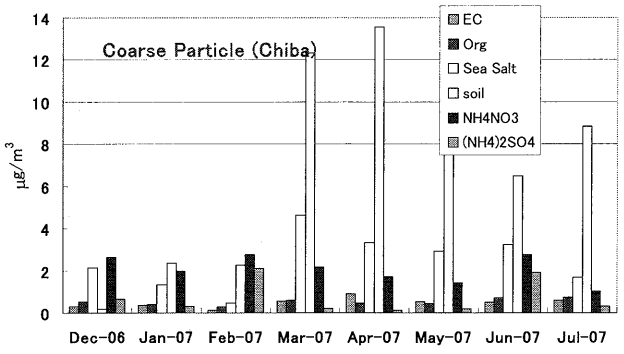

Fig. 2b) Coarse particle concentration of Chiba aerosol in early 2007. Concentration of soil is large.

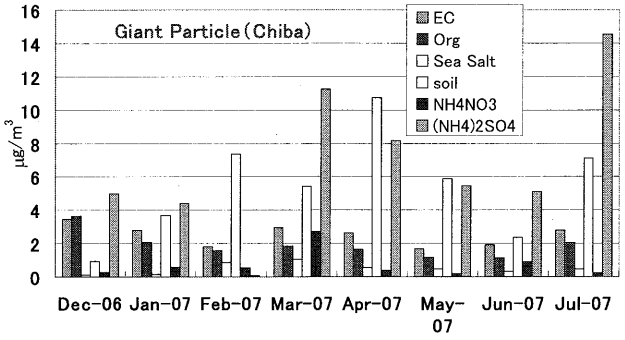

Fig. 2c) Giant particle concentration of Chiba aerosol in early 2007.

in Chiba city, the ratio of EC and Org is high in fine particle, especially in Manila. This is due to the effect of heavy traffic and air pollution.

6. Backward Trajectory

As mentioned above, the backward trajectory is important for considering the source of aerosol origin. Some examples (February, April, and June) of wind trajectory are shown in Fig. 3. In this season, in Chiba, the wind is westerly from Japan Sea, and in Manila, the wind is north-easterly from Pacific Ocean. In these examples, the wind direction at 500 m, 1000 m, and 1500 m are shown. The altitude dependence of wind are not found except in February in Manila.

7. Single Scattering Albedo

If we know the composition of aerosol, then we can estimate single scattering albedo (SSA)[4] for the average particle size profile for dry season, assuming aerosol particle size distribution measured in Chiba.. The terminology of mr and mi mean real part and imaginary part of refractive index, respectively. SSA values in Chiba are between 0.869 and 0.757 for external mixture, half internal mixture and internal mixture. Those in Manila are between 0.749 and 0.662. The

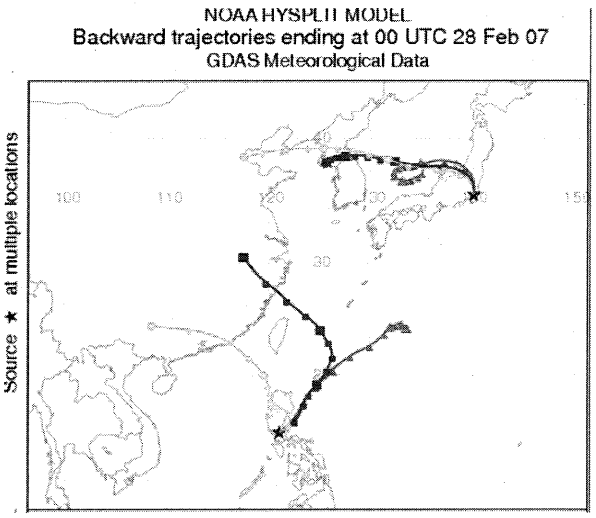

Fig. 3a) Three day backward trajectory at sampling sites in February, 2007. (starting at red: 500m ASL, blue: 1000m ASL, green: 1500m ASL)

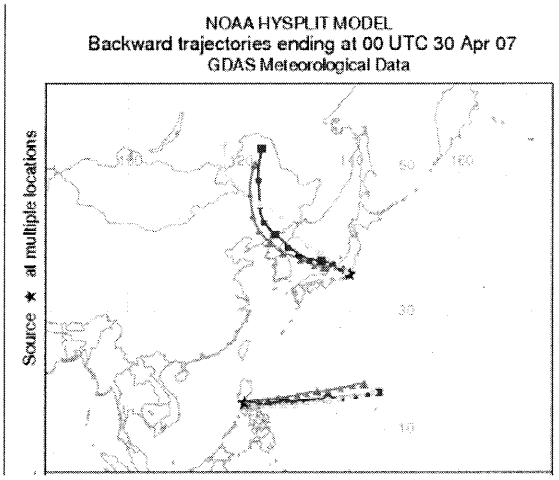

Fig. 3b) Three day backward trajectory at sampling sites in April, 2007. (starting at red: 500m ASL, blue: 1000m ASL, green: 1500m ASL)

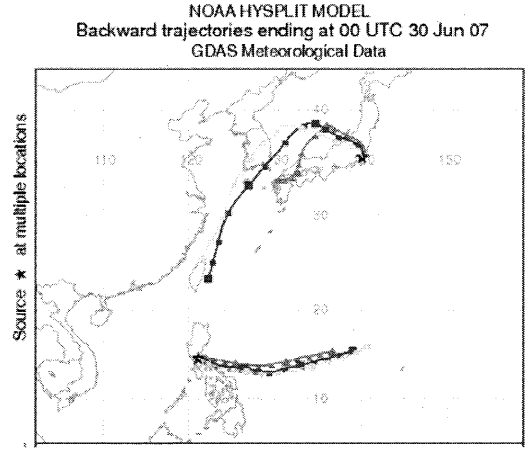

Fig. 3c) Three day backward trajectory at sampling sites in April, 2007. (starting at red: 500m ASL, blue: 1000m ASL, green: 1500m ASL)

Table 2 Albedo in Chiba for average particle size profile.

	m_r	m_i	SSA
External mixture	1.477	0.016	0.869
Half internal mixture	1.488	0.025	0.818
internal mixture	1.526	0.040	0.757

Albedo in Manila for average particle size profile

	m_r	m_i	SSA
External mixture	1.504	0.044	0.749
Half internal mixture	1.516	0.057	0.707
internal mixture	1.531	0.075	0.662

lower value in Manila is due to large concentration of EC.

7. Summary and Discussion

Aerosol components in two Asian coast cities (Chiba and Manila) are investigated in dry season, 2007, based on the result of CHN-coder and ion-chromatography .analysis. Soil component are derived from the amount of non-sea salt calcium. Here the fraction is adjusted the estimated value not to exceed the total collected value. The amount in Chiba looks reasonable, however that in Manila looks too large. The composition of soil may be different in Chiba and Manila. So the fraction of N.S.S.Ca^{++} may be different in Manila.

Other features are as follows:

1. Both cities have similar trend in composition. However, soil component is high in Manila. There is possibility that the actual Ca^{++} concentration of soil is high, so that the apparent soil amount looks large.
2. Elemental Carbon and Organics are high in fine particle, especially in Manila, probably due to heavy traffic and air pollution.
3. In fine particle, ammonium sulfate is substantial. In both cities, the amount of nitrate aerosol is not large. This means NOx amount is not specially large.
4. Sea salt is outstanding in coarse particle. However sea salt is not dominant in the total fraction, although two cities are coastal.

In order to make the industrial and traffic effects clear, further investigation is necessary.

Acknowledgements

This symposium is sponsored by the Ministry of Education, Science, Sports and Culture, Japan (MEXT), and National University Corporation Chiba University.

References

1) N.Takeuchi, et al.; Long-term Variation of Chemical Component and Optical properties of SPM in Chiba and etc. 16th Nucl. & Atmos. Aerosol, 2004, pp. 736-739.
2) S. Fukagawa, et.al., Characterization of seasonal variation of tropospheric aerosols in Chiba, Japan Atmospheric Environment 40, 2160-2168 (2006).
3) **http://www.arl.noaa.gov/ready/hysplit4.html**
4) H. Tsuruta, M. Yabuki *Kisho-Kenkyu Note (Meteorological Research Note)*, **218**, 45-66 (*in Japanese*), Meteorological Society of Japan(2008).

Short-term Calibration of MTSAT-1R Solar Channel Using Desert Targets

Hyoung-Wook Chun and Byung-Ju Sohn

School of Earth and Environmental Sciences, Seoul National University, Seoul, 151-747, Korea :
chunhw@eosat.snu.ac.kr and sohn@snu.ac.kr

Abstract

In this study, we propose the calibration algorithm for the solar channel (550 ~ 900 nm) of MTSAT 1R which is the Japanese geostationary satellite launched on 26 Feb. 2005 and located at 140°E. We developed a method utilizing MODIS-derived BRDFs for the solar channel calibration over the bright desert area. Targets are selected based on the desert's brightness, spatial uniformity, temporal stability and spectral stability. The 6S model has been incorporated to account for directional effects of the surface using MODIS-derived BRDF parameters within the spectral interval in interest. Results based on the analysis for the period from November 2007 to June 2008 suggest that MTSAT-1R solar channel measurements have a low bias within 5%.

Keywords: Solar channel calibration, BRDF, COMS, MTSAT-1R, MODIS, SeaWiFS

1. Introduction

The Multi-Functional Transport Satellite 1R (MTSAT 1R) succeed the Geostationary Meteorological Satellite (GMS) series as the next generation satellite series covering the East Asia and the Western Pacific regions. The Japanese Advanced Meteorological Imager (JAMI) aboard the MTSAT 1R measures the reflected solar radiation within a spectral band (550 ~ 900 nm) as well as emitted infrared radiation at 4 spectral bands. The retrieval of quantitative parameters requires absolute calibration of the radiometer and monitoring of its drift. As no in-flight calibration device is available for the solar channel, vicarious calibration is needed for producing level 1.5 data.

In this study we develop a method of utilizing satellite-derived BRDF for calculating the TOA radiance which then will be used for the solar channel calibration. Bright desert targets are chosen because the atmospheric contribution to the TOA radiance is fractionally smaller, compared to the surface contribution over the bright surface. Spatial and temporal variations of MODIS-derived nadir bidirectional reflectance distribution function (BRDF) and NDVI are examined over the Australian Simpson desert in order to select the bright surface area. Seasonally varying BRDFs over the selected targets are used as inputs to the 6S radiative transfer model to simulate visible channel radiances. And finally we estimate the calibration coefficient of MTSAT 1R and compared with the original calibration coefficient.

* *Corresponding author address:* Byung-Ju Sohn, School of Earth and Environmental Sciences, Seoul National University, Room 501-523,
e-mail : sohn@snu.ac.kr

2. Methods

2.1 Surface characterization

Since surface reflectance varies with positions of sun and satellite, information on the bidirectional reflectance distribution function (BRDF) is necessary for accurate calculation of the TOA radiance. In this study, BRDF information derived from MODIS/TERRA measurements is used, which is from the composite of all available cloud-free, atmospherically corrected, spectral surface reflectance observations over a 16-day period with a semi-empirical, kernel-driven BRDF model (Lucht et al., 2000). The theoretical basis of this kernel-driven BRDF model is that the land surface reflectance can be modeled as a sum of three kernels representing basic scattering types: (1) isotropic scattering, (2) radiative transfer-type volumetric scattering from horizontally homogeneous leaf canopies, and (3) geometric-optical surface scattering from scenes containing 3-D objects that cast shadows and are mutually obscured from view at off-nadir angles (Lucht et al., 2000).

The black and white sky albedos are used in this study. The black sky albedo is the reflectance from direct illumination source taking places over the 2 solid angle. This albedo is derived from integration of BRDF over the hemisphere (2 solid angle), so it is a function of solar zenith angle. The black sky albedo at the solar zenith angle of 10 is used for the calculation of the spectral surface reflectance (see 2.3 section). Because the white sky albedo is the reflectance in all directions from isotropic diffuse source, it can be obtained by integrating black sky albedo over illumination hemisphere and therefore is independent of angles. The white sky albedo is used as input to the radiative transfer model, along with BRDF.

2.2 Target selection

We use the brightness, spatial uniformity, temporal stability and spectral stability as criteria for selecting bright targets (Mitchell et al. 1997). The brightness of the target is important because the impact of uncertainties on measurement and characterization leads to the relative error inversely related to the brightness. The nadir BRDF (N. BRDF) is used for the brightness test. Spatial uniformity is also important because unavoidable registration error introduces significant uncertainty into the calibration method when the surface is not spatially uniform. Cosnefroy et al. (1996) computed the coefficient of variation (CV) which was defined by the ratio of normalized standard deviation to the mean of normalized TOA reflectance on a moving 41 x 41 pixel window in the METEOSAT-4 image. In this study, CV of N. BRDF is calculated at a 5 x 5 grid (about 20 x 20 km) window. Temporal stability is considered important for the sensor drift monitoring whereas spatial homogeneity is important element for the target selection. The NDVI is used for the spectral stability check at 11 potential targets given in Fig. 1. The potential targets (marked by gray circles in Fig. 1) are chosen when N. BRDF > 0.2, CV < 0.06, temporal standard deviation < 0.06, and NDVI < 0.2.

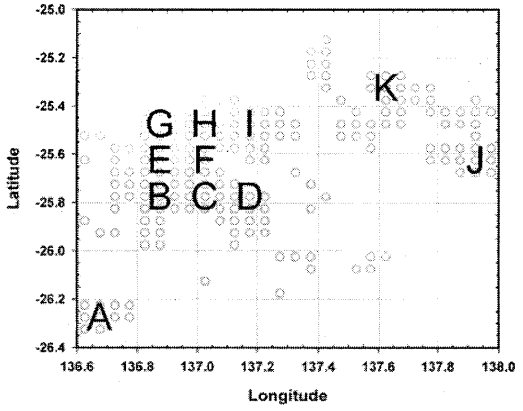

Figure 1. The location of 11 selected targets (A - K). The gray circles represent targets satisfying the target criteria.

2.3 Conversion of narrow band BRDF parameters to broad band parameters

Considering that COMS/MI solar channel will measure radiance over the broad band from 550 nm up to 800 nm, the MODIS BRDF parameters in seven bands are to be interpolated into the predefined wavelengths. The proposed method is based on the comparison of the black-sky albedo estimated at each MODIS band $\bar{\alpha}_{MO}(\mathbf{band, target, time})$ with the surface spectra from the ASTER spectral library (http://speclib.jpl.nasa.gov). The ASTER spectral library provides the spectral black sky-albedo at a 10° solar zenith angle $\alpha_{AS}(\lambda, \mathbf{type})$ from 400 nm up to 14000 nm for 41 surface types. The $\alpha_{AS}(\lambda, \mathbf{type})$ is converted into the spectral albedos at seven MODIS bands $\bar{\alpha}_{AS}(\mathbf{band, type})$ by applying MODIS response functions to $\alpha_{AS}(\lambda, \mathbf{type})$. Linear regression equation is obtained by relating $\bar{\alpha}_{MO}(\mathbf{band, target, time})$ to $\bar{\alpha}_{AS}(\mathbf{band, type})$. The surface type is selected at each target when the regression coefficient is largest. Then the spectral black sky albedo $\alpha(\lambda, \mathbf{target, time})$ is estimated from $\alpha_{AS}(\lambda, \mathbf{type})$ by applying the regression equation of the chosen soil type. Assuming the spectral variation of black-sky albedo $\partial\alpha/\partial\lambda$ is equal to that in BRDF parameters, MODIS BRDF parameters at seven bands are interpolated to wavelength band in interest using the spectral variation of BRDF parameters.

2.4 TOA radiance simulation over desert target

The TOA radiance is simulated using the 6S radiative transfer model (Vermote et al. 1997) for the given surface and atmospheric conditions. The spectral BRDF and albedo used for the specification of surface property are derived by interpolating spectral BRDF parameters at 7 MODIS bands into ones at each 2.5 nm between from 450 to 900 nm. Because the atmospheric contribution to the TOA radiance is much weaker than the surface contribution over the bright desert, the atmospheric conditions are specified with climatological values, i.e.: total precipitable water from NCEP, total ozone from OMI, and aerosol optical thickness at 500 nm of 0.1 representing the continental aerosol model.

3. Result

3.1 Algorithm test using reference satellite sensor

As surface characteristics of the desert are assumed to be accurate and stable over the time, the main error sources are from the instrumental radiometric noise and uncertainties associated with inaccurate atmospheric parameters (Govaerts and Clerici, 2004). The ratios of calculated radiance to observed value over the 16-day period at each target is averaged to reduce temporal random errors. Then ratio representing the target is obtained by taking an average of pixel-based ratios in the target under the assumption that the surface characterization errors are not correlated to each other -- see Fig. 2 for the MODIS case and Fig. 3 for the SeaWiFS case.

The temporally and spatially averaged ratios for MODIS (See Fig. 2) and SeaWiFS (See Fig. 3) show that the computed radiance errors are in 5% uncertainty range except June. The ratios during June are removed using quality flag provided with BRDF parameters. The 5% uncertainty range obtained from both MODIS and SeaWiFS measurements.

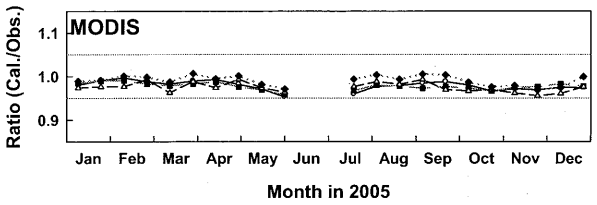

Fig. 2. The taget-averaged ratio of 6S model-calculated to the MODIS-observed value: Band 1 (open circle), band 2 (solid square), band3 (open triangle), band 4 (solid diamond). The red line represent ± 5% error.

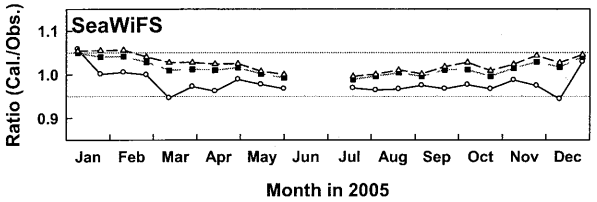

Fig. 3. Same as in Fig. 4 except for the SeaWiFS : Band 5 (open circle), band 6 (solid square), band7 (open triangle).

Table 1 shows the annual mean of spatially averaged ratio of calculated radiance to observed radiance at each MODIS and SeaWiFS bands. If we make the annual mean ratio, the relative bias between calculated and satellite-estimated values are within ±5% for all MODIS and SeaWiFS bands.

Table 1. The annual mean of spatial averaged ratio of calculated to observed radiances at each band.

Sensor	Band	Spectral range	Annual mean of Ratio
MODIS	Band 1	620 ~ 670 nm	0.971 ± 0.026
	Band 2	841 ~ 876 nm	0.970 ± 0.026
	Band 3	459 ~ 479 nm	0.975 ± 0.011
	Band 4	545 ~ 565 nm	0.988 ± 0.014
SeaWiFS	Band 5	545 ~ 565 nm	0.975 ± 0.032
	Band 6	660 ~ 680 nm	1.005 ± 0.038
	Band 7	745 ~ 785 nm	1.015 ± 0.038

3.2 MTST 1R calibration

The calibration coefficient of MTSAT 1R are retrieved using linear regression between simulated radiance and satellite observed digital count from November 2007 to June 2008. – see fig. 4. The black dashed line represents the relation between radiance and digital count using the original calibration coefficient as 0.4258. The red line represents the regression line using desert target. There are many scattered at the early March (81~88 Julian day) and late June (153~160 Julian day). These cases have some problem for cloud screening.

Linear regression equation is obtained by relating observed radiance to simulated radiance for desert target every 8 day, and the time series of slope (the calibration coefficient), intercept, R^2 and RMSE are showed in Fig. 5. The slope (the calibration coefficient) is in 5% uncertainty range (gray dashed line) except for late March and early June.

4. Conclusion

This paper describes a solar channel calibration algorithm for the visible channel calibration using bright desert target. Surface characterization was performed over the bright Australian desert by combining the MODIS BRDF parameter with the ASTER spectral database. Simulated radiances over the selected desert targets were compared with MODIS and SeaWiFS measured spectral radiances in order to examine the feasibility of the developed calibration method. Results suggest that the relative bias between calculated and satellite-estimated radiances are within ±5% uncertainly range when a large number of pixels are averaged over all selected desert targets, suggesting that the vicarious method developed in this study is suitable for calibrating the visible senor within the suggested error range. The calibration coefficient of MTSAT 1R is retrieved within 5% error range for the original calibration coefficient (0.4258).

ACKNOWLEDGEMENTS

This research has been supported by the Korean Geostationary Program (COMS) granted by the KMA, and by the BK21 Project of the Korean Government.

REFERENCES

Cosnefroy, H., M. Leroy, and X. Briottet, 1996. Selection and characterization of Saharan and Arabian desert sites for the calibration of optical satellite sensors. *Reomte Sensing Env.*, 58, pp. 101-114.

Govaerts, Y. M. and M. Clerici, 2004. Evaluation of radiative transfer simulations over bright desert calibration sites. *IEEE Trans. Geosci. Remote Sensing*, 42, pp. 176-187.

Lucht, W., C. B. Schaaf, and A. H. Strahler, 2000. An Algorithm for the Retrieval of Albedo from Space Using Semiempirical BRDF Models. *IEEE Trans. Geosci. Remote Sensing*, 38, pp. 977-998.

Mitchell, R. M., D. M. O'Brien, M. Edwards, C. C. Elsum, and R. D. Graetz, 1997. Selection and Initial characterization of bright calibration site in the Strzelecki desert, South Australia. *Canadian J. Remote Sensing*, 23, pp. 342-353.

Vermote, E. F., D. Tanre, J. L. Deuze, M. Herman, and J. J. Morcrette, 1997. Second simulation of the satellite signal in the solar spectrum, 6S: An overview. *IEEE Trans. Geosci. Remote Sensing*, 35, pp. 675-686.

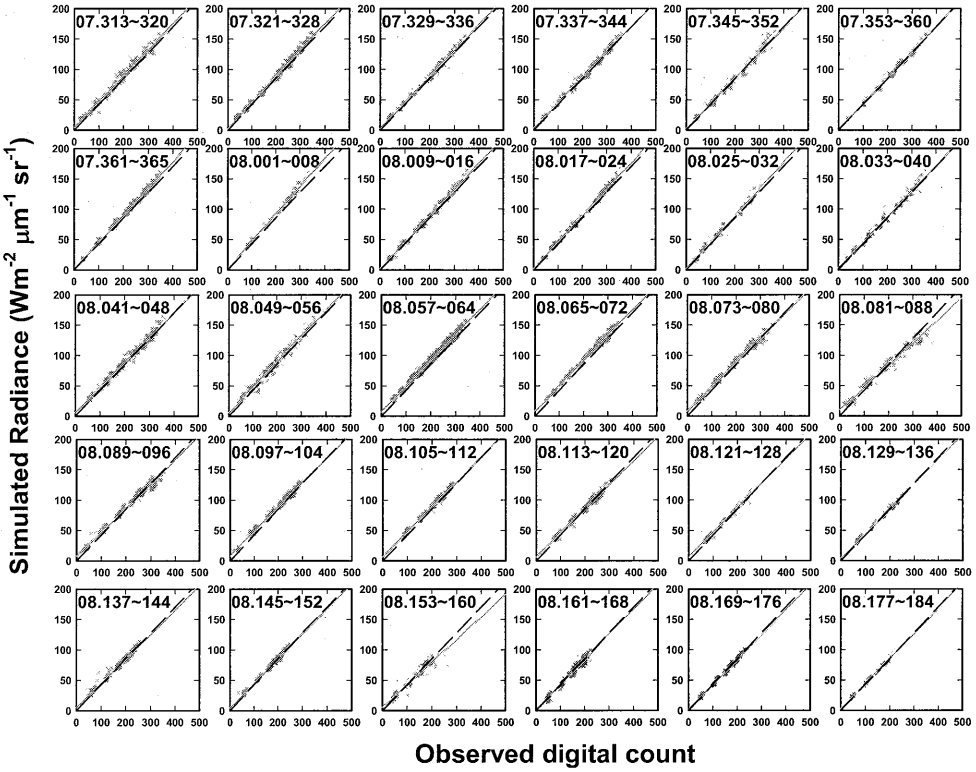

Fig. 4. The scatter plot of simulated TOA radiance at MTSAT 1R visible band and observed digital count.

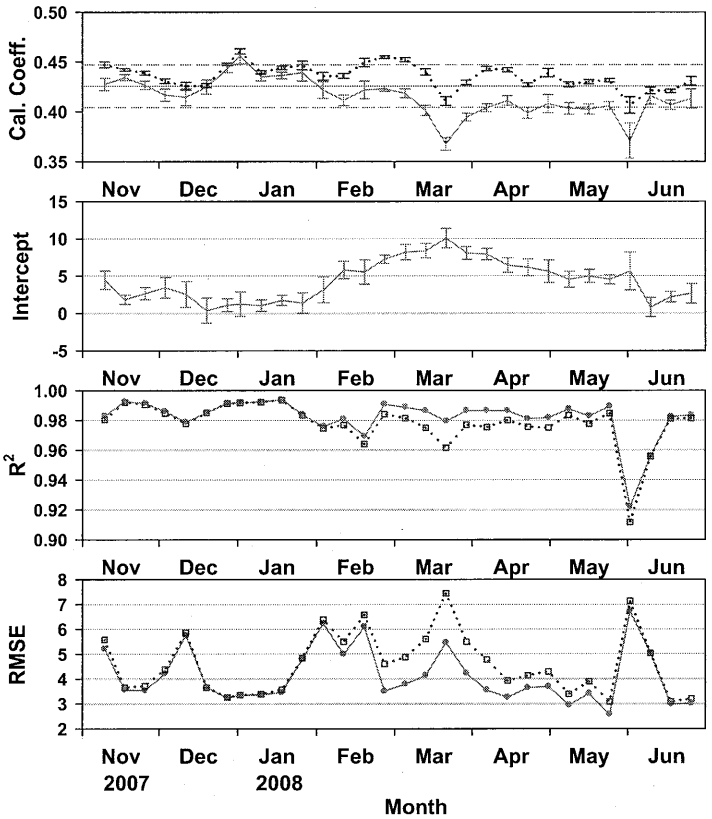

Fig. 5. Time series of calibration coefficient (slope), intercept, R^2, and RMSE for MTSAT 1R visible band using desert target. The red solid line represent statistics values for normal linear regression, and the blue dotted line for linear regression though the origin.

Geostationary Imager Visible Recalibration

Arata OKUYAMA[1], Toru HASHIMOTO[1*], Ryuichiro NAKAYAMA[1], Yoshihiko TAHARA[1], Toshiyuki KURINO[1], Hideaki TAKENAKA[2], Satoru FUKUDA[3], Takashi NAKAJIMA[4], Akiko HIGURASHI[5], Miho SEKIGUCHI[6], Tamio TAKAMURA[2], Teruyuki NAKAJIMA[3]

[1] *Meteorological Satellite Center, Japan Meteorological Agency*
3-235 Nakakiyoto, Kiyose, Tokyo 204-0012, Japan,okuyama.arata@met.kishou.go.jp
** Present Affiliation: Ministry of the Environment, Tokyo, Japan*
[2] *Center for Environmental Remote Sensing, Chiba University (CEReS)*
[3] *Center for Climate System Research, University of Tokyo (CCSR)*
[4] *Tokai University*
[5] *National Institute for Environmental Studies*
[6] *Tokyo University of Marine Science and Technology*

Abstract

The re-construction of the GMS-5 visible channel calibration table is examined. It is based on the comparison of satellite observation with reference. To obtain the reference, satellite radiance is simulated over various reference targets of clear sea area, clear land area and cloud top as dark, medium and bright references, respectively. Parameters necessary to compute the radiance are prepared independently from GMS-5 observations. The recalibrated visible table improves the GMS-5 data. That is confirmed from the improvement of aerosol and cloud products retrieved from the GMS-5 data.

Keywords **:** Visible channel, Vicarious calibration, Radiative transfer calculation, GMS-5, MTSAT-1R

1. Introduction

The visible channel of a satellite imager captures sunlight scattered and reflected by the surface and substance in atmosphere like cloud and aerosol. Visible observation data from the imager enables us to obtain climatological parameters such as optical characteristics of aerosol and cloud, solar radiation budget on the ground and surface albedo. For accurate researches using the visible observation data, the data should be well-calibrated.

A calibration table links observed raw digital counts from the imager to physical values such as temperature and reflectivity. The calibration table of the GMS-5 (Geostationary Meteorological Satellite - 5) visible channel was created at just after the launch and used during the GMS-5 operation period without update. However, the sensitivity of the channel had an aging degradation trend for its lifetime. Therefore, the estimation of accurate calibration table is expected by the climate researches.

2. Methods

2.1. Digital count to Voltage

GMS-5 visible data are preserved as digital count. The recalibration is examined to compute the relationship between digital count and physical value, radiance. Fig. 1 shows the relationship between the digital count and

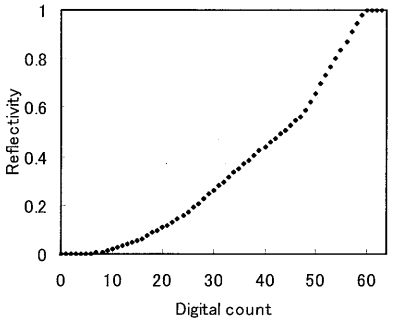

Fig.1. The relationship between digital count and

reflectivity used during the GMS-5 operation, which is expressed by quadratic-curve-like broken lines. It is difficult to re-construct the broken lines, directly. In order to ease the recalibration computation, digital count is converted to sensor output voltage, which is linear to radiance captured by the GMS-5 visible sensor.

2.2. Adjustment between Detectors

The GMS-5 visible channel consists of four detectors. Instead of constructing the calibration tables of all the detectors, the table of the detector number 2, which is the most stable one among four[5], is generated first. Then, the tables of other detectors are generated from the table of the detector number 2 associated with detector difference evaluated beforehand.

2.3. Reference Radiance on Targets

The re-construction of the calibration table is examined by comparing with reference radiance. To obtain the reference radiance, this study uses radiative transfer computation with independent data over secure targets for the reliable computation.

The radiative transfer code used is the latest version of the radiative transfer calculation package RSTAR[1], which is developed by Dr. NAKAJIMA at CCSR, Univ. of Tokyo. As for the targets, cloud-free sea surface, cloud-free land area, and uniform and flat cloud top are selected as a dark, medium, and bright reference, respectively.

a) Cloud-free sea target

The radiative transfer computation over the cloud-free sea target needs the parameters of atmospheric profile, sea surface wind speed, total ozone amount, aerosol optical thickness and angstrom index. The atmospheric profile and sea surface wind speed are obtained from JRA-25 (Japan Reanalysis – 25 years). The total ozone amount is the TOMS/Earthprobe data of NASA. Aerosol optical characteristic is retrieved from MODIS/Terra data by using REAP[2], which is an aerosol analysis package developed by Dr. HIGURASHI at the National Institute for Environmental Studies. REAP computes the aerosol optical thickness and Angstrom index on the ocean area from two channels of satellite data, visible and near infrared. The aerosol absorption and scattering parameters and particle radius distribution are non-absorption characteristics by Higrashi and Nakajima[3].

On the cloud-free sea target, important factors for the radiative transfer calculation are aerosol and sea surface wind speed. For the accurate simulation, open ocean areas far from land is selected, since there are much mineral particles such as air pollutant or yellow dust near the land. Areas where strong surface wind blows are also rejected from the target, since much whitecap makes sea surface reflectivity higher, and its accurate computation difficult. In addition, a sun glint area is rejected, since the whitecap effect appears stronger.

b) Cloud-free land target

The radiative transfer computation over the cloud-free land target needs the parameters of atmospheric profile, total ozone amount, aerosol optical thickness, angstrom index and Ground surface reflectivity. The atmospheric profile and total ozone amount are the same as those used for the cloud-free sea target. Aerosol optical characteristics are the ground observation data of BoM (Bureau of Meteorology). The ground surface reflectivity, which is the most effective factor for the computation, is estimated from the NASA MODIS BRDF (Bidirectional Reflectivity Distribution Function) product.

Aerosol is also an important factor for radiative transfer calculation. To estimate aerosol amount precisely, the land target is selected a point at which aerosol ground observation is operated. BoM has ground observation sites on the central part of the Australia continent, Alice Springs and Tennant Creek. These two sites are selected as land target.

c) Uniform cloud target

The radiative transfer computation over the uniform cloud target needs the parameters of atmospheric profile, sea surface wind speed, total ozone amount, cloud optical thickness and cloud particle effective radius. The atmospheric profile, sea surface wind speed and total ozone amount are the same as those used for the cloud-free sea target. The cloud optical characteristic is retrieved from MODIS/Terra data by using CAPCOM[4], which is an cloud analysis package developed by Dr. NAKAJIMA at Tokai Univ. CAPCOM computes the cloud optical thickness and cloud particle effective radius from three channels of satellite data, visible, near infrared and infrared.

On the cloud target, the characteristic of cloud particle is an important factor for the radiance computation. The uniform and flat clouds are selected. The cloud uniformity is checked by evaluating infrared channel observation. Thick clouds with optical thickness between 20 and 40 on the ocean are selected to reject thin transparent clouds and improve the radiative transfer calculation. Only water clouds are selected as well. Clouds within the sun glint area are rejected by the same reason as the sea surface target selection.

2.4. Evaluation Using MODIS

To evaluate the radiance computation, the radiance of Terra/MODIS channel 1 (0.66 μm) at the top of atmosphere is simulated and compared with actual observation. Fig. 2 shows the result. The difference between simulation and observation is about 1%. The reason of such small difference is that the comparison is dependent. The Channel 1 data is used to retrieve aerosol and cloud parameters. However, the validity of this radiance computation using the three different

targets, the atmospheric fields, surface parameters and the radiative transfer code RSTAR is recognized from Fig. 2.

3. Calculation and Validation

3.1. Reprocess of Calibration Table

a) The calibration table

Fig. 3 shows the example of radiance comparison between GMS-5 observation in voltage and computed radaince. The scatter plot shows a linear relationship. A new calibration table is generated from the regression line. The voltage corresponds to zero-radiance in Fig. 3 is about 0.032 [V], which is consistent to the voltage corresponds to the observation of deep space.

The differences of the new from old tables are shown in Fig. 4. The radiation values in the new table are increased from ones in the old table. The degradation of the sensor sensitivity is corrected by the new table.

b) Comparison with ISCCP coefficients

The GMS-5 calibration tables are computed monthly for the period from March 2000 to May 2003, during which MODIS data is available. Fig. 5 shows the temporal sequence of the coefficients in 2001 with those of ISCCP[6]. It is confirmed that the coefficients of new calibration table is more stable than the ones of ISCCP.

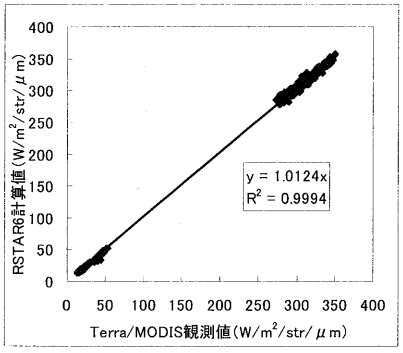

Fig.2. The comparison between simulated and observed radiance of Terra/MODIS channel 1. The slope of the regression line is almost 1 and the error is 1%.

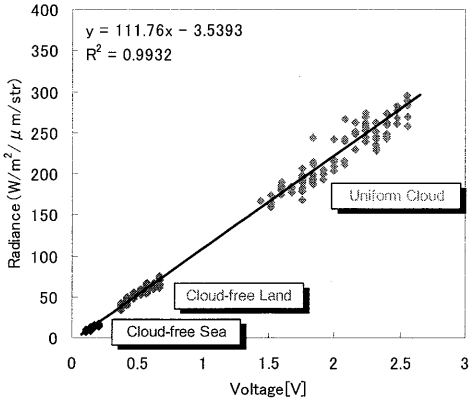

Fig.3. The comparison between the computation and the observed voltage. Cloud-free sea, cloud-free land and uniform cloud top targets are shown. The scatter plots show linear relationship, the regression line brings new calibration table. The data period is Apr.2001

3.2. Validation –Aerosol optical thickness –

MSC has generated aerosol product, which includes aerosol optical thickness, from geostationary meteorological satellite data since December 2002[6]. The aerosol product is retrieved from visible data on cloud-free sea surface. Therefore, the new calibration table in a low brightness region can be verified by regenerating the aerosol product.

JMA operates three aerosol ground observation sites in Japan. The aerosol products from the original and new GMS-5 calibration tables are compared with the ground aerosol observations. Fig. 6 shows the results. The mean differences from the ground observations are about –0.15 for the original table and –0.01 for the new table, respectively. It

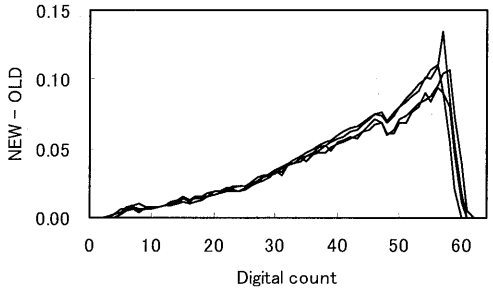

Fig.4. The difference of new and old table. The four lines in the figure are the difference value for each detector. The figure shows the value in the new table is higher than the one in the old one.

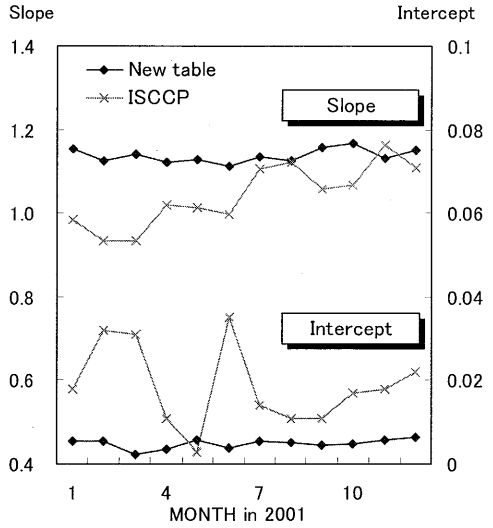

Fig.5. The history of the comparison between ISCCP coefficient [7] and the new calibration table, 2001.

is clear that the new calibration table improves the aerosol product.

3.3. Validation – Cloud optical thickness –

To validate the new calibration table in a high brightness region, cloud optical thickness is retrieved from GMS-5 visible data of both new and original tables. As reference, the same thickness is computed from Terra/MODIS data. For the calculation, CAPCOM is used. Fig. 7 shows the results. The mean difference of the GMS-5 cloud optical thickness to the Terra/MODIS one is about –9.95 for the original table and +1.25 for the new table, respectively. It is confirmed that the new calibration table is reasonable for the high brightness region.

4. Conclusion and Future plan

The methodology for vicarious calibration of visible channel is examined by using GMS-5 data. This method is based on the comparison of satellite observation with reference. To obtain the reference, satellite radiance is simulated over the targets of cloud-free sea area, cloud-free land area and uniform cloud top. The comparison shows a linear relationship between computed radiance and GMS-5 observation in voltage. Using the linear relationship, the new calibration table is generated. The new calibration table is validated by producing aerosol product and cloud optical thickness. It is confirmed that the new table improves the accuracy of the products.

The use of uniform ice cloud is under investigation. The new target is expected to increase reference data as the brightest target.

This visible calibration method is expected to be applicable to MTSAT-1R visible calibration. From a preliminary experiment, a linear relationship between computed radiance and the MTSAT-1R observation is obtained as well as GMS-5.

Acknowledgements

The authors are grateful to the Dr. B.Forgan in BoM for providing the aerosol ground observation data and for supporting their processing.

References

1) Nakajima, T., and M. Tanaka, 1988: Algorithms for radiative intensity calculations in moderately thick atmospheres using a truncation approximation, J.Quant.Spec.Rad. Trans.,40, 51-69.

2) Higurashi, A., and T. Nakajima, 1999: Development of a Two Channel Aerosol Retrieval Algorithm on Global Scale Using NOAA / AVHRR., J. Atmos. Sci., 56, 924-941.

3) Higurashi, A., and T. Nakajima, 2002: Detection of aerosol types over the East China sea near Japan from four-channel satellite data., Geophys. Res. Lett., 29, 1836-1839.

4) Nakajima, T.Y., and T. Nakajima, 1995: Wide area determination of cloud microphysical properties from NOAA AVHRR measurement for FIRE and ASTEX region., J. Atmos. Sci., 52, 4043-4059.

5) Kurihara, Shigehisa and Masami Tokuno, 2001: The Status of Calibration of VISSR on board GMS-5. Meteorological Satellite Center Technical Note, No. 38, 53-68.

6) ISCCP web site (http://isccp.giss.nasa.gov/).

7) Hashimoto, Toru, 2006: Aerosol Optical Thickness. Meteorological Satellite Center Technical Note Special issue, 121-124

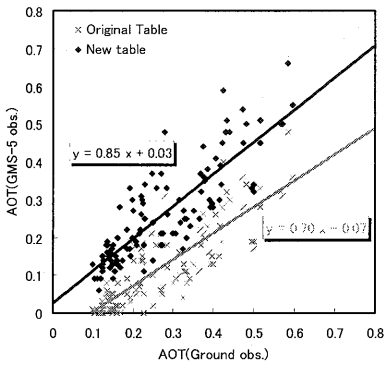

Fig.6. The scatter plot of MSC aerosol product and ground observation. The "x" mark shows the product based on original calibration table, and the diamond mark shows the product based on the new calibration table.

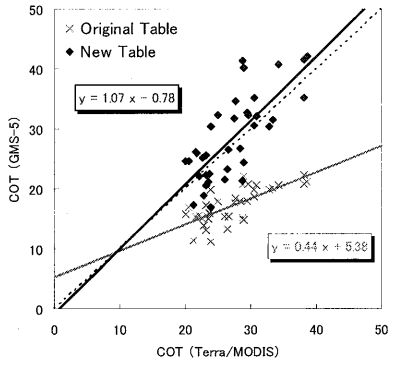

Fig.7. The scatter plot of cloud optical thickness. (COT) The retrieved COT from GMS-5 and Terra/MODIS are compared. The "x" mark shows the COT based on original table, and the diamond mark shows the COT based on the new table.

MTSAT-1R Infrared Intercalibration on GSICS

Yoshihiko Tahara[1], Koji Kato[1], Arata Okuyama[1], Ryuichiro Nakayama[1], Toshiyuki Kurino[1], GSICS Research Working Group (chaired by Fred Wu)[2]

[1] *Meteorological Satellite Center, Japan Meteorological Agency*

3-235 Nakakiyoto, Kiyose, Tokyo 204-0012, Japan, y-tahara@met.kishou.go.jp

[2] *http://www.star.nesdis.noaa.gov/smcd/spb/calibration/icvs/GSICS/*

Abstract

MTSAT-1R infrared intercalibration with the hyper sounder AIRS and IASI is operated at MSC. Comparison methodology is on the basis of algorithm determined in GSICS, one of the components of WMO. To match-up data of two sensors, observation time difference, satellite zenith angle difference and environment uniformity are checked. To adjust spectral response difference, a super channel is generated from hyper sounder to have the same SRF as a MTSAT-1R infrared channel. In case that there are spectral gaps or failed channels in hyper sounder, their radiances are estimated with good accuracy by using observations and beforehand simulated radiances of hyper sounder. The intercalibration is examined once a day, and results are posted on the MSC webpage (http://mscweb.kishou.go.jp/monitoring/calibration.htm).

Keywords **:** GSICS, Intercalibration, MTSAT-1R

1. Introduction

The Meteorological Satellite Center (MSC) in the Japan Meteorological Agency (JMA) operationally compares Multi-functional Transport Satellite 1R (MTSAT-1R) infrared data with those from high-spectral-resolution sounders (hyper sounder), such as the AIRS equipment on the AQUA satellite and the IASI instrument on the Metop-A satellite.

Intercalibration methodology is on the basis of algorithm determined in the Global Satellite Intercalibration System (GSICS)[3], which is one of the space components of the World Meteorological Organization (WMO) and established to provide users with high-quality and inter-calibrated measurements from operational satellites.

2. Collocation

To compare observations between the MTSAT-1R imager and hyper sounder, the intercalibration collects observing information simultaneously measured by the different sensors. The collocation examines to find the observations of MTSAT-1R and a hyper sounder satisfying conditions with respect to observing time difference, satellite zenith angle difference and environment uniformity. An average value for MTSAT-1R radiances over a box of 3 x 3 pixels (FOV) is compared with a sounder radiance, since the footprint size of AIRS and IASI is about 12 km at nadir whereas that of MTSAT-1R is 4 km.

- Observation time difference check

Difference of observing times between MTSAT-1R t_{mtsat} and hyper sounder $t_{sounder}$ is evaluated pixel by pixel using

$$\left|t_{mtsat} - t_{sounder}\right| < dt_{\max},$$

- Satellite zenith angle difference check

Difference of satellite zenith angles between MTSAT-1R SZA_{mtsat} and hyper sounder $SZA_{sounder}$ is evaluated using

$$\left|\cos(SZA_{sounder}) / \cos(SZA_{mtsat}) - 1\right| < MaxSZA$$

- Environment uniformity check

To mitigate differences between the observation conditions of the two sensors due to time difference, optical path difference, navigation error, etc., only measurements over uniform scenes are selected and compared. In this check, the uniformity of MTSAT radiance data I_{mtsat} over a box of 9 x 9 pixels (ENV) is tested using

$$\underset{ENV}{STDV}(I_{mtat}) < MaxSTDV$$

- Normality check

The MTSAT radiance data in FOV should represent the data in ENV. The normality of the MTSAT radiance data in FOV is checked using

$$\frac{9 \times \left| \underset{FOV}{AVE}(I_{mtsat}) - \underset{ENV}{AVE}(I_{mtsat}) \right|}{\underset{ENV}{STDV}(I_{mtsat})} < Gaussian$$

Table 1 shows criteria used in the intercalibration between MTSAT-1R and AIRS/IASI. The variables differ according to weather conditions. If the brightness temperature of MTSAT-1R channel IR1 (10.8 μm) is higher than 275 K, the scene condition is categorized as clear. Otherwise, it is

Table 1: Criteria for collocation between MTSAT-1R and AIRS/IASI

MTSAT-1R Channel	Condition	dt_{max} (min)	*MaxSZA*	*MaxSTDV* (mW/m^2.sr.cm^{-1})	*Gaussian*
IR1 (10.8 μm)	Clear	5	0.01	1.65	2
	Cloudy	5	0.03	3.31	2
IR2 (12.0 μm)	Clear	5	0.01	1.82	2
	Cloudy	5	0.03	3.64	2
IR3 (6.8 μm)	Clear	5	0.01	0.311	1
	Cloudy				
IR4 (3.8 μm)	Clear	5	0.01	0.0151	2
	Cloudy	5	0.03	0.0302	2

categorized as cloudy.

3. Spectral Adjustment

To compare observed radiances between MTSAT-1R imager and hyper sounder, the spectral responses of the two sensors should be adjusted. This intercalibration introduces a new spectral adjustment approach consisting of two techniques.

3.1. Super Channel

A super channel is generated by the constraint method[1] accumulating the channels of hyper sounder so that the spectral response of the super channel is close to that of a simulating broadband channel like a MTSAT-1R channel.

The radiance of the super channel I_s is computed by

$$I_s = \sum_i w_i I_i \Big/ \sum_i w_i , \qquad (1)$$

where I_i is the radiance of the hyper sounder channel i. The weights $\{w_i\}$ are computed by solving an optimization problem

$$\min J(w_i) = \int \left(S_b - \sum_i w_i S_i \right)^2 dv ,$$

where S_b and S_i are the spectral response functions (SRF) of the broadband channel and the hyper sounder channel i respectively, and v is wavelength (or wavenumber).

3.2. Spectral compensation

AIRS covers the spectral observing range from 650 to 2665 cm^{-1} including some spectral gaps between the AIRS detector modules. In addition, there are some failed channels. IASI covers the spectral observing range from 645 to 2760 cm^{-1} without gap and failed channel. However, IASI does not cover the spectral band of the MTSAT-1R channel IR4 (3.8 μm) fully as well as AIRS. These spectral gaps, shortage and failed channels yield the spectral difference of the super channel from the simulating broadband channel, and cause the degradation of the intercalibration. To compensate the spectral difference, the radiances of the spectral gaps, shortage and failed channels are estimated[2] from valid AIRS observations.

In advance of the compensation, virtual channels named *gap channels* are introduced to fill the spectral gaps and shortage. The gap channels are defined to be similar to the channels of hyper sounder having similar bandwidth and spectral resolution. Using the gap channels in addition to hyper sounder channels in (1), the SRF of the super channel can be almost equivalent to that of the broadband channel, and the spectral compensation problem is transformed to a problem to estimate radiances of the gap and failed channels.

The radiances of the gap and failed channels are estimated from the observed radiances of hyper sounder by referring to the simulated radiances of the hyper sounder and the gap channels with respect to eight atmospheric model profiles of

- U.S. standard,
- U.S. standard with cloud at 500 hPa,
- U.S. standard with cloud at 200 hPa,
- Tropic,
- Tropic with cloud at 500 hPa,
- Tropic with cloud at 200 hPa,
- Mid-latitude summer,
- Mid-latitude winter.

An equation to estimate the radiance of the hyper sounder and gap channels i is defined by

$$\log I_i^{est} = c_0 + \sum_k c_k \log I_{i,k}^{cal} , \qquad (2)$$

where $I_{i,k}^{cal}$ is the simulated radiance of the channel i and the model profile k. Logarithm radiance is introduce to (2) in order to increase estimation accuracy and avoid negative radiance estimated. c_0 and c_k are coefficients computed by solving a least square problem applying validly observed radiances of hyper sounder $I_{i,k}^{obs}$ to (2) in place of I_i^{est},

$$\min E(c_k) = \sum_{i=exist(I_i^{obs})} \left\{ \log I_i^{obs} - \left(c_0 + \sum_k c_k \log I_{i,k}^{cal} \right) \right\}^2 .$$

It might be possible to apply all observations of hyper sounder to (2) to estimate all failed and gap channels at once. However, it causes large estimation error practically. In the intercalibration computation, (2) is generated for each

broadband channel and each observing point.

The benefit of this spectral compensation method is not to use radiative transfer computation in intercalibration operation. That prevents from introducing biases contained in radiative transfer code and atmospheric state fields into super channel radiance. In addition, the method is applicable to cloudy weather conditions, where accurate radiative transfer computation is very difficult.

3.3. Validation

Figure 1 (a) shows the SRFs of MTSAT-1R channel IR3 (6.8 μm) (red lines) and AIRS channels (green lines) including failed channels (purple lines) and gap channels (orange lines). Figure 1 (b) shows the SRF of an AIRS super channel (green lines) to simulate that of IR3 (red lines), and Figure 1 (c) shows the weights of the super channel w_i. The sequence of the weights shows some variation. However, the SRF of the AIRS super channel well corresponds to that of IR3. Simulated brightness temperature differences between the super channel and IR3 are less than 0.01 K with respect to the atmospheric model profiles in Section 3.2.

Figure 2 shows an example of estimated radiances (black lines) by (2). Even though the sequence of the AIRS observed radiances (red boxes) varies widely due to the strong and diverse water vapor absorption and emission, the estimated radiances show very good agreement with the AIRS observations.

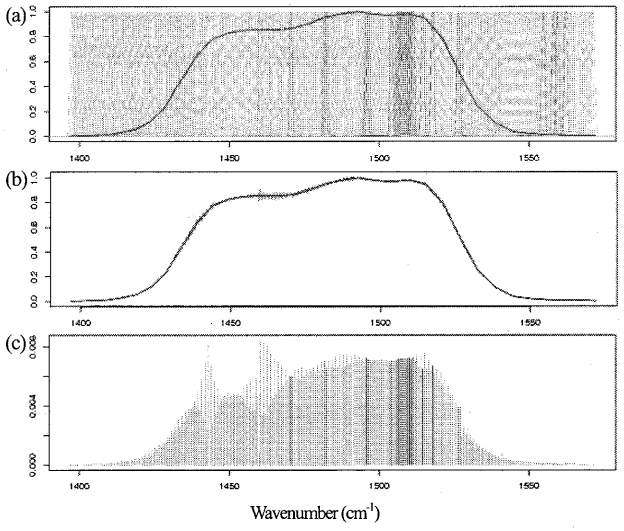

Figure 1 (a): Spectral response functions (SRF) of MTSAT-1R channel IR3 (3.8 μm) (red), and AIRS channels (green) including failed channels (purple) and gap channels (orange). (b): SRF of an AIRS super channel (green) to simulate IR3 (red). (c): Weights for the AIRS channels to generate the super channel.

To evaluate the impact of the AIRS failed channels and spectral gaps on the radiance computation of the AIRS super channel, IASI super channel is used to simulate the AIRS super channel. Since IASI fully covers the IR3 spectral band, the super channel consisting of only IASI channels S^{all} can be assumed to be true neglecting IASI observation error. Then, two IASI super channels are evaluated,

S^{gap}: The same as S^{all}, but excluding IASI channels corresponding to the AIRS failed and gap channels,

S^{est}: The same as S^{all}, but spectral compensation applied to the IASI channels excluded in S^{gap}.

Figure 3 shows SRF of the super channel S^{gap} (green lines). Due to wide spectral gaps and some failed channels of AIRS, the SRF shows spectral lack and departure from the simulating IR3 SRF (red lines).

Figure 4 (a) shows the brightness temperature residuals of the super channel S^{gap} from S^{all}. The residuals are originated from the SRF differences shown in Figure 3. Without the spectral compensation, systematic bias is anticipated in the computation of the AIRS super channel. The range of the brightness temperature residuals is about –0.5 K to 0.3 K, and root mean square (RMS) is 0.103 K. The residuals may prevent from accurate intercalibration analysis using AIRS.

Figure 4 (b) shows the same residuals as (a), but the

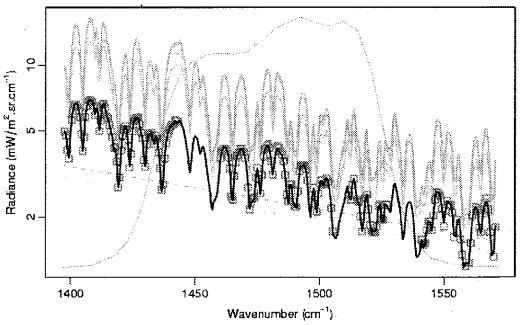

Figure 2: Example of AIRS observed radiances (red boxes), estimated ones (black lines) and simulated ones (colored lines) with SRF of MTSAT-1R channel IR3 (3.8 μm) (gray lines)

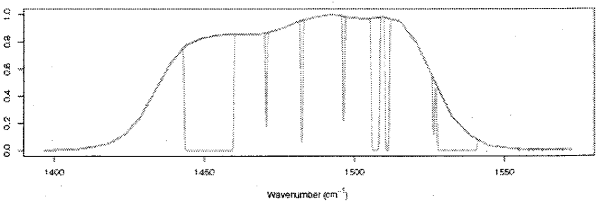

Figure 3: SRFs of IASI super channel for MTSAT-1R channel IR3 (3.8 μm) (red) and the same channel but excluding IASI channels corresponding to AIRS failed and gap channels (green).

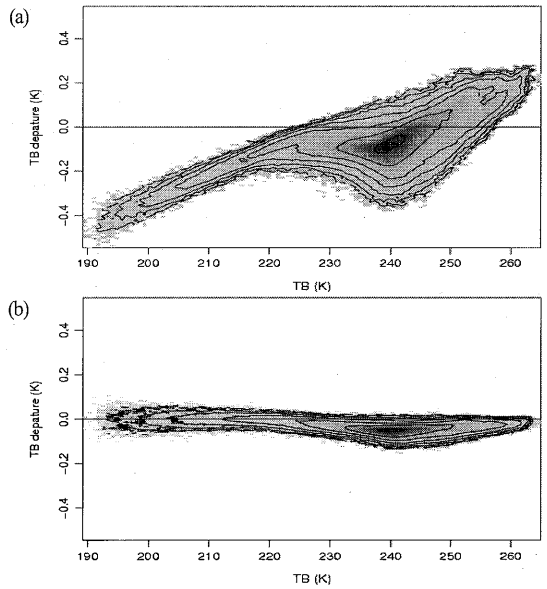

Figure 4 (a): Density plot of brightness temperature residuals of an IASI super channel for MTSAT-1R channel IR3 (3.8 μm) excluding IASI channels corresponding to the AIRS failed and gap channels from the same super channel but using all IASI channels. (b): The same density plot as (a), but the residuals of an IASI super channel using estimated radiances for the excluded IASI channels. One month IASI data in August 2008 over the west Pacific region are used.

brightness temperature residuals of the super channel S^{est} from S^{all}. The impact of the compensation for the AIRS failed and gap channels on super channel radiance can be evaluated. The residuals are significantly decreased from Figure 4 (a). The range is about –0.1 K to 0.1 K, and RMS is 0.048 K. Moreover, the trend of the residuals observed in Figure 4 (a) is reduced. The results clearly show that the spectral compensation improves the intercalibration using AIRS.

4. MTSAT-1R Intercalibration System

The intercalibration between MTSAT-1R and AIRS/IASI is conducted once a day at MSC in operation. Analysis results are posted on the MSC Webpage[4] (Figure 5). Currently, outcomes are brightness temperature differences at reference temperatures, regression coefficients between MTSAT-1R and AIRS/IASI radiances and those between MTSAT-1R digital count and AIRS/IASI radiance. These parameters are monitored in temporal sequence charts, scatterplot charts and text tables.

This intercalibration system is in an early phase. It is planned to be updated associated with future GSICS discussion. Furthermore, the other operational centers of geostationary satellites, such as the European Organization for the Exploitation of Meteorological Satellites

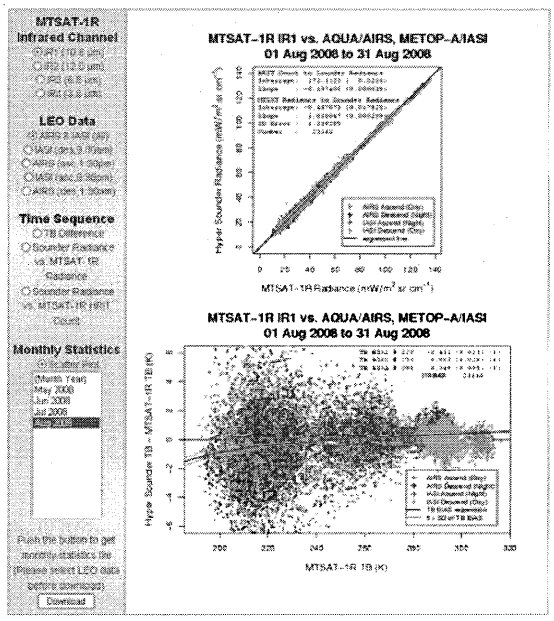

Figure 5: Webpage of MTSAT-1R infrared intercalibration with AIRS and IASI.

(EUMETSAT), the National Oceanic and Atmospheric Administration (NOAA) / the National Environmental Satellite, Data and Information Service (NESDIS) in the United States and the National Satellite Meteorological Center (NSMC) / the China Meteorological Administration (CMA), will operate the intercalibration of their own geostationary satellites with the hyper sounders. Those GSICS results are expected to contribute to the development of products from global geostationary satellite data.

References

1) Tahara, Yoshihiko, 2008: New Approach to Intercalibration Using High Spectral Resolution Sounder. Meteorological Satellite Center Technical Note, No. 50, 1-14.

2) Tahara, Yoshihiko and Koji Kato, 2009: New Spectral Compensation Method for Intercalibration with High Spectral Resolution Sounder. Meteorological Satellite Center Technical Note, No. 52 (planed to be published)

Webpages

3) GSICS Coordination Center (GCC), http://www.star.nesdis.noaa.gov/smcd/spb/calibration/icvs/GSICS/index.php

4) MSC: Monitoring of MTSAT-1R Navigation and Calibration, http://mscweb.kishou.go.jp/monitoring/calibration.htm

Geostationary Satellite Re-Analysis
-Aerosol Retrieval-

Satoru Fukuda[1], Teruyuki Nakajima[1], Hideaki Takenaka[2], Tamio Takamura[2], Arata Okuyama[3], Toru Hashimoto[3]*, Ryuichiro Nakayama[3], Yoshihiko Tahara[3], Toshiyuki Kurino[3], Takashi Y. Nakajima[4], Akiko Higurashi[5], and Miho Sekiguchi[6]

[1]Center for Climate System Research, The University of Tokyo,
5-1-5 Kashiwanoha, Kashiwa-city, Chiba, 277-8568, JAPAN,
satoru@ccsr.u-tokyo.ac.jp, teruyuki@ccsr.u-tokyo.ac.jp
[2]Center for Environmental Remote Sensing, Chiba University,
1-33 Yayoi-cho, Inage-ku, Chiba, 263-8522, JAPAN,
takenaka_ceres@graduate.chiba-u.jp, takamura@faculty.chiba-u.jp
[3]Meteorologiccal Satellite Center, Japan Meteorological Agency,
3-235 Nakakiyoto, Kiyose-city, Tokyo, 204-0012, JAPAN,
okuyama.arata@met.kishou.go.jp, r-nakayama@met.kishou.go.jp,
y-tahara@met.kishou.go.jp, tkurino@met.kishou.go.jp
**Present Affiliation: Ministry of the Environment*
Godochosha No.5, 1-2-2, Kasumigaseki, Chiyoda-ku, Tokyo 100-8975, JAPAN
TORU_HASHIMOTO@env.go.jp
[4]Tokai University,
2-28-4 Tomigaya, Shibuya-ku, Tokyo, 151-0063, JAPAN,
nkjm@yoyogi.ycc.u-tokai.ac.jp
[5]National Institute for Environmental Studies,
16-2 Onogawa, Tsukuba-city, Ibaraki, 305-8506, JAPAN,
hakiko@nies.go.jp
[6]Tokyo University of Marine Science and Technology,
2-1-6 Etchujima, Koto-ku, Tokyo, 135-8533, JAPAN,
miho@e.kaiyodai.ac.jp

Abstract

Under the project of R-VISSR, Aerosol Optical Thickness from GMS-5/R-VISSR in 2001 is retrieved. As a Angstrom Exponent, Monthly mean values of MODIS Level 3 product are used. In this study, we use both spherical and nonspherical model as aerosols' shape. The probability density function of aerosol optical thickness is quite influenced by the assumption of aerosols' shape. The seasonal variation of aerosol optical thickness derived by this study is consistent with that of MODIS.

Keywords **:** GMS-5, R-VISSR, aerosol, remote sensing

1. Introduction

Aerosols have a significant impact on earth's radiation budget, but the uncertainty is still large[1)]. GMS-5 (Himawari 5) is a geostationary meteorological satellite, which was launched in 1995, instrumented 4 channels from visible to thermal infrared, and its observational areas are East Asia, the Western Pacific, and Oceania. Generally speaking, geostationary satellites have an advantage of its high time resolution compared with polar satellites, but they also have disadvantages such as fewer available channels, lower space resolution, and limited observational area. East Asia, which is one of observed areas of GMS-5, is an interesting region from a view of aerosols, because it is highly influenced by anthropogenic or dust aerosol. It is considered possible that we can follow the time developing process of aerosols in East Asia by using of the merit of GMS-5. Because the signal of aerosols is not strong, it is necessary that an accurate calibration, when you want to discuss the aerosols' effect

quantitatively. The vicalious calibration of the Visible and Infrared Spin-Scan Radiometer (VISSR) onboard GMS-5 is done by Meteorological Satellite Center (MSC) and other institutes, so it is expected that more accurate aerosol remote sensing.

2. Methodology

We assume bi-modal lognormal distribution function as a size distribution function:

$$\frac{dV}{d\ln r} = \sum_{n=1}^{2} c_n \exp\left\{-\frac{1}{2}\left[\frac{\ln(r/r_{m,n})}{\ln S_n}\right]^2\right\}$$

where, r_1=0.17μm, r_2=3.44μm, s_1=1.3, s_2=2.75 [2)3)]
We perform radiative transfer calculation by RSTAR[4)5)] and construct Look Up Tables (LUTs). We retrieve aerosol optical thickness (τ) by using Light-REAP, which is a modified version of REAP[2)]. The Algorithm flow chart of this study is showed in Figure 1.

GMS-5 has just one channel in visible region, so we can only get τ. It is impossible to estimate α, which is an index of aerosol size. α is defined as follows[2)]

$$\alpha = -\frac{d(\ln\tau)}{d(\ln\lambda)}$$

In this study, we use monthly mean value of α produced by MODIS Level 3 product. Figure 2 shows examples of monthly mean α. Generally speaking, α has small value near land area, and large value far from land.

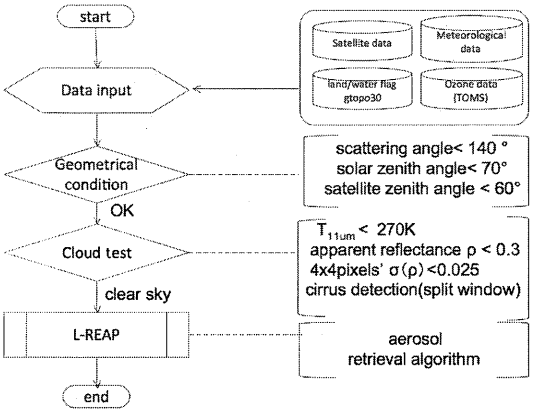

Figure 1: Algorithm flow chart

Figure 3 shows an example of aerosol optical thickness retrieval. In this figure, you can see large τ area around Yellow Sea and East China Sea.

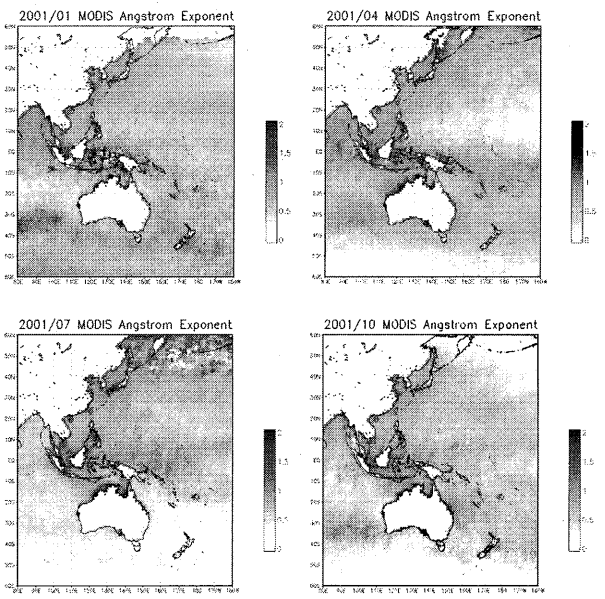

Figure 2: Monthly mean Angstrom exponent by MODIS Level 3 product on January (upper left), April (upper right), July (bottom left), and October (bottom right) in 2001.

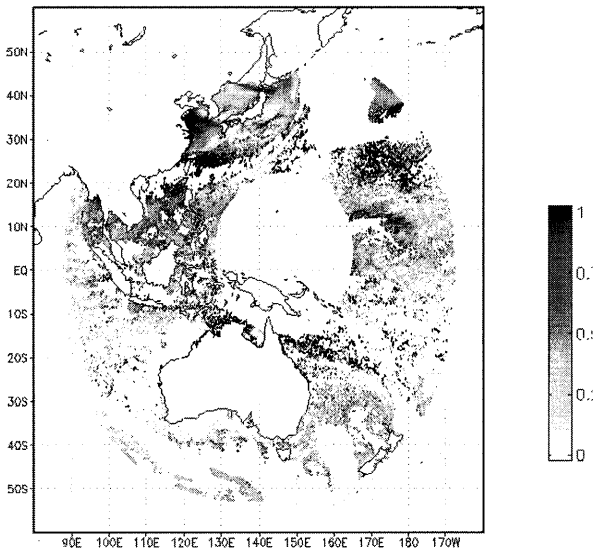

Figure 3: Aerosol optical Thickness at 500nm estimated by GMS-5/R- VISSR on 13 April 2001.

3. Influence of nonsphericity

As aerosols' shape, both spherical model and nonspherical model are used. We used Pollack and Cuzzi's semi-empirical model[6)] as nonspherical aerosol model. The nonspherical parameter of Pollack and Cuzzi are set as (x0, G, r) =(7.0, 10.0 , 1.1) [3)6)7)]. Figure 5 shows the histogram of aerosol optical thickness. X-axis mean aerosol optical thickness, and Y-axis mean probability density function. Monthly mean τ of each time (from 00UTC to 06UTC) in April 2001 are shown. Upper figure

of figure 5 shows the case of spherical model, and down figure shows the case of nonspherical model. In nonspherical case, the shape of graph of each time is relatively close. But, in spherical case, the shape of graph depends on time. We can see the decrease of τ in the noon. The assumption of the shape of aerosol is important when we want to see one day's time development of τ.

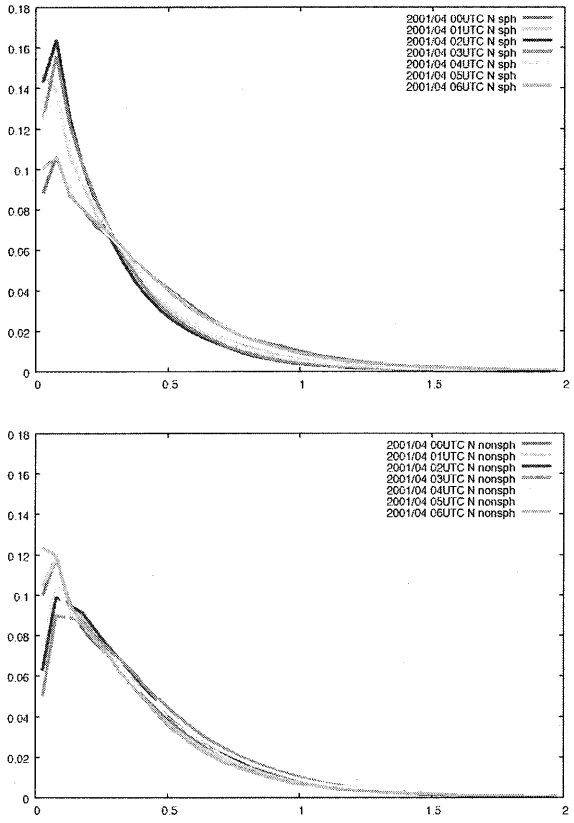

Figure 5: Histograms of τ_a. Spherical model (up) and nonspherical model (bottom) are used. X- axis are τ, and Y-axis are probability density function. We use τ value in northern part of R-VISSR area (N60-EQ, E80-W20)

4. Seasonal variation and comparison with MODIS product

Figure 6 shows monthly average of τ at 500nm by GMS-5/R-VISSR in January, April, July, and October. Figure 7 shows zonal means of τ. Generally speaking, southern hemisphere has smaller value of τ compared with northern hemisphere. Zonal mean of Aerosol Optical Thickness in southern hemisphere is about 0.1~0.2. Especially speaking, t has a very small value in July over the South Pacific Ocean and the Indian Ocean. In April, you can see a large τ in the North Pacific Ocean. This is thought to be the influence of yellow sand events. In April, zonal mean of τ value is about 0.4~0.5 around N40.

Figure 8 shows monthly mean of τ by MODIS Level 3 product. Roughly speaking, the pattern of τ derived by GMS-5/R-VISSR seems to be consistent with MODIS product. Our products have more missing pixels around the equator compared with the product of MODIS. This is because the differences of cloud detection method and the space resolution. MODIS can do detailed cloud detection . Sampling rate is very different between these products. GMS-5 did much more observations than MOIDS in one day. This difference can make some influence for the products.

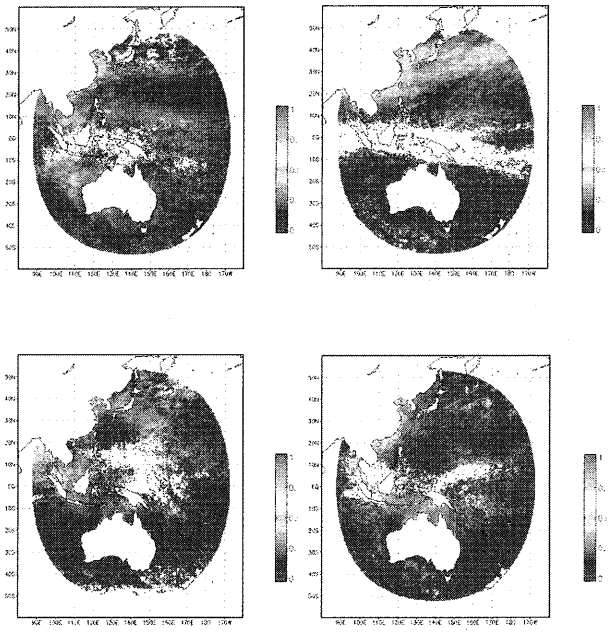

Figure 6: Monthly mean Aerosol Optical Thickness estimated by GMS-5/R-VISSR on January (upper left), April (upper right), July (bottom left), and October (bottom right) in 2001.

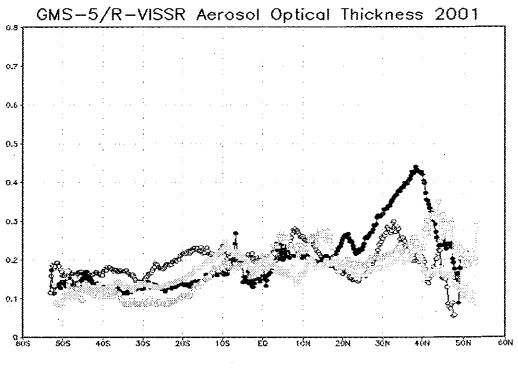

Figure 7: Zonal mean of Aerosol Optical Thickness estimated by GMS-5/R-VISSR. White, black, green, and yellow line mean January, April, July, and October in 2001 respectively.

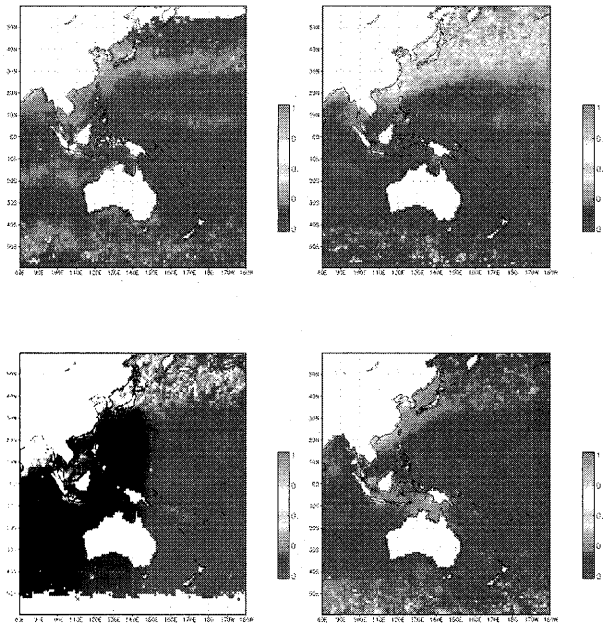

Figure 8: Monthly mean Aerosol Optical Thickness by MODIS Level 3 product on January (upper left), April (upper right), July (bottom left), and October (bottom right) in 2001.

References

1) Intergovernmental Panel on Climate Change (IPCC), Climate Change 2007: The Physical Science Basis, edited by S. Solomon et al., Cambridge Univ. Press, 2007.

2) A. Higurashi and T. Nakajima, 1999: Development of a Two Channel Aerosol Retrieval Algorithm on Global Scale Using NOAA/AVHRR. J. Atmos. Sci., 56, 924- 941.

3) K. Masuda, Y. Mano, H. Ishimoto, M. Tokuno, Y. Yoshizaki, and N. Okawara, 2002: Assessment of the nonsphericity of mineral dust from geostationary satellite measurements, Rem. Sens. Environ., 82, 238-247.

4) T. Nakajima, and M. Tanaka, 1986: Matrix formulations for the transfer of solar radiation in a plane-parallel scattering atmosphere. J. Quant. Spectrosc. Radiat. Transfer, 35, 13-21.

5) T. Nakajima, and M. Tanaka, 1988: Algorithms for radiative intensity calculations in moderately thick atmospheres using a truncation approximation. J. Quant. Spectrosc. Radiat. Transfer, 40, 51-69.

6) J. B. Pollack, and J. N. Cuzzi, 1980: Scattering by nonspherical particles of size comparable to a wavelength: a new semi-empirical theory and its application to tropospheric aerosols, J. Atmos. Sci., 37, 868-881.

7) T. Nakajima, M. Tanaka, M. Yamano, M. Shiobara, K. Arao, and Y. Nakanishi , 1989: Aerosol optical characteristics in the yellow sand events observed in May, 1982 at Nagasaki-Part II Models, J. Meteorol. Soc. Japan, 67, 279-291.

Geostationary Satellite Re-Analysis
-Estimation of radiation budget-

Hideaki Takenaka[1], Satoru Fukuda[2], Arata Okuyama[3], Toru Hashimoto[3*], Ryuichiro Nakayama[3], Yoshihiko Tahara[3], Toshiyuki Kurino[3], Takashi Y. Nakajima[4], Akiko Higurashi[5], Miho Sekiguchi[6], Tamio Takamura[1], and Teruyuki Nakajima[2]

1. Center for Environmental Remote Sensing, Chiba University
2. Center for Climate System Research, The University of Tokyo
3. Meteorological Satellite Center, Japan Meteorological Agency
**Present Affiliation: Ministry of the Environment*
4. Department of Network and Computer Engineering, Tokai University
5. National Institute for Environmental Studies, Japan
6. Tokyo University of Marine Science and Technology

Abstract

In this study, we analyze Refined - Visible and Infrared Spin-Scan Radiometer (R-VISSR) data set. An accurate calibrated data propose the better accuracy for analysis of cloud and radiation budget. Therefore, in Asian Atmospheric Particle Environmental Change Studies (APEX) - E2 period, diffuse component and aerosol optical thickness showed the pattern that looked like well. Thus, analysis of 12 months of 2001 was executed that the results indicate a feature trend of the direct and the diffuse component of downward solar radiation from East Asia to North Pacific Ocean. Moreover, contrast is clear between East Asia and South side of Australia in direct and diffuse components.

Keywords **:** Geostationary satellite, GMS-5/VISSR, Solar radiation, Radiation budget

1. Introduction

Clouds has an important role to be cool the Earth by reflecting solar radiation and also to keep it warm by absorbing and emitting terrestrial radiation. These effect are important in the energy balance at the surface and the Top of the Atmosphere (TOA) and connected into the Earth system through the complicated climate feedback processes. Thus, understandings of the influence of the clouds on radiation budget by an accurate observations have been requested. Wetherald and Manabe discussed the cloud feedback process using a General Circulation Model (GCM) [Wetherald and Manabe, 1988][1]. Tsushima and Manabe tested the cloud feedback sensitivity to global mean surface temperature based on explicit definition of feedback processes. GCM has strong sensitivity for global mean surface temperature although analysis of sensitivity based on observations are negligible [Tsushima and Manabe, 2001][2]. Cloud modeling is a big uncertainty for the climate model and long term analysis for the global change would be estimated. It is important to evaluate the influence of cloud for Earth's radiation budget based on observations.

Geostationary Meteorological Satellite - 5/Visible and Infrared Spin-Scan Radiometer (GMS-5/VISSR) observes every hour on geostationary orbit. The optical characteristics of particles (aerosols and clouds) can be retrieved from the consecutive observational data of seven years. In this study, we newly analyzed Refined

- VISSR (R-VISSR) data set. The R-VISSR data set promote the better calibration quality for atmospheric analysis. An accurate calibrated data propose the better accuracy for analysis of cloud and radiation budget. In this study, we report the estimated solar fluxes and discuss the influence of cloud for solar fluxes.

2. Data set

The VISSR sensor has four channels of visible (VIS) and infrared (IR). Three IR channels are calibrated simply by equipped Blackbody. The VIS channel is calibrated by vicarious calibration using the Terra satellite equipped Moderate Resolution Imaging Spectroradiometer (Terra/MODIS) data. The vicarious calibration with sea surface, land surface and clouds provides an accurate dataset that is validated from ground observations. Therefore, Refined - VISSR (R-VISSR) data set is applied to retrieve aerosols and the clouds particles optical characteristics for analysis of radiation budget. An atmospheric profiles data are used Japanease 25-year Re Analysis (JRA-25).

3. Algorithm

We develop a high speed and accurate algorithm based on Neural Network (NN). The advantages of the NN approach are to be speed of the computations and allows to produce numerous parameters since it does not require a large data base. Figure 1 indicates a three layers network structure. Neuro-link Network solver (NN solver) is built by improved learning algorithm "Dist.-BP" that has an anti-local minimum and a survival rule of neuron depending on nerves activities [Takenaka et al., 2008][3].

$$\Delta W^{(s+1)} = -\eta \left.\frac{\partial E}{\partial W}\right|_{W=W^{(s)}} + \alpha \Delta W^{(s)}$$

$$\Delta V^{(s+1)} = -\zeta \left.\frac{\partial E}{\partial V}\right|_{V=V^{(s)}} + \beta \Delta V^{(s)}$$

The NN solver traces radiative transfer code System for Transfer of Atmospheric Radiation (RSTAR) [Nakajima and Tanaka, 1986, 1998][4,5] for high speed and accurate computation (Figure 2). The Extreme speed and Approximation module Multiple drive System (EXAM SYSTEM) controls NN solvers by multi-threading. EXAM SYSTEM applies to MTSAT-1R, estimates the solar radiation at the TOA and the surface with semi-real

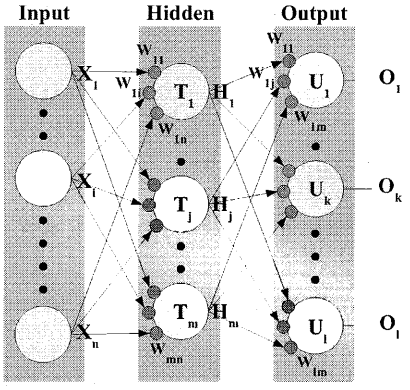

Figure 1 : Structure of three layer neural network. It has three components of layer (Input, Hidden, Output). Each layer has m,n,l number of neurons.

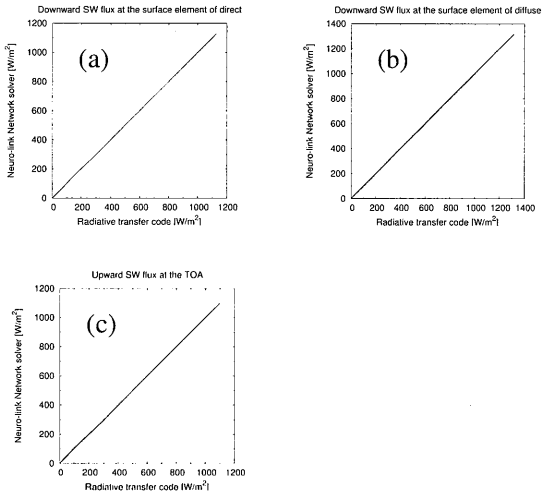

Figure 2 : Comparison of calculation results between radiative transfer code and NN solver. (a)direct component (b)diffuse component (c)upward SW flux at the TOA.

time, and evaluated against *in situ* observations. The EXAM SYSTEM uses eight Central Processing Unit (CPU) cores, And logically sliced target area (from 60N,80E to 60S,160W) is processed with high speed. It is validated in Chiba/SKYNET site. Achieved accuracy is rms =112.23 and the correlation between the estimates and measurements is 0.92. Moreover, NN solvers are also enabled for feature bands. By-products of the algorithm include Ultraviolet rays A, B (UV-A, UV-B), and Photosynthetically Active Radiation (PAR) fluxes as well as direct and diffuse components with semi-real time. These fluxes products promotes detail information of the influence of clouds for each spectral bands.

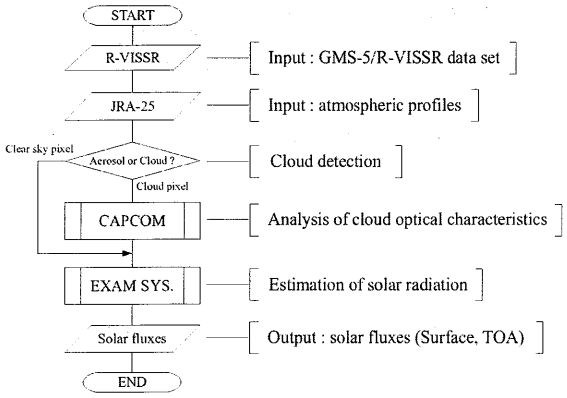

Figure 3 : Flow chart of estimation of solar radiation. It executed combination of EXAM SYSTEM and Comprehensive analysis Program for cloud Optical Measurement (CAPCOM) [Nakajima and Nakajima, 1995][6].

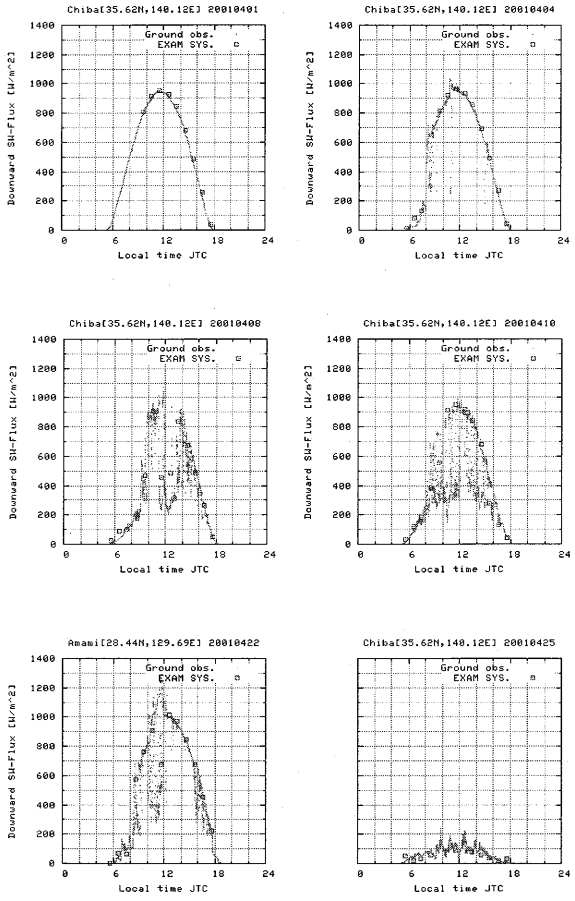

Figure 4 : Typical example of ground validation for downward SW flux at the surface, location is 35.62N, 140.12E Amami/SKYNET site in APEX-E2 period. Clear sky and cloudy condition indicate a good relation to estimation and observation. However, because very small phenomenon, broken clouds are caused problems.

4. Results and discussions

The flow chart of estimation of solar radiation is shown in Figure 3. Cloud optical characteristics are analyzed by Comprehensive analysis Program for cloud Optical Measurement (CAPCOM). Aerosols retrieval is skipped. Figure 4 shows one of the validation results of downward SW flux at the surface based on ground measurements in Asian Atmospheric Particle Environmental Change Studies (APEX) -E2 at. (35.62N and 140.12E) Amami/SKYNET site. Clear sky and cloudy condition are good relation. However, broken cloud condition has problem. Because it is very small sub-pixel phenomenon, satellite sensor can not capture yet. Figure 5 presents monthly average upward SW flux at the TOA. The observation is unstable since July at northern hemisphere (45S to 60S). In January (Fig.5a), high latitude area (45S to 60S) has strong reflecting flux. In April and July, the strong reflecting are in East Asia and North Pacific Ocean. Figure 6 indicates a monthly average downward SW flux at the surface. It has strong flux in the vicinity of Australia in January and October. A weak flux line is the influence of clouds of Intertropical Convergence Zone (ITCZ) in the equator. In April, North Pacific Ocean has strong downward flux, however, it is more higher than July. Figures 7 and 8 are direct and diffuse components of down ward SW flux at the surface. These fluxes indicate the influence of clouds for downward SW flux. In January and October, Because, it has few clouds, Australia has strong direct component. However, diffuse component increases in a wide region in the ocean of the south of Australia. In East china sea to North Pacific Ocean, it has same trend. And, July is most strong. Moreover, direct component decrease in from East china sea to North Pacific Ocean at April and July, however, south side of Australia has not decreasing of direct component. They might have closely related aerosols and cloud activity in East Asia (Fig.9). The strong diffuse components are brought by thin clouds. On the other hand, thin cloud (about tau=1to5) blocks the direct component of solar radiation. In April, from East china sea to North Pacific Ocean are kept bright by cloud scattering. And In July, blocking of direct component and strong diffuse component are predominant in North Pacific Ocean. This area has also strong reflection of upward SW flux at the TOA.

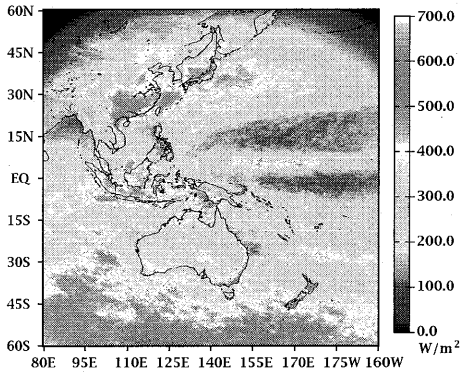

(a) January, 2001

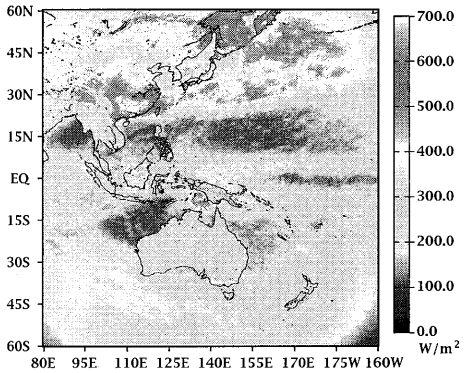

(b) April, 2001

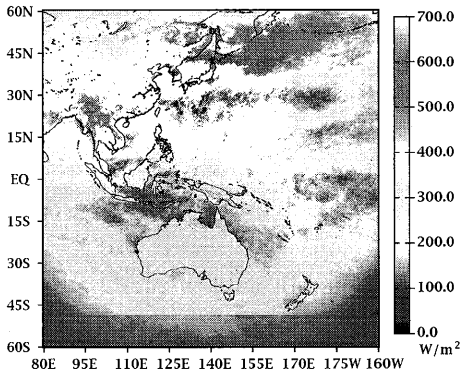

(c) July, 2001

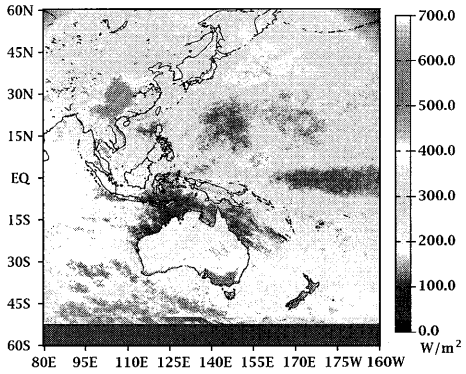

(d) October, 2001

Figure 5 : Monthly average upward SW flux at the TOA at 03UTC. (a)January (b)April (c)July (d)October in 2001.

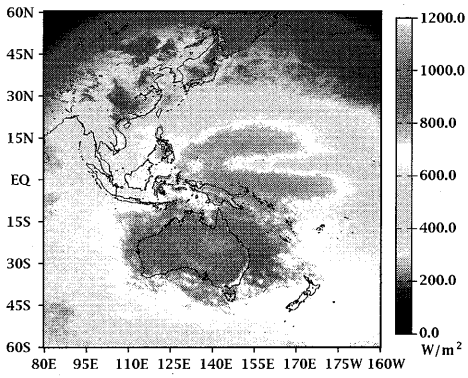

(a) January, 2001

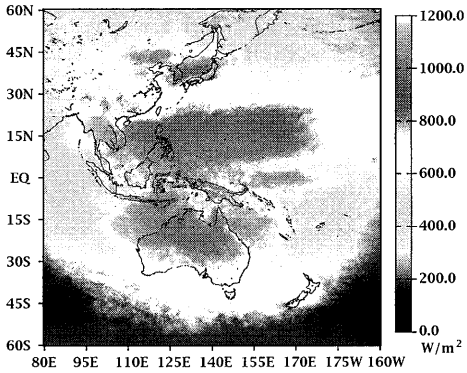

(b) April, 2001

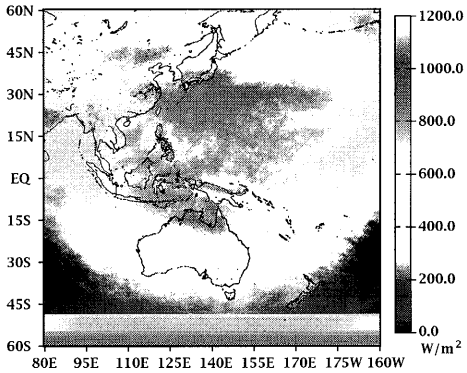

(c) July, 2001

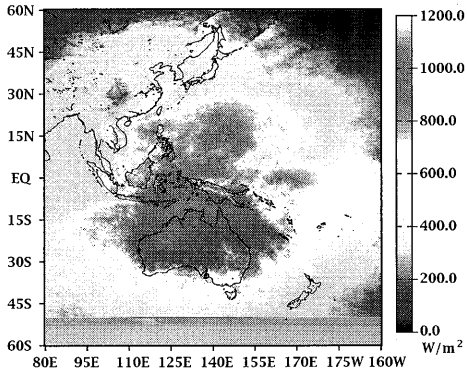

(d) October, 2001

Figure 6 : Monthly average downward SW flux at the surface at 03UTC. (a)January (b)April (c)July (d)October in 2001.

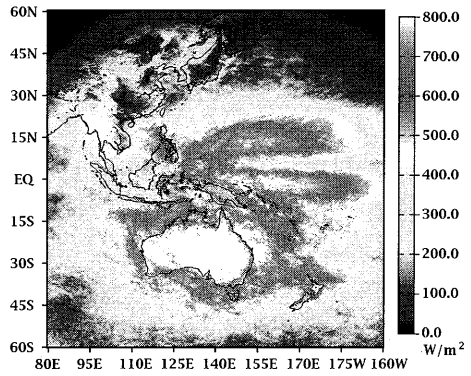

(a) January, 2001

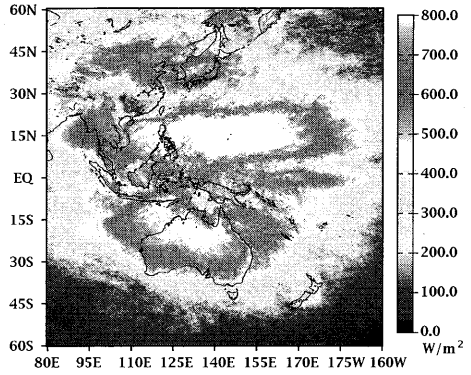

(b) April, 2001

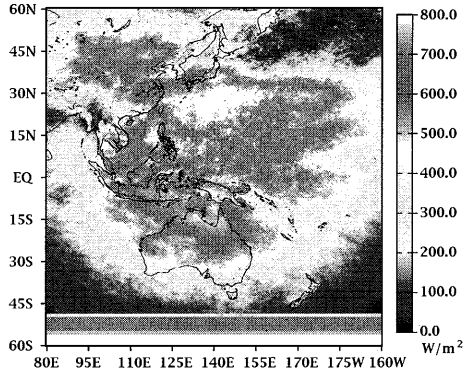

(c) July, 2001

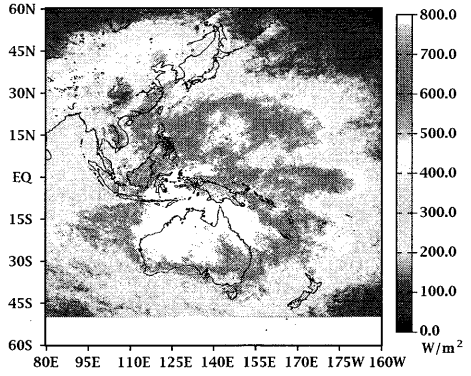

(d) October, 2001

Figure 7 : Same as Figure 6, but for direct component. (a)January (b)April (c)July (d)October in 2001.

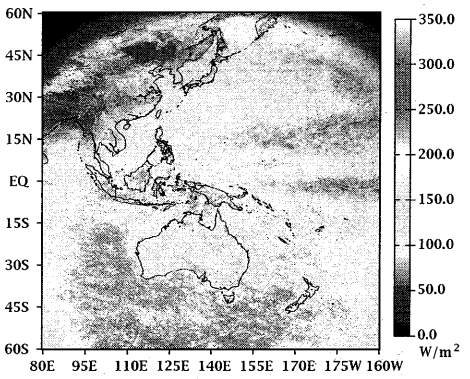

(a) January, 2001

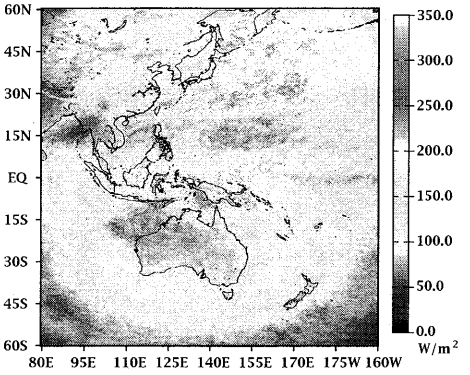

(b) April, 2001

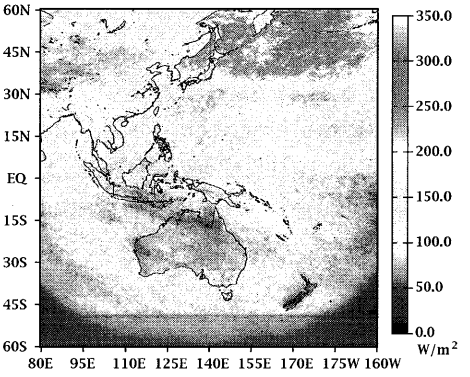

(c) July, 2001

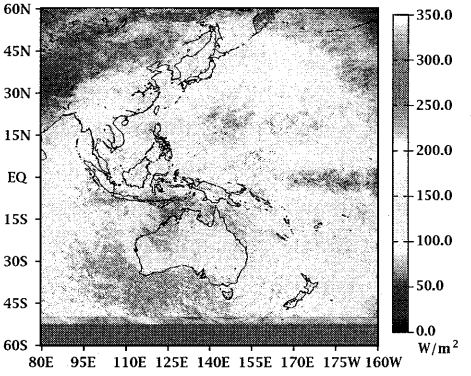

(d) October, 2001

Figure 8 : Same as Figure 6, but for diffuse component. (a)January (b)April (c)July (d)October in 2001.

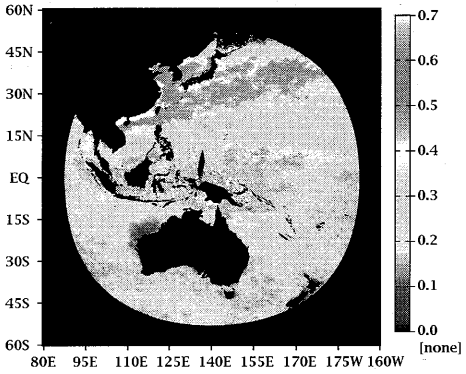

(a) April, 2001

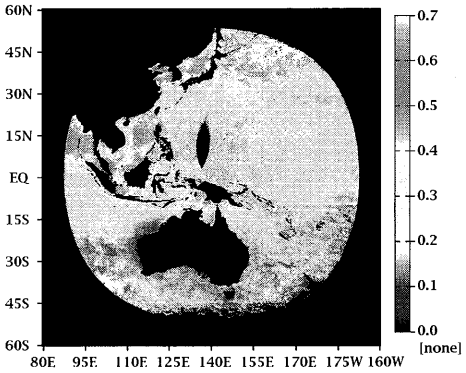

(b) July, 2001

Figure 9 : Monthly average aerosol optical thickness at the ocean surface (01UTC to 06UTC). Analyzed by Retrieval of Aerosol Optical Properties (REAP) [Higurashi and Nakajima, 1999, 2002; Fukuda et al., 2008][7,8,9)]

Acknowledgements

This study is based on Center for Climate System Research (CCSR), University of Tokyo and Meteorological Satellite Center of Japan Meteorological Agency (MSC/JMA) joint research.

This study was partly supported by Virtual Laboratory for the earth's climate diagnostics, formation of CCSR (Center for Climate System Research), HyARC (Hydrospheric Atmospheric Research Center), CEReS (Center for Environmental Remote Sensing), CAOS (Center for Atmospheric and Oceanic Studies).

References

1) Wetherald, R. T. and S. Manabe (1988), Cloud feedback processes in a general circulation model , J. Atmos. Sci., 45(8), 1397-1415.
2) Tsushima, Y. and S. Manabe (2001), Influence of cloud feedback on annual variation of global mean surface temperature , J. Geophys. Res., 106(D19), 22,635-22,646.
3) Takenaka, H., T. Y. Nakajima, A. Higurashi, A. Higuchi, T. Takamura, R. T. Pinker, Estimation of Solar radiation by Neural Network, J. Geophys. Res. (submitted).
4) Nakajima, T., and M. Tanaka (1986), Matrix formulations for the transfer of solar radiation in a plane-parallel scattering atmosphere, J. Quant. Spectrosc. Radiat. Transfer,35, 13-21.
5) Nakajima, T., and M. Tanaka (1988), Algorithms for radiative intensity calculations in moderately thick atmospheres using a truncation approximation, J. Quant. Spectrosc. Radiat. Transfer, 40, 51-69.
6) Nakajima, T. Y., and T. Nakajima (1995), Wide-area determination of cloud microphysical properties from NOAA AVHRR measurements for FIRE and ASTEX regions, J. Atmos. Sci., 52, 4043-4059.
7) Higurashi, A., and T. Nakajima (1999), Development of a two channel aerosol retrieval algorithm on global scale using NOAA / AVHRR, J. Atmos. Sci., 56, 924-941.
8) Higurashi, A., and T. Nakajima (2002), Detection of aerosol types over the East China Sea near Japan from four-channel satellite data., Geophys. Res. Lett., 29(17), 1836, doi:10.1029/2002GL015357.
3) Fukuda, S., T. Nakajimal, A. Higurashi, N. Kikuchi, and T. Y. Nakajima (2008), Aerosol retrieval from GLI over land and its comparison with ground observation, CEReS symposium 2008.

The impact of El Niño and the positive Indian Ocean Dipole on rainfall variability in the Indo-Pacific region

Bannu, Josaphat Tetuko Sri Sumantyo, Musali Knishnaiah, Hiroaki Kuze
Center for Environmental Remote Sensing, Chiba University
1-33 Yayoi-cho, Inage-ku, Chiba 263-8522, Japan, E-mail: bannu@graduate.chiba-u.jp

Abstract

In the tropics including the Indonesian maritime continent, the atmosphere is highly sensitive to sea surface temperature variations, especially on interannual time scales, which significantly affect precipitation and atmospheric circulation at these latitudes. Here we study the relative influence of the El Niño (EN) and positive Indian Ocean Dipole (pIOD) events on the Indonesian rainfall variability using long-term observational datasets (1948-2008) based on satellite as well as ground-based observations. The empirical orthogonal function (EOF) analysis of Indonesian rainfall anomaly is employed to extract the modes of variability relevant to the regional rainfall index, defined for three separate regions representing typical rainfall patterns. Since an ordinary correlation between IOD and Indonesian rainfall might be contaminated by the concurrent EN signal, partial correlation technique and composite analysis methods are used on the monthly rainfall anomalies in the three separate regions to extract the apparent teleconnection patterns. The analysis reveals that the pIOD impact on the rainfall is generally overwhelmed by that of EN when the two are in co-occurence. Nevertheless, it is found that the IOD influence remains high (most negative correlation) with a significance of above 95% confidence level after proper removal of the EN influence. Strong EN events influence all regions in Indonesia, whereas the effect of strong pIOD events is most remarkable in western and central regions. The relationship between pIOD and Indonesian rainfall seems to be sustained through pIOD (not negative IOD) occurring in the presence of El Niño events.

Keywords: El Niño, positive IOD, EOF analysis, partial correlation technique.

1. Introduction

The Pacific Ocean exhibits prominent sea surface temperature (SST) variations on timescales that range from interannual to interdecadal. The interannual fluctuations are primarily associated with the El Niño-Southern Oscillation (ENSO), which results from the interactions between the tropical Pacific Ocean and the overlying atmosphere[1]. The SST of the world's oceans plays a fundamental role in the exchange of energy, momentum, and moisture between the ocean and atmosphere[2]. The SST variability is crucial for understanding such interactions, in relation to the regional as well as global climate. Since Indonesia is located between the Pacific and Indian Oceans and between the Asian and Australian Continents, the influence of global climate phenomena vary across the region due to the island topography and/or the regional behavior of ocean–atmosphere fluxes. The Indonesian region, also known as the "Maritime Continent", has been identified as an area of major climatic importance both locally and globally[3].

Recently, there has been more interest in the climate of the Indian Ocean basin as a whole, yielding the description of the Indian Ocean dipole (IOD)[4,5]. Saji et al. (1999) identified an interannual mode of variability in Indian Ocean SSTs that has an east-west structure and is distinct from the basin-wide warming attributed to the remote response to El Niño (EN). They argued that the zonal mode identified in their analysis was independent of EN because the years when the zonal mode was most active were not always EN years. Most research on the climate of the Indian Ocean basin and of the countries around the rim of the Indian Ocean has focused on the evolution of the Asian-Australian monsoon. Furthermore, it has usually been assumed that the influence of the Indian Ocean is secondary to ENSO in controlling the climate of India, Africa, and Indonesia.

On the planetary scale, it is expected that Indonesian rainfall is strongly affected by both the EN and the IOD phenomena. Relationships between ENSO/IOD and rainfall in various regions have been investigated[4,6,7,8,9,10]. Briefly, the results indicated that generally the regional SST anomaly and rainfall anomaly data show strong correlation during the EN and positive IOD (pIOD) periods. As an extension of these previous works, here we extract strong EN and pIOD events from a time span of 60-years (1948-2008), highlighting the essential aspects of their influence on the regional rainfall in Indonesia.

2. Data and method

The basic SST dataset used in this study are the $2^{\circ}\times2^{\circ}$ extended NOAA reconstructed SST version 3 (ERSST v3) dataset. This was constructed by using the recently available International Comprehensive Ocean Atmosphere Dataset (ICOADS) SST data and improved statistical methods that allow stable

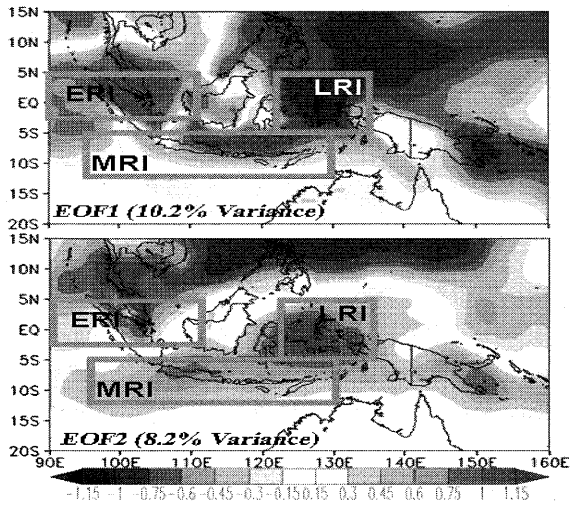

Fig. 1 Top two EOF modes of box averaged monthly mean rainfall anomaly in Indonesia region. The amplitudes are in °C. For each boxed region, a regional rainfall index (RRI) is defined: the monsoonal rainfall index (MRI), equatorial rainfall index (ERI), and local rainfall index (LRI).

reconstruction using sparse data[11]. The ENSO/IOD indices recalculated herein are based on the spatially averaged SSTs in wider regions relevant to ENSO/IOD. The obtained data are then used to generate the monthly Niño-3.4 SST anomaly index which represents the strength of EN over the eastern equatorial Pacific (5°S-5°N, 120°-170°W)[12]. Following Saji et al. (1999), we consider the IOD index as the SST anomaly difference between the tropical western Indian Ocean (10°S-10°N, 50°-70°E) and the tropical south-eastern Indian Ocean (10°S-eq, 90°-110°E). For precipitation analysis, here we use the National Centers for Environmental Prediction-National Center for Atmospheric Research (NCEP/NCAR) reanalysis dataset based on a state-of-the-art global data assimilation system[12]. With all of these data, we first calculate monthly variables throughout the full record period (January 1948 to May 2008) and then anomalies are obtained by subtracting the average values over the preceding 30 years from the monthly values.

The empirical orthogonal function (EOF) analysis of Indonesian rainfall anomaly is employed to extract the modes of variability relevant to the regional rainfall index, defined for three separate regions representing typical rainfall patterns. Since an ordinary correlation between IOD and Indonesian rainfall might be contaminated by the concurrent EN signal, partial correlation technique and composite analysis methods are used on the monthly rainfall anomalies in the three separate regions to extract the apparent teleconnection patterns. The significance levels for composite and partial correlation analyses are obtained by the standard 2-tailed Student's t-test.

3. Results and discussion

3.1. Regional Rainfall, ENSO, and IOD indices

Using EOF analysis, the leading EOF modes of the monthly rainfall anomaly over the Indonesia region are presented in Fig 1. The first EOF (EOF1) explains about 10.2% of the total variation of anomalous rainfall for the period between January 1948 and May 2008. The second EOF (EOF2) explains about 8.0% of the anomalous rainfall variability. Characteristic to the EOF1 is a reversal in sign of SST anomaly across the basin during EN and pIOD events. To analyze the possible correlation among various parameters, we generate a set of the regional rainfall indices (RRIs) by averaging monthly anomalies of rainfall in the three regions defined in Fig. 1. Hereafter these indices are called the monsoonal rainfall index (MRI), equatorial rainfall index (ERI), and local rainfall index (LRI). The RRIs are constructed from gridded reanalysis data products based on satellite as well as ground (gauge) observations. The 2.5°×2.5° NCEP-NCAR reanalysis data is a dataset that merges satellite and rain-gauge data[13].

The long-term variations of the EN/IOD indices and the RRI for each region (MRI, ERI, and LRI) are shown in Fig. 2 (left panel), here we show appropriately normalized values. As indicated by the correlation coefficients (r_1 for EN and r_2 for IOD), we find a negative correlation between each of the regional rainfall index and EN/IOD indices. Peaks and troughs in the RRIs tend to show a time lag of a few months against the EN/IOD indices, as analyzed in the following. Although generally a good relationship is found, not every EN (or p IOD) or La Niña (or negative IOD) episode results in a peak or trough in the RRIs. The significant influence of EN and positive IOD (pIOD) variability can be highlighted by classifying the EN/IOD events according to the time series of SST-based index as shown in Fig. 2 (left panel). Here the time-periods corresponding to strong EN (La Niña) are determined by proposing a new threshold based on standard deviation. Namely, a time-period is here classified as an EN (La Niña) event if SST anomalies in the Niño-3.4 region are +0.86°C (-0.86°C) or more for at least six consecutive months, and the months should include Dec-Jan-Feb (DJF). During 1948-2008, there are nine significant EN events (1957/58, 1963/64, 1965/66, 1972/73, 1982/83, 1986/87, 1991/92, 1997/98, and 2002/03) from the SST anomalies detected in the Niño-3.4 region (Fig. 2, left panel). A positive (negative) IOD event, on the other hand, is defined when the SST difference in the IOD regions is more than +0.35°C (less than -0.35°C) for at least six consecutive months. The months of SST anomaly peak should include September-October-November (SON) for IOD event. Nine events (1961/62, 1963/64,

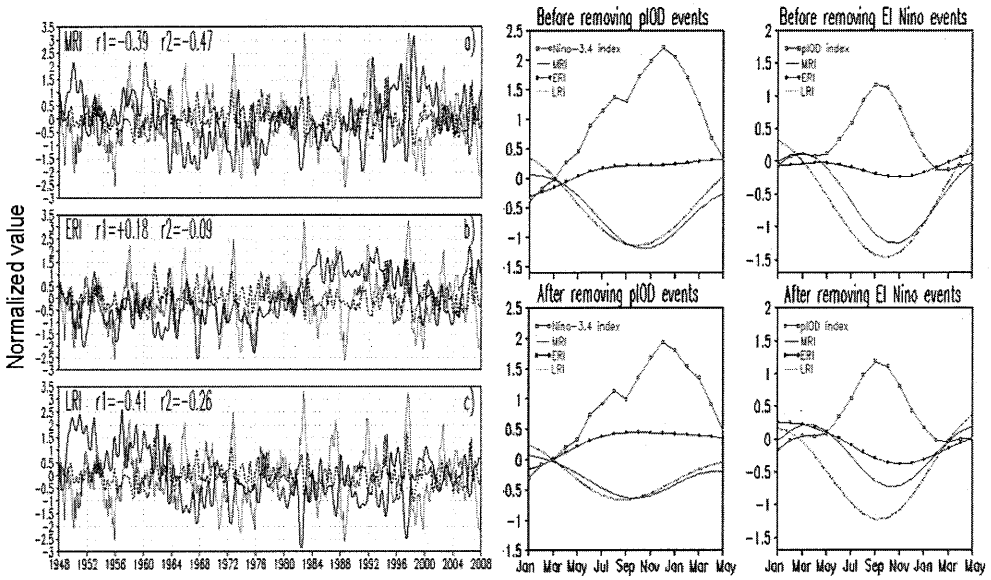

Fig 2 [Left panel] Long-term relationship between the regional rainfall indices (RRIs, solid lines) and EN (thin line)/IOD (broken line) indices: (a) MRI region (95°-130°E; 5°-12.5°S), (b) ERI region (90°-110°E; 2.5°S-5°N), and (c) LRI region (122.5°-135°E; 5°S-5°N). [Right panel] Composite analysis of the RRIs and EN/IOD index during strong EN and pIOD events as defined in the text. All indices are normalized, and correlation coefficients r_1 (RRI vs. El Niño index) and r_2 (RRI vs. IOD index) are shown in the panel.

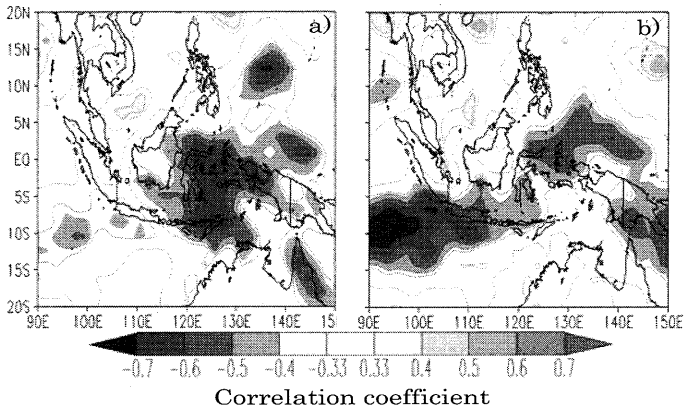

Fig. 3 Distribution of temporal correlation coefficient of the rainfall anomaly in Indonesian region with the EN index during (a) strong EN events (after removing pIOD events), and with the IOD index during (b) strong pIOD events (after removing EN events). All results are derived for strong EN and pIOD events during 1948-2008.

1967/68, 1972/73, 1977/78, 1982/83, 1994/95, 1997/98, and 2006/07) were found to be the pIOD years. Since both phenomena give phase locking to the seasonally cycle, it is useful and meaningful to derive a composite analysis for better understanding of the evolving nature of atmospheric and oceanic variables during different phases of ENSO and IOD events. Among all the warm events, we extract strong EN/pIOD events so as to study the time span corresponding to the peak phase (Fig 2, right panel). The strong EN is associated with relevant index values of $\geq 1.61^{\circ}C$ while the strong pIOD with the value of $\geq 0.84^{\circ}C$. For the period of 1948-2008, we can identify four extreme EN events (in 1957-58, 1972-73, 1982-83 and 1997-98) and five extreme pIOD events (in 1961-62, 1972-73, 1994-95, 1997-98, and 2006-07). Any year (during 1948-2008) that does not meet the above criteria of the warm (EN/pIOD) or cold (La Niña/negative IOD) events is here defined as a normal year. Thus, there are 32 years categorized as normal years during the 60-years period of 1948-2008.

3.2. Partial correlation analysis

To provide more systematic and comprehensive features of the ENSO and IOD influences on the Indonesian rainfall both spatially and temporally, we employ two dimensional version of partial correlation method. Figures 3 show the two-dimensional representation of the partial correlation coefficient (with no time lag) of the rainfall anomaly against the Niño-3.4 index and IOD index, respectively. Here no time lag is considered in view of the relatively small time-lag effects found in Fig 2. From Fig. 2 (right panel), it is evident that highly negative correlations are found between the MRI/LRI indices and the Niño-3.4/IOD indices. It is noticeable that the impact of ENSO and IOD events on ERI region is relatively small (uncorrelated), which is consistent with Fig. 3a. Also, Fig. 3a indicates that the effect of a strong EN event is significant over a wide region of Indonesia with mostly negative

correlations ($r \geq$ -0.33, 95% confidence level), while a weak EN event affects only limited regions (figure not shown). On the other hand, Fig. 3(b) shows that the pIOD yields negative correlations ($r \geq$-0.33, 95% confidence level) over the western region, particularly in the south-western Indian Ocean. This result for the strong IOD is basically in agreement with the result (Fig. 4) of Saji et al. (1999).

4. Conclusions

On the basis of the present analysis, here we summarize the spatial effect of both EN and IOD on the Indonesian rainfall, paying attention to the comparison between EN and pIOD events. We have systematically studied the influence of EN and IOD on the three separate regions of Indonesia, categorized in accordance with distinct rainfall patterns. Using the empirical orthogonal function (EOF) analysis of Indonesian rainfall anomaly, we have extracted the modes of variability relevant to the regional rainfall index or RRI (MRI, ERI and LRI), defined for three separate regions. The most negative correlations are found for the strong EN/pIOD events of region MRI and region LRI. This result clearly indicates the usefulness of the categorization method in discussing the effects of global SST anomalies on the regional rainfall anomalies. In our lag-time correlation analysis, typically a delay of 2 months was found for the RRI indices against the EN index, suggesting the possible use of EN/IOD indices for early warning of drought (EN) or flood (La Niña). Correlation studies have also shown that only the strong EN can affect the entire Indonesian region. Only the western part is strongly affected by the positive IOD, but not by the negative IOD. Besides, both the EN and La Niña events are influential to the eastern region. Future work should address the effects of other modes of climatic variability, as well as the hydrologic effects of interactions between EN/IOD events and other anomalous climate patterns.

References:

1) **Bjerknes, J. (1969)**, Atmospheric teleconnections from the euqatorial Pacific, *Mon.Wea. Rev., 97*, 163-172.
2) **Wang, C., S.-P. Xie, and J.A. Carton, (2004):** A global survey of ocean–atmosphere interaction and climate variability. *Geophys. Monograph*, **147**,1-19.
3) **Qu, T., Y. Du, J. Strachan, G. Meyers, and J. Slingo, (2005):** Sea surface temperature and its variability in the Indonesian region, *Oceanography*, **18:4**, 50-61.
4) **Saji, N.H., B. N. Goswami, P. N. Vinayachandran, and T. Yamagata (1999):** A dipole mode in the tropical Indian ocean, *Nature*, **401**, 360-363.
5) **Webster, P. J., A.M. Moore, J.P. Loschnigg and R.R. Leben, (1999):** Coupled ocean-atmosphere dynamics in the Indian Ocean during 1997-98. *Nature*, **401**, 356-360.
6) **Rasmusson, E.M., and T.H. Carpenter, (1982)**: Variations in tropical sea surface temperature and surface wind fields associated with the Southern Oscillation/El Niño. *Mon. Wea. Rev.*, **110**, 354-384.
7) **Yamagata T, Behera S.K, Rao S.A, Guan Z, Ashok K. (2002)**. The Indian Ocean dipole: a physical entity. *CLIVAR Exchanges* **24**: 15–18.
8) **Hendon, H.H, (2003):** Indonesian rainfall variability: impacts of ENSO and local air-sea interaction. *J. Climate*, **16**, 1775-1790.
9) **Saji, N.H. and T. Yamagata (2003)**, Possible impacts of Indian Ocean Dipole events on global climate, *Climate Res., 25,* 151-169.
10) **Yamagata T, Behera S.K, Rao S.A, Guan Z, Ashok K, Saji H.N, (2003).** Comments on the 'dipoles, temperature gradients, and tropical climate anomalies. *Bull. Amer. Meteor. Soc.,* **84,** 1418-1421.
11) **Smith, T. M., and R. W. Reynolds (2005)**, A global merged land air and sea surface temperature reconstruction based on historical observations (1880-1997). *J. Clim.*, **18**, 2021-2036.
12) **Trenberth, K.E., (1997)**: The Definition of El Niño. *Bull. Amer. Meteor.Soc.,* **78**, 2771–2777.
13) **Kalnay, E., and coauthors, 1996:** The NCEP/NCAR 40-year reanalysis project. *Bull. Amer. Meteor. Soc.,* **77**, 437-471.

Extraction of Mangrove forest in Bangladesh using Landsat data

○Md. Mijanur Rahman[1], B. Erdenee[2], Ryutaro Tateishi[3]

[1,2,3] *Center for Environmental Remote Sensing (CEReS), Chiba University, 1-33 Yayoi-cho, Inage-ku, Chiba 263-8522, Japan,*

[1]*E-mail: Mijan@graduate.chiba-u.jp*

[2]*E-mail: erdene@graduate.chiba-u.jp*

[3]*E-mail: tateishi@faculty.chiba-u.jp*

Abstract

As one of the series of CEReS International Symposiums, a symposium entitled "Remote Sensing of the Bangladesh, the world' s largest stretch of mangroves forests (Sundarbans Reserved Forest). Around half of the forests of the country occur in the coastal zone. Remote sensing provides various options for continuous monitoring of mangrove over time. Determining the most cost-effective sensor-technique combination for accurate classification of mangrove is essential. Different approaches to the classification of remotely sensed data of mangroves are reviewed, and four different methodologies identified like Supervised classification, Unsupervised classification, Band ratio classification and Visual Interpretation. Landsat ETM data of mangroves from Bangladesh were classified using each method. Classification accuracy of Band ratio method was higher than other method of Landsat ETM. The most accurate combination of sensor and image processing method for mapping the mangroves of Bangladesh is identified.

The most accurate combination of sensor and image processing method is Landsat TM and Band ratio; if the discrimination between mangrove and no mangrove vegetation is required over a large area, at relatively low time and money cost.

Keywords: Supervised Classification, Band Ratio Classification, Unsupervised Classification, Normalization, Accuracy Assessment.

1. Introduction:

The term 'mangrove' describes both the ecosystem and the plant families that have developed specialized adaptations to live in this tidal environment (Tomlinson, 1986). Mangrove forests known, as 'rainforests' by the sea' are one of the most important coastal ecosystems in the world in terms of primary production and coastal protection. Mangrove forest of Bangladesh is the world's largest mangroves forest (Sundarbans Reserved Forest), stretches for almost 6,000 square miles across India and Bangladesh, a natural barrier against tsunamis and frequent cyclones that blow in from the Bay of Bengal. Mangrove plantations are increasing in area but they are losing growing stock. To arrest this, Bangladesh has adopted several strategies.

- ✧ The 'Sustainable Ecosystem Management' strategy has now been adopted
- ✧ Biodiversity conservation and enhancement has been taken as a key management
- ✧ A zoning system is being developed for both production and protection purposes.

2. Importance of mangroves:

The importance of mangroves as a coastal resource is well established. Mangroves support the conservation of biological diversity by providing habitats, spawning grounds, nurseries and nutrients for a number of animals. A wide range of commercial and non-commercial fish and shellfish also depends on these coastal forests. Mangroves play important roles in Nutrient retention and water quality improvement through filtration of sediments and pollutants; Global Carbon Cycle. This importance is reflected in the economic value of mangroves depending on use (Stevenson 1996).

The mangrove forest of Bangladesh, locally known as Sundarbans, is believed as the largest continuous mangrove forest of the world (Hussain & Karim 1994; Anon. 2001b; Siddiqi 2001). The Sundarbans mangrove forest is used as the basis for various commercial and subsistence activities. About 10 million people of the coastal regions are dependent directly or indirectly on the mangrove for a variety of purposes such as agriculture, fishing, cattle rearing, human settlement, collection of housing materials, fuel wood and human foods and employment opportunities.

3. Importance of Study:

Mangrove forests are an important economic and ecological resource in Bangladesh. For coastal managers and scientists, the most important information regarding mangrove ecosystems is location boundaries, area of clearance, and mangrove density (Green et al. 2000).

Remote sensing applications have been applied mainly for mangrove inventory and mapping, change detection, and for management purposes. This study emphasizes mangrove conservation and sustainable utilization. Accessible spatial information is critical for the support of management planning, monitoring, and implementation of zoning and other management actions for mangrove conservation and sustainable use. So this study is important -------

1. To monitor changes over time
2. To monitor deforestation and aquaculture activity
3. Resource inventory and mapping

Moreover the study area has been declared as world heritage.

4. Objectives:

The objectives of present study are as follows.

1. Extraction of Mangrove forest using different Classification methods
2. Identification of the most accurate method and Mapping.

5. Study area:

The Sundarbans mangrove forest is located at the south of the Tropic of Cancer and at the northwest of the Bay of Bengal (21° - 22° N, 89° - 90° E) within the Khulna administrative division and extending over parts of Khulna, Satkhira and Bagerhat districts. The Sundarbans mangrove forest covering an area of 10,000 km^2 of which 65% (6500 km^2; FAO, 2003) fall within the territory of Bangladesh. Mangroves in Bangladesh have two major regional distributions of which the largest one is in the southwest region covering greater Khulna District, and the other is in the southeast region covering greater Chittagong District, named the Chakaria Sundarbans.

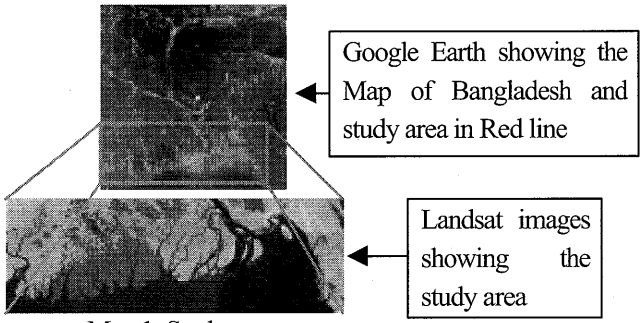

Map 1: Study area

6. Data & Methodology:

Landsat ETM images (p138r044 of 2000/11/17, p138r045 of 2000/11/17, p137r045 of 2000/11/26, p137r044 of 1999/11/24, p136r045 of 1999/12/19, p136r044 of 2001/02/07) with band 1-5, 7 & Spatial Resolution (30m x 30m) were used for this study. For Training area selection, Google Earth and photograph had been considered. For accuracy assessment, GLCNMO (Visual assessment) and Landsat ETM with local knowledge had been used.

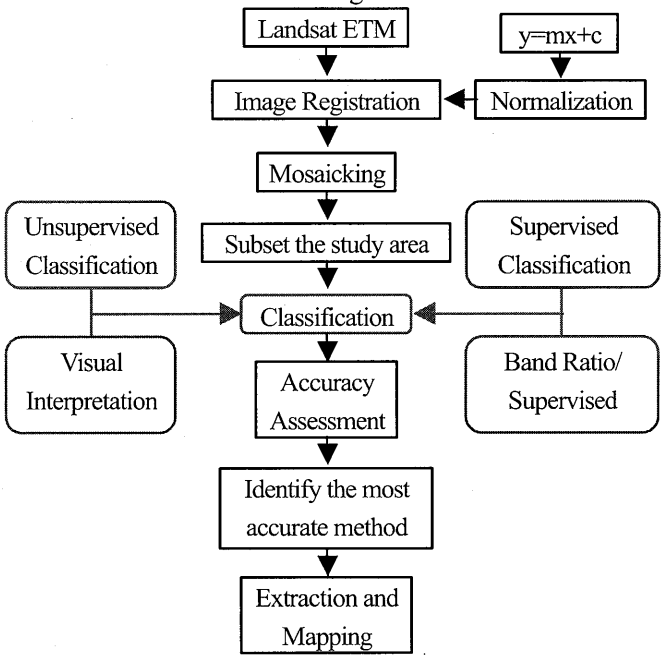

Flow Chart of Methodology

7. Normalization:

Based on the scene p136r044, overlapping area has been cut and compared the DN of both image and then averaged. The average DN value in each band applied to the entire band.

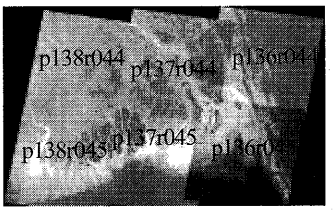

Fig 1: Before Normalization

Fig 2: After Normalization

7.1 Procedure followed for Normalization:

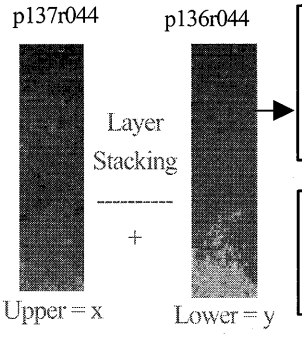

Find out the Linear Regression (y=mx+c) of lower (y) image for each band considering the same band of upper (x) image.

Convert the all bands of lower image using derived y=mx+c,then making a new image.

7.2 Examples of Correlation coefficient:

P137r044 band 1 versus p136r044 band 1

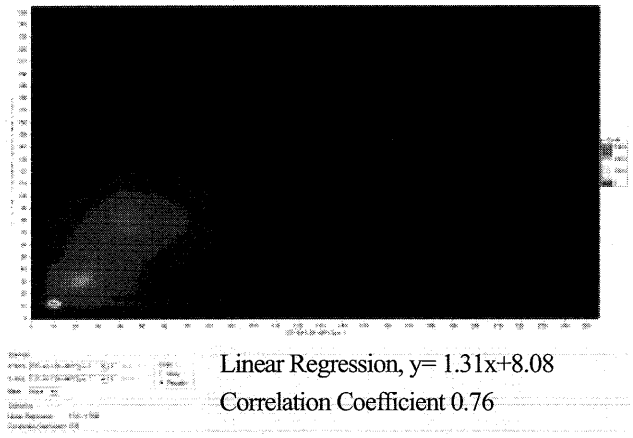

Fig 3: Correlation coefficient of P137r044 band 1 versus p136r044 band 1

P137r044 band 2 versus p136r044 band 2

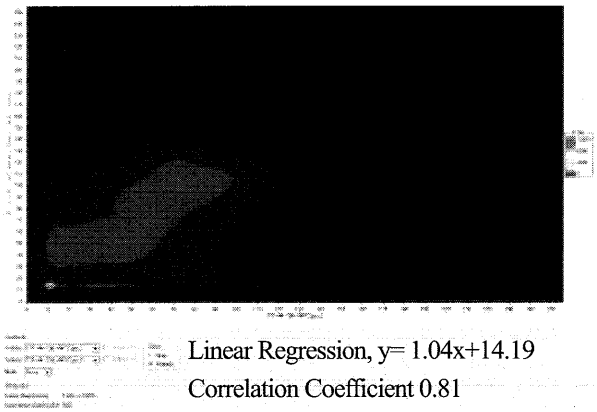

Fig 4: Correlation coefficient of P137r044 band 2 versus p136r044 band 2

8. Training area Collection:

	Mangrove	Forest	Crop land	Water	Urban/ Built-up area	Sandy land
No. of regions	266	10	7	11	12	12
Total cells	300	188	219	162	105	104
Area in Km^2	0.24	0.15	0.18	0.13	0.09	0.08

9. Image classification Methods:

This study performed unsupervised, supervised, Visual Interpretation and Band ratios classification methods for classification to Landsat image. After the image classification, accuracy assessment had been done. Based on the highest overall accuracy, finally Band ratios classification Method had been considered for extracting the Mangrove forest in Bangladesh. More detailed about the different classification methods had been describe below.

9.1 Unsupervised classification:

Image data have been processed using an unsupervised classification. Image enhancement was not performed. An unsupervised classification of the image using the K-Means clustering algorithm was set up to produce 50 user-defined classes with maximum iterations of 10. Mangrove classes were identified and edited with reference to field data then merged into a single mangrove category with other classes.

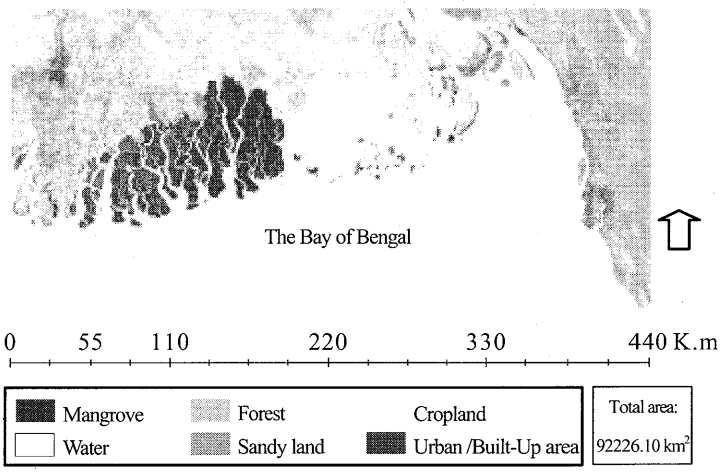

Map 2: Unsupervised Classification

9.2 Supervised Classification:

This study also performed supervised classification using the maximum likelihood decision rule. Field data or photographs, local experiences and QuickBird image have been used as training data. A 3×3 edge enhancement filter was applied to the imagery for determining the boundaries between mangrove classes and non-mangrove vegetation.

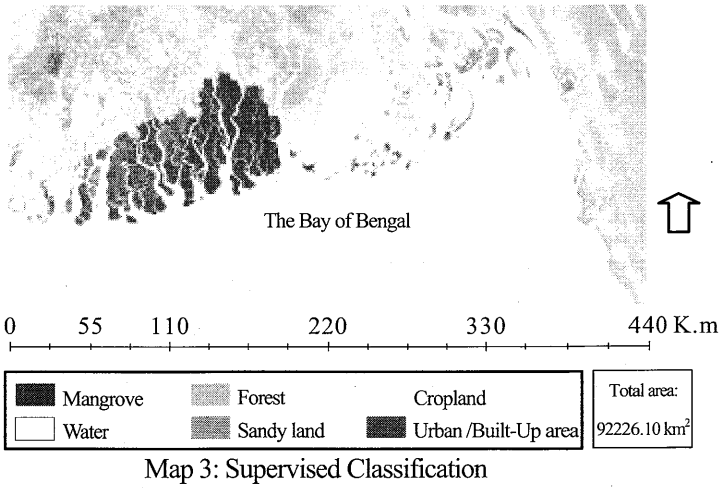

Map 3: Supervised Classification

9.2 Band ratio Classification:

Band ratios in remote sensing studies of vegetation it is somewhat surprising that this approach has not been employed more regularly for mangroves. The selection of band ratios should be based on the physical properties and canopy spectra of mangrove vegetation. Landsat TM bands 3 and 4 are either side of Caribbean mangroves' red-edge (Ramsey and Jensen 1996). Gray et al. (1990) on mangroves in Belize who used Band ratios 3/5 and 5/4. This method was based on the approach of Gray et al (1990). TM bands 3, 4 and 5 also produced the best visual discrimination of the Mangrove/non-mangrove boundary. So ratios of 3/5 and 5/4 were used primarily but classification result is not good for this study area. Finally all the Band ratios (1/2, 2/3, 3/4, 4/5, 5/7, 7/1) with supervised classification were performed using the maximum likelihood decision rule. For Band ratios classification method, same training pixels was used that were used for Supervised Classification method. To the best of our knowledge this approach has not been used in the Remote sensing for mangroves Mapping.

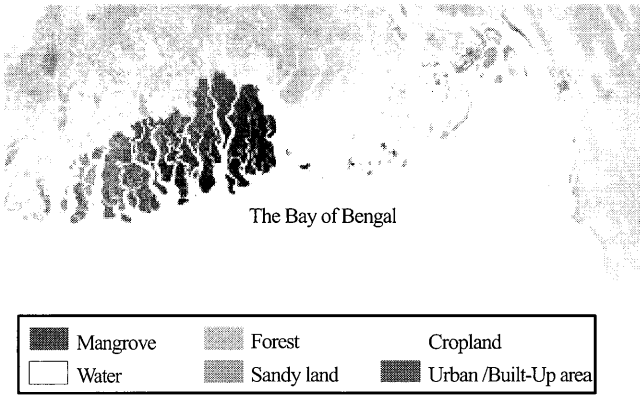

Map 4: Band Ratio Classification

10. Result of Land cover analysis by different Classification

Classification types						Class name
Unsupervised		Supervised		Band Ratio		
Area in km^2	% of Area	Area in km^2	% of Area	Area in km^2	% of Area	
7954.1	8.6	7106.7	7.7	6927.5	7.5	Mangrove
10447.1	11.3	12531.9	13.6	14429.9	15.6	Forest
20138.2	21.84	21737.3	23.5	20002.6	21.7	Crop land
49342.9	53.50	48906.8	53.0	48929.8	53.1	Water
2684.6	2.91	580.0	0.62	580.3	0.63	Urban/Build-up area
1659.3	1.79	1363.4	1.47	1356.2	1.47	Sandy land

11. Accuracy assessment:

Classification accuracy was determined using three complementary measures, which are based on error matrices derived from independent field data. An error matrix compares true reference data (from habitats visited in the field) to the habitat types predicted from image classification.

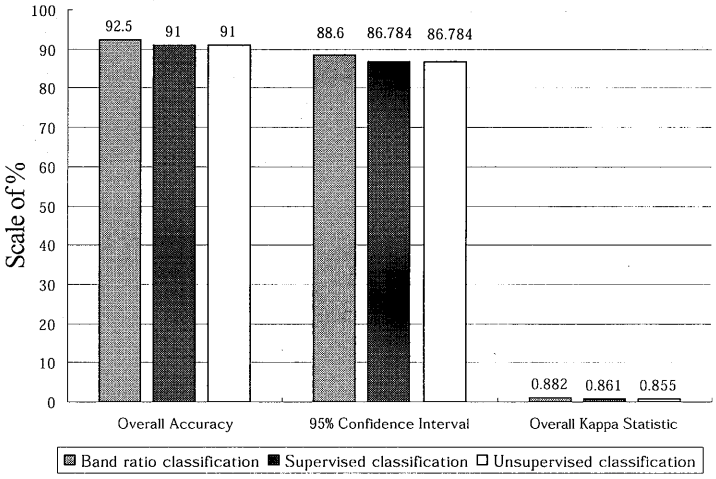

12. Conclusion:

Remote sensing provides various options for continuous monitoring of mangrove over time. Determining the most cost-effective sensor-technique combination for accurate classification of mangrove is essential.

The most accurate combination of sensor and image processing method is Landsat TM with Band ratios; if the discrimination between mangrove and non-mangrove vegetation is required over a large area, at relatively low time and money cost.

References

1) Green, E. P., Clark, C. D., Mumby, P. J., Edwards, A. J. and Ellis, A. C. (1998), *'Remote sensing techniques for mangrove mapping,* International Journal of Remote Sensing, 19:5, 935 – 956

2) Iftekhar, M.S.& Islam, M.R. (2004), *Managing mangroves in Bangladesh: A strategy analysis*, Journal of Coastal Conservation 10: 139-146

3) Md. Shahidul Islam & Mahfuzul Haque (2004), *The mangrove-based coastal and nearshore fisheries of Bangladesh: ecology, exploitation and management,* Fish Biology and Fisheries 14: 153-180, Springer 2005.

4) Wang, Yeqiao, Bonynge, Gregory, Nugranad, Jarunee, Traber, Michael, Ngusaru, Amani, Tobey, James, Hale, Lynne, Bowen, Robert and Makota, Vedast (2003), *Remote Sensing of Mangrove Change Along the Tanzania Coast*, Marine Geodesy, 26:1, 35 - 48

Space-based Global Positioning System measurements for the Numerical Weather Prediction studies

D. Rajan , VS. Prasad and AK. Bohra

Ministry of Earth Sciences
National Center for Medium Range Weather Forecasting
email: drajan@ncmrwf.gov.in
A-50, Sector 62, Noida 201307, India

The technology of remote sensing and science of meteorology have immensely improved over the recent years. The atmospheric water vapor plays a crucial role in Earth's energy and water cycles through absorbing solar and infrared radiation, releasing latent heat, transporting water, forming clouds and precipitation. Water vapor is the most abundant and most important greenhouse gas in the atmosphere, thus it plays an important role in Numerical Weather Prediction (NWP) activities. The Precipitable Water (PW), which is also referred as total column or integrated water vapor, the total water vapor contained in an air column from the Earth's surface to the top of the atmosphere.

Networks of Global Positioning System (GPS) receivers are now routinely used to provide near-real-time estimates of PW for use in NWP studies. The advantages of the GPS derived PW data include continuous measurements, long-term stability, low cost, etc. In this paper an hourly data set of atmospheric PW (produced from the zenith path delay) derived from ground-based GPS measurements are examined.

In India the primary mission of NCMRWF is to make available accurate and reliable weather forecasts in the medium range over the country using deterministic dynamical techniques. Currently NCMRWF is running the dynamical forecast model with triangular truncation at 254 in spectral space and 64 layers in vertical, abbreviated as T254/L64.

Reanalysis is a comprehensive global, multi-decadal gridded datasets generated by the latest numerical data assimilation technique using various past observations. Global atmospheric Japanese reanalysis (JRA25) products also used for these diagnostic studies of ground based GPS measurements. The global model used in the JRA-25 reanalysis has a spectral resolution of T106 and 40 vertical layers. This paper evaluates various diagnatic results, the diurnal variation; comparison PW data obtained from GPS measurements along with the T106/L40 and T254/L64. In addition this reanalysis product does not uses the GPS-PW data sets appealing for validating these GPS measurements. This study found that the reanalysis are deficient in reproducing the variability and trends of atmospheric precipitable water especially over the tropical oceans.

In near future the Indian satellite Oceansat-2 will be launched. The Italian Space Agency (ASI) agreed to mount the Radio Occultation (ROSA) on-board the Oceansat-2 satellite. The features of the ROSA also presented in this paper.

Optical characteristics of the atmosphere retrieved from spectral measurements of direct and scattered solar radiation

Naohiro Manago[1], Masanori Yabuki[1], Hiroaki Kuze[1]

[1] *Center for Environmental Remote Sensing, Chiba University, 1-33 Yayoi, Inage, Chiba, 263-8522, JAPAN*

manago@restaff.chiba-u.jp

yabuki@restaff.chiba-u.jp

hkuze@faculty.chiba-u.jp

Abstract

We describe a method for characterizing atmospheric properties from spectral measurements of direct and scattered solar radiation under clear sky conditions. A compact, stable spectro-radiometer is employed for the measurement in a spectral range of 300-1000 nm. The analysis of the measured spectra by means of the MODTRAN4 code provides us with a set of optical parameters describing tropospheric aerosols as the major product. As by-products, precipitable water amount and column ozone amount are retrieved. A year's worth of field data have been acquired at the Center for Environmental Remote Sensing, Chiba University, Japan. We report essential aspects on the regional aerosol properties as well as instrumental details including the calibration procedure.

Keywords **:** aerosol, solar radiation, spectroscopy

1. Introduction

The consideration on light scattering and absorption of aerosol particles in the atmosphere is in many cases essential in the analysis of satellite remote sensing data of the Earth's surfaces. Also aerosols play an important role in environmental problems such as the global warning due to their influence on the Earth's radiation budget. In this respect, it is required to establish methodology that enables measurements of aerosol amounts and characteristics in the real atmosphere.

Methods for retrieving aerosol characteristics from the measurements of direct solar radiation (DSR) and scattered solar radiation (SSR) have been the topic of a number of researches, among which the inversion method developed by Nakajima et al. [1] is widely employed to derive aerosol parameters from the observed data. In this paper, we propose an alternative approach, which can be called a forward calculation and feedback method (FCFM). In this approach, we adjust the aerosol characteristics so that the spectra of DSR and SSR calculated by means of the radiation transfer code, MODTRAN4[2], reproduce the measured spectra. Since this algorithm basically requires only the forward calculation, it enables detailed parameterization as input to the MODTRAN code, leading to the possibility of constructing more realistic aerosol models. Technically, the recent development of PC resources has made it possible to implement this type of forward calculation and subsequent parameter adjustments, which is inevitably a time consuming procedure.

In this work a compact, stable spectro-radiometer has been used to measure both DSR and SSR spectra, and the resulting data have been analyzed using the FCFM technique explained in Sec. 2.3. In Sec. 2.1, we describe on the detection system and measurement procedure, and Sec. 2.2 describes the calibration method. Sec. 3 gives the results and discussion, followed by the conclusion in Sec. 4.

2. Methods

2.1 Observation

The measurement of DSR and SSR has been undertaken at CEReS, Chiba University (35.6°N, 140.1°E) since August 2007 till now. The campus of Chiba University is located at about 3 km from the Tokyo bay, surrounded by residential and industrial areas (Fig. 1).

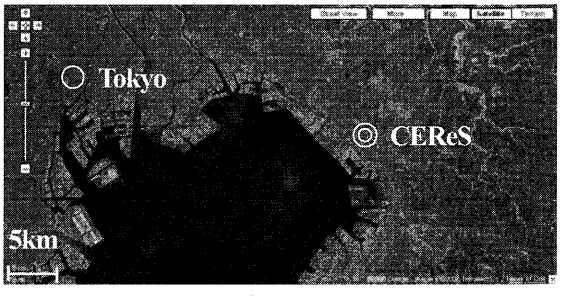

Fig. 1 Satellite picture around CEReS

The DSR and SSR spectra are measured with a portable spectro-radiometer (EKO, MS720). Specifications of the instrument are summarized in Table 1. Although the original field-of-view (FOV) angle of the spectro-radiometer is 180°, here the FOV is intentionally limited by attaching an entrance

tube with baffle rings (homemade, about 30 cm long) on top of the detection window. The inside of the tube is covered with polyurethane sheet having spectral reflectance of about 1.5% in the wavelength range between 250 nm and 2.5 μm. Stray light causes no measurable effects according to a ray tracing simulation. For SSR measurement, a FOV of 20° (total angle) is adopted so as to minimize the observed portion of the sky while keeping sufficient signal-to-noise ratio. For DSR measurement, two additional baffle rings are attached to obtain a smaller FOV of 5°. For aureole measurement, an additional sunshade is attached to view the annular region between 2.5° and 10° from the sun.

Wavelength Range	300 – 1140 nm
#Channels	256
Resolution (FWHM)	10 nm
Exposure Time	5ms – 5s

Table 1 Specification of MS720

All the observations were made under clear sky (no visible cloud) conditions. The SSR spectra were obtained for a total of 24 directions, with four horizontal angles of 11°, 92°, 194°, and 266° (clockwise from the north direction) and six elevation angles of 15°, 30°, 45°, 60°, 75°, and 90°. DSR and aureole spectra were measured before and after each SSR measurement.

2.2 Calibration

Any systematic errors in the DSR spectral measurement may cause a large bias in the resulting aerosol properties, since the optical effect of aerosols generally appears as a minute change in the observed intensity. In order to minimize such effects, we have performed the irradiance and temperature calibration of the MS720 instrument. Two identical instruments were employed for this purpose.

The radiation calibration was undertaken at the top of the Mauna Kea in Hawaii during the daytime on March 20 to March 22, 2008. Under the clear sky conditions, the DSR spectra were measured as the irradiance values. From the temporal data, the extra-terrestrial irradiance can be inferred by applying the Langley plot method [3]. The calibration coefficients were determined so as to obtain agreement between the resulting spectral irradiance with the literature value[4] used by the MODTRAN code. For the two MS720 instruments, the wavelength-dependent calibration coefficient of the first one was determined in this way, and that of the second one was derived by comparing the readings of the two instruments. The results are shown in Fig. 2, which indicates that the correction factor is nearly the same for the two instruments. The six curves obtained from the Langley plot (am and pm measurements for three days) agree well with each other, with a small statistical error of less than 0.2% in the visible range of the spectrum. Both the correction factor and its error bar become larger at the wavelengths of H_2O and O_2 absorption spectra.

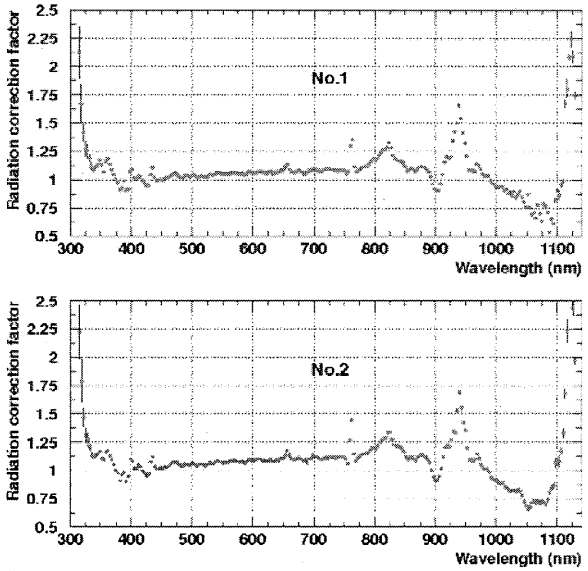

Fig. 2 Radiation correction factor for MS720

The temperature dependence of the radiation measurement was checked by comparing the readings between the target (temperature controlled) and reference (at room temperature) instruments. A 1000 W halogen lamp was employed for this measurement. The target MS720 was placed in a thermally shielded box, while the reference MS720 was placed in a temperature controlled room, both observing the light from the halogen lamp. As seen from Fig. 3, it is apparent that the temperature dependence of the correction factor for the target MS720 behaves as a spline function with knots at 0, 10, 20 and

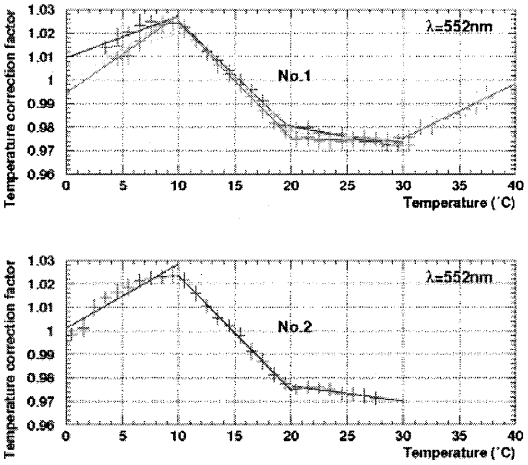

Fig. 3 Temperature correction factor for MS720

30 degree Celsius. A very similar tendency was found also for the other instrument. Such temperature dependence of the correction factor can be ascribed to the insufficient correction of the temperature response of the photodiode detector, which was originally provided from the manufacturer. For conventional usage of the spectro-radiometer, a correction of 3% is of little importance, but it is significant for precise retrieval of aerosol properties from DSR and SSR.

2.3 Analysis

When a solar ray with wavelength λ comes to the atmosphere with a zenith angle θ, the irradiance E of DSR at the ground level (z=0) is given as

$$E(\lambda,\theta)=E_0(\lambda)T(\lambda,\theta,0,\infty), \quad (1)$$

where E_0 denotes the solar irradiance at the top of the atmosphere, and T is the atmospheric transmission:

$$T(\lambda,\theta,z_1,z_2)=\exp\left[-\int_{z_1}^{z_2}\alpha_{ext}(\lambda,z)\frac{|dz|}{\cos\theta}\right]. \quad (2)$$

In Eq. (2), α_{ext} is the extinction coefficient, which can be written as a sum of the molecular scattering coefficient α_{ms}, molecular absorption coefficient α_{ma}, aerosol scattering coefficient α_{as}, and aerosol absorption coefficient α_{aa}:

$$\alpha_{ext}=\alpha_{ms}+\alpha_{ma}+\alpha_{as}+\alpha_{aa}. \quad (3)$$

The molecular scattering coefficient and molecular absorption coefficient are considered to be known parameters, as they can be calculated from the weather condition. The single scattering albedo (ω) is defined as

$$\omega=\frac{\alpha_{as}}{\alpha_{as}+\alpha_{aa}}. \quad (4)$$

When a solar ray comes to the atmosphere with a zenith angle θ_1, scattered to a direction with a zenith angle θ_2 (scattering angle χ), and detected at the ground level, the corresponding radiance L of SSR can be written as

$$L(\lambda,\theta_1,\theta_2)=\int_0^{\infty}E_0(\lambda)\times$$
$$[\alpha_{ms}(\lambda,z)f_R(\lambda,\chi)+\alpha_{as}(\lambda,z)f_M(\lambda,\chi)]\times$$
$$T(\lambda,\theta_1,z,\infty)T(\lambda,\theta_2,0,z)\frac{dz}{\cos\theta_2}, \quad (5)$$

where f_R and f_M are the phase function of the Rayleigh and Mie scattering, respectively. In this manner, the spectral intensity of DSR and SSR can be calculated by means of molecular and aerosol parameters. The use of the radiation transfer code MODTRAN4 makes it possible to include more detailed processes associated with the multiple scattering. Although the MODTRAN code is provided with some typical aerosol properties (aerosol models such as maritime, urban, etc.), here we give the parameters to the code in order to optimize the aerosol characteristics.

Here, we describe the basics of the FCFM technique. Here aerosol particles are assumed to be spherical. According to the Mie theory, knowledge on aerosol size distribution and complex refractive index leads to optical parameters such as the extinction coefficient (with its wavelength dependence), single scattering albedo, and scattering phase function. Here we further assume that aerosol is composed of three types as shown in Fig. 4. Component 1-3 correspond, respectively, to the water-soluble aerosols (including minerals), sea-salt aerosols, and soot particles. The size distribution of each component is expressed by a single component lognormal distribution.

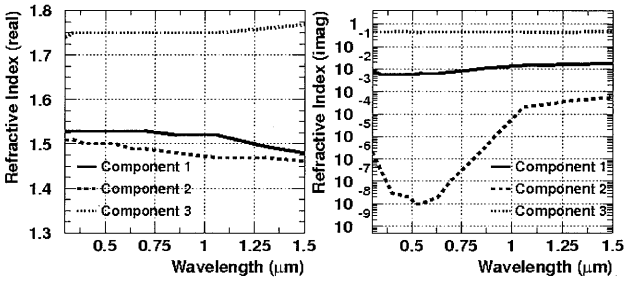

Fig. 4 Complex refractive indexes

The spectra for DSR and SSR are calculated by providing the MODTRAN4 code with aerosol optical parameters, which are derived from the Mie scattering calculation as a function of aerosol amount (in the form of ground visibility), mixing ratio, mode radius and mode width of each component. These parameters are optimized to reproduce the measured spectra. In this process, we rely on the wavelength ranges that are not affected by molecular absorption effects. For the ranges with water vapor and ozone absorption, on the other hand, the water scaling factor and ozone scaling factor prepared in the code are used to adjust the absorption intensity of these molecular species.

3. Results and Discussion

Figure 5 shows an example of the aerosol optical parameters derived from the present analysis. The data analyzed here are those taken on May 5, 2008 under clear sky conditions. On this day, no clouds were detected around Chiba area either on satellite images. The aerosol extinction coefficient (normalized

to the value at 550 nm), single scattering albedo, asymmetry factor, and the scattering phase function at 550 nm are shown in Fig. 5. The amount of precipitable water and ozone column density obtained from the analysis is 0.52 g/cm^2 and 361 DU, respectively. The resulting aerosol parameters have not yet been fully optimized; further improvement in the choice of fitting parameters and parameter ranges will be needed along with the data correction methods.

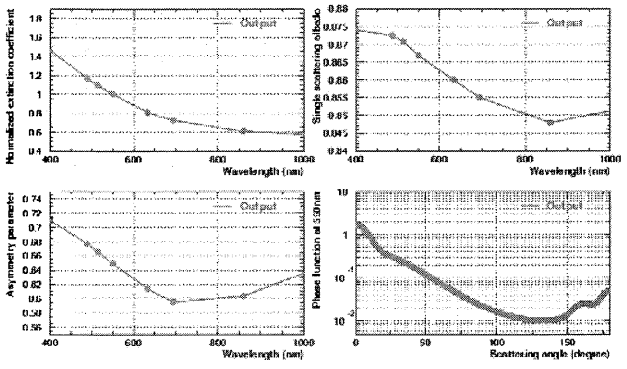

Fig. 5 Aerosol optical parameters (preliminary)

Figure 6 shows the temporal change of the precipitable water for two hours. The data are from observations on August 15, 2007, also a clear day. Comparison between the data from the present retrieval and the microwave radiometer of SKYNET observation site[5] indicates that both measurements give consistent results throughout the observation period.

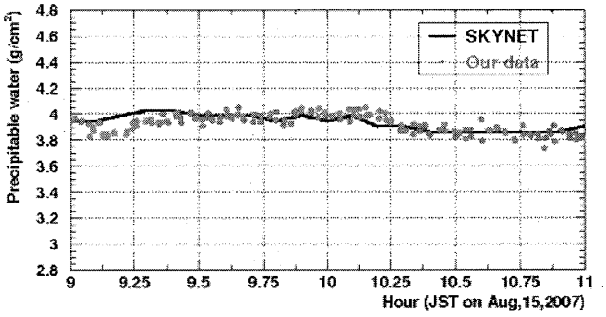

Fig. 6 Precipitable water

Ozone column density obtained from the observations in May 2008 is compared with the data from the Ozone Monitoring Instrument (OMI)[6] sensor onboard the AURA satellite. As a whole, reasonable agreement is seen between the ground and satellite results. The remaining difference is presumably due to the difference in the observation points and observation time.

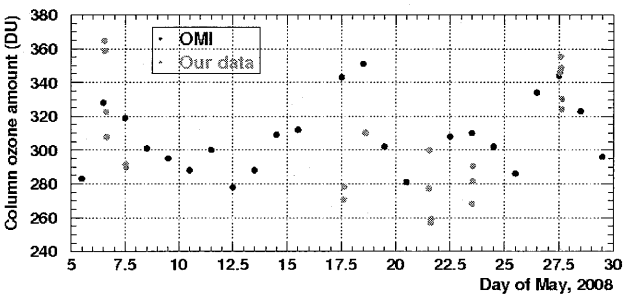

Fig. 7 Column ozone amount

4. Conclusion

We have developed the forward calculation and feedback method for the retrieval of aerosol and molecular absorption properties of the atmosphere from the direct and scattered solar light under clear sky conditions. Protocols for radiation and temperature calibration of the spectro-radiometer have been described. So far we have attained stable analysis for the molecular absorption part, and further efforts are being made to perform reliable fitting of aerosol parameters.

Acknowledgements

We wish to thank the members of the SUBARU Telescope, National Astronomical Observatory of Japan, for supporting our calibration work on Mauna Kea. We also thank the SKYNET team for providing useful data to check our data.

References

1) T. Nakajima, M. Tanaka, and T. Yamauchi, "Retrieval of the optical properties of aerosols from aureole and extinction data" , Appl. Opt. 22, 2951-2959 (1983).
2) G. P. Anderson et al., "MODTRAN4 version 2: radiative transfer modeling", Proc. SPIE, Vol. 4381, 455-459 (2001)
3) M. Tanaka, T. Nakajima, and M. Shiobara, "Calibration of a sunphotometer by simultaneous measurements of direct-solar and circumsolar radiations", Appl. Opt. 25, 1170-1176 (1986).
4) R. L. Kurucz, "The solar irradiance by computation", in Proceedings of the 17th Annual Conference on Atmospheric Transmission Models, PL-TR-95-2060, G. P. Anderson, R. H. Picard, J. H. Chetwind, eds. (Phillips Laboratory Directorate of Geo-physics, Hanscom Air Force Base, Mass.), 333-334 (1995).
5) T. Takamura, T. Nakajima, SKYNET community group, "Overview of SKYNET and its Activities", OPTICA PURA Y APLICADA, 37(3), 3303-3308 (2004).
6) P. F. Levelt, G. H. J. van den Oord, M. R. Dobber, A. Malkki, H. Visser, J. de Vries, P. Stammes, J. O. V. Lundell, and H. Saari, "The Ozone Monitoring Instrument", IEEE Trans. Geosci. Remote Sens. 44 1093-1101 (2006).

Determination of the optical thickness of aerosol at 1.6μm and 2.2μm using Skyradiometer

Nobuyuki Kikuchi

National Institute for Environmental Studies, 16-2 Onogawa, Tsukuba, Ibaraki 305-8506, Japan,
kikuchi.nobuyuki@nies.go.jp

Abstract

A method is presented for determining of the optical thickness of aerosols from the direct solar radiation at 1.6 um and 2.2 um measured by Skyradiometer POM-02. Because 1.6 um and 2.2 um band are weakly absorbed by water vapor, these bands need to subtract the optical thickness of water vapor from the measured optical thickness. Skyradiometer has a channel at 0.94 um water which can obtain the column water vapor. The optical thickness of water vapor at the 1.6 um and 2.2 um channels is calculated using the column water vapor. The optical thickness of aerosol at 0.94 um has been corrected with the optical thickness of aerosol at 0.87 um and 1.02 um bands.

Keywords **:** aerosol, optical thickness, skyradiometer

1. Introduction

Skyradiometer POM-02 is a radiometer for deriving aerosol properties from the direct and defuse solar radiation measurements. Skyradiometer POM-02 has channels at 1.6 um and 2.2 um to derive cloud properties such as the effective radius of cloud particle. We developed a method determining the aerosol optical thickness at 1.6 um and 2.2 um using the direct solar radiation measured by Skyradiometer POM-02 for validation of the aerosol properties of GOSAT TANSO-CAI [1](Nakajima et. al, 2008). It is a problem of deriving aerosol properties using these two channels that there is weak absorption by water vapor at 1.6 um and 2.2 um. Using water vapor amount derived from 0.94 channel of Skyradiometer POM-02, effect of water vapor absorption at 1.6 um and 2.2 um can be reduced.

2. Determination of water vapor amount

Skyradiometer POM-02 has been used to measure the direct solar radiation at discrete wavelength between 0.315 and 2.2um. Skyradiometer POM-02 has a channel for water vapor absorption band at 0.94 um which can derive column water vapor amount. We calculate the relationships between the absorption and the water vapor amont using rstar4b radiation transfer code including LOWTRAN 7 [2](Kneizys et. al, 1988). Rstar4b is modified for satellite data analysis, which calculates the reflected radiance at the top of atmosphere. We calculated the reflectance of ground surface instead of the transmittance of the atmosphere. The surface is assumed to be lambertian and the ground albedo 0.5. The solar zenith angle is 60 degree, and the radiometer nadir angle is 0 degree. Airmass (optical path length) is 3 for water vapor.

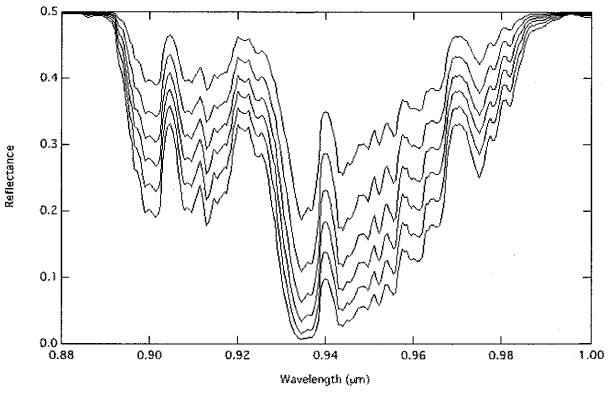

Fig. 1. Calculations of reflectance at ch8 (0.94□m) as a function of wavelength for water vapor.

Figure 1 illustrates the reflectance of solar radiation at 0.94 um as a function of wavelength at 0.5 nm intervals for 7 atmosphere models (tropical, mid latitude summer, mid latitude winter, high latitude summer, high latitude winter, US standard and US standard except for no water vapor).

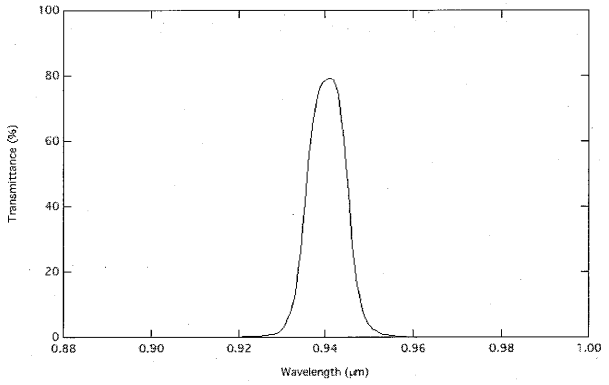

Fig. 2. Filter transmittance of ch8 (0.94□m) as a function of wavelength.

Figure 2 illustrates the transmittance of the interference filter at 0.94 um as a function of wavelength.

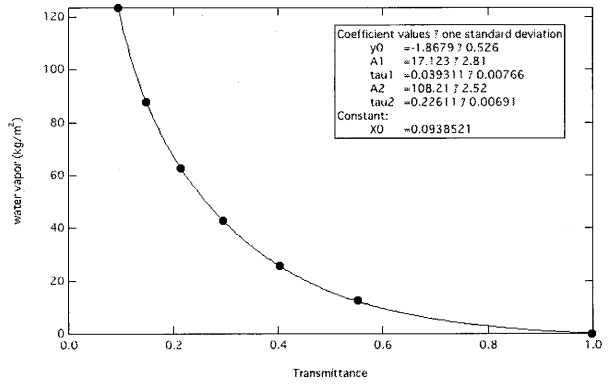

Fig. 3. Calculations of water vapor as a function of transmittance for the direct solar radiation.

Figure 3 illustrate the transmittance of direct solar radiation as a function of water vapor amount (dot) which is calculated with the results of Fig.1 and Fig. 2. Curve fitted line can be written as:

$wv(Tr_{wv0.94}) = y_0 + A_1\exp(-(Tr_{wv0.94} - x_0) / tau_1)) + A_2\exp(-(x-x_0) / tau_2)$, … (1)

where y_0=-1.8679, A_1=17.123, tau_1=0.039311, A_2=108.21, tau_2=0.22611, x_0=0.0938521. Using the optical thickness determined with 0.87 um and 1.02 um channels, we can calculate the transmittance of aerosols at 0.94 um given by,

$Tr_{a0.94} = \exp(-(0.53 * tau_{a0.87} + 0.47 * tau_{a1.02}) / \cos(theta_0))$. … (2)

The transmittance of water vapor can be calculated as follows,

$Tr_{wv0.94} = Tr / Tr_{a0.94}$, … (3)

where Tr is the transmittance measured by Skyradiometer POM-02 at 0.94um. Column water vapor is given by

$wv_c = wv(Tr_{wv0.94}) * \cos(theta_0)$. … (4)

3. Determination of aerosol optical thickness at 1.6um and 2.2um

Skyradiometer POM-02 has channels at 1.6 um and 2.2 um which are weakly attenuated by water vapor absorption. We calculate the relationships between water vapor amount and transmittance of direct solar radiation at 1.6 um and 2.2 um using rstar4b. Figure 4 and 5 illustrates the reflectance of solar radiation as a function of wavelength at 1.6 um and 2.2 um respectively for lanbertion surface with 0.5 albedo.

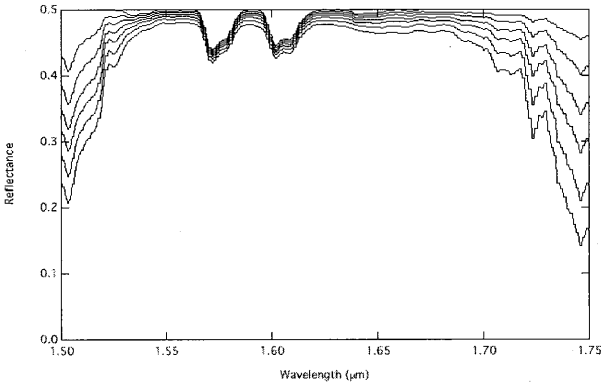

Fig. 4. Calculations of reflectance at ch10 (1.6 um) as a function of wavelength.

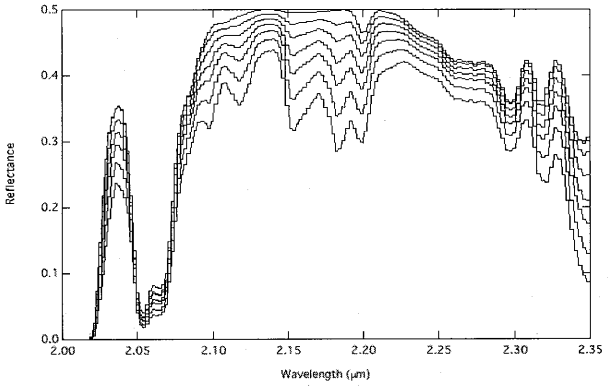

Fig. 5. Calculations of reflectance at ch11 (2.2 um) as a function of wavelength.

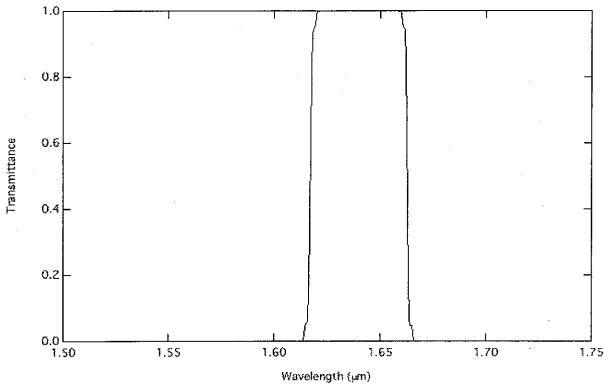

Fig. 6. Filter transmittance of ch10 (1.6 um) as a function of wavelength.

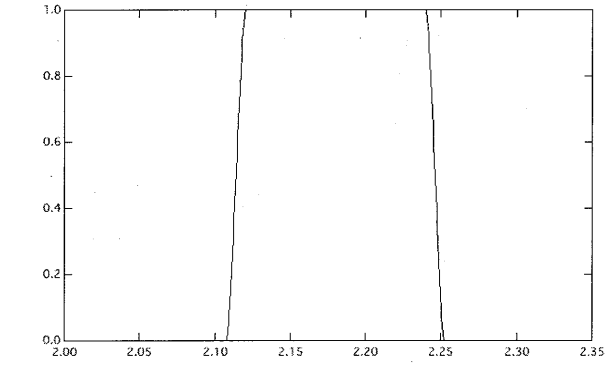

Fig. 7. Filter transmittance of ch11 (2.2 um) as a function of wavelength.

Figure 6 and 7 shows the transmittance as a function of wavelength for the interference filter at 1.6 um and 2.2 um.

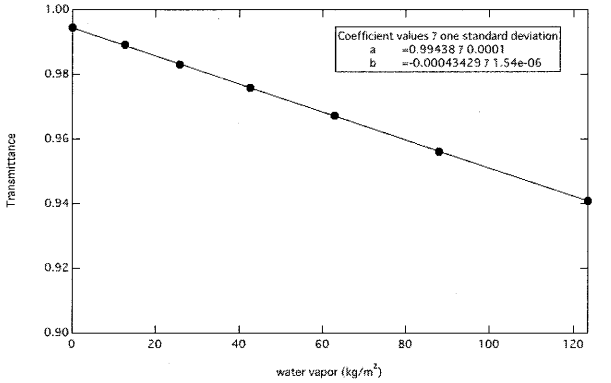

Fig. 8 Calculations of transmittance at ch10 (1.6 um) as a function of water vapor.

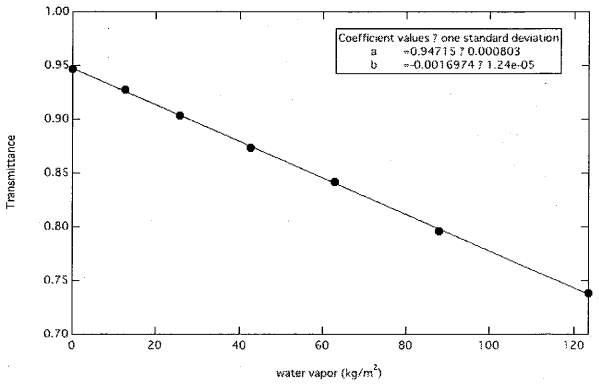

Fig. 9 Calculations of transmittance at ch11 (2.2 um) as a function of water vapor.

Figure 8 shows the transmittance of direct solar radiation as a function of the water vapor amount at 1.6 um calculated with results of Fig. 4 and Fig. 6. Curve fitted line can be written as:

$$Tr_{wv} = a + b*wv, \ldots \quad (5)$$

where a = 0.99438, b = -0.00043429. When water vapor amount is 0.0, transmittance is not 1.0 due to the absorption with other gaseous compositions of the atmosphere. The optical thickness of gaseous composition except for water vapor is $tau_{o1.6}$ = 0.00018 and coefficients for a $_{1.6}$ = 1.0, b $_{1.6}$ = -0.00043674.

Figure 9 is same as Fig. 8 except for 2.2 um channel and curve fitted which can be written same as Eq. (5) where a = 0.94715, b = -0.0016975. The same as 1.6 um channel, the optical thickness of gaseous composition except for water vapor is $tau_{o2.2}$= 0.0181 and coefficients of Eq. (5) will be $a_{2.2}$ = 1.0 and $b_{2.2}$ = -0.00017922. After subtracting affect water vapor absorption from transmittance measured by Skyraiometer using water vapor amount derived from 0.94 um, we can determine the aerosol optical thickness at 1.6 um and 2.2 um as follows,

$$tau_{a1.6} = -\log(Tr / Tr_{wv1.6}(wv)) \cos(theta_0) - tau_{o1.6}, \ldots \quad (6)$$

$$tau_{a2.2} = -\log(Tr / Tr_{wv2.2}(wv)) \cos(theta_0) - tau_{o2.2}. \ldots \quad (7)$$

4. Results from the observation

We have applied the method described

heretofore to the measurements obtained from Skyradiometer at Fukuejima one of the SKYNET observatory site. Figure 10 illustrates the aerosol optical thickness at 0.34 um, 0.4 um, 0.5 um, 0.675 um, 0.87 um, 1.02 um, 1.6 um, 2.2 um and the column water vapor amount as a function of time on 3 Apr. 2008. Calibration constants of Skyradiometer channels were determined using these measurements because Fig. 10 shows that atmosphere condition was stable and low water vapor.

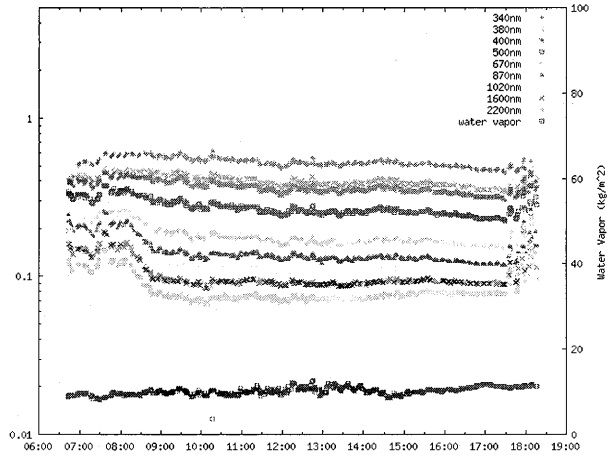

Fig. 10 Aerosol optical thickness at 0.34, 0.38, 0.40, 0.50, 0.67, 0.87, 1.02, 1.6, 2.2 um and water vapor amount on 3 Apr. 2008.

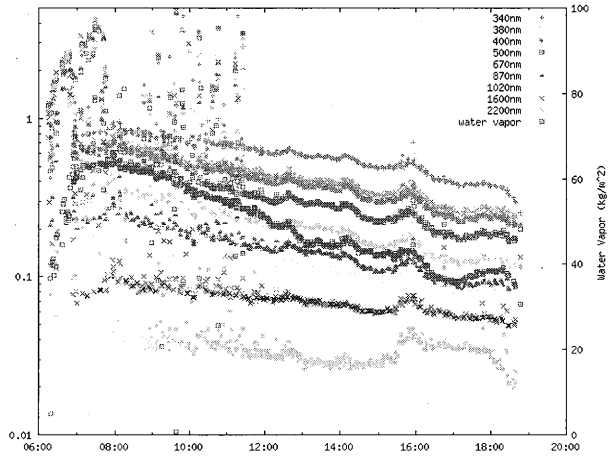

Fig. 11 Same as Fig.10 execpt on 6 Aug. 2008.

Figure 11 is same as Fig. 10 except for date on 6 Aug. 2008. Figure 11 shows that the aerosol optical thickness at 1.6 um and 2.2 um indicate the same variation as the optical thickness of the other channels. This means that the effects of water vapor absorption is successfully removed.

5. Summary

A method has been presented for determining the aerosol optical thickness from direct solar radiation measurements using Skyradiometer POM-02 at 1.6 um and 2.2 um that are weakly absorbed by water vapor. It is shown that we can remove the effect of absorption by water vapor using 0.94 um channel of Skyradiomter,.

References

1) T. Nakajima, T. Y. Nakajima, A. Higurashi, I. Sano, T. Takamura, H. Ishida and N. Schutgens, A study of aerosol and cloud information retrievals from CAI Imager on board GOSAT Satellite. J. Remote Sens. Soc. Jp., 28, 178-189, 2008

2) F. X. Kneizys, E. P. Shettle, L. W. Abreu, J. H. Chetwynd, G. P. Anderson, W. O. Gallery, J. E. A. Selby, and S. A. Clough, 1988: Users Guide to LOWTRAN 7. AFGL-TR-88-0177.

Aerosol retrieval from GLI over land and its comparison with ground observation

Satoru Fukuda[1], Teruyuki Nakajima[1], Akiko Higurashi[2], Nobuyuki Kikuchi[2], and Takashi Y. Nakajima[3]

[1]*Center for Climate System Research, The University of Tokyo, 5-1-5 Kashiwanoha, Kashiwa-city, Chiba, 277-8568, JAPAN, satoru@ccsr.u-tokyo.ac.jp, teruyuki@ccsr.u-tokyo.ac.jp*

[2]*National Institute for Environmental Studies, 16-2 Onogawa, Tsukuba-city, Ibaraki, 305-8506, JAPAN, hakiko@nies.go.jp, kikuchi.nobuyuki@nies.go.jp*

[3]*Tokai University, 2-28-4 Tomigaya, Shibuya-ku, Tokyo, 151-0063, JAPAN, nkjm@yoyogi.ycc.u-tokai.ac.jp*

Abstract

Aerosol optical properties such as optical thickness and Angstrom exponent are retrieved over land using ADEOS-II/GLI data in 2003. The retrieval results are compared with AERONET data. In some areas, such as North America and Europe, these GLI-derived aerosol optical thickness shows good comparison with ground observation. But, in some areas such as Southeast Asia, South Asia, and near Sahara desert region, GLI-derived aerosol optical thickness is smaller than AERONET-derived aerosol optical thickness.

Keywords: aerosol, remote sensing, GLI

1. Introduction

Aerosols have a significant influence on not only human health, but also earth radiation budget. Because there is still a large uncertainty about radiative forcing created by aerosols[1)], investigating aerosols' spatial and temporal distribution is important. The Global Imager onboard the Advanced Earth Observing Satellite-II (ADEOS-II/GLI), which was launched on December 2002, has 36 channels from near ultraviolet to infrared. In these channels, 380nm is a unique channel for GLI, and it is thought to be good for aerosol remote sensing over land. Because land surface reflectance at the wavelength is very small (mostly less than 0.1) (Figure 1) except for ice or snow area, we can extract aerosols' information from the radiance of the channel.

2. Algorithm description

In aerosol retrieval over land, the estimation of ground albedo (Ag) is one of the most important points. We assume a Lanbertian surface, and calculate Ag by selecting the minimum reflectance pixels for every 28 days and correcting Rayleigh scattering. As an aerosol model, we use a spherical model. Under these assumptions, radiative transfer calculation is performed and Look Up Tables (LUTs) are constructed by the radiative transfer codes RSTAR[2)3)] and PSTAR. Using these Ag and LUTs, aerosol properties are retrieved. Figure 2 shows algorithm flow chart. We use NCEP re-analysis data as meteorological data and TOMS ozone data. In enough vegetated area, 380nm and 678nm are used, and both aerosol optical thickness (τ) and Angstrom exponent (α) are retrieved. In not enough vegetated area, on the other hand, only 380nm is used, and τ is retrieved. This is because 678nm is too noisy to use in bare land region. Figure 3 shows one example of our retrieval. You can see an aerosol plume around central Europe. Angstrom exponent is an index of aerosol size. Small α means large particle, and large α indicates small particle. Around desert area, α has large value compared with other area in figure 3.

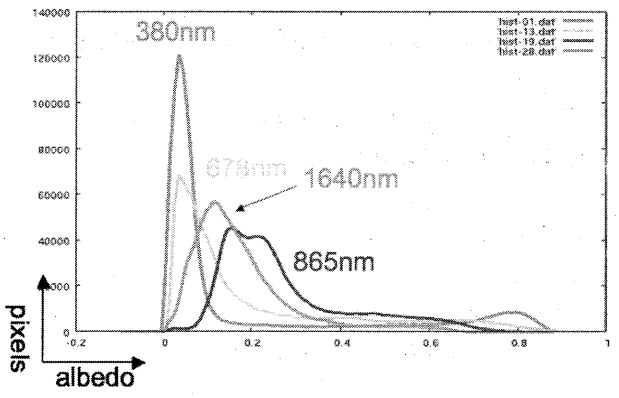

Figure 1. Histogram of ground albedo. 3-28 April 2003. X-axis means albedo and Y-axis means probability density function. Red, green, blue, pink means 380nm, 678nm, 865nm, 1640nm, respectively.

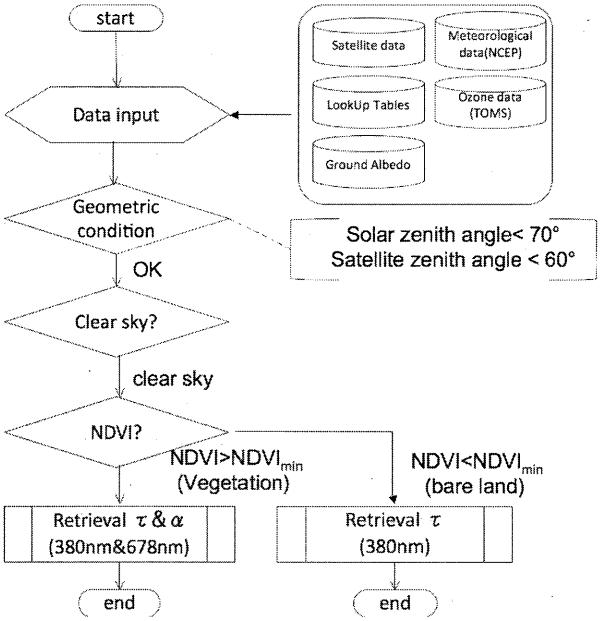

Figure 2. Algorithm flow chart

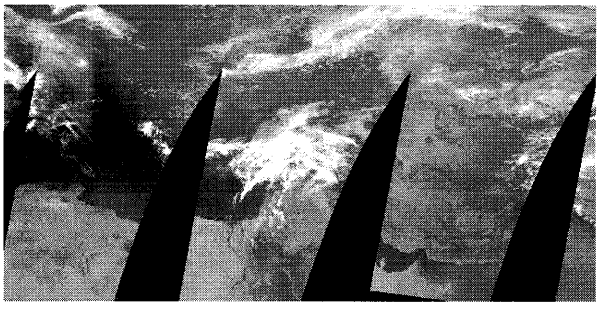

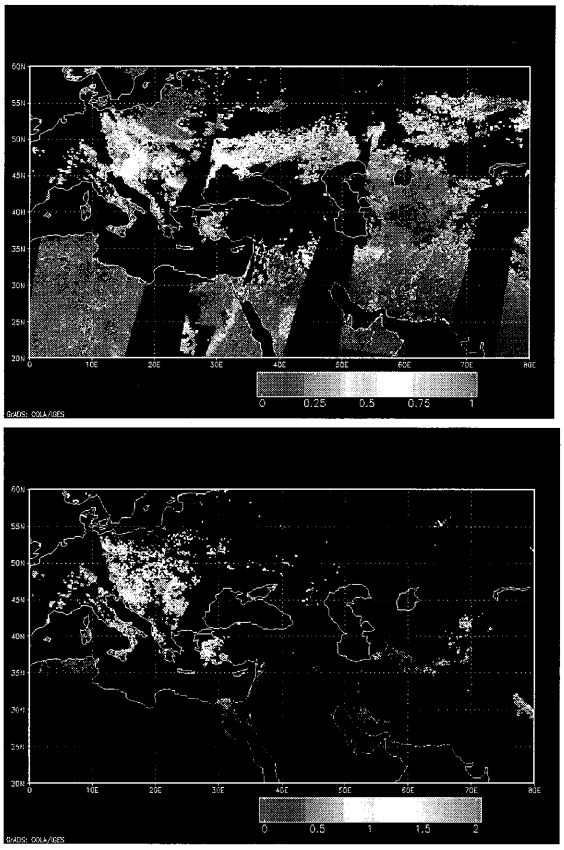

Figure 3. True color RGB image (up), τ at 550nm (center), Angstrom exponent (down) on 25 April 2003 derived from ADEOS-II/GLI

3. Seasonal variation

Figure 4 shows monthly mean τ derived by GLI on April, June, August and October. This algorithm is applied over land, and I connected the product of the two channel method (Higurashi et al., 1999, 2000)[3)4)] over ocean. You can see seasonal variations of τ in some regions. In east Siberia, you can find a large τ in October. This is thought to be forest fires. In east Asia, you can also see large aerosol optical thickness in June. Here, aerosols flow out from East Asia to North Pacific Ocean. In southern Africa, there is a large τ area, but the seasonal dependency is not clear. This aerosol signal is thought to be a mixture of biomass burning and dust aerosol from Sahara desert. In India, west Asia, and Sahara region, there is a very clear contrast between land and ocean. In that region, τ derived over land is quite smaller than that over ocean. The reason for this is thought to be that aerosols' optical properties over these areas are not good. More and more tuning of aerosol parameters is needed.

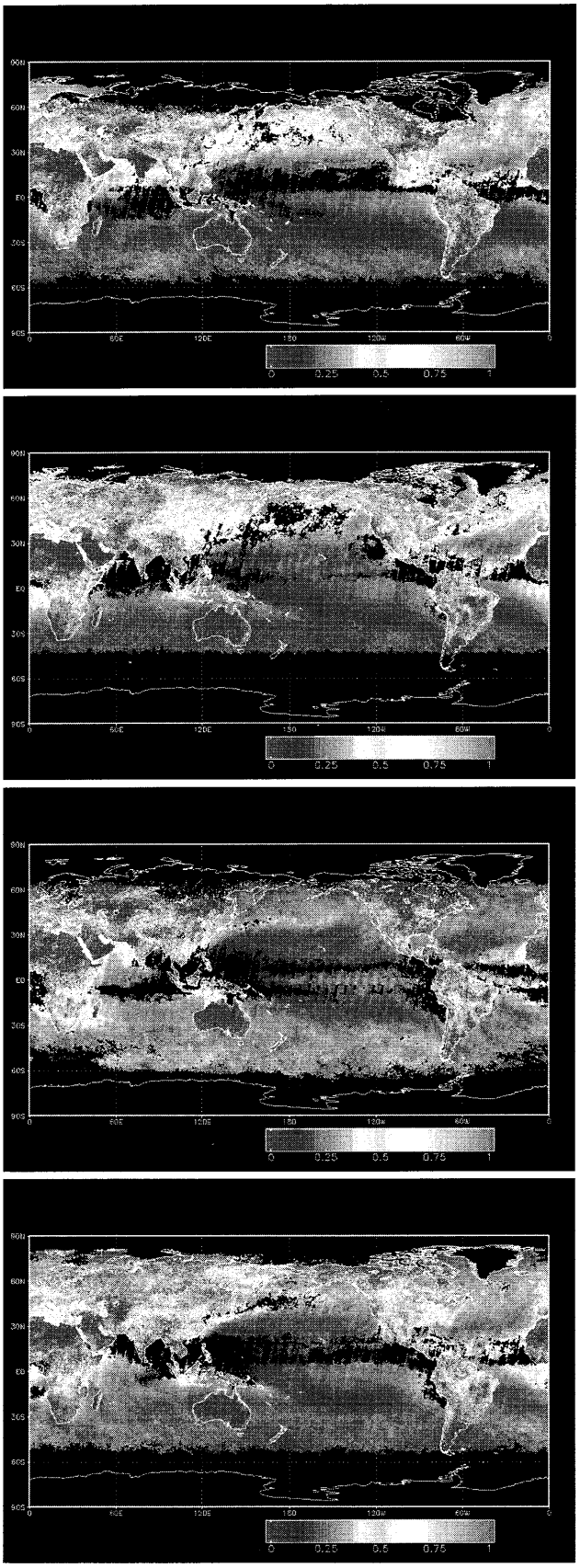

Figure 4: Monthly mean τ derived by GLI on April, June, August and October (in descending order) in 2003.

4. Comparison with AERONET

We also compare these results with data form AErosol RObotic NETwork (AERONET)[6], which is ground-based remote sensing network managed by NASA/Goddard Space Flight Center. The comparison period is April to October in 2003. The number of stations that we use in this study is more than 70. The quality checks of this study are as follows: (1) 16 grid points (4x4 square) are selected near each AERONET site. (2) If more than 3 pixels are retrieved successfully and standard deviation of the optical thickness is less than 0.1, then the average value is used. We use AERONET level 2.0 data within 60 minutes of GLI observation.

In some stations, the correlation results are good. But other stations, there are large differences between GLI-derived τ and AERONET-derived τ. Figure 5 shows the mean error (ME) of both τ. ME is defined as follows;

$$ME = \sum_i \left(\tau_i^{AERONET} - \tau_i^{GLI} \right)$$

In Southeast Asia, South Asia, and near Sahara Desert region, ME has relatively large positive value. This distribution of ME seems to show Single Scattering Albedo (SSA) information. In other words, the areas that have large positive ME, are considered to have small SSA.

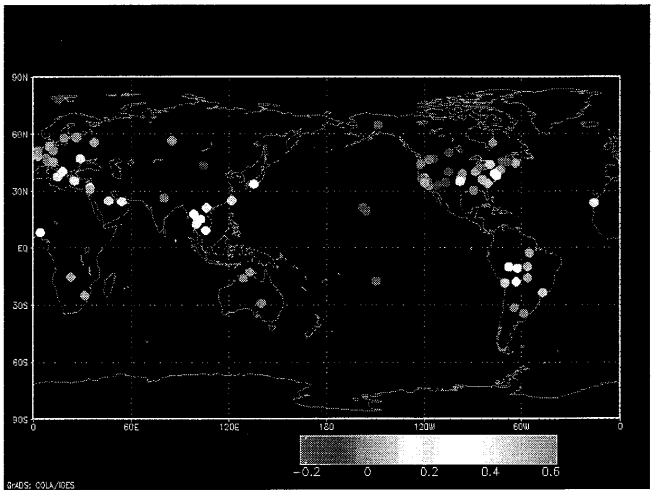

Figure 5. ME of $\tau_{AERONET}$ and τ_{GLI}

Acknowledgements

We would like to thank JAXA/EORC for supplying the GLI data. We also thank the AERONET PIs and their staff for establishing and maintaining the sites used in this study.

References

1) Intergovernmental Panel on Climate Change (IPCC), Climate Change 2007: The Physical Science Basis, edited by S. Solomon et al., Cambridge Univ. Press, 2007.

2) T. Nakajima, and M. Tanaka, 1986: Matrix formulations for the transfer of solar radiation in a plane-parallel scattering atmosphere. J. Quant. Spectrosc. Radiat. Transfer, 35, 13-21.

3) T. Nakajima, and M. Tanaka, 1988: Algorithms for radiative intensity calculations in moderately thick atmospheres using a truncation approximation. J. Quant. Spectrosc. Radiat. Transfer, 40, 51-69.

4) A. Higurashi, and T. Nakajima, 1999: Development of a Two-Channel Aerosol Retrieval Algorithm on a Global Scale Using NOAA AVHRR, J. Atmos.Sci., 56, 924-941.

5) A. Higurashi, T. Nakajima, B. N. Holben, A. Smirnov, R. Frouin, B. Chatenet, 2000: A Study of Global Aerosol Optical Climatology with Two-Channel AVHRR Remote Sensing, J. Climate, 13, 2011-2027

6) B. N. Holben, T. F. Eck, I. Slutsker, D. Tanre, J. P. Buis, A. Setzer, E. Vermote, J. A. Reagan, Y. J. Kaufman, T. Nakajima, F. Lavenu, I. Jankowiak, and A. Smirnov, 1998: AERONET – A federated instrument network and data archive for aerosol characterization, Rem. Sens. Environ., 66, 1–16.

2008 **Dust Field Experiments over Northwest China**

Jianrong Bi[1], Jianping Huang[1], Wu Zhang[1], Zhongwei Huang[1], Jinsen Shi[1], Guoyin Wang[1], Si-Chee Tsay[2], Zhanqing Li[3]

[1]*College of Atmospheric Sciences, Lanzhou University, Lanzhou, 730000, China*

[2]*NASA Goddard Space Flight Center, Greenbelt, Maryland, ETATS-UNIS*

[3]*Department of Atmospheric and Oceanic Science and the Earth System Science Interdisciplinary Center, University of Maryland, College Park, Maryland, ETATS-UNIS*

Abstract

Northwestern china, as one of the primary dust storm source region, transports a mass of desert aerosol particles into the atmosphere every year. Dust aerosols could influence on climate and climate change, which are direct and indirect climate effect, and may contribute to global warming. However, because lack of the size distribution, spatial and temporal variety of dust aerosols, these effect actions still exist much uncertainty. This extended abstract is to introduce the 2008 confederative dust field campaigns over Northwest China.

Keywords **:** dust storm, climate change, direct and indirect climate effect

1. Introduction

Global warming has become the governmental and people's focusing topic, recently. And it seriously influences on people's living and producing activities, and may have contributed to the desertification of the Northwest China (Huang et al, 2006a, b). According to some authoritative departments' research, the increasing speed of yearly average temperature is about 0.03042℃/year over Loess Plateau region, which is 8 times over the whole China. Is dust aerosol the cause of the remarkable warming over Loess Plateau region? If that, how the dust aerosol affect these warming? Which way is the dust aerosol absorbing energy?

In order to answer those questions, we took a China-US joined dust field campaigns over Northwest China during March to May, 2008.

2. Field Campaign

The field campaigns includes one permanent observatory and two mobile sites, which is SACOL (35.946^{0}N, 104.137^{0}E, 1970m), Jingtai (37.337^{0}N, 104.139^{0}E, 1592m) and Zhangye (39.019^{0}N, 100.276^{0}E, 1460m), respectively. Semi-Arid Climate and Environment Observatory of Lanzhou University (SACOL) has been established since 2005 (Huang et al, 2008). It is about 48km away from the centre of Lanzhou city, situated at the southern bank of Yellow River in Gansu province, Northwestern China. It located on so called China-Loess Plateau is about 1965.8m above sea level. SACOL consists of a large set of instruments, for instance, surface radiation fluxes, cloud and aerosol properties, temperature and water vapor profile, sky conditions, sensible heat and latent heat fluxes, energy balance of land-atmosphere, meteorology of boundary layer and ambient air monitoring systems, and so on. It has joined in CEOP, AERONET and MPLNET (*Huang et al., 2008*).

Jingtai site is a mobile facility and located in the north of SACOL (Fig. 1). It is about 200km north from Lanzhou city. And it situated at the southern of Tenggeli Desert, which is about 40km south away from the desert. It is mainly including surface radiation fluxes, CE318 sun photometer, MPL lidar, three wavelength nephelometer, Total Sky Imager, surface meteorological, sensible heat and latent heat fluxes, soil temperature, vapor water content of soil and soil heat flux.

Zhangye site is the NASA mobile facility and consists of so called SMART (Surface Measurements for Atmospheric Radiative Transfer) and COMMIT (Chemical, Optical, and Microphysical Measurements of In-situ Troposphere), located in the northwest of SACOL and Jingtai, which situated at the southern of Taklimakan Desert and near by the Maowusu Desert (Fig. 1). SMART and COMMIT are come from the NASA mission. This article is mainly to discuss some primary result of the Jingtai mobile facility.

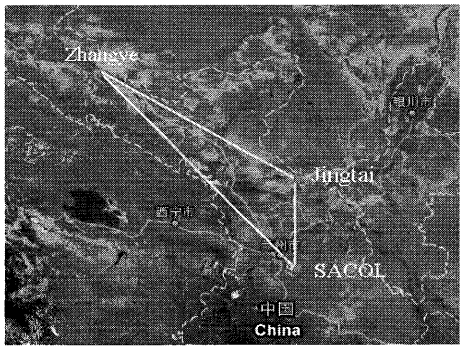

Fig. 1 Three sites of 2008 Field Campaign

3. Preliminary Results

As example, we only present some preliminary results from the Jingtai mobile facility. More detail results please see our poster. Figure 2 shows the Downward Irradiance per 12 hours average (daytime) of Solar (CM21 pyranometer) and Terrestrial (CG4 pyrgeometer) Radiation of April, 2008. From Fig. 2, indicate that the diurnal variability (daytime) of solar radiation is more distinct than terrestrial radiation.

Fig. 3 (a) is the diurnal variability of Micro-Pulse Lidar (MPL) normalized relative backscatter's for April 26, 2008, and (b) is the corresponding time's sky conditions. From 08:00-14:00 (Beijing Time), there is a cloud layer with dust at about 4km height, but the aerosol particles near surface is almost free. However, a dust storm started at about 15:00, and it becomes stronger around 17:00 as displayed from both MPL and the total sky imager (TSI 440).

Fig. 4 (a), (b) is the comparisons of MODIS Aqua retrieved downward shortwave and longwave radiations with Jingtai ground-base observation from March 1 to May 31, 2008. For clear sky, the comparative result of SW is much better than that cloudy sky. The shortwave radiation from Aqua retrieval is a litter more than ground observation. For the clear sky, the bias is 8.71 Wm^2 (1.09%), and the standard deviation is 70.16 Wm^2 (8.81%). Whereas, when it is cloudy, the comparative result of LW is better than that clear sky. The longwave radiation from Aqua retrieval is less than ground observation, about -30.29 Wm^2 (9.91%), and the standard deviation of the difference is 43.1 Wm^2 (14.11%).

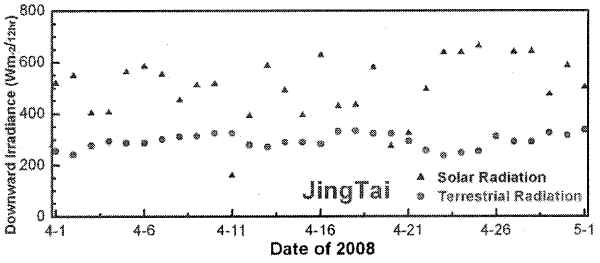

Fig. 2 Downward Irradiance of Jingtai

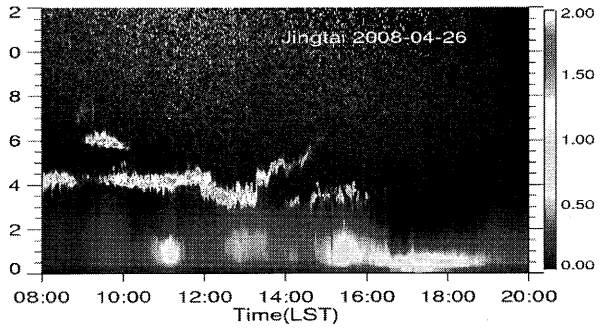

Fig. 3(a) MPL normalized relative backscatter at Jingtai of April 26, 2008.

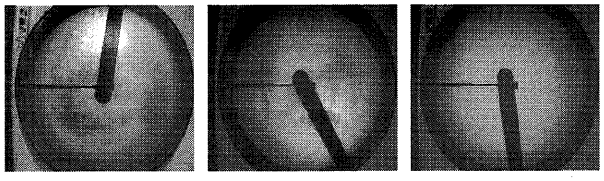
10:00 15:30 16:30

Fig. 3(b) Sky Conditions of TSI 440 (LST)

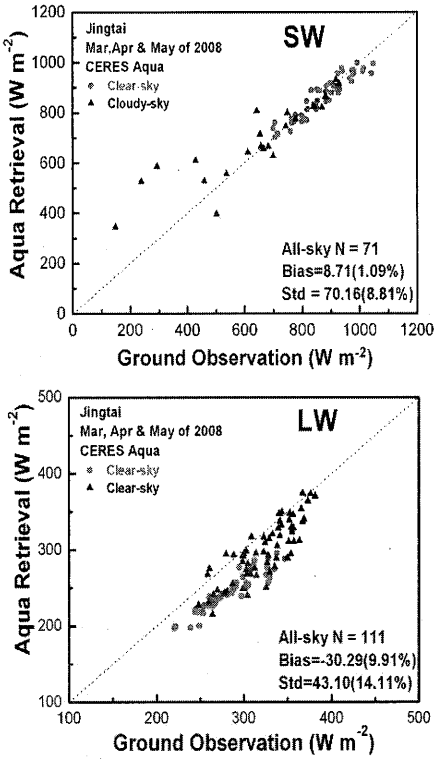

Fig. 4 Comparisons of MODIS Aqua retrieved downward shortwave (a) and longwave (b) radiations with ground-base

observation.

4. Conclusions and Discussions

Although there are a lot of dust radiative effect researches, the uncertainty is still remarkable due to lack of field observational experiments, especially over the Northwest China. To improving our understanding of the uncertainty, our mobile facility trailer, together with SACOL site, will take field campaign every year. We believe, these measurements will help to understand the dust radiative effect.

5. References

Huang, J., and co-authors, 2008a:, An overview of the semi-arid climate and environment research observatory over Loess Plateau, *Advance in Atmospheric Sciences,* ***25***(6), 1-16.

Huang, J., and co-authors, 2006a: Dusty cloud radiative forcing derived from satellite data for middle latitude regions of East Asia, *Progress in Natural Science.* ***16***(10), 1084-1089.

Huang, J., and Co-authors, 2006b: Satellite-based assessment of possible dust aerosols semi-direct effect on cloud water path over East Asia, *Geophys. Res. Lett.,* Vol. 33, doi: 10.1029/2006GL026561.

Radiative Characteristics of Heavily Loaded Aerosols Observed at Mandalgobi, Mongolia 2002

Shin-ichi Kaneta[1], Cui Yu[2], Itaru Okada[2], Tamio Takamura[2], Yoshiaki Honda[2]

[1]*Asia Air Survey Co.,Ltd., 1-2-2 Manpukuji, Asao-ku, KAWASAKI 215-0004, JAPAN, sni.kaneta@ajiko.co.jp*

[2]*Center for Environmental Remote Sensing(CEReS), Chiba University, 1-33 Yayoi-cho, Inage-ku, CHIBA 263-852, JAPAN, cuiyu@graduate.chiba-u.jp, takamura@faculty.chiba-u.jp,yhonda@faculty.chiba-u.jp*

Abstract

Heavy aerosol loading phenomena have been observed during an intensive field campaign of Aug. 10 to 19, 2002 over Mandalgobi, Mongolia. These phenomena continued during several days. Due to sky radiometer measurements, the optical characteristics are analyzed for optical thickness and single scattering albedo of the aerosol. In parallel, downward solar radiation has been also observed. As a result, the radiative effects of such aerosols were estimated to be 47.0W/m2 for the optical thickness 0.48, compared with 10.2W/m2 for 0.07 in AOT before the phenomena. Simultaneous analysis of the single scattering albedo shows the similar values of 0.97-0.98, that is relatively non absorptive aerosol.

Keywords : SKYNET, Biomass Burning, Atmospheric Aerosol

1. Introduction

Smoke aerosol from biomass burning around South American continent have been well studied in many papers (Holben et al. 1996, Kaufman et al. 1998, Remer et al. 1998). In contrast Asian region has less information about it. The SKYNET is ground based observation network around Asia. Its main target is radiative characteristics of atmospheric aerosol using the combination of sky radiometer and pyranometer and other instruments. Mandalgovi is one of the SKYNET observation site for steady observation. The long-term background aerosol characteristics which are not contaminated by human-induced emissions are observed at this site. In addition to that observation, Center for Environmental Remote Sensing, Chiba University and other organizations had annually conducted an intensive observation every summer since 1996 synchronize with satellite vegetation monitoring. In summer of 2002 heavy aerosol loading phenomena was observed during the intensive observation. This kind of phenomena had not been happened in other years especially in summer season.

This paper presents result from an analysis of radiative characteristics of atmospheric aerosol under heavy aerosol loading phenomena during August 2002 around Mandalgobi, Mongolia.

2. Instrumentation and Analysis Method

In order to observe aerosol and radiation, two major instruments were set with meteorological instruments as listed in Table 1.

Sky radiometer POM-01 (PREDE, Japan) is a kind of spectral radiometer, which has seven filters ranging from 315 to 1020nm including water vapor channel (Table 1). It is designed for measuring direct and diffuse solar radiance at preset angles. A sky radiometer has a unique feature which is no requirement of traditional calibration such as a use of Langley method to estimate aerosol optical thickness. It needs only solid view angle (SVA) for diffuse solar radiance measurement. SVA is dependent on each instrument but not changed with time, unlike filter system. Also it has basically no dependence on wavelength. The time variation of SVA of the sky radiometer (S/N:PS090212) settled in Mandalgobi Airport during 1999 to 2004. The entire average of SVA is 2.49×10^{-4} str and the standard deviation is within $\pm$ 3%.

SKYRAD.pack is the software suite developed for sky radiometer analysis(ref). It can estimate optical properties of aerosol such as optical thickness (AOT), single scattering albedo (SSA) and size distribution. The latest version (V.4.2) has a retrieval ability of SSA for each channel and also Improved Langley method capability for instrumental calibration system. SSA is sensitive to diffuse(scattered) radiation. Due to this feature, sky radiometer can give AOT and SSA simultaneously. The reliable calibration constants are required through these procedures. The Improved Langley method has been applied to get them using more than 75 cases during 1 June to 5 August in 2002 for each wavelength. The maximum RMSE is 3.8 % at 400 nm and minimum RMSE 1.5 % at 675 nm (

Table 2).

Table 1. Instruments for Estimating Aerosol Radiative Characteristics at Mandalgobi Mongolia.

Instrument	Manufacturer	Obs. Duration	Remarks	Location
Sky radiometer	POM-01, Prede, Japan	10 Min	315,400,500, 675,870,940, 1020	Airport
Pyranometer	CM21, K & Z, Holland	10 Sec	305-2800nm (50%point)	Field
Humidity/Temp Probe	HMP45A Vaisala, Finland	10 Sec		Field
Barometer		1 Sec		Field

Radiative effects of aerosol can be estimated by using downward solar radiation observed by a pyranometer CM21(Kipp & Zonen, Holand). The accuracy of the instrument is less than 10W/m2 for 1000W/2 at the normal incidence.

The radiative effect of aerosol, ARE_{SFC}, is estimated by

$$ARE_{SFC} = \overline{F}^{\downarrow}_{SFC.AER}\ (1-R), \qquad (1)$$

where R is surface reflectance and,

$$\overline{F}^{\downarrow}_{SFC.AER} = \frac{\int_t \left[F^{\downarrow}_{OBS}(t) - F^{\downarrow}_{SFC.RAY}(t)\right] dt}{24*3600}. \qquad (2)$$

$F_{OBS}(t)$ and $F_{SFC.RAY}(t)$ are solar irradiance observed by the pyranometer and estimated by a calculation of radiative transfer including water vapor effect, respectively. Equation (1) means a direct effect of aerosol.

Table 2 Calibration constants F0 of sky radiometer (S/N:PS090212) by improved Langley method during 1 June to 5 August 2002.

wavelength[nm]	400	500	675	870	1020
F0	1.236E-04	2.463E-04	2.942E-04	2.384E-04	1.365E-04
std.dev.	4.6E-06	4.9E-06	4.5E-06	3.8E-06	2.8E-06
RMSE[%]	3.8	2.0	1.5	1.6	2.0
num. of data[half day]	82	78	75	81	83

Fig 1. The location of observation site. Mandalgobi, Mongolia (latitude: 45.44315N, longitude: 106.15583E) and sonde observation site Ulaan-baatar Mongolia (latitude: 47.91N, longitude: 106.86), Erenhot China (latitude: 43.65N, longitude: 112.00E).

3. Data

Mandalgobi is the capital of the Dundgovi Province on the border of the Gobi Desert, about 300km south of Ulaanbaator, Mongolia(Fig.1). The observation area shows a great plain with any trees. It is a grass field in summer and sandy in winter season.

The atmospheric observation was routinely performed at the Mandalgobi Airport since 1999, and an intensive observation was conducted during 10 – 19 Aug 2002 for a satellite validation activity.

Through the intensive campaign period, we met heavy aerosol loading phenomena such as white sky. It is interesting to analyze such optical characteristics of aerosol before and after the phenomena. Fig 2 is time variation of AOT (@500nm) and Angstrom's parameter alpha during this observation period. We selected typical three days due to sky conditions, Aug. 2 for clear sky, Aug. 15 for typical hazy day and Aug. 25 for light hazy day.

A downward solar radiation for an aerosol-free atmosphere is required in order to clarify radiative effects of aerosol. The radiative transfer code RSTAR 5b is a powerful tool using a discrete ordinate method (Nakajima and Tanaka, 1988). Also the AOT and SSA of aerosol derived from the sky radiometer data should be confirmed through the calculation of downward solar radiation. Ancillary data in the transfer calculation are supplied from the regional objective analysis data of the Japan Meteorological Agency (JMA/GPV), such as pressure, temperature, and water vapor. Atmospheric parameters for missing data such as ozone, carbon dioxide etc is introduced from the subarctic summer model of McClatchey's model (Kneizys et al. 1988).

Surface reflectivity was estimated by MODIS Terra/Aqua, as shown in Table 3. It is dependent on wavelength and interpolated into each wavelength of the transfer calculation.

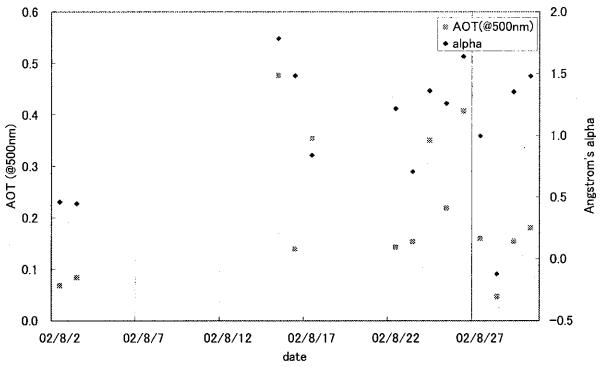

Fig 2. Variation of AOT and Angstrom's alpha.

Table 3. Surface spectral reflectance estimated by MODIS.

SCENE	DATE	Sat.	Solar zenith angle (deg.)	AOT	Band and wavelength (nm) band3 459-479	band4 545-565	band1 620-670	band2 841-876nm	band5 1230-1250	band6 1628-1652	band7 2105-2155	Remarks
MOD021KM.A2002214.0400	02.Aug.	Terra	30.65	0.07	0.08	0.13	0.18	0.24	0.29	0.31	0.27	Clear day with AOT known
MOD021KM.A2002223.0350	11.Aug.	Terra	33.44	0.14	0.07	0.12	0.16	0.24	0.28	0.29	0.24	Clear day with AOT known
MYD021KM_A2002223_0530	11.Aug.	Aqua	31.19	0.14	0.08	0.14	0.19	0.27	0.31	0.32	0.27	Clear day with AOT known
MOD021KM.A2002224.0435	12.Aug.	Terra	31.14	0.07	0.09	0.14	0.18	0.28	0.32	0.32	0.26	Clear day with AOT known
MYD021KM_A2002224_0615	12.Aug.	Aqua	34.67	0.07	0.07	0.12	0.17	0.25	0.28	0.28	0.24	Clear day with AOT known
MOD021KM.A2002225.0340	13.Aug.	Terra	35.09	0.09	0.07	0.12	0.17	0.26	0.29	0.30	0.25	Clear day with AOT known
MYD021KM_A2002225_0520	13.Aug.	Aqua	31.32	0.09	0.08	0.14	0.19	0.28	0.32	0.32	0.27	Clear day with AOT known
MOD021KM.A2002228.0410	16.Aug.	Terra	33.44	0.14	0.08	0.13	0.18	0.27	0.31	0.32	0.26	Clear day with AOT known
MOD021KM.A2002234.0335	22.Aug.	Terra	38.14	0.14	0.08	0.13	0.18	0.27	0.31	0.32	0.26	Clear day with AOT known
MOD021KM.A2002237.0405	25.Aug.	Terra	36.55	0.22	0.08	0.13	0.18	0.26	0.31	0.32	0.27	Clear day with AOT known
MOD021KM.A2002240.0435	28.Aug.	Terra	36.20	0.05	0.09	0.15	0.21	0.30	0.34	0.35	0.30	Clear day with AOT known
MOD021KM.A2002217.0430	05.Aug.	Terra	29.39	0.08	0.08	0.14	0.19	0.26	0.31	0.32	0.28	Clear day with supposed AOT
MOD021KM.A2002233.0430	21.Aug.	Terra	34.06	0.10	0.11	0.15	0.19	0.28	0.32	0.33	0.27	Clear day with supposed AOT
MYD021KM_A2002233_0610	21.Aug.	Aqua	36.88	0.14	0.08	0.13	0.17	0.25	0.29	0.30	0.25	Clear day with AOT known
MYD021KM_A2002237_0545	25.Aug.	Aqua	36.40	0.22	0.11	0.16	0.21	0.29	0.33	0.33	0.28	Clear day with AOT known
Average					0.08	0.14	0.18	0.27	0.31	0.31	0.27	
Deviation					0.012	0.012	0.013	0.018	0.017	0.016	0.015	

4. Results and discussion

First of all we compare the downward global solar irradiance with observed aerosol parameters (AOT, SSA) and other atmospheric parameters and surface reflectance estimated by MODIS with pyranometer observation value.

The consistency between calculation and observation was summarized in Table 4. In this table cloud contaminated data were screened manually. We used smoothness of Pyranometer data for as a criterion of this screening. We also eliminate the data with large solar zenith angle (larger than 80°) to minimize the error of levelness of the pyranometer installation. The RMSE of entire data is 8.00 W/m2. The maximum relative error is -2.37 %. The error under heavy aerosol condition (Aug 15) is larger than the other days.

Table 4. Comparison of global solar irradiance under the clear sky condition.

date	time	SZA(deg.)	obs.[W/m2]	calc.[W/m2]	error[W/m2]	error [%]
2-Aug	12:00:04	30.3	902.99	896.50	-6.49	-0.72
	13:00:03	27.4	931.73	925.10	-6.63	-0.72
15-Aug	12:00:04	33.6	815.53	804.79	-10.74	-1.33
	13:00:04	31.1	832.79	832.20	-0.59	-0.07
	15:00:04	40.1	742.57	725.40	-17.17	-2.37
	15:54:27	48.0	620.40	614.88	-5.52	-0.90
25-Aug	8:00:04	71.2	264.93	267.78	2.85	+1.06
	9:00:04	60.8	458.04	451.72	-6.32	-1.40
	10:00:04	51.0	618.77	614.97	-3.80	-0.62
	11:00:04	42.5	749.81	741.82	-7.99	-1.08
	12:00:04	36.5	827.83	820.74	-7.09	-0.86
RMSE					8.00	[W/m2]

Aerosol radiative effects estimated by above aerosol and other atmospheric conditions are summarized in Fig 3. Each point indicates calculated ARE by observed aerosol parameters (AOT and SSA), solid lines indicate the width of error caused by solid view angle of sky radiometer. Four dotted lines indicate the simulated values with different SSA values (constant value for all wavelengths) as rough reference. Aug. 2 was clear sky condition and pre-heavy loading phenomena. Aug. 15 was the just a middle of heavy loading phenomena. Aug 25 was 10 days after since heavy loading. But AOT of Aug. 25 indicates that the influence of this phenomena being still remained.

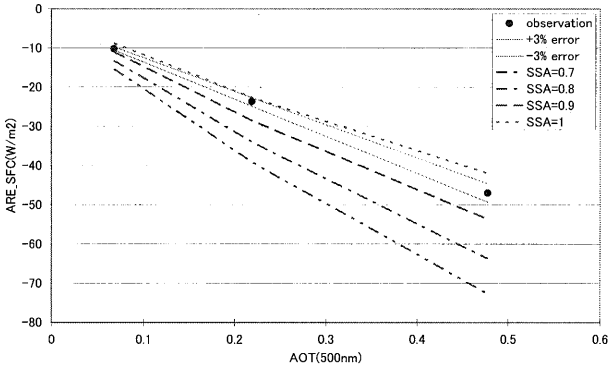

Fig 3. Relationship between AOT(@500nm) and ARE at the surface.

Noticeable points of this figure are,

1. SSA was not changing during this period (before and after the forest fire).
2. No significant absorption is found under heavy aerosol loading event (Aug 15, 25).
3. Maximum error of ARE cause by solid view angle is 2 W/m^2.

Then we tried to estimate error of other factors such as water vapor and ground reflectance. We used sonde sounding data to estimate the error of water vapor density profile used in our calculation. We assumed the variation of sonde sounding data which are scattered around Mandalgobi as magnitude of error of JMA/GPV water vapor density. Erenhot, China (station number: 53068, latitude: 43.65N, longitude: 112.00E) and Ulaan-Baartor (station number: 44292, latitude: 47.91N, longitude: 106.86) were the nearest sonde station around Mandalgobi (see Fig 1). We used precipitable water content of both data for error estimation. Table 5 is the result of this error estimation. The maximum

error cause by water vapor density is about 10W/m^2.

Table 5. Effect of water vapor error to the global solar irradiance.

date	PWC(mm)			daily average [W/m2]			error [W/m2]	
	sonde data		JMA-GPV	sonde data		JMA-GPV		
	Erenhot	Ulaan-Baator		Erenhot	Ulaan-Baator		Erenhot	Ulaan-Baator
2-Aug-02	33.14	14.92	27.82	337.84	350.88	340.91	-3.08	9.97
15-Aug-02	18.61	19.98	16.69	325.73	324.59	327.22	-1.49	-2.63
25-Aug-02	40.12	13.75	17.05	291.69	314.52	304.82	-13.13	9.70

Error due to the surface reflectance is also summarized in Table 6. We used deviation of 15 days data for error estimation. The maximum error is about 0.2 W/m^2.

Table 6. Effect of surface reflectance error to the global solar irradiance.

date	Daily average [W/m2]			Error [W/m2]		Error [%]	
	mean	mean+sigma	mean-sigma	mean+sigma	mean-sigma	mean+sigma	mean-sigma
2-Aug-02	340.91	341.11	340.73	0.20	-0.19	0.00	0.00
15-Aug-02	327.22	327.41	327.05	0.19	-0.16	0.00	0.00
25-Aug-02	304.82	305.00	304.66	0.18	-0.16	0.00	0.00

The discrepancy between observation and calculation of global solar irradiance (maximum 8.0 W/m^2 see Table 4) is within the total error of water vapor density profile (maximum 10.0 W/m^2) and solid view angle of sky radiometer (maximum 2.4 W/m^2). Effect of surface reflectance error is almost negligible.

5. Summary

We have performed several kinds of solar radiation measurements in Mandalgobi, Mongolia during August 2002. In this period heavily loaded aerosol were observed in this area. We estimate the aerosol radiative effect using sky radiometers data and compared with global solar irradiance observed by pyranometer. As a result, the radiative effects of such aerosols were estimated to be 47.0W/m2 for the optical thickness 0.48, compared with 10.2W/m2 for 0.07 in AOT before the phenomena. Simultaneous analysis of the single scattering albedo shows the similar values of 0.97-0.98, that is relatively non absorptive aerosol.

Acknowledgements

The intensive observation at Mandalgobi 2002 was conducted by Prof. Honda of the Chiba University. The continuous observation at Mandalgobi airport have been maintained by National Remote Sensing Center State committee for Nature and Environmental Control Ulaabaatar, Mongolia and SKYNET community.

References

B. N. Holben, A. Setzer, T. F. Eck, A. Pereira, I. Slutsker, Effect of dry-season biomass burning on Amazon basin aerosol concentrations and optical properties, 1992-1994, *J. Geophy. Res.*, *101*, 19465-19481, 1996.

Y. J. Kaufman, P. V. Hobbs, V. W. J. H. Kirchhoff, P. Artaxo, L. A. Remer, B. N. Holben, M. D. King, D. E. Ward, E. M. Prins, K. M. Longo, L. F. Mattos, C. A. Nobre, J. D. Spinhirne, Q. Ji, A. M. Thompson, J. F. Gleason, S. A. Christopher, S. –C. Tsay, Smoke, Clouds, and Radiation-Brazil (SCAR-B) experiment, *J. Geophy. Res.*, *103*, 31783-31808, 1998.

T. Nakajima, G. Tonna, R. Rao, P. Boi, Y. Kaufman, B. Holben, Use of sky brightness measurements from ground for remote sensing of particulate polydispersions, *Applied Optics*, *35*, 2672-2686, 1996.

L. A. Remer, Y. J. Kaufman, B. N. Holben, A. M. Thompson, D. McNamara, Biomass burning aerosol size distribution and modeled optical properties, *J. Geophy. Res.*, *103*, 31879-31891, 1998.

Kneizys, F. X., E. P. Shettle, L. W. Abreu, J. H. Chetwynd, G. P. Anderson, W. O. Gallery, J. E. A. Selby, and S. A. Clough, 1988: Users Guide to LOWTRAN 7. AFGL-TR-88-0177.

Nakajima, T., and M. Tanaka, Matrix formulations for the transfer of solar radiation in a plane-parallel scattering atmosphere. *J. Quant. Spectrosc. Radiat. Transfer*, *35*, 13-21, 1986.

Nakajima, T., and M. Tanaka, 1988: Algorithms for radiative intensity calculations in moderately thick atmospheres using a truncation approximation. *J. Quant. Spectrosc. Radiat. Transfer*, *40*, 51-69, 1988.

Shettle, E. P., and R. W. Fenn, 1979: Models for the aerosols of the lower atmosphere and the effects of humidity variations on their optical properties. AFGL-TR-79-0214.

SKYNET web page, http://atmos.cr.chiba-u.ac.jp/

Aerosol optical properties derived from AERONET Sun-photometer measurement over Dalanzadgad

Batbayar Jadamba[1], Tugjsuren Nas-Urt[2]

[1]*Mongolian University of Science and Technology, E-mail:tchbayar@yahoo.com*

[2]*Mongolian University of Science and Technology, P.O.B-157,Ulaanbaatar-46,Mongolia, E-mail:tugjsurn@must.edu.mn*

Abstract

The AERONET is global ground-based network of Sun/sky automated radiometers supported by NASA's Earth Observing System (EOS) and other international research institutions. AERONET Sun-photometer has been used to make measurements of solar radiation and aerosol properties at the Dalanzadgad site in Mongolia since February 1997. We have analyzed Aerosol Optical Thickness (AOT), and derived Angstrom exponent acquired by an AERONET Sun-photometer at Dalanzadgad of Mongolia. Monthly means computed from quality-assured daily means, seasonal trends are presented and discussed. Spring and early summer has the maximum seasonal average AOT and minimum seasonal average appears in winter of 2002-2003. Monthly average Angstrom exponents are indicates that aerosol mixtures of both coarse and fine mode particles, specially dust aerosol pattern over Dalanzadgad dominantly in spring (March-April).

Keywords: AERONET, AOT, Angstrom exponent

1. Introduction

One of the main problems of the regional climate understanding is atmospheric aerosol variability. The atmospheric aerosols have a complicated non-uniform structure, characterization and their optical properties. Thus ground based continuous monitoring of their physical and optical properties is necessary. The AERONET provides quality-assured data for aerosol optical properties measured by the Sun/sky multiwavelength radiometer over the World. AERONET facility processes and archives these data according to a standardized procedure for the retrieval of aerosol properties. One of the AERONET site at Dalanzadgad of Mongolia has been operated continuously since 1999. Recently, studies on the aerosol monitoring over Eastern Asia using AERONET Sun-photometer acquired aerosol optical thickness and Angstrom exponent measurement have been conducted in the research on Aerosol properties in a Chinese semiarid region (Xia Xiango at al., 2003), Seasonal and monthly variations of columnar aerosol optical properties over east Asia determined from multi-year MODIS, LIDAR, and AERONET Sun/sky radiometer measurements, (Sang-woo Kim at al., 2006), Analysis of column-integrated aerosol optical thickness in Beijing from AERONET observations (Xuehua Fan at al., 2006). This paper addressed to the aerosol optical properties over arid region of Mongolia that observed from representative site of the Global AERONET Sun-photometer measurement at Dalanzadgad. In this research, we adopt AERONET Sun-photometer data acquired from Dalanzadgad site for 2002-2003 years, which has continuously full measurement over this period. The results of the analysis for monthly and seasonal mean AOT and Angstrom exponent and size distribution over Mongolian arid region are presented in this research.

2. AERONET site and Instrument description

The AErosol RObotic NETwork (AERONET) site Sun-photometer was installed 23 February 1997 at Dalanzadgad at 43.57722° N, 104.41917° E, and 1470 m above the sea level, in South part of Mongolia and is still undertaken. Operational time at Dalanzadgad site is 3162 days (8.663 years). The direct Sun measurements has been made once every 15 min at 340, 380, 440, 500, 675, 870, 935, and 1020nm, AODs for each channel except for 935 nm wavelength were retrieved from these direct Sun measurements. The Angstrom 440-870nm includes the 440, 500, 675 and 870nm AOD data.

3. Data

In this research Aerosol optical properties data acquired with AErosol RObotic NETwork (AERONET) ground-based sun-photometer. Ground based aerosol optical thickness, Angstrom exponent and size distribution data from December 2001 to November 2003 acquired from AERONET Sun photometer which available Level 2.0 Quality Assured Data at the Dalanzadgad site in Mongolia.

The AERONET data are pre and post field calibrated, automatically cloud cleared and manually inspected.

3. Results and discussion

3.1. Monthly variations of aerosol optical properties

The AERONET retrieval for AOT (τ) is performed at four wavelengths (λ) 340, 500, 870 and 1020nm, and the Angstrom exponent ($\alpha_{500\text{-}870}$) is evaluated at 500 and 870nm for the representative site Dalanzadgad in Mongolia. The monthly averages of aerosol optical thickness at 500nm (τ_{500}), and Angstrom exponent ($\alpha_{500\text{-}870}$) are summarized in Table 1. Generally, monthly average high value of AOT at 500 nm with greater than 0.15 in April-May and August-September of 2002 and in March, May-June of 2003. The maximum values observed 0.22 in April of 2002 and 0.43 in June of 2003. Furthermore, mostly higher values of monthly average of AOT 0.22 at April and 0.20 at August, respectively, occurred in 2002, and 0.25 at May and 0.43 at June respectively, observed in 2003. The Angstrom exponent provides a rough measure of aerosol particle size. In general, the small values of Angstrom exponent (α) indicate the large particles, and the large values represent small particles. The monthly mean Angstrom exponents values observed mostly in range 1.0-1.93 during 2002-2003. However, low values in range 0.58-0.76 in the March and April of 2002, it is indicating dust aerosol pattern over Dalanzadgad dominantly in spring (March-April).

The monthly mean AOT at four wavelengths (λ) 340, 500, 870 and 1020nm for 2002-2003 illustrated in Fig. 1.
According to spectral dependence for annual variation of AOT (τ) in the ultraviolet and visible wavelengths (λ_{340}, λ_{500}) have maximum values in spring (April-May), late summer and early autumn (August-September) and minimum values in middle winter (January) of 2002 and maximum values in late spring, early summer and minimum values in winter of 2003. At the near infrared wavelengths (λ_{870} and λ_{1020}) 870, 1020nm, AOT maximum value in middle spring (April) and minimum in middle winter (January) of 2002. Although AOT annual variation trend of near infrared wavelengths (λ_{870} and λ_{1020}) showed similar trend with AOT of ultraviolet and visible wavelengths (λ_{340}, λ_{500}) during 2003. Indeed, AOT maximum value at ultraviolet and visible wavelength (λ_{340} and λ_{500}) appears 0.43 and 0.61 respectively, in early summer (June) and decreases to a minimum in the winter (December) then increases again to spring and early summer in the all visible and near infrared wavelengths.

The Angstrom exponent (evaluated at 500 and 870nm) variation during 2002-2003 is presents in Fig. 2. The monthly mean minimum value of Angstrom exponent ($\alpha_{500\text{-}870}$) within range 0.58-0.76 appears in spring (March and April) of 2002, it indicates background conditions dominated by coarse mode (dust aerosols) aerosols. Moreover, mostly fine aerosol particles except spring season in 2002-2003.

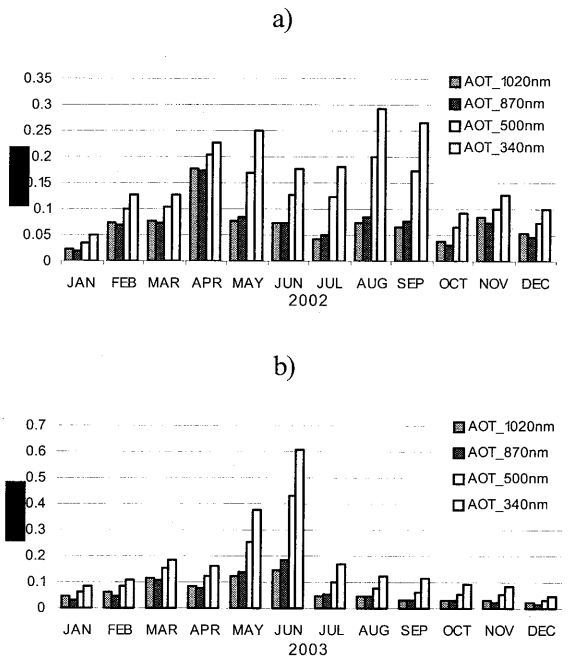

Fig 1. Monthly mean aerosol optical thickness (AOT) at 440nm, 500nm, 870nm, 1020nm for the 2002 (a) and 2003 (b) at Dalanzadgad AERONET site.

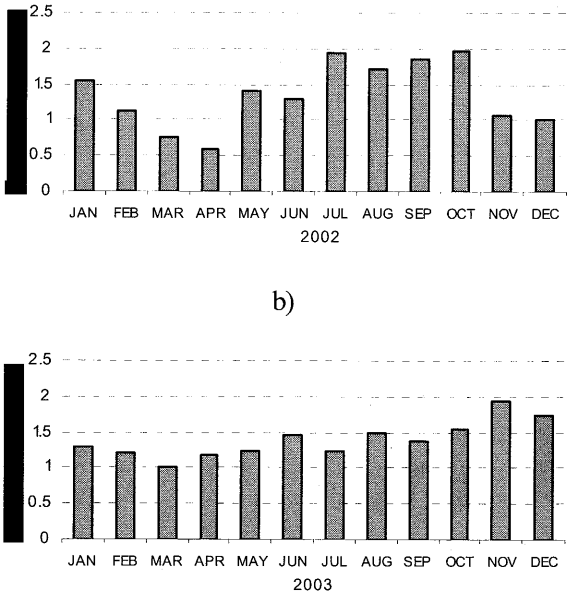

Fig 2. Monthly mean Angstrom exponent at 500-870 nm for the 2002 (a) and 2003 (b) at Dalanzadgad AERONET site.

Table 1. The monthly averages of Aerosol optical thickness, τ_{500nm}, and Angstrom exponent, $\alpha_{500\text{-}870nm}$

Months	I	II	III	IV	V	VI	VII	VIII	IX	X	XI	XII
						2002						
τ_{500nm}	0.04	0.10	0.10	0.22	0.17	0.13	0.12	0.20	0.17	0.07	0.10	0.07
$\alpha_{500\text{-}870nm}$	1.54	1.13	0.76	0.58	1.40	1.28	1.93	1.71	1.85	1.98	1.08	1.00
						2003						
τ_{500nm}	0.06	0.08	0.15	0.13	0.25	0.43	0.10	0.07	0.06	0.05	0.06	0.03
$\alpha_{500\text{-}870nm}$	1.29	1.19	1.00	1.19	1.23	1.47	1.24	1.50	1.37	1.53	1.93	1.74

3.2. AOT and Angstrom exponent dependence

The scatterplots of Angstrom exponent $\alpha_{500\text{-}870}$ versus aerosol optical thickness, τ_{500} for each season are shown in Fig. 3. As shown on these scatterplots it seems similar dependence between Angstrom exponents, $\alpha_{500\text{-}870}$ and AOT, τ_{500} for range 0.0-0.3 of AOT for four seasons. Particularly, the Angstrom exponent ranges 0.1- 3.6 for τ_{500}< 0.3. Mostly broad spread observed of Angstrom exponent for 0.0-3.2 to 0.6 of AOT in spring and summer season. Moreover, narrow spread of Angstrom exponent for 1.0-2.0 appears in range 0.5-1.5 of AOT in summer and autumn.

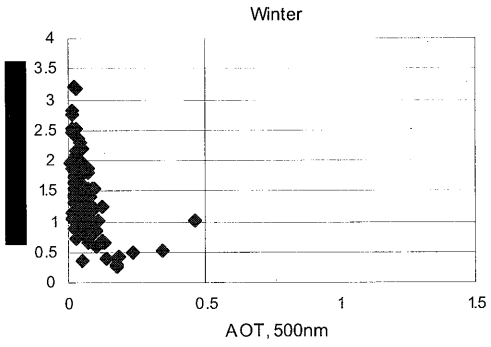

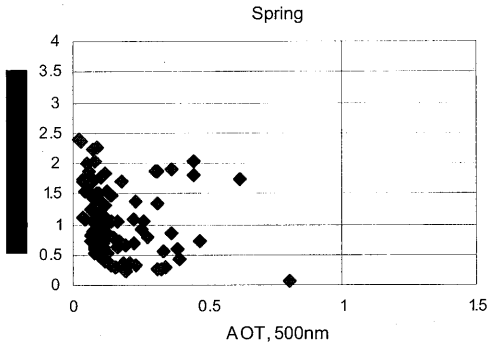

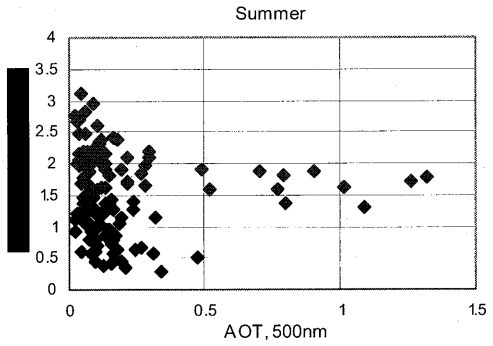

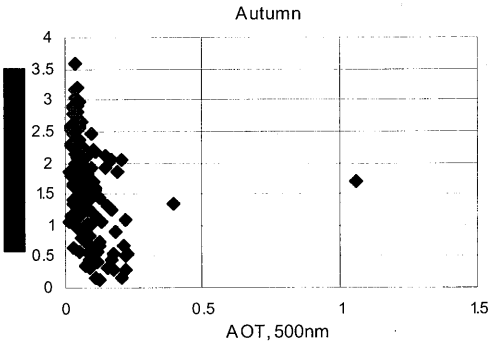

Fig. 3. Scatterplots of daily mean Angstrom exponent, $\alpha_{500\text{-}870}$ versus aerosol optical thickness, τ_{500} for each season at Dalanzadgad AERONET site.

3.3. Aerosol size distributions

Seasonal averages of aerosol volume size distribution parameters at Dalanzadgad AERONET Sun-photometer site are summarized in Table 1. The second, forth columns represents effective radius, R_{eff}, third, fifth columns are columnar volume, C_v for fine and course mode, respectively, and sixth is total columnar volume of particles, C_v. As shown in this table aerosol effective radius, R_{eff} (in μm) and columnar volume of particles per unite section of atmospheric column, C_v ($\mu m^3/\mu m^2$) by two aerosol modes such as fine and course mode.

Studies on net long-wave radiation on clear days in Hefei region

Zhen-zhu Wang[1], Jun Zhou[1], Chao Li[1], Tamio Takamura[2], Nobuo Sugimoto[3]

[1]*Anhui Institute of Optics and Fine Mechanics, Hefei 230031, China, zzwang@aiofm.ac.cn*

[2]*Center for Environmental Remote Sensing, Chiba University, Japan*

[3]*National Institute of Environmental Studies, Japan*

Abstract

Net long-wave radiation is an important component of radiation budget. The knowledge of induced factors (such as water vapor, aerosol) of radiation budget provides an opportunity for understanding the impact of environmental changes on climate. Utilizing the radiation data observed by pyrgeometer at definite times every day from 2003 to 2007 at SKYNET Hefei site in East China, the characteristic of net long-wave radiation over grassy land is discussed on 293 clear days. Meanwhile, based on these five years observations of integrated water vapor by microwave radiometer WVR-1100, variability of the atmospheric water vapor on sunny days has been statistically analyzed. And the aerosol optical property in the corresponding period is also obtained by an automated two wavelength (1064nm, 532nm) polarization (532nm) lidar. For the value of integrated water vapor, validation is given by a local radiosonde and good agreement is shown. As to the lidar dataset, we apply the Fernald's method to derive the extinction coefficient. The profile of aerosol extinction coefficient is compared with anther lidar system PML and indicates great agreement. Then the AOD under the height of 3 km is calculated by layer-integrated extinction coefficient. This study mainly addresses the daily and seasonal variations of net long-wave radiation, integrated water vapor and AOD as well. We attempt to characterize the optical property of aerosol and the value of integrated water vapor and their effects on the net long-wave radiation over Hefei. The results show that some certain negative correlations are considered to occur between the latter two kinds of factors and the net long-wave radiation. And especially in summer the effects of water vapor and the aerosol on net long-wave radiation are very obvious. Large water vapor and aerosol loading lead to a very low net long-wave radiative effect.

Keywords: net long-wave radiation; integrated water vapor; AOD

1. Introduction

The radiation balance of the Earth system is an accounting of the incoming and outgoing components of radiation. Net long-wave radiation is an important component of radiation budget. And it is a measure of the difference between outgoing long-wave radiation from the earth surface and incident atmospheric long-wave counter-radiation. Many factors determine the value of net long-wave radiation[1)]. In this paper, we analyze the seasonal variation of net long-wave radiation, integrated water vapor and aerosol optical depth as well using the observed data on clear day from 2003 to 2007 at SKYNET Hefei site (31.90N, 117.16E) in East China. Some relationships are found among the three foregoing parameters. Besides, in order to validate these data, good agreements are acquired by blind validations.

2. Instruments and validation

The measurement site is located at Anhui Institute of Optics and Fine Mechanics, 15 km west of Hefei city. The institute is surrounded by farmland, lake and villages. The factory district is centered in the eastern suburbs of the city. Therefore, influence of urban plume

and industrial emission on the observed data is less important. Data obtained from two pyrgeometers, a microwave radiometer, and a NIES Lidar is analyzed in this paper. The instruments were placed at a height of 1.5 m over short non-irrigated grass and they are operated continuously.

The pyrgeometers (model PIR), manufactured by the EPPLEY LAB.INC., were calibrated by Precision Infrared Radiometer in Eppley's Blackbody Calibration System. Downward and upward long-wave radiation was measured by them in continuous operation. Thus, they were inspected several times per week and an alternate method of calibration was also been done each year to compare the PIR against another calibrated working standard PIR in a cloudless night sky.

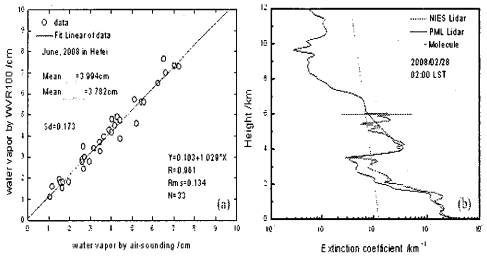

Fig. 1(a) Scatter plot of water vapor retrieved from microwave radiometer data vs. that measured by radiosonde; (b) Comparison extinction profiles at 532nm measured by PML Lidar with NIES Lidar

The Radiometrics WVR-1100 portable water vapor radiometer receives microwave radiation from the sky at 23.8 GHz and 31.4 GHz for total Integrated Water Vapor and Cloud Liquid Water. This instrument does not need to be always calibrated if no change shows in the plot of noise diode injection temperature (i.e. the instrument is sufficiently calibrated.). In this paper, we compared the value of integrated water vapor retrieved from microwave radiometer data and that measured by radiosonde. Figure 1(a) shows the results. It was found from the retrieval results of the microwave radiometer data taken at Hefei in June, 2008 that on average, the retrieved value of water vapor was 0.212 cm greater than that measured by radiosonde and the standard deviation was 0.173 cm; the linear correlation coefficient between the two value is 0.961, and the Rms error was 0.134 cm. In general, good agreement was shown except small difference because of certain non-comparable fact[2].

The NIES Lidar[3] employs 1064-nm fundamental and 532-nm second harmonic of a flash-lamp pumped Nd:YAG laser and the direction of measurement is vertical. The scattered light is received with a 20-cm Schmidt-Cassegrain telescope. The received light is collimated to 1064-nm channel and two 532-nm polarization channel. It is operated automatically, and the 5-minute averaged lidar profiles are recorded every 15 minutes in the continuous observation mode. We apply the Fernald's method iteratively with non-zero boundary value at 6 km to derive the extinction coefficient for the data without clouds. And the aerosol optical depth (i.e. AOD) under the height of 3 km is calculated by layer integrated extinction coefficient. In order to check the reliability of observed data by this Lidar, the profile of aerosol extinction coefficient is compared with anther lidar system PML[4]. The results are shown in the Figure 1(b). The Figure clearly indicates that aerosol extinction profiles for 532 nm measured by the two lidars agree very well. During these 5 years, the number of clear days in every month is shown in Table 1.

Table 1 Number of clear days in every month in Hefei region during 2003-2007

Season	Winter		Spring			Summer			Autumn			
Month	12	1	2	3	4	5	6	7	8	9	10	11
Number	36	29	26	30	30	24	14	7	13	20	30	34	293

3. Results and discussion

3.1. Typical daily variation

Net long-wave radiation was determined from measured upward and downward long-wave radiation by the flux difference between them. This section gave a typical example of the daily variation of long-wave radiation, aerosol optical depth and integrated water vapor. Meanwhile the relationships between net long-wave radiation and anther two parameters were shown.

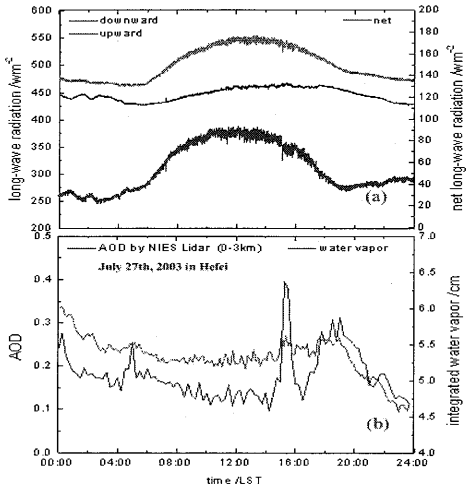

Fig. 2 the diurnal variation of long-wave radiation, AOD and water vapor observed in Hefei on July 27th, 2003

Figure 2 shows that the 24 hours variations of long-wave radiation, AOD and water vapor were observed in Hefei on July 27th, 2003. It was a sunny day except for the occurrence of low cloud at a height of 2-3km occasionally. From figure 2 (a), we can see the downward, upward and net long-wave radiation experience an obvious variation with big value in the daytime and small at night. Figure 2 (b) gives us that the diurnal variation of AOD and integrated water vapor has similar trend. We can also find the value of AOD rises quickly due to clouds (e.g. at about 15:00 pm). Furthermore, the results on figure 2 show that some certain negative correlations are considered to occur among these three parameters (i.e. the relative variation of net long-wave radiation is effected by whether aerosol and water vapor rise or fall at a certain degree). Because the mass of water vapor and aerosol in the air increase, the downward long-wave radiation will enhance. Accordingly, the net long-wave radiation will decrease to some extent.

Besides, many other factors, such as the existence of cloud and the temperature of air or surface, can cause changing of the net long-wave radiation. We do not discuss them in this essay.

3.2. Statistical seasonal variation

In order to investigate the net long-wave radiation under the influence of aerosol and water vapor furthermore, the seasonal variation of long-wave radiation, integrated water vapor and AOD were presented and discussed in detail. The results obtained in figure 3: the value of long-wave radiation and integrated water vapor is monthly mean daily one and the value of AOD (0.03-3.0 km) is derived from lidar by averaging every one in correspondence month. According to the measurements, the downward and upward long-wave radiation have same trend in every month during these 5-year. The lowest monthly mean daily value of them is in January and the maximum long-wave radiation flux occurred in the summer season (see figure 3(a)). But the seasonal variation of net long-wave radiation is widely different marked by summer the lowest and spring the highest value, and the discrepancy between winter and fall is feeble (see the red line in figure 3(b)). And a maximum monthly mean daily net long-wave radiation equals to 96.85 Wm^{-2} on May and a minimum one occurs to 53.04 Wm^{-2} on August.

Interestingly, the seasonal variation of water vapor has the similar tendency with down/upward long-wave radiation, and the minimum monthly mean daily value of integrated water vapor is only 0.29 cm in

winter and the maximum is 5.20 cm in July to August with a big leap (see the blue line in figure 3(b)). From figure 3(c), the lidar derived monthly average AOD (0.03-3.0 km) shows no great fluctuant. But it still appears much larger average value in spring and summer and a relative small one in July. That's because the dust weather sometimes happen in spring and increase the value of AOD. And the summer rainfall in July makes the air in Hefei cleanly and decreases the value of AOD.

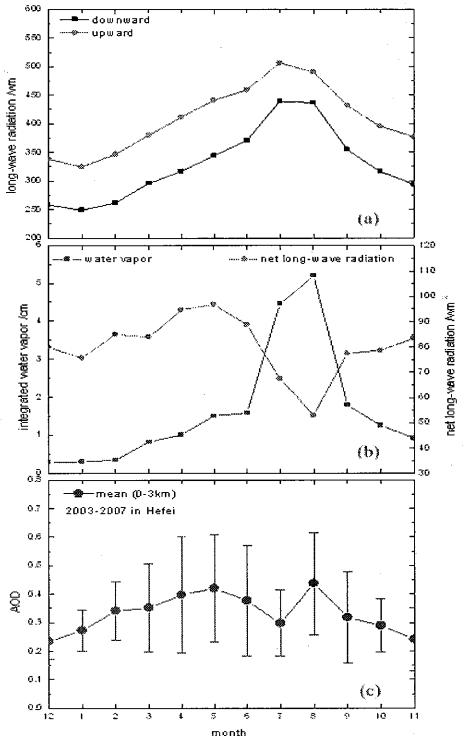

Fig. 3(a) the monthly mean daily value of long-wave radiation; 3(b) the monthly mean daily value of net long-wave radiation (red line) and integrated water vapor (blue line); 3(c) the lidar derived monthly average AOD (0.03-3.0 km) over Hefei from 2003 to 2007 on clear days

Well, in figure 3 we can conclude that in summer the effects of water vapor and the aerosol on net long-wave radiation are obvious. To some extent, negative correlations are considered to come up like the daily variation. Large water vapor and aerosol loading lead to a very low net long-wave radiative effect. However, in other seasons these relationships are not very evident. In my opinion, many other factors, such as the existence of cloud and the temperature of air or surface, maybe play an important role in the net long-wave radiation and we will discuss them in the near future work.

4. Summary

Net long-wave radiation is of major importance for all radiative balance studies. Under different weather/climate, many factors affected on net long-wave radiation must be discussed. We have primarily analyzed the changing of water vapor and aerosol could lead to variation of net long-wave radiation over Hefei in clear days. In some cases, the two parameters are playing a great role in net long-wave radiation (e.g. in summer) and maybe the other factors should be required for more detailed analyses.

Reference

1) Xiquan Dong, Baike Xi, Patrick Minnis, Observational Evidence of Changes in Water Vapor, Clouds, and Radiation at the ARM SGP site, Submitted to Science as a report (May 25, 2006).

2) LIU Chaoshun, LV Daren, DU Bingyu, A study on Ground-Based Remote Sensing of Atmospheric Integrated Water Vapor and Cloud Liquid Water, J. of Nanjing Institute of Meteorolog, 29(5), 606-612, 2006.

3) N. Sugimoto, A. Shimizu, I. Matsui, et al. Study of Dust Transport Using a Network of Continuously Operated Polarization Lidars, Water, Air, and Soil Pollution: Focus 5, 145-157, 2005.

4) Z. Z. Wang, R. L. Chi, B. Liu, et al. Depolarization properties of cirrus clouds from Polarization Lidar measurements over Hefei in Spring. CHINESE OPTICS LETTERS, Vol. 6(4): 235-237, 2008.

From this table, we have seen aerosol volume size distribution in seasonal pattern at Dalanzadgad site that the effective radius (R_{eff}), is varied 0.141-0.154 for fine mode and 1.506-2.268 for course mode during 2002-2003. The columnar volume of particles (C_V) ranges from 0.005 to 0.030 for fine and 0.014-0.111 for course mode, respectively.

Hence, in this table, larger of effective radius (1.918-2.268) with course mode occurred in summer and autumn seasons, while the large of columnar volume (0.111) observed in spring season of this period. The large of columnar volume in spring associated with a strong wind occurrence season and dry situation of period over this arid region.

Table 2. Seasonal averages of aerosol volume size distribution parameters at Dalanzadgad AERONET Sun-photometer site; Reff is the effective radius (in μm) and Cv is the columnar volume of particles per unit cross section of atmospheric column

	Fine mode		Coarse mode		Total
	R_{eff} (μm)	$C_v(\mu m^3/\mu m^2)$	R_{eff} (μm)	$C_v(\mu m^3/\mu m^2)$	$C_v(\mu m^3/\mu m^2)$
			2002		
Winter	0.141	0.009	1.597	0.024	0.054
Spring	0.148	0.015	1.506	0.111	0.125
Summer	0.141	0.020	2.030	0.029	0.050
Autumn	0.140	0.029	2.268	0.020	0.048
Year	0.142	0.018	1.850	0.051	0.069
			2003		
Winter	0.152	0.006	1.575	0.027	0.032
Spring	0.149	0.015	1.644	0.026	0.041
Summer	0.154	0.030	2.124	0.024	0.053
Autumn	0.146	0.005	1.918	0.014	0.019
Year	0.150	0.014	1.815	0.023	0.036

4. Concluding remark

In order to characterize aerosol optical properties, we analyzed ground measured aerosol optical thickness, Angstrom exponent and size distribution data obtained from AERONET Sun-photometer site at Dalanzadgad of Mongolia, over the two-year period 2002-2003. We performed our analysis on monthly and seasonal characterization over the south arid region of Mongolia.

As a result, spring and early summer has the highest seasonal average AOT and minimum seasonal average appears in winter of 2002-2003. The monthly mean Angstrom exponent values occurred mostly in range 1.0-1.93 during 2002-2003. However, low values of Angstrom exponent appears within range 0.58-0.76 in spring. Hence, monthly average Angstrom exponents are indicates that aerosol mixtures of both coarse and fine mode particles, specially dust aerosol pattern over Dalanzadgad dominantly in spring (March, April).

According to spectral dependence of annual variation of AOT (τ) in the ultraviolet and visible wavelengths (λ_{340}, λ_{500}) have maximum values occurred in spring, late summer and early autumn and minimum values in winter during the study period. At the near infrared wavelengths (λ_{870} and λ_{1020}) 870, 1020nm, AOT maximum value in middle spring and minimum in middle winter of 2002. Although, AOT annual variation trend of near infrared wavelengths (λ_{870} and λ_{1020}) showed similar trend with AOT of ultraviolet and visible wavelengths (λ_{340}, λ_{500}) during 2003. AOT maximum value at ultraviolet and visible wavelength (λ_{340} and λ_{500}) appears 0.43 and 0.61, respectively, in early summer and decreases to a minimum in the winter then increases again to spring and early summer in the all ultraviolet, visible, near infrared wavelengths.

The aerosol volume size distribution in seasonal pattern at Dalanzadgad site that the effective radius (R_{eff}), is varied 0.141-0.154 for fine mode and 1.506-2.268 for course mode during 2002-2003. The columnar volume of particles (C_V)

ranges from 0.005 to 0.030 for fine and 0.014-0.111 for course mode, respectively.

Also the result showed that larger of effective radius (1.918-2.268) with course mode occurred in summer and autumn seasons, while the large of columnar volume (0.111) observed in spring season of this period. The large of columnar volume in spring associated with a strong wind occurrence season and dry situation of period over this arid region.

References

1) Sang-woo Kim, Soon-Chang Yoon, Jiyoung Kim and Seung-Yeon Kim., 2007. Seasonal and monthly variations of columnar aerosol optical properties over east Asia determined from multi-year MODIS, LIDAR, and AERONET Sun/sky radiometer measurements, Journal of the Atmospheric Environment, Vol. 41, Issue 8, 1634-1651.
2) Xia Xiango, Chen Hongbin, and Wang Pucai., 2004. Aerosol properties in a Chinese semiarid region, Journal of the Atmospheric Environment, Vol. 38, 4571-4581.
3) Xuehua Fan, Hongbin Chen, Philippe Goloub, Xiango Xia, Wengxing Zhang and Bernadette Chatenet., 2006. Analysis of column-integrated aerosol optical thickness in Beijing from AERONET observations, China Particuology, Vol. 4, No. 6, 330-335.

Seasonal characteristics of aerosol optical thickness over Mongolia and relationship to land surface variability

Batbayar Jadamba[1], Tugjsuren Nas-Urt[2]

[1]*Mongolian University of Science and Technology, E-mail:tchbayar@yahoo.com*
[2]*Mongolian University of Science and Technology, P.O.B-157,Ulaanbaatar-46,Mongolia, E-mail:tugjsurn@must.edu.mn*

Abstract

Aerosols vary widely in space and time and thus satellite-based observation of their physical and optical properties is important. MODIS TERRA aerosol products were employed to analyze the temporal and spatial variability of aerosol distribution over Mongolia. The main data used in this study are MODIS TERRA gridded atmosphere monthly global products (MOD08_M3) of aerosol optical thickness (AOT) at 550nm. The monthly average MOD08_M3 products are given at a spatial resolution 10km x 10km. Moreover, the MODIS standard products, such as VI's; Normalized Differences Vegetation Index (NDVI), Enhanced Vegetation Index (EVI) are adopted. The NDVI and EVI maps depicting spatial and temporal variations in land surface process and vegetation activity has derived using MODIS data from atmospherically corrected and nadir adjusted surface reflectances. These data sets are being used to evaluate climatologically and seasonal variations of aerosols, and also to assess aerosol optical thickness distribution in the above study area. High value of AOT (0.6-1.42) appeared in spring and summer seasons over southeastern and eastern region (Gobi dessert and Eastern steppe area) of Mongolia. However, the low value of AOT (0.0-0.3) observed in autumn and winter seasons. The Gobi desert over southeastern and eastern arid and semi-arid region of Mongolia, which has AOT more than 0.6 and dry and windy climate condition causes mostly affected by dust storms in spring and summer seasons. Moreover, the AOT distribution and land surface variability relationship is analyzed and discussed.

Keywords: Aerosol optical thickness, MODIS, EVI, NDVI

1. Introduction

In the recent years, it is reported in the several papers on atmospheric aerosols has been originated extremely from Eastern Asian subcontinent, especially natural aerosols due to dust storm from northern China and Gobi desert region of Mongolia.

The present decades achievements in spaceborne remote sensing of aerosol properties are presented in the work of Stove et al., Huser et al., Herman., Tanre et al., Kaufman et al., (1997) Martonchik et al., (1998), Goloub et al., Higurashi and Nakajima , King et al., (1999).

Aerosols affect our environment at the local, regional and global levels. Atmospheric aerosols may affect climate through both direct and indirect mechanisms. Indirect mechanisms include, for example, the aerosols reflect sunlight back to space, thus cooling the planet. By direct effect involves aerosol particles acting as cloud condensation nuclei, spreading the cloud's liquid water over more, smaller droplets. The aerosol optical depth (τ_a) retrieved at 10km spatial resolution from the Moderate-Resolution Imaging Spectroradiometer (MODIS) sensor on board the TERRA and AQUA satellites are already providing important information on global aerosol climatology (Remer et al., 2005).

The regional and local analysis is needed to investigate the overall impact of aerosol radiative forcing on climate change. Accordingly, first are meant to give broad evaluation of aerosol effects to climate change. In this paper we focus on seasonal and spatial distribution of aerosol optical thickness and relationships to land surface variables over whole Mongolian territory. In order to evaluate the relationship between aerosol optical properties and land surface variables we analyzed the data on AOT and VI's of MODIS products for Mongolian huge area. We performed our analysis on monthly mean AOT and MODIS VI's such as NDVI and EVI for 2001-2005.

2. Study area

In the present study we select the rectangular geographical region between 80^0-120^0E and 43^0-52^0N including whole area of Mongolian territory. Mongolia is a country in Northeast Asia, which has unique ecological system consisting of the southernmost fringe of boreal forest of the Great Siberia, the northernmost deserts, vast steppes of Central Asia. The climate of Mongolia has high annual and diurnal temperature fluctuations, and low rainfall. The annual precipitation amount is low, averaging 200-220 mm and ranging from less than 50 mm per year in the South (Gobi desert region) to 400 mm per year in limited areas in the North. (Climate Change and its Impacts in Mongolia).

3. Data sources

The many data products derived from MODIS observations describe features of the land and atmosphere that can used for studies of process and trends on local, regional and continental scales. MODIS data products are available from several sources. The four data sets are used in this study; the MODIS atmosphere products of aerosol optical thickness (AOT), land products of Vegetation Indexes (VI); such as Normalized Differences Vegetation Index (NDVI) and Enhanced Vegetation Index (EVI) were chosen for mapping and analyses relationships between above atmosphere and land products over Mongolia. The data consists of MODIS TERRA atmosphere monthly global products (MOD08_M3) of aerosol optical thickness (AOT) at 550nm on 2001-2005. The monthly average MOD08_M3 products are given at a spatial resolution 10km x 10km. The MODIS standard products, such as MODIS VI's; Normalized Differences vegetation index (NDVI), Enhanced vegetation index (EVI) are on 2001-2005.

4. Data processing

The MODIS TERRA atmosphere monthly global products (MOD08_M3) of aerosol optical thickness were pre-processed for the monthly mean AOT distribution images. Then we have been processed maps of AOT distribution over all territory of Mongolia by using Kriging interpolation methodology. Because there were some few points lost values of AOT in data sets, so the Kriging interpolation method was applied for AOT distribution maps. Moreover, in this study we processed MODIS VI's such as NDVI and EVI images are for the present analyze. The NDVI and EVI images depicting spatial and temporal variations in land surface process and vegetation activity has derived using MODIS data from atmospherically corrected and nadir adjusted surface reflectances. Geometric correction was done to the images. The MODIS images are downloaded from Land Processes Distributed Active Archive center (LP DAAC) of NASA's Earth Observing System (EOS).

5. Results and Discussion

5.1. Aerosol optical thickness spatial distribution

We adopt in this analyze the MODIS TERRA sensor derived monthly mean aerosol optical thickness data. The MODIS TERRA atmosphere monthly global products (MOD08_M3) of aerosol optical thickness were preprocessed for the monthly mean AOT distribution images over Mongolia. However, there were few points lost values of aerosol optical thickness in data sets for our study area. Consequently, in order to generate aerosol optical thickness maps for whole Mongolian territory, we tried to fill the area by applying Kriging interpolation method. Figure 1 presents a generated seasonal mean aerosol optical thickness distribution maps for 5 years: from December 2000 to November 2005.

The aerosol optical thickness spatial distribution images were evaluated by visual interpretation analyzing method. Generally, aerosol optical thickness values observed with range 0.0-1.41 throughout the study period. For all the years primary proportion of aerosol optical thickness distribution observed dominantly in spring and secondarily in summer, when there are occurred windy situation in arid and semi arid region. Particularly, larger optical thickness values are seen in southeastern and eastern region in spring and southeastern region in summer (specially 2001-2003). Lower values of the aerosol optical thickness represents in winter during study period (except most eastern borderland area). In autumn large optical thickness values also seen only in southeastern area of this study region. And the AOT distribution is shown the similar pattern in autumn during the 5 years period. On the other hand, we have seen that aerosol optical thickness dominantly occurred in southeastern and eastern arid and semi-arid region of the study area over observed period. The Gobi desert over southeastern and eastern region of Mongolia, which has AOT more than 0.6 and dry and windy climate condition causes mostly affected by dust storms in spring and summer seasons.

Furthermore, we should note that has been observed highly seasonal pattern of aerosol optical thickness distribution. Hence our analysis found that most aerosol mobilization is from nature and the source region appears in southeastern and eastern part of Mongolia.

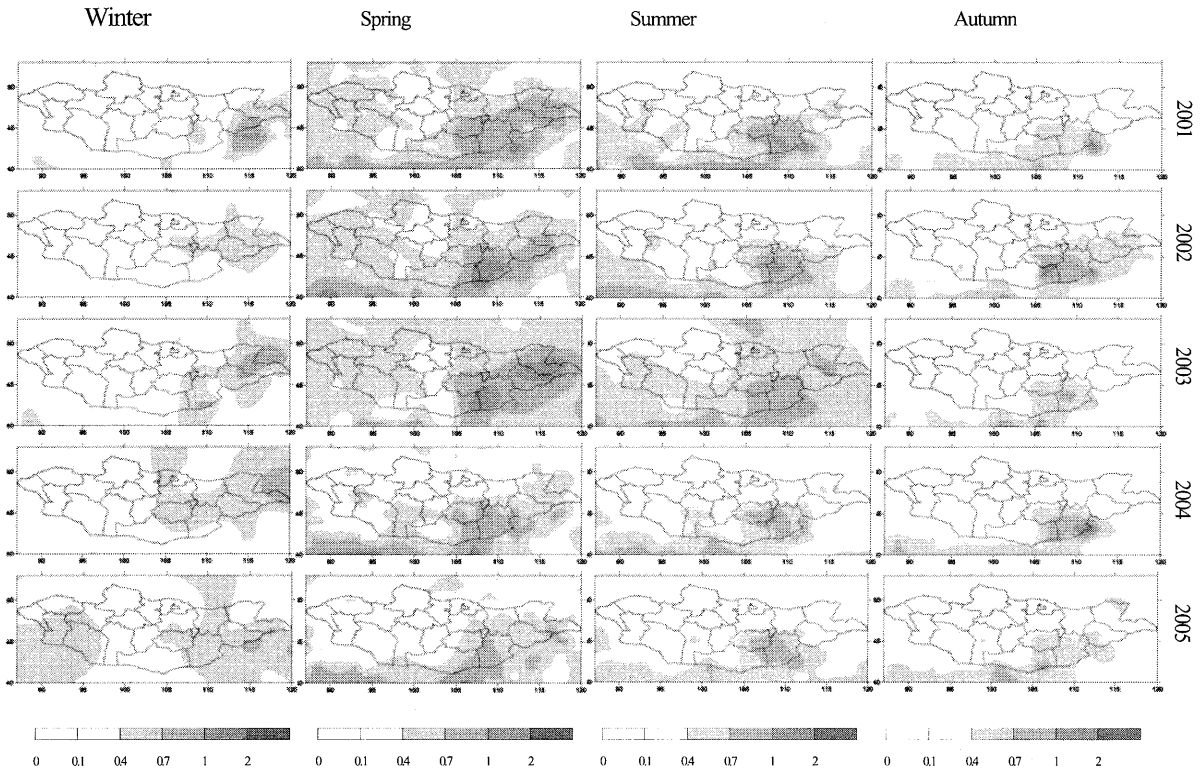

Fig.1. Seasonal aerosol optical thickness distribution over Mongolia, 2001-2005

5.2. Relationship between AOT and MODIS VI's

As we known, vegetation background is closely linked to important physical processes occurring at the land surface-atmosphere interface. In this research, two vegetation indexes of MODIS products were evaluated to determine vegetation background in Mongolian territory. The normalized difference vegetation index (NDVI) will maintain continuity with the AVHRR-NDVI data record, which has provided a time series of seasonal and interannual variations since 1982 and an enhanced vegetation index (EVI), which will extend sensitivity into dense forested biomes and agricultural areas while reducing canopy background and aerosol sources of noise. The NDVI was originally developed to enhance the vegetation signals over sparsely vegetated rangelands. The EVI has been developed to optimize the vegetation signal while minimizing aerosol and canopy background sources of uncertainty [1]. In order to characterize vegetation background, we pre-processed MODIS VI's such as NDVI and EVI images by growing seasons (spring, summer, autumn) for 2001-2005. (Not illustrated here).

The distributions of vegetation cover allow us to analyze the effect of surface background which sensitive to the soil condition to aerosol loadings. The information of vegetation indexes is used to investigate the relationship between aerosol optical thickness distribution and vegetation background.

Figure 2 presents relationship between AOT and NDVI for growing seasons including spring, summer and autumn of 2001. Large values of aerosol optical thickness (0.3-1.21 in spring, 0.3-1.42 in summer, 0.3-1.23 in autumn) are appeared in the small values (0.05-0.14 in spring, summer and autumn) of NDVI in this scatterplot over all growing seasons. It is indicates larger optical thickness distribution associated with lower vegetation background, which is sparsely vegetated area (such as bare soil) in 2001. Moreover, slightly broad spread of aerosol optical thickness observed in spring than summer and autumn seasons.

Figure 3 presents relationship between AOT and EVI for growing seasons including spring, summer and autumn of 2001. In this scatterplot, almost similar pattern of relationship among aerosol optical thickness and enhanced vegetation index with relations between AOT and NDVI above mentioned growing season. However, smaller spread of aerosol optical thickness appeared in relatively smaller values of EVI than NDVI values in all season of 2001.

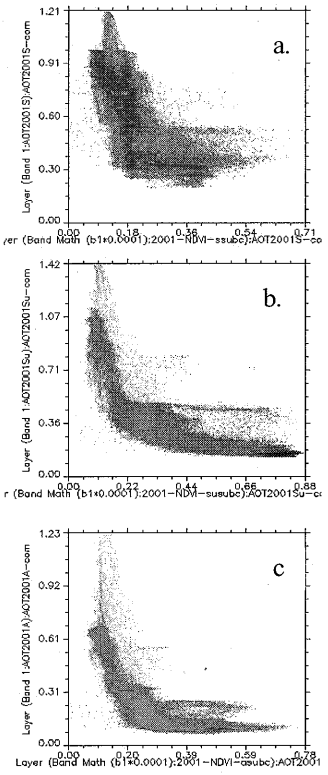

Fig. 2. Relationship between AOT and NDVI
(a) spring, (b) summer, (c) autumn for 2001

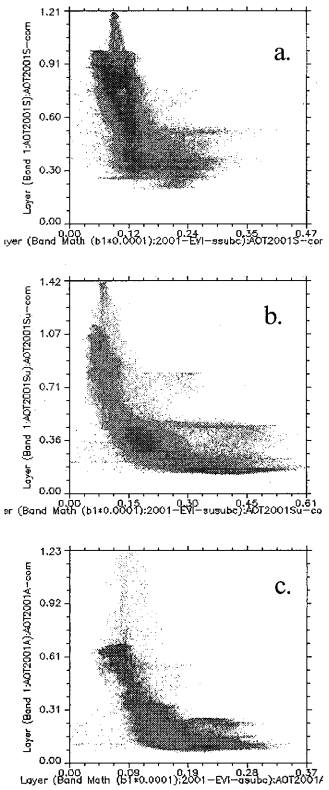

Fig. 3. Relationship between AOT and EVI,
(a) spring, (b) summer, (c) autumn in 2001

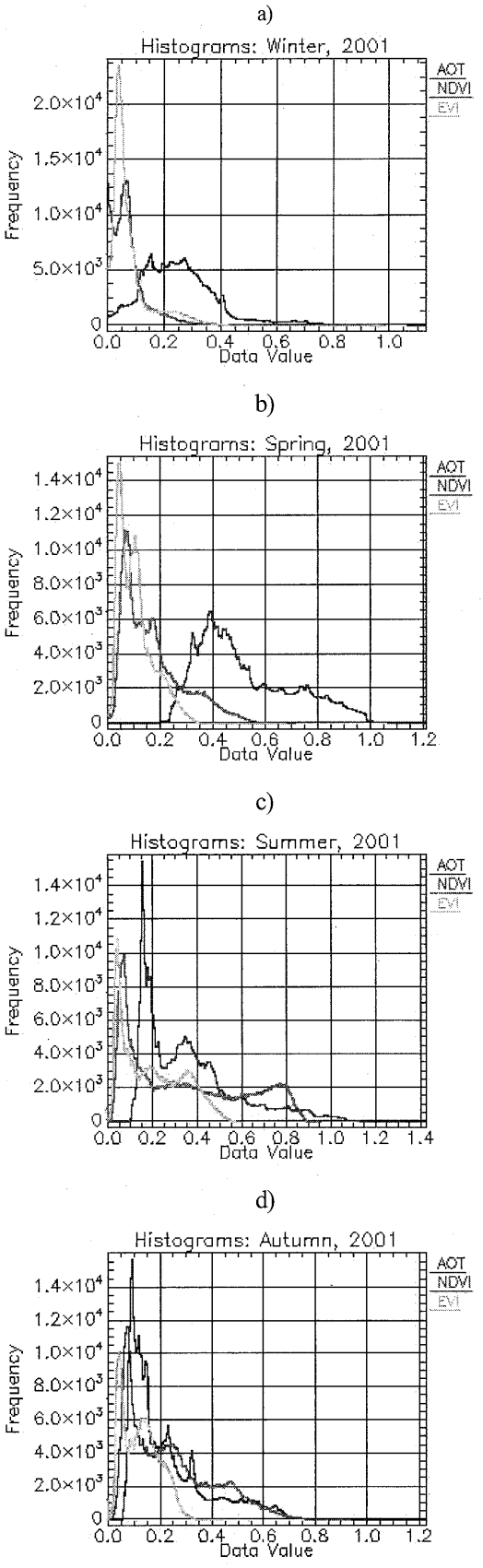

Fig. 4. Histogram of seasonal frequency of occurrence for AOT, NDVI and EVI, (a) winter, (b) spring, (c) summer, (d) autumn in 2001

In figure 4 shows the seasonal frequency distribution of occurrence of aerosol optical thickness, NDVI and EVI for each season (a. winter, b. spring, c. summer, d. autumn) in 2001.

The larger distribution of occurrence of aerosol optical thickness varied range 0.5-2.0 (with frequency 1.6 x 10^4) was in summer and spring while lower values 0.0-0.2 of NDVI and EVI (with frequency 1.0 x 10^4 and 1.15 x 10^4, respectively). In other words, the frequency of occurrence of AOT in summer and autumn is almost identical. The maximum frequencies of AOT are found around 0.1-0.15. The lower frequency distributions of AOT are broad in having values 0.0-0.5 (with frequency 5.0 x 10^3) in winter. In spring, the frequency of distribution of occurrence of AOT values is broad, varied range 0.25-1.0 (with frequency 6.2 x 10^3).

6. Conclusion

The aerosol spatial distribution maps obtained from MODIS monthly mean aerosol optical thickness data have greatly improved the knowledge about the seasonal pattern of aerosols over Mongolia. The aerosol optical thickness spatial distribution images were evaluated. Generally, aerosol optical thickness values observed with range 0.0-1.42 throughout the 2001-2005.

During study period primary proportion of aerosol optical thickness distribution observed dominantly in spring and secondarily in summer, when there are occurred windy situation in southeastern and eastern arid and semi-arid region of Mongolia. Particularly, larger optical thickness values are seen in southeastern and eastern region in spring and southeastern region in summer (specially 2001-2003). Lower values of the aerosol optical thickness occurred in winter during study period. In autumn large optical thickness values also seen only in southeastern area and the AOT distribution is shown the similar pattern in autumn over the 5 years period.

Finally, we have seen that aerosol optical thickness dominantly occurred in arid and semi-arid region and most aerosol mobilization is from nature and the source region appears in southeastern and eastern part of Mongolia.

References

1) Christopher O. Justice, Eric Vermote et al., 1998. The Moderate Resolution imaging Spectroradiometer (MODIS): Land Remote Sensing for Global Change Research, IEEE Transactions on Geoscience and Remote Sensing, Vol. 36, No 4, 1228-11249.
2) Remer L.A. et al., 2005. The MODIS aerosol algorithm, products, and validation, Journal of the Atmospheric science, Vol. 62, 947-973.
3) Shilong Piao, Anwar Mohammat, Jingyun Fang, Qiang Cai and Jianmeng Fenggand., 2006. NDVI-based increase in growth of temperate grasslands and its responses to climate changes in China, Journal of the Global Environmental change, Vol. 16, 340-348.
4) Toshihiko Takemura and Teruyuki Nakajima., 2002. Single-scattering Albedo and Radiative Forcing of various Aerosol Species with a Global Three-Dimensional Model, Journal of Climate, Vol.15, No. 4, 333-352.

Real-time, wide field-of-view monitoring of the atmosphere by means of a novel imaging lidar system

Kohei Shinomiya[1], Kenji Masuda[1], Masanori Yabuki[1], Makoto Sasaki[2], Hiroaki Kuze[1]

[1] *Center for Environmental Remote Sensing, Chiba University, 1-33 Yayoi-cho, Inage-ku, Chiba 263-8522, Japan, hkuze@faculty.chiba-u.jp, shinomiya@graduate.chiba-u.jp*

[2] *Institute for Cosmic Ray Research, University of Tokyo, 5-1-5 Kashiwa-no-Ha, Kashiwa City Chiba 277-8582, Japan, sasakim@icrr.u-tokyo.ac.jp*

Abstract

An imaging lidar system has been constructed on the basis of the All-sky Survey High Resolution Air-shower (Ashra) telescope, originally developed for detecting cosmic-ray particles with extremely high energy. In this study, we describe the system performance of the imaging lidar system, including the noise-reduction capabilities and its application to aerosol and cloud monitoring.

Keywords: aerosol, imaging lidar

1. Introduction

The remarkable features of the All-sky Survey High Resolution Air-shower (Ashra) telescope system are a wide field-of-view (FOV) (40×40 deg), high angular resolution (1 arcmin = 0.29 mrad), and a high-speed, highly sensitive imaging system with an intelligent triggering capability.[1)] By employing this novel telescope, we have constructed an imaging lidar system[2)] for monitoring aerosols and clouds in the troposphere. In the bistatic mode of operation, the telescope is placed apart from the laser source. While the laser beam direction is scanned in the FOV range of the telescope, the scattered light is detected in the scattering-angel range of $0<\theta<180$ deg. Although bistatic measurements of aerosols have so far been reported[3,4)] the laser beam direction was mostly fixed near the zenith direction, giving the detection near the backscattering scheme. In contrast, forward scattering yields high signal-to-noise ratio (S/N) owing to the general property of the Mie scattering from aerosols. Since the wavelength range of the Ashra telescope is in the UV range of 300-420 nm, here the bistatic measurement is made using the laser wavelength of 351 nm. This ensures relatively eye-safe lidar operation, since the level of maximum permissible exposure (MPE) is very high in the UV compared with the visible wavelength region.

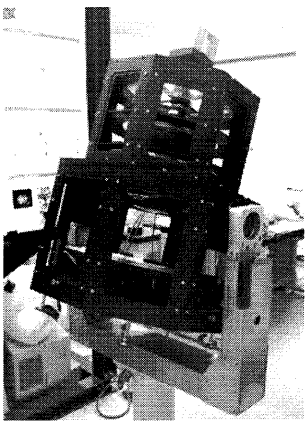

Fig. 1 1/3-scale Ashra telescope image

2. 1/3-Scale Ashra telescope

The 1/3-scale Ashra telescope (Fig. 1) is equipped with a 60-cm diameter main mirror and three corrector lenses (Baker-Nunn system), as shown in the schematic (Fig. 2). A UV-pass absorption filter is used to eliminate the longer wavelength light. The image is formed at the input plane of a 6-inch electro-static image intensifier (II, Toshiba TETD), which reduces the size of the image to about 13 mm. The resulting image, in turn, is sent through a high-speed gated II (Hamamatsu) and detected by a cooled CCD camera (Bitran, BN51LN). The field-of-view angle and the angular resolution of this telescope system have been measured to be 31 deg and 4.3 arcmin (1.26 mrad), respectively.

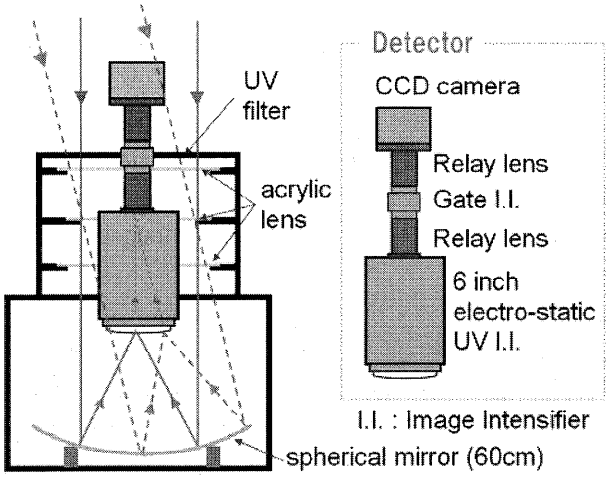

Fig. 2 Schematic of 1/3-scale Ashra telescope

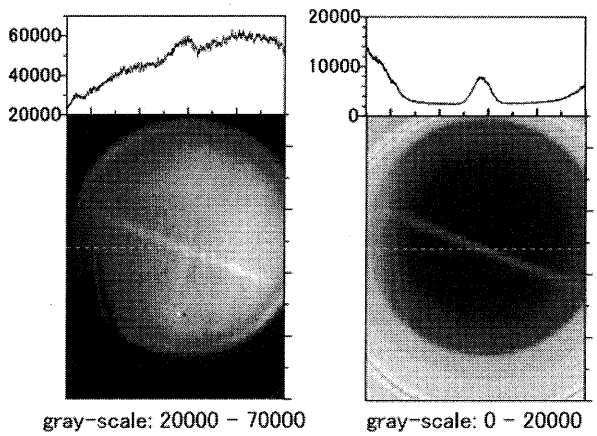

Fig. 3 Images obtained from the imaging lidar observation: (a) continuous mode, and (b) gated mode with a gate width of 20 μs,: exposure time 1s, repetition rate 800Hz

The elimination of background light is important in the imaging lidar measurement. We have applied the gating synchronized with the laser pulse repetition rate (800 Hz). As shown in Fig. 3, the background noise due to the night skylight is reduced to a level of a few percent.

3. Bistatic lidar theory

In the bistatic measurement, a laser and a telescope are located separately, with a baseline distance of L (Fig. 4). The laser is illuminating a direction θ_{laser} in elevation, while the telescope is observing the beam path toward a direction θ_{view}. In this bistatic measurement, the lidar equation is written as

$$P = P_0 \; K \; \frac{A}{r^2} \; ds \; \beta(\theta_{scat}) \; T, \qquad (1)$$

where P is the received signal intensity, P_0 the emitted laser intensity, K the efficiency of the receiving optics, A the area of the telescope mirror, r the distance between the target (aerosol particle) and the telescope, θ_{scat} the scattering angle, and T the transmittance along the combined laser path and viewing path. The portion of the laser beam path subtended by the FOV for a single pixel of the array detector is denoted as ds, which is given as

$$ds = \frac{r \; \theta_{FOV}}{\sin(\theta_{scat})} \; . \qquad (2)$$

The side-scattering coefficient, $\beta(\theta_{scat})$, is defined as

$$\beta(\theta_{scat}) = \alpha_1 \; f_1(\theta_{scat}) + \alpha_2 \; f_2(\theta_{scat}) \; . \qquad (3)$$

Here, θ_{FOV} is the FOV for a single pixel, α the extinction coefficient, and f the phase function. Subscript 1 is for aerosol and 2 for air molecule. Combining Eqs.(1) and (2), one can see that the signal is proportional to r^{-1}, indicating less stringent requirement for the system dynamic range.

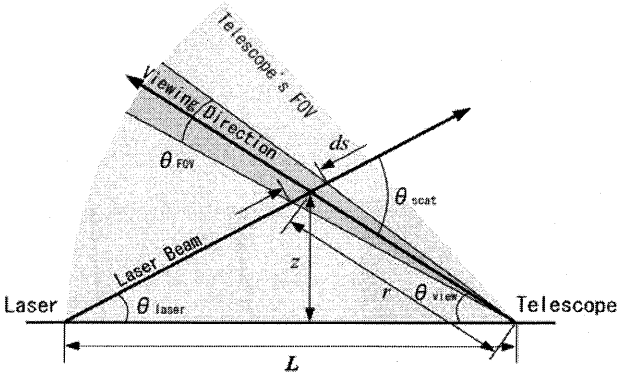

Fig. 4 Configuration of bistatic lidar measurement

4. Bistatic observation

The bistatic observation was carried out by locating the Ashra telescope at about 40 m from the laser location. The experimental setup is shown in Fig. 5. The telescope axis was fixed toward the zenith, so that when the elevation angle of the 351 nm laser beam was 60 deg, for instance, laser traces are recorded in an altitude range of 50-130 m. The exposure time was 1 s and the gate width was 20 μs.

Fig. 6(a) shows the laser traces obtained by subtracting the background (laser-off) image from the laser-on image. Fig. 6(b) shows the resulting intensity obtained by accumulating the digital number (DN) values across the laser beam trace. Comparison between the experimental result (Fig. 6(b)) and

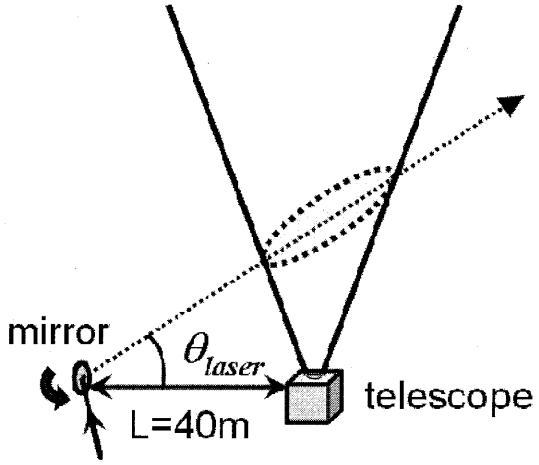

Fig. 5 Experimental setup for the bistatic measurement with the Ashra telescope

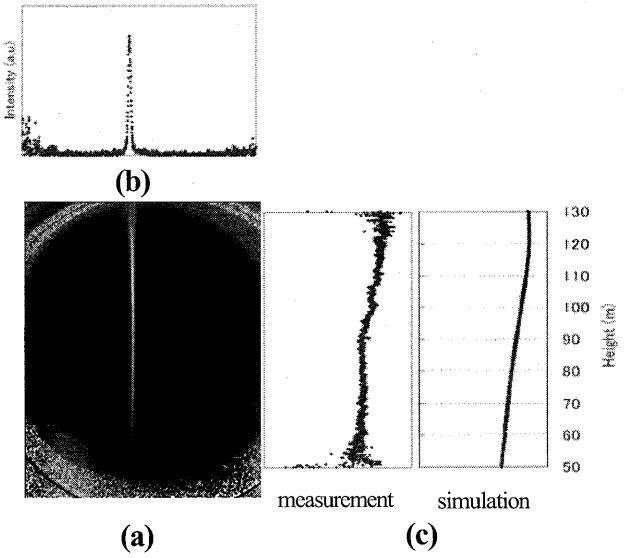

Fig. 6 (a) image of the UV laser beam, (b) cross- sectional signal intensity and (c) measured and simulated intensity of the scattered light.

simulation (Fig. 6(c)) indicates that we have a reasonable agreement between them. Because of the high-sensitivity of the Ashra telescope, it is possible to obtain two-dimensional distributions of aerosols and clouds by scanning the laser beam direction in the telescope FOV.

5. Cloud observation using the Ashra telescope

Fig. 7 shows an example of cloud images continuously observed with the Ashra telescope system. In this experiment, both the laser beam and telescope axis directions were fixed vertically. The bright spot indicates the point at which the laser beam hits the cloud bottom, where multiple scattering effects occasionally causes the spatial spread of return images.

For the sake of quantitative evaluation of cloud optical properties, we have undertaken a simulation in which the imaging lidar observation using the Ashra telescope can be exploited to derive the information on cloud droplet sizes. The following form of C1 cloud distribution is assumed:

$$n(r) = C\left(\frac{r}{R_m}\right)^{\nu_p} \exp\left(-\frac{r \cdot \nu_p}{R_m}\right) \qquad (4)$$

Here C is a normalization constant and r is the particle radius. The parameter ν_p stands for the width of the distribution, and R_m is the geometrically averaged mean radius: here we fix ν_p=6, while varying R_m in a range of 1-20 μm (1 μm step) (Fig. 8). The Mie theory for spherical particles is employed to calculate the scattering phase function assuming the complex refractive of m= 1.33-0.00i. Fig. 9 shows the resulting phase functions for various values of the droplet mean radius, R_m. In this figure, the variation is shown in the scattering angle (θ_{scat}) range of 170-180 deg, with all the curves normalized at θ_{scat} =180 deg. As seen from this figure, maxima in phase functions appear in the rage of θ_{scat} = 174 -179 deg. This result indicates that a close examination of this scattering angle regime might enable determination of droplet radius for clouds having R_m<10 μm.

Next, we consider the case in which the elevation angle of the laser beam is fixed and only the position of laser emission is changed (Fig. 10). In this case we assume an elevation angle of 85 deg. Fig. 11 shows the relation

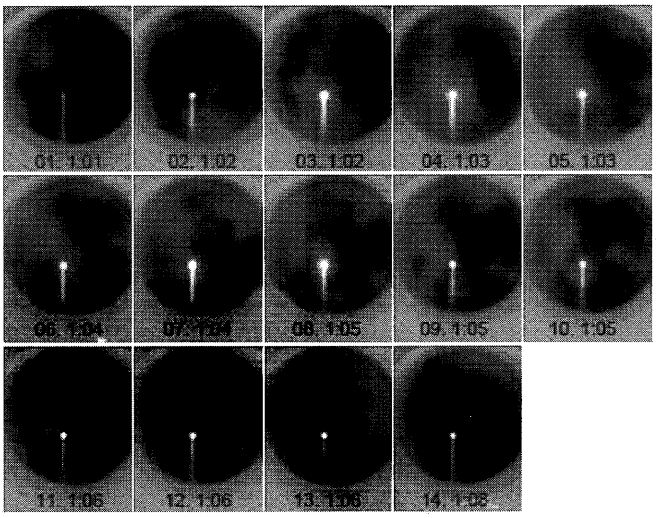

Fig. 7 Temporal change of cloud return with the vertically emitted laser beam.

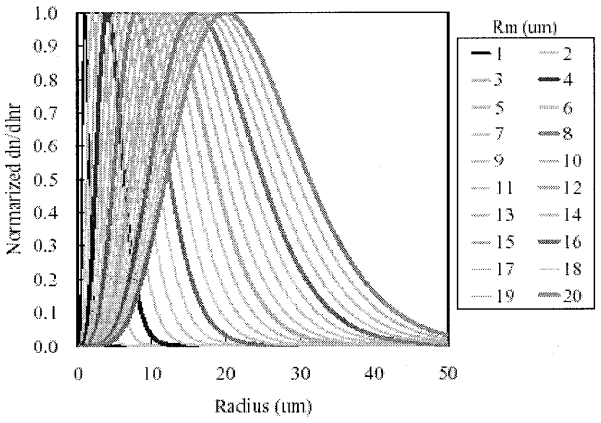

Fig. 8 Size distribution of cloud droplets assumed in the present simulation

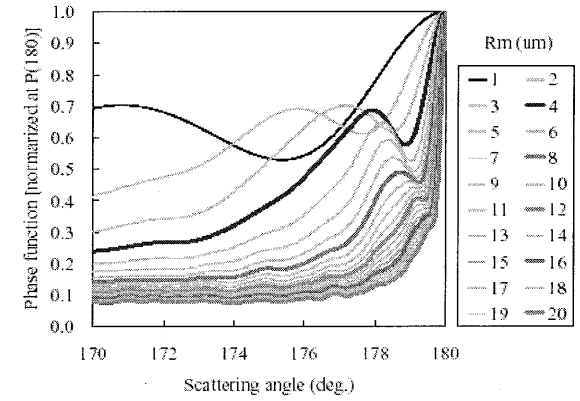

Fig. 9 Variation of phase function for various values of droplet mean radius

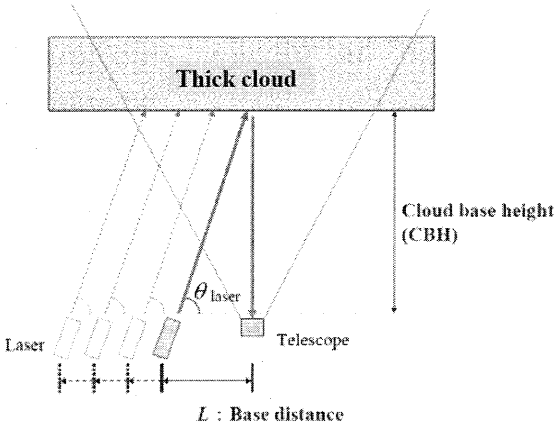

Fig. 10 Proposed observation scheme

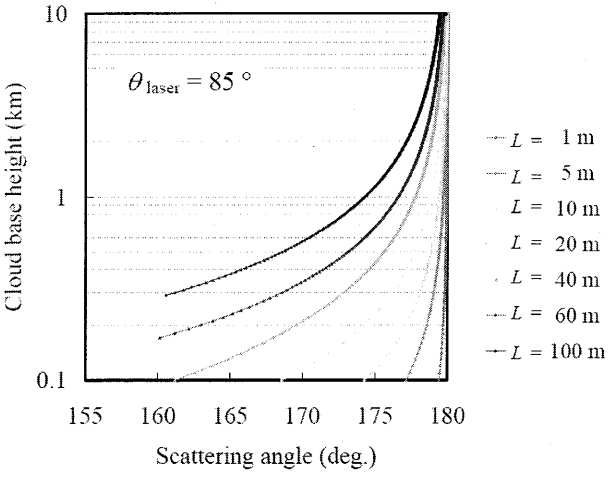

Fig. 11 Relation between the cloud base height and the observational range of the scattering angle for various distances between the laser and telescope

between the cloud base height and the observational range of the scattering angle for various distances between the laser and telescope. When the base distance L is changed between 1 and 100 m, the possible range of the scattering angle is 161.2 - 179.4 deg the cloud base height (CBH) of 100 m, 168.6 - 179.9 deg for CBH = 500 m, and 177.7 - 179.9 for CBH = 1 km. Since the present measurement of the Ashra telescope can be carried out with L = 5 to 40 m, one can see that observations with θ_{scat} =175.6 - 179.4 deg is feasible for clouds with CBH = 500 m, and θ_{scat} =177.8 - 179.7 deg for those with CBH = 1 km, leading to coverage of the scattering angle range which characterizes the variation in the phase functions as shown in Fig. 9.

Details on the relevant experiment will be shown in the presentation.

Acknowledgements

This work was supported by the Grant-in-aid for Scientific Research from the Ministry of Education, Culture, Sports, Science and Technology, Japan.

References

1) Sasaki, M. A. Kusaka, Y. Asaoka, 2002: Design of UHECR telescope with 1 arcmin resolution and 50°field of view, Nucl. Instr. Meth. Phys. Res. A492, 49-56.

2) Kouga, I. Y. Yamaguchi, S. Fukagawa, N. Takeuchi, H. Kuze, M. Sasaki, Y. Asaoka, S.Ogawa, 2006: Bistatic Measurement of Atmospheric Aerosol Distributions by Using an Imaging Lidar, Proc.23rd Int. Laser Radar Conf., 211-214.

3) Meki, K., K. Yamaguchi, X. Li, Y. Saito, T.D. Kawahara, and A. Nomura, 1996: Range-resolved bistatic imaging lidar for the measurement of the lower atmosphere, Opt. Lett. 21 (17), 1318-1320.

4) Barnes, J.E., S. Bronner, R. Beck, N. C. Parikh, 2003: Boundary Layer Scattering Measurements with a Charge-Coupled Device Camera Lidar, Applied Optics, 42 (15), 2647-2652.

The retrieval of the aerosol optical properties based on the spheroids model

Eriko Kobayashi[1], Akihiro Uchiyama[2], Akihiro Yamazaki[3], and Rei Kudo[4]
Japan Meteorological Agency, Meteorological Research Institute,
1-1, Nagamine, Tsukuba, Ibaraki 305-0052, Japan
[1]*kobaerk@mri-jma.go.jp,* [2]*uchiyama@mri-jma.go.jp,*[3]*akyamaza@mri-jma.go.jp,* [4]*reikudo@mri-jma.go.jp*

Abstract

We applied the aerosol retrieval algorithms based on the spheroids model [Dubovik et al.,2006] to the Skyrad software package [Nakajima et al.,1996], and tested it using the simulated data and observed data. The difference of the results between the spheroids model and the Mie theory is small. However, we verified that we can retrieve the dustlike aerosol optical properties stably with the spheroids model.

1. Introduction

The Skyrad package (SKYRAD.pack) is one of the well-known software which analyzes the sky radiometer data, and its aerosol retrieval algorithms is based on the Mie theory [Nakajima et al., 1996][1]. However, it is need to account for particle non-sphericity in modeling the optical properties of dustlike aerosols. We applied the method for the retrieval of the optical properties of non-spherical aerosol based on the spheroid model [Dubovik et al.,2006][2] to the Skyrad package and tested it using the simulated data and observed data.

2. Methods

The sky radiometer can observe the monochromatic direct solar flux density F($Wm^{-2}\,\mu\,m^{-1}$) and the monochromatic diffuse sky flux density E($Wm^{-2}\,\mu\,m^{-1}$). And the input data of the Skyrad package are R(Θ) (the ratio of the E to F; Θ: scattering angle) and aerosol optical thickness (τ_a).

$$R(\Theta) \equiv \frac{E(\Theta)}{Fm_o \Delta\Omega},$$

m_o : optical air mass, $\Delta\Omega$: solid view angle

The single-scattering properties of randomly oriented spheroids were approximated as follows:

$$\tau_{scat} P_{ii'}(\Theta,\lambda) \approx \sum_{p,k} \frac{dn(\varepsilon_p)}{d\ln\varepsilon} \frac{dV(r_k)}{d\ln r} K_{ii'}(\Theta,\lambda,n,k,\varepsilon_p,r_k)$$

$$\tau_{ext/scat} \approx \sum_{p,k} \frac{dn(\varepsilon_p)}{d\ln\varepsilon} \frac{dV(r_k)}{d\ln r} K_{ext/scat}(\lambda,n,k,\varepsilon_p,r_k)$$

τ_{ext} : the extinction optical thickness
τ_{sca} : the scattering optical thickness
$P_{ii'}$: the elements of the scattering matrix

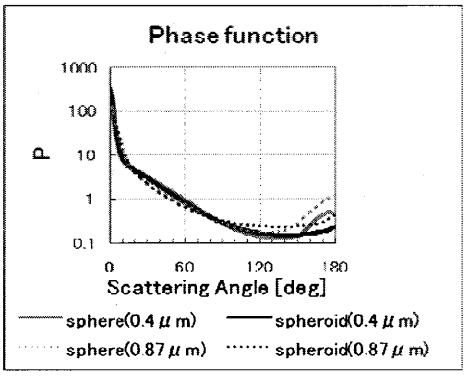

Fig.1
Comparison of phase function of the Mie theory and the spheroid model.

ε : axis ratio of the spheroid
r : radius of the particle
dV/dlnr : the volume size distribution
λ : wavelength
n,k : the real and imaginary part of the refractive index

The Kernels $K_{ii'}$, K_{ext} and K_{sca} can be precomputed.

We used the Kernel look-up tables of phase function, extinction and absorption which were calculated for polydisperse randomly oriented spheroids instead of the look-up tables based on the Mie theory. Two methods were used for computing these Kernel look-up tables. For size parameters below x(=$2\pi r/\lambda$) ~30-60, the simulation were performed using the T-matrix method [Mishchenko and Travis, 1994][3]. For size parameters exceeding the T-matrix convergence limits, the approximated geometric-optics-integral-equation method [Yang and Liou, 1996][4] was used. We used the fixed axis ratio distribution which is an equiprobable distribution of prolate and oblate

spheroids. The spherical-nonspherical differences in the scattering phase function is large around 120° and 180°(Fig.1). Therefore if the measurement is carried out in a wide scattering angle range, that differences can cause differences in the retrieved aerosol optical properties.

3. The sensitivity test with simulation data

We tested the Skyrad package which adopted the spheroid kernel look-up tables with some simulated dustlike aerosol models and verified the new method can retrieve aerosol optical properties with enough accuracy (Fig.2).

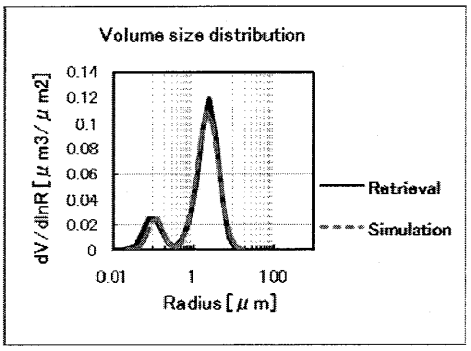

Fig.2

Retrieved volume size distribution of simulated aerosol model. Input simulation data are R(Θ) and τ_a.

4. Application to observed data

We tested the Skyrad package based on the spheroid model with observed data. In the case of the input observed data are R(Θ) and τ_a, the difference between the Mie theory and the spheroid model was small. However, several cases those input data are R(Θ) only (on the assumption that τ_a is unknown), there were large differences in retrieved aerosol optical properties(Fig.3).

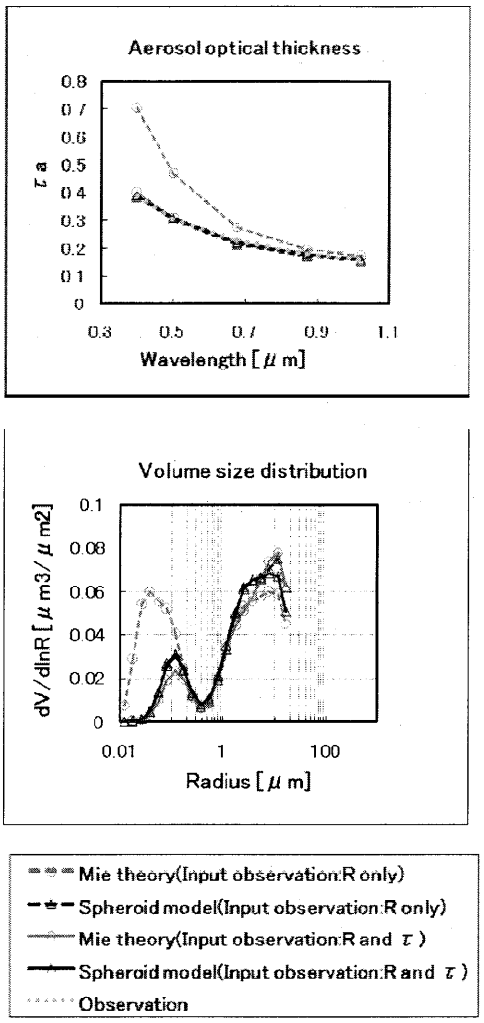

Fig.3

Retrieved aerosol optical thickness(upper) and volume size distribution(lower) of observed data. Site:Tukuba,Japan(2004,April)

5. Conclusion

We applied the new Kernel look-up tables which based on the spheroid model to the Skyrad package and verified that we can retrieve the dustlike aerosol optical properties stably with it.

We also tested the new method with observed data. In the case of the aerosol optical thickness is unknown, the new method which based on the spheroid model can improve the retrieval of dustlike aerosol optical properties.

Acknowledgements

We would like to acknowledge the use of the data of the SKYNET site. We are grateful to Dr.O.Dubovik for the kernels and software package.

References

1) Nakajima, T., and G. Tonna et al., Use of sky brightness measurements from ground for remote sensing of particulate polydispersions, Appl. Opt., 35, 2672-2686, 1996.

2) Dubovik, O., and A. Sinyuk et al., Application of spheroid models to account for aerosol particle nonsphericity in remote sensing of desert dust, J.Geophys.Res., 111, D11208,2006.

3) Mishchenko, M. I., and L. D. Travis, T-matrix computations of light scattering by large spheroidal particles, Opt. Commun., 109, 16-21, 1994.

4)Yang, P., and K. N. Liou, Geometric-optics-integral-equation method for light scattering by nonspherical ice crystals, Appl. Opt., 35, 6568-6584, 1996.

Separation of cloud-affected data for PREDE sky radiometer data analyses and then study of aerosol climatology in an urban atmosphere of Chiba, Japan

Pradeep Khatri[1] and Tamio Takamura[2]
[1]CEReS, Chiba University, Chiba, Japan, Email: pradeep.nep@gmail.com
[2]CEReS, Chiba University, Chiba, Japan, Email: takamura@faculty.chiba-u.jp

Abstract

This paper firstly describes an algorithm to screen cloud-affected data for sky radiometer data analyses. The proposed algorithm is observed to screen cloud-affected more effectively in comparison to other algorithms. Secondly, aerosol climatologies in an urban atmosphere of Chiba studied by using cloud-screened data are presented. Aerosols in an urban atmosphere of Chiba are observed to show distinct seasonal variations in magnitudes and diurnal cycles of optical properties as well as magnitudes of aerosol radiative forcing. The study suggests the influence of complicated air masses in the spring season, whereas aerosols existing in the autumn season are suggested to be more capable to trap energy in the atmosphere by creating comparatively larger radiative forcing efficiency difference at that top of the atmosphere and the surface.

1.Introduction

Though aerosols are known to play an important role on atmospheric heat budget, their effects on climate change are still subject of debate. This is due to the uncertainties in aerosol optical properties and spatial distributions of aerosols. Therefore, both the quality check of data and collection of information regarding aerosol effects on atmospheric heat budget in different regions of climatic significance are important.

The continuous collection of data in SKYNET network by various instruments, including PREDE sky radiometer, are very useful for expanding our knowledge regarding aerosol effects of climate change, however, one of the challenges for using PREDE sky radiometer data is to separate clear sky and cloudy sky periods. Additionally, as several major field campaigns were mainly held over the ocean or costal regions, data of urban atmospheres are relative sparse. In view of those recognitions, this paper focuses on two important topics: (i) Development of a cloud screening algorithm for PREDE sky radiometer data analyses and (ii) study of aerosol optical properties and direct radiative forcing in an urban atmosphere of Chiba, Japan using data collected by PREDE sky radiometer.

2. Development of a cloud-screening algorithm

A detailed description of a cloud-screening algorithm is reported in a separate publication.[1)] In brief, the algorithm consists three tests: (i) test with global irradiance data, (ii) spectral variability test, and (iii) statistical analyses test. Though the test with the global irradiance data is the most powerful test, our study shows that it has some limitations, which can sometimes cause some clear sky data to be detected as cloud-affected data. In order to cope this problem, a modified version of spectral variability algorithm[2)] is proposed. As the second test, the modified spectral variability algorithm is applied to filter clear sky data from data detected as cloud-affected by the first test. Finally, statistical analyses tests (diurnal stability test, data smoothness test, and three standard deviation criteria test) are performed to remove any outlier, if exists, from clear sky data detected by the first and second tests. It is shown that our proposed algorithm can screen cloud-affected data more effectively in comparison to other cloud screening algorithms (Table 1 of Khatri and Takamura (2008)). As an example, Figure 1 shows scatter plots of aerosol optical thickness at 500nm (τ_{500nm}) and angstrom exponent (α) before and after

cloud screenings for one year data of 2006 collected in Chiba. Approximately 77% of initial data remained after cloud screening. As shown in Figure 1(b), some data with τ_{500nm} of around 1.5 still exist. Those data are less likely to be cloud-afffected because of their high values of α. Similarly, some data with high τ_{500nm} and small α (indicated by dotted closed oval) also exist. Those data are noted to fall in the spring season. Furthermore, the present algorithm is applied to dust-loaded atmospheres by taking data collected in Dunhuang in the spring season of 2006. It is discussed that the present algorithm may screen cloud affected data effectively even in the dust loaded atmosphere. For Dunhuang data, the mean value of τ_{500nm} (α) is observed to decrease (increase) by ~0.12 (~0.073) by eliminating ~36.9% of initial data after an application of cloud screening algorithm.

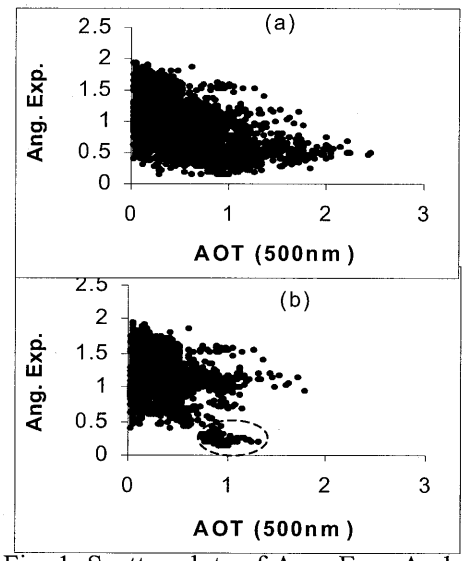

Fig. 1. Scatter plots of Ang. Exp. And AOT (500nm) (a) before cloud screening and (b) after cloud screening.

3. A study on aerosol climatology in an urban atmosphere of Chiba, Japan

a. Diurnal variations of aerosol optical properties

The results presented hereafter are for data collected in Chiba in 2006 and 2007, and are analyzed using skyrad.pack (ver. 4.2) software.[3] Figure 2 shows diurnal departures of (a) AOT (500nm), (b) Ang. Exp., and (c) SSA (500nm) from their mean values in various seasons. The diurnal variations shown in Figure 2 are related to local meteorology and/or local or foreign aerosol sources. Figure 2(a) shows that AOTs(500nm) have weak (except spring season) and strong peaks in beforenoon and afternoon periods. On that contrary, Figure 2(b) shows that Ang. Exps. have pronounced peaks in the beforenoon period than those in afternoon (except spring season) period, indicating that small and large size ranged aerosols were responsible for increasing AOTs(500nm) in the beforenoon and afternoon periods. Regardless of the season, wind speed increased in the afternoon periods, which suggested that foreign aerosols could easily transport over the observation area in the afternoon periods. SSAs (500nm) showed relatively low values (except spring season) in the beforenoon hours, which might be due to the emissions of light absorbing aerosols from automobiles in the morning hours. The interesting behavior of diurnal cycle in the spring season indicates that complex air masses influences the observation area in this season.

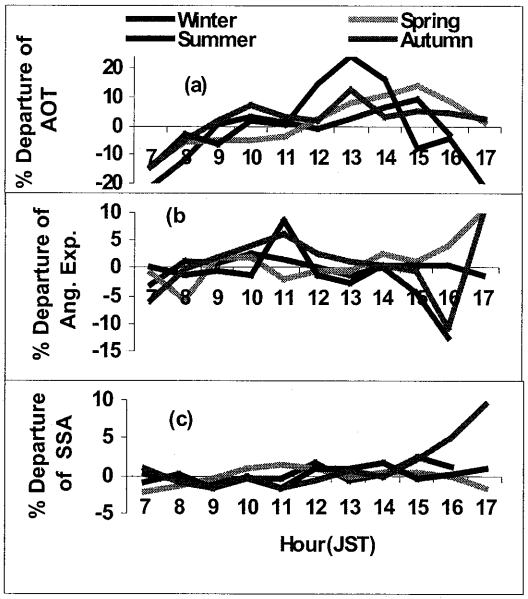

Fig. 2. Diurnal departure percentages of aerosol optical properties from their mean values at various seasons.

b. Seasonal variations of aerosol optical properties

Table 1 shows statistical analyses of aerosol optical properties for various seasons. It is understood from Table 1 that AOTs(500nm) are high in spring and summer seasons and low in winter and Autumn seasons. The moderate Ang. Exp. for the spring season indicates the mixtures of various aerosol species. Similarly, aerosols in the autumn season are observed to be strongly light absorptive in nature, wheraeas, aerosols in the spring season are comparatively more light scattering in nature. Figure 3 gives a more clear indication that aerosols in the spring season are indeed complex in nature. As observed in Figure 3, frequency distributions of AOT(500nm) and Ang. Exp. for the spring season are quite different from other seasons. Clear bimodal distribution of AOT(500nm) is evident in the spring season. Additionally, a multimodal distribution of Ang. Exp. for the same season indicates the different origins of aerosols. Further, bimodal distributions of both AOT(500nm) and Ang. Exp. in the Summer season are also interesting to be noted. Though a weak mode of AOT(500nm) with relatively high values are observed, they have Ang. Exp. higher than around 1.0, indicating that they are less likely to be natural aerosols. It is possible that excessive amount of water vapor in an atmosphere in this season increases the size of aerosols and increases AOT (500nm).

Table1. Statistical analyses of aerosol optical properties

	AOT(500nm)	Ang. Exp.	SSA(500nm)	ASY(500nm)
Win.	0.19± 0.11	1.4± 0.27	0.88± 0.08	0.68± 0.04
Spr.	0.38± 0.21	1.11± 0.41	0.93± 0.07	0.68± 0.03
Sum.	0.47± 0.28	1.31± 0.30	0.89± 0.08	0.71± 0.04
Aut.	0.23± 0.12	1.34± 0.24	0.82± 0.07	0.69± 0.04

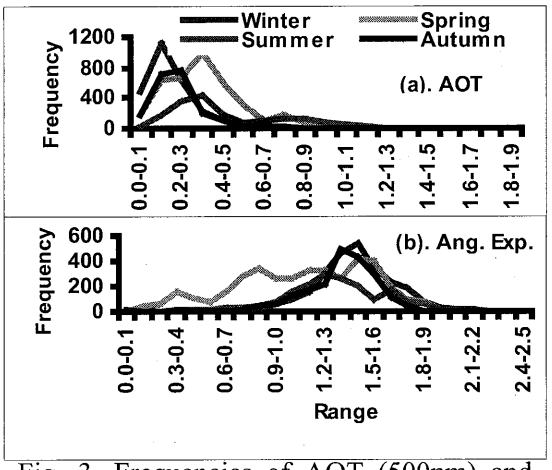

Fig. 3. Frequencies of AOT (500nm) and Angstrom Exponent on various seasons.

b. Seasonal variations of aerosol direct radiative forcing

In order to understand the effects of aerosols on atmospheric heat budget, aerosol radiative forcings at the surface and top of the atmosphere (TOA), and atmospheric radiative forcing are estimated for each season. The calculations are made using a SBDART radiative transfer model.[4] The major inputs in a radiative transfer model are spectral data of AOT, SSA, ASY, precipitable water content measured by a microwave radiometer, total ozone concentration measured by TOMS, and spectral data of reflectances measured by MODIS. The 24 hours average radiative forcings at TOA and surface were computed for clear sky observation days detected by our algorithm. Before estimating 24 hours average radiative forcings at TOA and surface, instantaneous values of downwelling global, direct, and diffuse irradiances measured by Kipp and Zonne's radiometers were compared with computed values using SBDART model. Those comparison showed satisfactory agreement. As an example, comparison of measured and computed global fluxes are shown in Fig. 5. On average, the modeled results agreed well with their measured components, however, close look of each observation datum indicates some discrepancies. This is likely due to uncertainty in either measured global irradiance or measured aerosol optical

parameters or certain assumption made during model simulation.

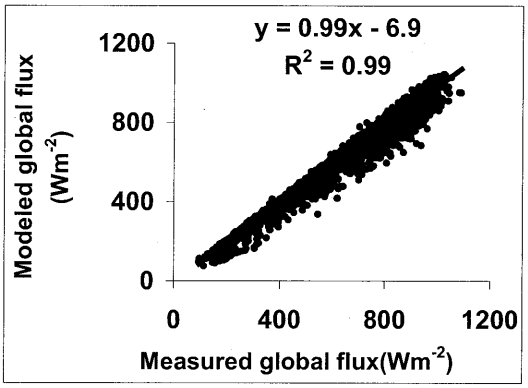

Fig. 5. A comparison between modeled and measured global irradiances.

Figures 5(a) and 5(b) show seasonal means with standard deviation of aerosol radiative forcings and aerosol radiative forcing efficiencies at the surface and TOA. The mean values of radiative forcings (radiative forcing efficiencies) in the winter, spring, summer, and autumn seasons at surface are $-12.25\pm5.21Wm^{-2}$ ($-65.74\pm15.41Wm^{-2}$), $-25.8\pm12.86Wm^{-2}$ ($-71.25\pm32.9Wm^{-2}$), $-26.53\pm15.71Wm^{-2}$ ($-60.2\pm34.68Wm^{-2}$) and $-15.49\pm5.05Wm^{-2}$ ($-64.93\pm18.12Wm^{-2}$), respectively. Similary, the respective values are $-6.95\pm3.46Wm^{-2}$ ($-37.86\pm12.75Wm^{-2}$), $-15.5\pm8.06Wm^{-2}$ ($-43.22\pm22.9Wm^{-2}$), $-11.84\pm10.98Wm^{-2}$ ($-22.6\pm11.91Wm^{-2}$) and $-5.81\pm4.71Wm^{-2}$ ($-20.45\pm9.83Wm^{-2}$) in the winter, spring, summer and autumn seasons, respectively. The radiative forcing (or radiative forcing efficiency) at TOA often reached above 0 Wm^{-2} in the autumn season for the days when SSAs(500nm) were low. The atmospheric forcing, which is a difference between radiative forcings at TOA and surface, is the highest with $14.7\pm9.5Wm^{-2}$, whereas it is the lowest with $5.3\pm3.8Wm^{-2}$ in the winter season. This indicated that more energy was trapped by aerosols in the summer season and less in the winter season. On the other hand, atmospheric forcing efficiency has the highest value with $44.5\pm20.5Wm^{-2}$ in the autumn season and the lowest value with $27.9\pm16.9Wm^{-2}$ in the winter season. This suggests that aerosols existing in the autumn season are more capable to absorb energy in the atmosphere in comparison to other seasons. Such trapped energy by aerosols is effectively used to heat the lower atmosphere.

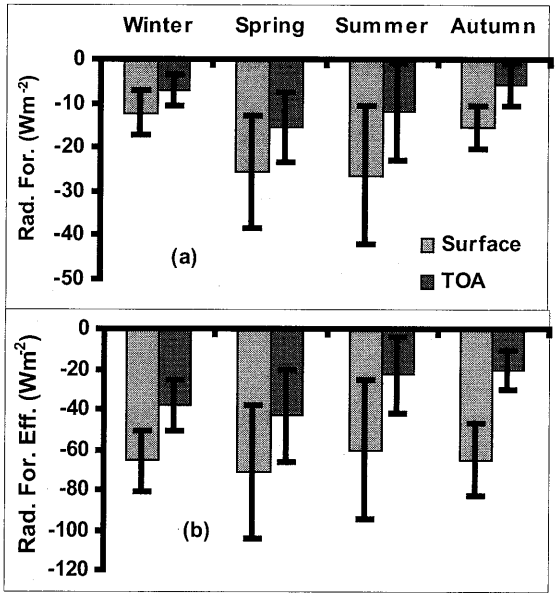

Fig. 5. Seasonal variations of (a) aerosol radiative forcing and (b) aerosol radiative forcing efficiency at top of the surface and top of the atmosphere (TOA).

Acknowledgements

This research is supported by the JSPS Fellowship Program, and also performed as a part of the SKYNET activities by the Observational Research Project for Atmospheric Change in the Troposphere (GEOSS program) of the Ministry of Education, Culture, Sports, Science and Technology, Japan.

References

1)Khatri, P. and T. Takamura, 2008:, *J. Meteor. Soc. Japan* (Submitted).

2)Kaufman, Y. J., G. P. Gobbi, and I. Koren, 2006:, *Geophys. Res. Lett.*, **33**, L07817, doi: 10.1029/2005GL025478.

3)Nakajima, T., G. Tonna, R. Rao, Y. Kaufman, and B. Holben, 1996: *Appl. Opt.*, **35**, 2672-2686.

4) Ricchiazzi, P., S. Yang, C. Gautier, and D. Sowle, 1998:, *Bull. Am. Meteorolo. Soc.*, **79**, 2101-2114.

High altitude cloud observations using dual polarization Raman lidar technique

Y. Bhavani Kumar[1], M. Krishnanaih[2,3] and H. Kuze [2]

[1]National Atmospheric Research Laboratory, P B No. 123, S V UniversityCampus,Tirupati517502,Indiaypbk@narl.gov.in
[2]Center for Environmental Remote Sensing, Chiba University Inage-Ku, Chiba, 2638522 Japan hkuze@faculty.chiba-u.jp
[3]Department of Physics, Sri Venkateswara University, Tirupati – 517502, Indiaprofkrishnaiah.m@gmail.com

Abstract

Results from Dual polarization Elastic Raman lidar observations of tropical high-altitude cirrus clouds are reported. The observations are made over a tropical site Gadanki (13.5°N, 79.2°E), India. Based on 120 hours of night-time measurements of cirrus clouds show that the cirrus cloud particles extinction to backscatter ratio are in the range of 4 to 10. These clouds depolarization ratio appears increasing with decreasing temperature. The clouds appear at altitudes between 12 and 16 km. Volume depolarization is found to be a sensitive parameter for the detection of subvisible cloud layers. Lidar derived observations of cirrus clouds are compared with atmospheric temperature. Observations will be discussed in light of present understanding of cirrus microphysics.

Keywords: Tropical cirrus, Raman Lidar, Lidar ratio

1. Introduction

Several remote-sensing observational techniques involving satellite infrared instruments (Prabhakara et al., 1993), satellite-limb occultation (Wang et al., 1996), ground-based lidar (Nee et al., 1998) and satellite lidar (Winker and Trepte, 1998) have revealed the frequent occurrence of thin cirrus layers located near the tropical tropopause at altitudes between 12 and 16 km. These thin layers are generally sub visible in nature and typically several hundred meters to one kilometer in vertical extent. These layers are spread over across several hundred kilometers horizontally (Winker and Trepte, 1998) and prevail from several hours to several days before they get evaporated. The occurrence of thin cirrus layers near the tropical tropopause can have significant impact on the radiative heating in the upper troposphere (McFarquhar et al., 2000).

Range resolved optical properties such as extinction coefficient in thin cirrus clouds are important for assessing the impact of cirrus on climate. Vertical profiles of cirrus extinction are important parameter for heating rate calculations, which plays a key role in radiative characteristics of cirrus. The extinction-to-backscatter ratio (also called lidar ratio) provides information on the transmission and reflection properties of cirrus clouds and also on the ice crystal properties due to its dependence on the shape, size and orientation of the particles. Moreover, the lidar ratio is required for validation of extinction retrievals from single wavelength elastic lidars. The availability of a reliable data set of lidar ratio for different cirrus types and conditions will greatly improve the quality of the cirrus properties derived from space, which will produce a global climatology of cirrus range resolved properties.

In this paper, we report a ground based observation of a thin cirrus layer from Indo-Japanese Lidar operated in Elastic and also in Raman mode of operation. These observations provide cloud backscatter ratio, its linear depolarization along with cloud extinction from Raman shifted wavelength. The Raman shifted wavelength information is also used for deriving the atmospheric temperature. Using this unique observational setup the thin cirrus cloud characterization is made for several cloud passes. In this study, we present a thin cirrus occurrence on 24 January 2003 as a case study.

2. Experimental mode of Raman observations

The Indo-Japanese lidar system has been providing the altitude profiles of temperatures in the range covering 30 to 80 km using Rayleigh scatter technique (Bhavanikumar et al., 2000;2006) and also has been used to derive the vertical structure of high altitude clouds such as the occurrence of tropical cirrus (Bhavanikumar et al., 2001). However, there is

a fundamental limitation in extending the Rayleigh scatter technique to lower heights because the Rayleigh scattering from air molecules suffers from the presence of Mie component caused by aerosol scattering. One can overcome this constraint by employing Vibrational-Rotational (Simply Vibrational technique) Raman technique in addition to Rayleigh-scatter technique. This technique has not been widely used for the study of the lower stratosphere because of the very low cross section of this scattering, 3 orders of magnitude smaller than the Rayleigh cross-section. The Indo-Japanese lidar system at Gadanki (13.5° N, 79.2° E), a rural site in the tropical part of India, is successfully experimented with the capability of acquiring vibrational Raman (inelastic) backscatter from atmospheric Nitrogen in addition to the elastic backscatter. The vibrational Raman backscatter from atmospheric Nitrogen has a characteristic shift of 2331 cm^{-1}, for 532 nm atmospheric excitation, which corresponds to a shifted wavelength of 607 nm. The experimentally tested results proved the capability of retrieving the atmospheric temperatures in the altitude range of 8 – 28 km using vibrational Raman technique with an error in temperatures of about 5 K, 2 K, 1 K and less than 1 K at 25 km, 20 km, 15 km and below 12 km respectively in two-hour integration (Bhavani Kumar and Mizutani, 2004). Using the simultaneously observed Raman shifted signal at 607 nm wavelength and elastic backscatter returns at 532 nm from polarization lidar provides unique means of studying the high altitude cloud structure and microphysics.

3. Calculation of Extinction Coefficient from Raman Lidar Measurements

In order to derive extinction coefficient form elastic lidar measurements the so-called Klett (1981) inversion method is used. This method, however, has the disadvantage that two physical quantities, the aerosol backscatter and extinction coefficients must be determined from only the elastic backscatter. This is not possible without assumptions about the relationship between the two and an estimate of a reference value of the aerosol extinction. These data are usually hard to assess and cause large uncertainties in the derived aerosol extinction coefficients. In contrast, the inelastic Raman backscatter signal is affected by aerosol extinction but not by aerosol backscatter. Therefore analysis of the Raman lidar signal alone permits the determination of the aerosol extinction.

The formalism to derive extinction from Raman lidar measurements was developed by Ansman et al. (1990). Accordingly, the aerosol extinction coefficient is obtained from the slope of the Raman nitrogen profile compared to the atmospheric density profile as:

$$\alpha(\lambda_L, z) = \frac{\left(\frac{d}{dz}\left\{\ln\left[\frac{N(z)}{z^2 P(z)}\right]\right\} - S_{mol}(\lambda_L, z) - S_{mol}(\lambda_R, z)\right)}{1+\left(\frac{\lambda_L}{\lambda_R}\right)^k} \quad \text{— (1)}$$

where $\alpha(\lambda_L,z)$ is the cloud extinction coefficient, N(z) is the atmospheric number density, z is the altitude of the measurement, S_{mol} is the molecular extinction coefficient, P(z) is the molecular lidar signal and λ_L and λ_R are the laser and the Raman shifted wavelengths, respectively. The wavelength dependence of the aerosol extinction coefficient is described by the parameter k. For aerosol particles with diameter comparable to the measurement wavelength k=1, while for particles considerably larger than the measurement wavelength, k=0. The main difficulty in deriving the extinction coefficient form equation (1) is associated with the calculation of the slope

$$\frac{d}{dz}\left\{\ln\left[\frac{N(z)}{z^2 P(z)}\right]\right\}$$

since the molecular signal, which can be quite noisy, usually requires significant averaging and smoothing before slope calculations can be performed. The Indo Japanese lidar system located at Gadanki (13.5° N, 79.2° E) transmits laser wavelength of 532 nm and measures the backscattered elastic (aerosol) return at the same wavelength for deriving the height profiles of atmospheric temperature in the upper atmosphere and height profiles of aerosol in the upper troposphere respectively. In addition, on an experimental mode, the height profiles of Raman shifted signal returns from atmospheric Nitrogen were received from the atmosphere at 607 nm. However, the

aerosol return at 532 nm is split into co-polarized and cross-polarized components, enabling the computation of the depolarization ratio Bhavani Kumar et al 2001, 2006). In order to derive cirrus extinction coefficient according to Eq. (1), the molecular nitrogen return at 607 nm is utilized and value of k=0 is assumed. Volume depolarization is found to be a sensitive parameter for the detection of subvisible cloud layers.

4. Observations

Figure 1(a) and (b) depict temporal variation of cloud backscatter ratio (BSR) and cloud linear depolarization ratio (LDR) observed by the Indo-Japanese lidar system on 24 January 2003 over Gadanki site, India. Figure 2 shows the elastic and Raman signal returns at 532 nm and 607 nm wavelengths. Figure 3 shows the derived extinction and backscatter coefficient profiles from Raman shifted and elastic backscatter signals respectively.

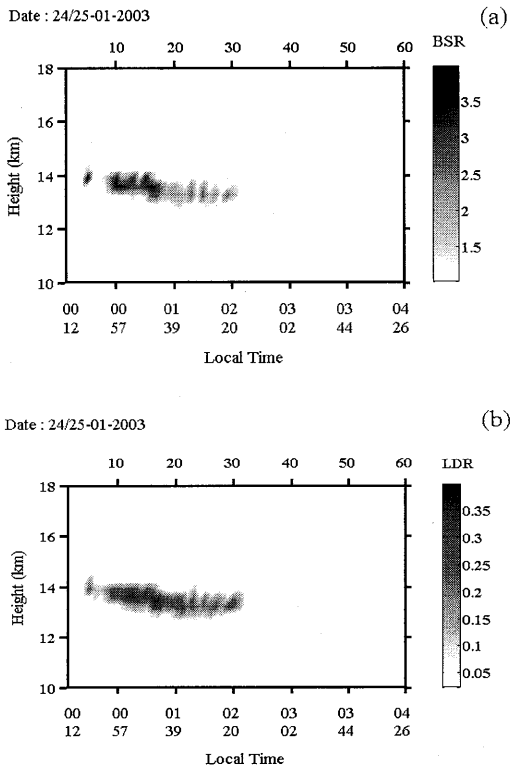

Figure 1. Indo Japanese Lidar observation of thin cirrus layer at altitudes between 13 and 15 km over Gadanki site, India on a winter night 24 january 2003. Figure 1(a) shows temporal variation of cloud BSR and figure 1(b) shows the cloud LDR

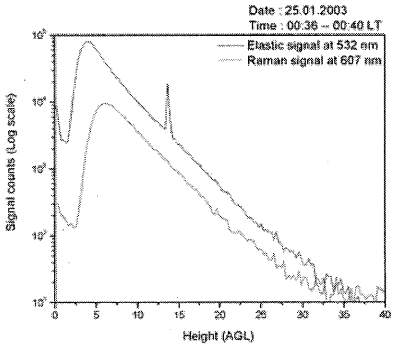

Figure 2. Height profiles of basic signal counts at 532 nm, elastic signal, and Raman shifted signal at 607 nm obtained using Indo-Japanese lidar system collected on mid night hours of 24 January 2003 over Gadanki site during thin cirrus cloud presence at 14 km altitude.

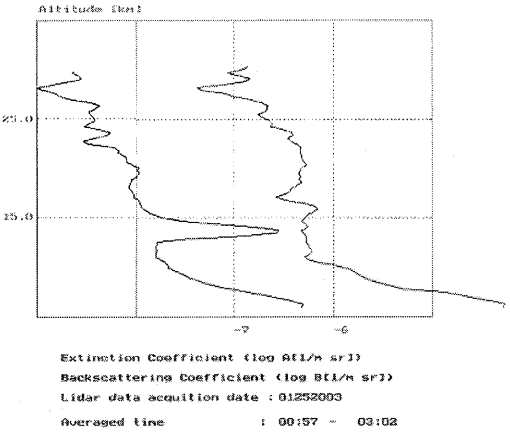

Figure 3. Backscatter and extinction coefficient profiles derived from Elastic and Raman shifted signal returns at 532 and 607 nm wavelengths from Indo-Japanese lidar system data obtained on 24 January 2003.

Some key microphysical parameters are the extinction coefficient, lidar ratio and depolarization ratio as well as the mid-altitude and the corresponding mid-cloud temperature of cirrus clouds. The lidar and depolarization ratios are considered to be of special importance since are related to microphysics properties of the ice crystals contained on cirrus clouds, while mid-altitude and mid-temperature play an important role in determining cloud radiative properties. Figure

4 shows the altitude profiles of cloud backscattering ratio (BSR), linear depolarization ratio (LDR), Extinction to backscattering ratio (lidar ratio) and mid cloud temperature.

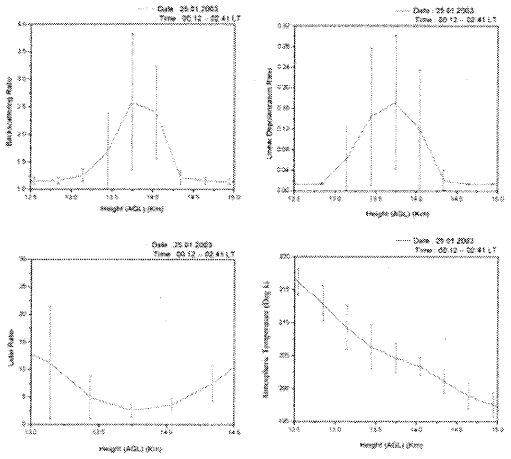

Figure 4 Profiles of (a) cloud backscattering ratio (BSR), (b) cloud linear depolarization, (c) Extinction to backscattering ratio (lidar ratio) and (d) atmospheric temperature in deg k. All the profiles are shown with its variability (standard deviation) for clarity on range of parameter deviation.

Conclusions

The accurate estimation of the extinction coefficient is possible through the Raman lidar technique and thus makes this method a powerful tool for cirrus studies. The independent measurement of backscatter and extinction profiles and thus lidar ratio profiles is only possible through the Raman method. Nevertheless, this method can be applied only for night-time measurements. We have also investigated the dependence of optical properties on temperature and geometrical characteristics. A maximum mid-cloud depth is in the range of 1.5 km at temperatures between −60°C and −70°C, and decreases both for lower and larger temperatures. An indication that mean lidar ratio and linear depolarization ratio increases with decreasing mid-cloud temperature is found, while a dependence of optical depth on the geometrical thickness of cirrus clouds was also found.

References

1. Prabhakara, C., D. P. Kratz, J. M. Yoo, G. Dalu, and A. Vernekar, Optically thin cirrus clouds; Radiative impact on the warm pool, *J. Quant. Spectrosc. Radiat. Transfer.*,*49*, 467-483, 1993.
2. Wang, P.-H., P. Minnis, M. P. McCormick, G. S. Kent, and K. M. Skeens, A 6-year climatology of cloud occurrence frequency from Stratospheric Aerosol and Gas Experiment II observations (1985-1990), *J. Geophys. Res., 101*, 29,407-29,429, 1996.
3. Nee, J.B., C.N. Len, W.N. Chen, and C.I. Lin, Lidar observation of the cirrus cloud in the tropopause at Chung-Li (25°N, 121° E), *J. Atmos. Sci*, *55*, 2249-2257, 1998.
4. Winker, D. M. and C. R. Trepte, Laminar cirrus observed near the tropical tropopause by LITE, *Geophys. Res. Let., 25*, 3351-3354, 1998.
5. Bhavani Kumar, Y., V.Siva Kumar, P.B.Rao, M. Krishnaih, Kohei Mizutani, Tetsu Aoki, Motoaki Yasui, and Toshikazu Itabe, Middle atmospheric temperature measurements using a ground based lidar from low latitude, *IJRSP*, *29*, 249-257, 2000.
6. Bhavani Kumar, Y., V.Siva kumar, A.R.Jain, and P. B Rao, Indian MST radar and lidar observations of tropical cirrus, *Ann. Geophysicae*, 19, 873-883, 2001
7. Bhavani Kumar, Y. and Kohei Mizutani, Raman lidar observations of height profiles of upper troposphere and lower stratosphere temperature over a tropical site Gadanki, SPIE proceedings, 2004
8. Bhavani Kumar, Y., Nageswara Raju, and M. Krishnaiah, Indo-Japanese Lidar observations of tropical middle atmosphere during 1998 and 1999, *Adv Atm Sci*, 23, 5, 2006
9. Ansman, A, M Riebesell, and C Weitkamp. "Measurements of atmospheric aerosol extinction profiles with Raman lidar." *Opt Lett* 15, 746-748, 1990.
10. Klett, JD, "Stable analytical solution for processing lidar returns." *App. Opt,* 20, 211, 1981.

Comparing water vapor mixing ratio profiles using Indo-Japanese Lidar in Raman mode of operation with GPS radiosondes

Y Bhavani Kumar[1], M.Krishnanaih [2,3]and H.Kuze [2]

[1] *National Atmospheric Research Laboratory, P B No. 123, S V University Campus, Tirupati – 517502,India,*
[1]*ypbk@narl.gov.in,* [2]*,profkrishnaiah.m@gmail.com and* [2]hkuze@faculty.chiba-u.jp

[2]*Center for Environmental Remote Sensing, Chiba University, 1-33 Yayoi-Cho, Inage-Ku, Chiba, 263-8522, Japan*
[3]*Department of Physics, Sri Venkateswara University, Tirupati – 517502, India*

Abstract

We derived the height profiles of atmospheric water vapor, during nocturnal time periods, using the Indo-Japanese Lidar system augmented with Raman capability in addition to existing elastic mode of observation on experimental basis for a period of five months between January and October 2003. The derived height profiles of water vapor are corrected for aerosol and molecular transmission. During night time, the profile extends typically up to 10 km ASL with a vertical resolution of 300 m and an integration time of 15 minutes. Statistical error is typically within 5% up to 6 km of altitude and stays within 10% in 6-10 km altitude range. The height profiles of water vapor mixing ratio profiles are compared using simultaneous GPS radiosonde data. A good comparison between the lidar and radiosonde derived mixing ratio profiles were observed in the height range of observation.

Keywords: Water vapor, Raman lidar, GPS Radiosonde

1. Introduction

Water vapor is a very important molecular species in the atmosphere. Although it is located primarily in the troposphere, its distribution is highly variable in both time and position. Its measurement is important for the following three main reasons [1].

1. The knowledge of the atmospheric water vapor distribution is essential for achieving a full understanding of the Earth's water cycle. Water vapor is one of the most dynamic and variable gases in the atmosphere, with its total content ranging from nearly 0% to 4% of the total volume of the atmospheric column, depending on time and location [2]. The amount of water vapor averages about one per cent by volume in the atmosphere and its distribution in time and space is highly variable: it comprises about 4 percent of the atmosphere by volume near the surface, but only 3-6 ppmv (parts per million by volume) above 10 to 12 km. Nearly 50% of the total atmospheric water is trapped in the planetary boundary layer (PBL, from 0 to 1~5 km) while less than 6 % of the water is above 5 km.
2. Water vapor is the predominant greenhouse gas and plays a major role in the global climate system. It is known fact that the atmospheric water vapor is one of the most active absorbers of infrared (IR) radiation and hence considered as the most important greenhouse gas in the atmosphere [3]
3. Water vapor distribution has a direct impact on some natural disasters, such as cyclones. Water vapor has been found to be the main energy source for cyclones and water vapor measurement can aid in estimating cyclone strength and direction [4]. Moreover, at any given location in the atmosphere, the water vapor content can vary markedly in a relatively short time span, owing to the passage of cold or warm fronts, precipitation etc. Because of the critical role that water vapor plays in most atmospheric processes, accurate water vapor profiles are needed in atmospheric modeling applications. Water vapor profiles are also needed for basic meteorology applications (i.e. the identification and study of frontal boundaries, dry lines etc.,), boundary layer studies (such as cloud formation/dissipation), development of climatological records, and for radiative transfer calculations (aerosol research).

2. Theory

The chemical property of water vapor of condensation on different types of aerosols found in the atmosphere is changing the chemical composition, shape and size of these particles, and at the same time it affects their optical properties and the direct radiative forcing. One of the methods of monitoring the water vapor mixing ratio in the atmosphere is by using a Raman lidar which is based on the Raman Effect. When a substance is subjected to an incident exciting wavelength, it exhibits the Raman Effect. It reemits secondary light at wavelengths that are shifted from the incident radiation. The magnitude of the shift is unique to the scattering molecule, while the intensity of the Raman band is proportional to the molecular number density [5]. The water vapor Raman lidar technique uses the ratio of rotational-vibrational Raman scattering

intensities from water vapor and nitrogen molecules, which is a direct measurement of the atmospheric water vapor mixing ratio. The water vapor and nitrogen Raman signals are given by equation 1

$$P_R(z) = \frac{K_s(\lambda_R, z)}{z^2} n_R(z) \frac{^{\pi}d\sigma(\lambda_L, \lambda_R, z)}{d\Omega} * \quad (1)$$
$$* \exp\left[- \int_0^z (\alpha_{\lambda_L}(z) + \alpha_{\lambda_R}(z)) dz \right] + b_{\lambda_R}(z)$$

P_R is the detected Raman lidar backscatter signal corresponding to nitrogen and water vapor, K_s is a system function that is dependent on the optical transmission and detector efficiency, the overlap function and the area of the collector mirror of the telescope, n_R is the number density of Raman active molecule, $\frac{^{\pi}d\sigma(\lambda_L, \lambda_R, z)}{d\Omega}$ is the differential Raman backscatter cross-section, α is the extinction coefficient and b is the background (noise) signal.

By taking the ratio of the two signals one can obtain the water vapor mixing ratio profile in equation 2.

$$\frac{P_{H_2O}(z)}{P_{N_2}(z)} = \left[\frac{K_{H_2O}}{K_{N_2}} \left[\frac{\left(\frac{d\sigma}{d\Omega}\right)_{H_2O}}{\left(\frac{d\sigma}{d\Omega}\right)_{N_2}} \right] \frac{T_{H_2O}}{T_{N_2}} \right] * q_{H_2O}(z) \frac{M_{air}}{M_{H_2O}} \quad (2)$$

where T is the transmission for the two wavelengths through the atmosphere and M represents the mass of water vapor in atmosphere and dry air P_{H_2O} and P_{N_2} are the water vapor and nitrogen Raman signals. The water vapor profile may be retrieved as expressed in equation 3.

$$q_{H_2O}(z) = \frac{K_{N_2}}{K_{H_2O}} \frac{\left(\frac{d\sigma}{d\Omega}\right)_{N_2}}{\left(\frac{d\sigma}{d\Omega}\right)_{H_2O}} \frac{T_{N_2}}{T_{H_2O}} \frac{M_{H_2O}}{M_{N_2O}} \frac{P_{H_2O}}{P_{N_2}} \quad (3)$$

where q is the water vapor mixing ratio in [g/Kg dry air] or in [ppmv].

Hence $$q_{H_2O}(z) = C * \Gamma * \left[\frac{P_{H_2O}}{P_{N_2}} \right] \quad (4)$$

where $\Gamma = \frac{T_{N_2}}{T_{H_2O}} \cong 1$ and C is the calibration function.

Its main limitation is the relatively small backscatter Raman cross- sections, that result in weak Raman signals compared with the elastic backscatters. As mentioned above one might observe that the method requires the use of a calibration constant towards the retrievals.

$$C = \frac{K_{N_2}}{K_{H_2O}} \frac{\left(\frac{d\sigma}{d\Omega}\right)_{N_2}}{\left(\frac{d\sigma}{d\Omega}\right)_{H_2O}} \frac{M_{H_2O}}{M_{N_2O}} \quad (5)$$

There have been many calibration techniques proposed and used along time [6-9]. Many methods suggest an approximate external calibration, a one point in situ value, is the method proposed in this paper

3. Indo-Japanese Lidar (IJL) system description

IJL system is a monostatic system that contains a Continuum Nd:YAG laser model PL8020 with 20 Hz repetition rate of operation. The performances and technical specifications of the transmitter and receiver along with a schematic of the lidar system are described in detail in Ref.10. The receive system configuration is modified to obtain Raman signals .A schematic of the modified receiver configuration is presented in figure 1.

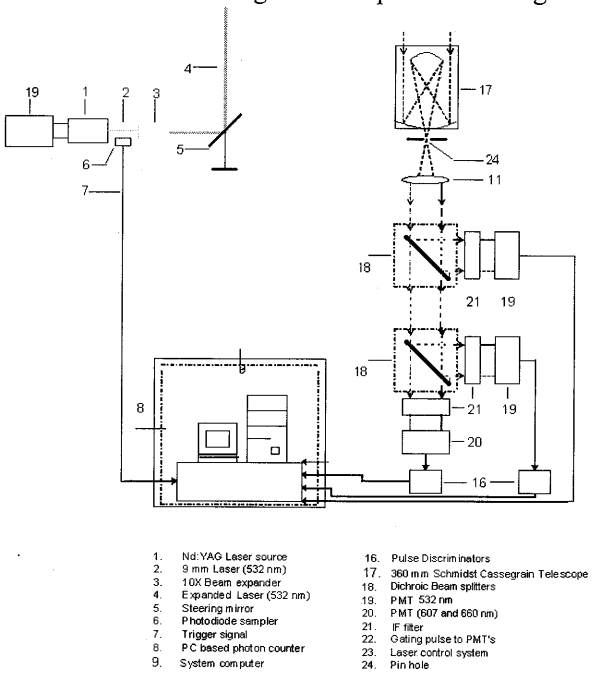

1. Nd:YAG Laser source
2. 9 mm Laser (532 nm)
3. 10X Beam expander
4. Expanded Laser (532 nm)
5. Steering mirror
6. Photodiode sampler
7. Trigger signal
8. PC based photon counter
9. System computer
16. Pulse Discriminators
17. 360 mm Schmidst Cassegrain Telescope
18. Dichroic Beam splitters
19. PMT 532 nm
20. PMT (607 and 660 nm)
21. IF filter
22. Gating pulse to PMT's
23. Laser control system
24. Pin hole

Fig. 1. Modified optical set-up of the receiver

The data acquisition is performed using MCS-plus pc based data acquisition cards working at 100 MHz sampling rate in photon counting mode and a discriminator which detects voltage pulses above a selected threshold in the range 0-10 mV. Typically an acquisition file contains 5000 shots averaged for each wavelength in photon counting mode of 1024 bins. This corresponds to a spatial resolution of 300 m at a time resolution of 250 sec. Water vapor and nitrogen profile measurements are thus performed and the obtained profiles are presented in Figure 2. By combining the

two profiles one can retrieve the relative humidity or water vapor mixing ratio in the lower troposphere.

3.1 Typical profiles

The typical lidar returns correspond to Nitrogen Raman at 607 nm and water vapor Raman at 660 nm are plotted in fig. 2. The signals are averaged over 30 minute time interval.

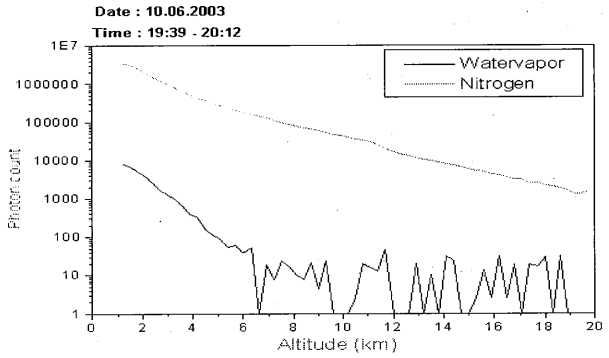

Fig. 2 Simultaneously obtained typical height profiles of Nitrogen and water vapor Raman profiles over Gadanki site on the night of 10 June, 2003.

3.2 Raman differential cross-section values

The accuracy of mixing ratio depends upon the differential backscattering cross-section values of trace traces. Table 3.1 shows the computed differential Raman backscatter cross section values of Nitrogen and Water vapor used in the derivation of water vapor mixing ratio. Published literature derived Raman backscatter cross-section values are shown in brackets [11].

Table 3.1 Comparison of theoretical and experimental values of Differential backscatter cross-section values of atmospheric Nitrogen and water vapor

Wavelength	N_2 Raman backscattering Cross-section (cm^2)	H_20 Raman backscattering Cross-section (cm^2)
532 nm	$3.93X10^{-31}$ ($5.642X10^{-31}$)	$1.101X10^{-30}$ ($1.26X10^{-30}$)

4. Water vapor mixing ratio measurements

The height profiles of water vapor mixing ratio is obtained on several days during clear sky nocturnal conditions. The mixing ratio profiles are corrected for aerosol profiles using the 532 nm elastic signal simultaneously obtained with the Raman signal returns.

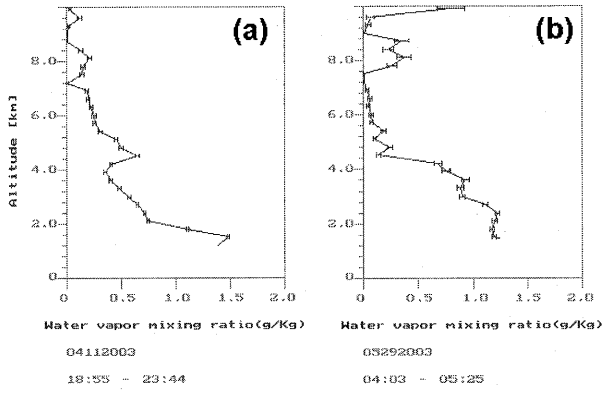

Fig. 3 Derived water vapor mixing ratio profiles observed on 11 April and 29 may 2003. Horizontal bars over the curve shows the standard error in the derived water vapor mixing ratio

The typical height profiles of derived water vapor mixing ratio is shown in Figure 3 a and b. Figure 3(a) shows water vapor mixing ratio obtained on 11 April 2003, where as 3(b) indicates water vapor mixing ratio obtained on 29 May 2003.

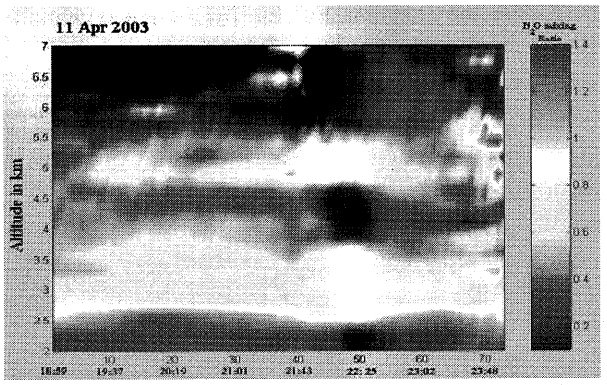

Fig. 4 Temporal variation of water vapor mixing ratio observed on 11 April 2003.

4.1 Raman Lidar signal and radiosondes based calibration method

The widely used method of water vapor calibration is using the lidar returns and the radiosonde data alone as main sources for correction is presented in the diagram in figure 5. The assumptions are that the parcels of air over both the radiosonde and the lidar location have similar meteorological characteristics at the times of data collection. The simplicity of the method consists in choosing a spatial range in the lidar data with very low noise where there are at least 2 or 3 radiosonds readings.

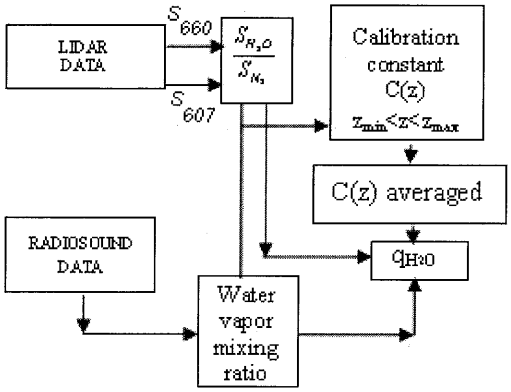

Fig. 5 Block diagram representing the combination of three sources of data in the attempt of calibration constant retrieval

By taking the ratio of the water vapor mixing ratio indicated by the radiosondes over the range and the lidar ratio of the 660 nm and 607 nm channels one can obtain the calibration constant. The retrieved relative humidity from the calibrated signal by use of this technique described above is plotted in fig 6.

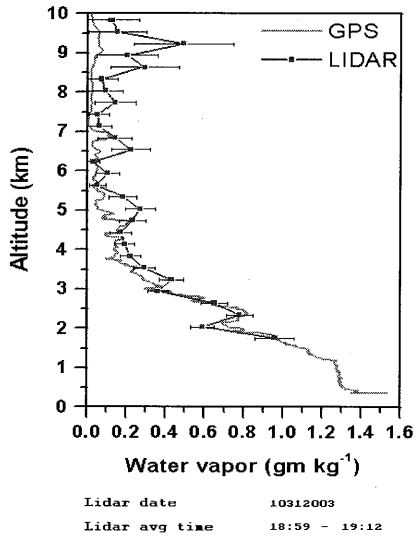

Fig. 6 Relative humidity measured by IJL lidar on October 31, 2003

5. Conclusions

The lidar data in Raman mode data was analyzed over cloud free days and validation of the retrievals is achieved by comparing the water vapor mixing ratio measurements using the vertical profiles of the mixing ratios measured by the GPS sondes at Gadanki site, India. The conclusion of this study is that has to be studied in more detailed way of calibrating lidar data by use of more radiosonde launches due to the high horizontal variability of the water vapor in the atmosphere that can lead to big discrepancies in estimations. The future work planned of incorporating this predictive data into the retrieval algorithms and statistical analyses should confirm the accuracy of the technique and provide the system with a mean calibration constant that can be used for the times when the complementary data sources are not available.

Acknowlegements: M. Krishnaiah would like to thank JSPS, Japan for the Invitation Fellowship 2008

References

1. Starr, D. O'C; and Melfi, S. H. eds: *The Role of Water Vapor in Climate A Strategic Research Plan for the Proposed GEWEX Water Vapor Project, NASA* CP-3120, 1991.
2. Eagleson, P.S., 2000: *The role of water in climate,* Proceedings of the American philosophical society, **144**(1).]
3. Sinha, A., and J. E. Harries (1995), Water Vapour and Greenhouse Trapping: The Role of far Infrared Absorption, *Geophys. Res. Lett.*, ***22*(16)**, 2147–2150.
4. Christopherson, Robert W.: *Geosystems: An Introduction to Physical Geography.* Maxwell Macmillian Int., 1992.
5. D.N.Whiteman, S.H.Maelfi, and R.A. Ferrare, *Raman lidar system for the measurement of water vapor and aerosols in the Earth's atmosphere* Applied Optics, Vol. 31, No. 16, June 1st, 1992
6. E.J.O'Connor, A.J. Illingworth, and R.J Hogan, *A technique for Autocalibration of Cloud Lidar,* American Meteorological Society, May 2004
7. J.A. Reagan, *Fellow, IEEE*, X. Wang, and M. T. Osborn, *Spaceborne Lidar Calibration From Cirrus and Molecular Backscatter Returns* IEEE Transactions on Geoscience and Remote sensing, vol. 40, No.10, Oct 2002
8. D. N. Whiteman@ all, *Scanning Raman Lidar Error Characteristics and Calibration For IHOP*, NASA/HQ
9. C. Weitkamp, *LIDAR range-resolved optical remote sensing of the atmosphere* , Springer *2005*
10. Y. Bhavani Kumar, Nageswara Raju, and M. Krishnaiah, *Indo-Japanese Lidar observations of tropical middle atmosphere during 1998 and 1999*, Adv Atm Sci, 23, 5, 2006
11. Measures, Raymond M.: *Laser Remote Sensing: Fundamentals and Applications.* John Wiley & Sons, Inc., 1984.

High altitude cloud observations using ground based lidar and simultaneous comparison with satellite lidar observations

Y Bhavani Kumar[1], M.Krishnanaih[2,3] ,Banuu[2]and H.Kuze [2]

[1] *National Atmospheric Research Laboratory, P B No. 123, S V University Campus, Tirupati 517502,India,*
[1]*ypbk@narl.gov.in,* [2]bannu@graduate.chiba-u.jp[3]*profkrishnaiah.m@gmail.com and* [2]hkuze@faculty.chiba-u.jp
[2]*Center for Environmental Remote Sensing, Chiba University, 1-33 Yayoi-Cho, Inage-Ku, Chiba, 2638522, Japan*
[3]*Department of Physics, Sri Venkateswara University, Tirupati – 517502, India*

Abstract

We report the observation of high altitude tropical cirrus clouds. The observations were performed using a mini backscatter Lidar system installed at National Atmospheric Research Laboratory (NARL), Gadanki (13.5°N, 79.2°E), India. The portable lidar is a backscatter lidar, developed at NARL site.The lidar operates on the principle of micro pulsing. The lidar direction of probing is upwards and the operational wavelength of the lidar is 532nm. The lidar is compact (25 kg total mass) and low cost version. The intrinsic altitude and time resolution for signal detection and acquisitions are respectively 30 m and 60 s. High repetition rate and photon count detection permits the lidar system to have good dynamic range for covering the entire troposphere. However, in order to improve SNR these values are degraded in the signal processing. We have compared our ground based lidar observations of high altitude clouds with that of satellite lidar (CALIPSO) pass over India on two different periods such as winter and SW monsoon time

Keywords: Tropical cirrus, lidar, satellite lidar

1. Introduction

The Tropics are characterized by warm sea surface temperatures and frequent convection. This convection occurs on a wide range of scales, from hundreds of meters in the case of fair weather cumulus to thousands of kilometers in the case of mesoscale convective systems. Deep convection often reaches the tropopause, which is found at 16 km to 18 km in the tropics Clouds in the tropics are ubiquitous in nature and their vertical and temporal distributions are very complex. Cirrus clouds occupy a special place among the earth's cloud formations. Their impact can be manifested through atmospheric warming or cooling (Cox 1971). Recurrence of cirrus clouds and their morphological and microphysical structures undergo significant variations as functions of latitude, season, and orography. Associated with convection are large-scale cirrus layers that are present much of the time. Cirrus clouds have been recognized as a fundamental factor influencing the climate. It's impact on the earth radiation budget and consequently on the climate has been addressed so far (Liou, 1986). Cirrus clouds can absorb long-wave outgoing radiation from Earth's surface while reflecting short-wave incoming solar radiation (McFarquhar et al., 2000). The radiative forcing of cirrus clouds is determined by macro and microphysical properties. Cirrus radiative forcing is not well understood because the incomplete knowledge of such properties. Lidar measurements are useful in deriving geometrical and optical properties of cirrus clouds, which are essential in understanding cloud-radiation effects. But in the tropics few measurements have been conducted in comparison with the measurements available at midlatitudes. This paper presents the results of the analysis of cirrus clouds from the portable lidar observations conducted at Gadanki (13.5°N, 79.2°E), a rural site in the tropical part of India. High altitude cloud observations were conducted using the backscatter lidar system operating at 532nm.

2. System description

The lidar transmitter is a microchip (all-in-one laser cavity) Nd:YAG laser. It is a diode pumped and acoustic Q switched. The lidar transmitter operates at 2500 pulses per second and outputs energy at 10 μJ (25 mW) at 532 nm wavelength. The laser beam diameter is 0.4 mm and its divergence is less than 1.5 mrad. A transmit Field of View (FOV) of about 200 μrad has been achieved using an 8X

beam expander in the transmit beam path. The lidar employs mono-axial configuration. The laser beam is sent into the atmosphere using two reflecting mirrors kept at 45° angles. The laser backscatter is collected using a 150 mm diameter cassegrain telescope. A set of narrow band filters is used to obtain laser backscatter during daytime. The lidar uses photon counting electronics. A high gain PMT is used as the photon detector. The pulse signal from PMT is passed through a discriminator and counted in a range resolved successive bins using a PC based multi-channel scalar (MCS). Usually 300000 shot integrated photon count profile constitutes a raw data profile, which corresponding to a time resolution of 120 sec. The dwell time of each range bin is set to 200 nsec, which corresponding to a range resolution of 30 m. The system transmit-receive full overlap occurs above 150 m ground level. The detailed system description is given elsewhere by Bhavani Kumar (2006 a&b). The basic lidar backscatter profiles recorded at 19:00 LT (during evening time) obtained on 14 February 2006 is shown in Figure 1. One can see the high altitude cirrus cloud returns clearly in the lidar data at around 12 km is observed with a thickness of about 1 km.

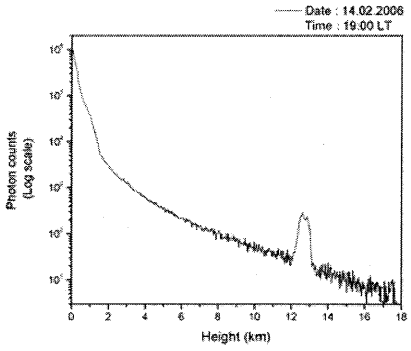

Figure 1.Portable lidar backscatter signal from boundary layer aerosol and a high altitude cirrus layer with base height of 12000 m. The profile was taken on 14 February 2006 between 19:00 and 19:02 LT averaged over 300000 pulses.

3. Observations

Portable lidar observations of tropical atmosphere have been carried out on regular basis at NARL site, Gadanki since January 2005. The lidar is capable of delineating the mixing layer depth, troposphere aerosol height profiles and real-time ranging of cloud heights (Bhavani Kumar, 2006b). In this paper, we compare the lidar observations of high altitude clouds passage over Gadanki site with that of CALIPSO satellite lidar observations. We present two typical case studies, one on monsoon day and the other on clear winter day. During the period of comparison, the CALIPSO satellite lidar derived cloud attenuated backscatter is presented for comparison with that of potable lidar derived range corrected data at 532 nm laser wavelength.

Case study –I

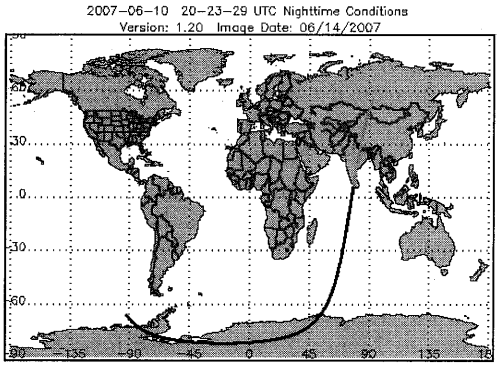

Figure 2a. CALIPSO- Satellite lidar pass over India on 10 June 2007 between 20:26 and 20:37 UTC.

The CALIPSO satellite lidar passage (nighttime condition) over India on 10 June 2007, typical monsoon period, was shown in Figure 2a. The pink line shows the path trajectory. The timings of passage were between 20:26 and 20:37 UTC, 01:56 and 02:07 LT of 11 June 2007. During the pass time, the Satellite lidar detected thick cirrus layers at heights between 15 and 19 km right from 12 to 25° N latitudes, as shown in Figure 2b. The occurrence of these clouds is due to on set of tropical easterly jet (TEJ) during this period in asian tropics. The TEJ is responsible for the long range transport of convectively generated cirrus in the Asian tropics during the NE monsoon period.

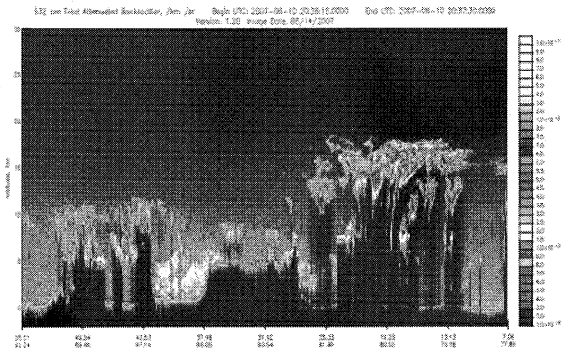

Figure 2b. CALIPSO- The Satellite lidar observation of high altitude clouds over India on 10 June 2007, monsoon period.

Moreover, the horizontal transport carried by the winds appears to be responsible for wide spread coverage of cirrus in the Asian tropics during monsoon period. However, the satellite lidar images do not reveal the presence of mixing layer due to thick clouds extinction of laser. But the satellite lidars can provide accurate information on cloud top height. The potable lidar system over Gadanki site, which located at 13.5°N latitude, observed the high altitude cirrus layers at heights between 15 and 19 km during 00 and 05 LT on 11 June 2007 is shown in Figure 3. The ground lidar system detects the cirrus layers above the local mixing layer. The local mixing layer tops around 3 to 4 km during monsoon periods due to high vertical winds. The ground lidar data is complimentary to the satellite lidar, so that cloud base and local mixing layer information can be obtained accurately.

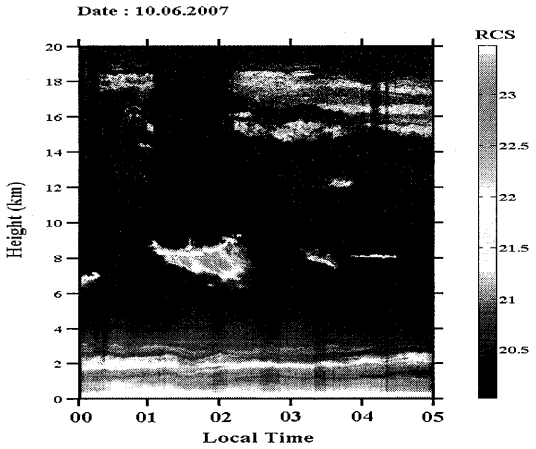

Figure 3. Portable lidar observation of high altitude clouds layers over Gadanki site on the night of 11 June 2007 between 00 and 05 LT.

Case study –II

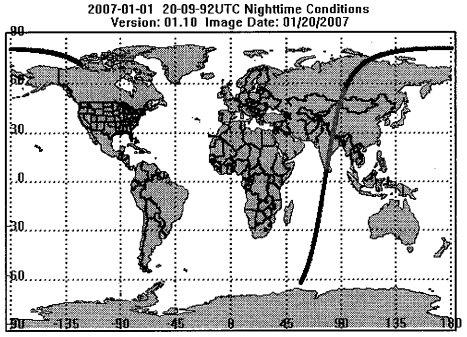

Figure 4a. CALIPSO- Satellite lidar pass over India on 03 January 2007 between 20:22 and 20:36 UTC.

The CALIPSO satellite lidar passage (nighttime condition) over India on 3 January 2007 typical winter period was shown in Figure 4a. The blue line shows the path trajectory. The timings of passage were between 20:22 and 20:36 UTC, 01:52 and 02:06 LT of 3 January 2007. During the pass time, the Satellite lidar detected thin layer of cirrus at height around 15 km between 9 and 16°N latitudes, as shown in Figure 4b. The potable lidar at Gadanki has detected the thin high altitude cirrus layer at heights between 15 and 16 km during 02 and 06 LT on 4 January 2007 as shown in Figure 5.

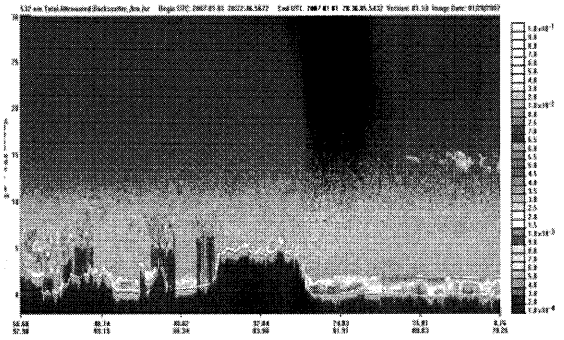

Figure 4b. CALIPSO- The Satellite lidar observation of high altitude clouds over India on 03 January 2007, winter period.

The ground lidar system detects the cirrus layers above the local mixing layer. Generally, the local mixing layer tops between 1.5 km and 2 km in winter periods over Gadanki site

due to benign winds and dry atmospheric conditions. The ground lidar data thus supplements the complimentary data to the satellite lidar, so that cloud base and local mixing layer height information can be obtained precisely.

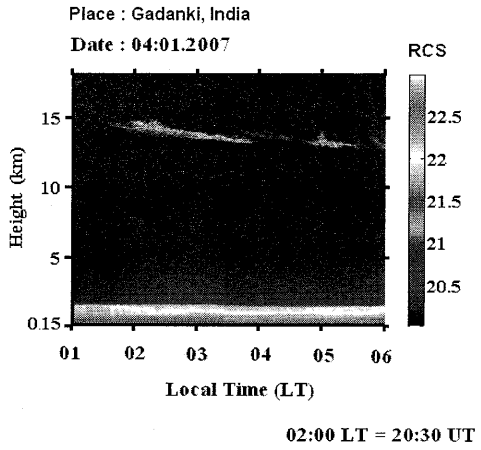

Figure 5. Portable lidar observation of high altitude thin cirrus layer over Gadanki site on the night of 03 January between 01 and 06 LT.

Conclusion

The observations of low cost portable lidar system at Gadanki site are useful for detection of the local mixing layer, profiling the tropospheric aerosols and ranging the high altitude clouds. The ground lidar systems data is complimentary to satellite lidars for supplementing information on local mixing layer and low and high level cloud base data etc. The examples of simultaneous observations shown on monsoon and winter periods illustrate the usefulness.

Acknowledgements

One of the authors, Y.Bhavani Kumar, would like to thank the National Atmospheric Research Laboratory (NARL), Department of Space, Government of India for funding the project boundary layer lidar (BLL). He also would like to thank Dr T G K Murthy, Programme Director, ASP, ISRO HQ for his encouragement in BLL development for atmospheric research.

The author M. Krishnaiah would like to thank JSPS, Japan for the Invitation Fellowship 2008

References

1. S.K. Cox , Cirrus clouds and the climate, *J. Atmos.Sci.*, 28, 1513-1515, 1971.

2. K.-N. Liou, The influence of cirrus on weather and climate processes: A global perspective, *Mon. Wea. Rev.,* 114, 1167-1199, 1986.

3. G.M. McFarquhar, A. J. Heymsfield, J. Spinhirne And B. Hart, Thin and Sub visual Tropopause Tropical Cirrus: Observations and Radiative Impacts, *J. Atmos. Sci.,* 57, 1841-1853, 2000.

4. Y. Bhavani Kumar, Portable lidar system for atmospheric boundary layer measurements *J. Opt. Eng*, 45, 7, 076201, 2006a

5. Y.Bhavani Kumar, A portable lidar system for atmospheric aerosol and cloud studies, *Proc. SPIE*, the International Society for Optical Engineering, 2006b
DOI: 10.1117/12.693489

Cloud particle characterization from multiple scattering images of LIDAR

H. Yoshida

Faculty of Engineering, Gifu University, Japan

e-mail: hiroki@gifu-u.ac.jp

Particle size distribution and number density of the cloud are important parameters for cloud characterization. The scattering image of laser beams in the clouds provides the valuable information related to cloud particles. In order to deduce them, a conventional LIDAR and Monte-Carlo technique are applied to the analysis of the multiple-scattering images of clouds.

The scattered images around the bottom of clouds were obtained by using the LIDAR. The laser system of it is Ti:sapphire CPA and Nd:YAG system operating at 10 Hz with output energy of 30 mJ (30 fs @780nm) and 180 mJ (7 ns @532 nm). The detection system, a 280mm diameter telescope and PMTs was combined with a digital camera (NIKON, D70) with a polarized filter to take the scattered images. The scattered images were numerically calculated by Monte-Carlo technique for 30 sized bin classes of the particle distribution with one million photons. The calculation was carried out with consideration of Mie scattering and light polarization in mixture of such 30 bin particles. To confirm the calculated results of scattering images, we first compared them with the measured signals from the water solutions of one-sized standard particles. After measurements of cloud images, the intensity profiles were t on the calculated one to deduce the particle size distribution and density.

This work was partly supported by by CDReS and NEDO.

Near-infrared and near UV absorption measurements of atmospheric trace species using differential optical absorption spectroscopy (DOAS)

Kenji Kuriyama, Daisuke Kataoka, Taku Matsumoto, Ippei Harada, Hiroaki Kuze
CEReS, Chiba University, tskmasu@graduate.chiba-u.jp

Abstract

Differential optical absorption spectroscopy (DOAS) is one of useful techniques in the optical remote sensing that enables measurement of atmospheric trace species over a long distance of a few kilometers. In the visible spectral range, the DOAS method based on aviation obstruction lights and/or PC projector sources has successfully been applied to the highly sensitive measurement of NO_2 and aerosol in the lower troposphere. In this paper we report on the extension of the technique in terms of the spectral range toward the near UV and near infrared. In the UV range, we have constructed a specially designed telescope, with which molecular species such as O_3 and SO_2 that exhibit absorption features in the near UV range can be measured using the UV light beam generated with a Xe arc lamp. In the case of near-infrared measurement around 1 μm wavelength, an InGaAs photodiode is employed to measure absorption of CO_2 and aromatic/non-aromatic air-pollution molecules. In this latter wavelength range, laboratory measurements are planned to obtain standard absorption spectra, since the region is outside the standard infrared absorption measurements.

Keywords **:** DOAS; Xe lamp; Air pollution distribution; Absorption cross section; Near-infrared; Near-UV; InGaAs photodiode

1. Introduction

In recent years, the atmospheric pollution in Japan, as a whole, has been improved as compared with situations couple of decades ago. However, we still have problems in places such as urban roadside areas, where the environmental standards have not been achieved. In this respect, efforts are required for monitoring anthropogenic air pollution, especially the combustion products such as nitrogen oxides and particulate matters.

The main pollution species in urban areas in Japan is the nitrogen dioxide (NO_2) and suspended particulate matter (SPM), usually referred to as PM_{10}. In the monitoring of such species, conventional point sampling at ground stations leads to concentrations for local environments. It is also valuable to obtain additional information of regional concentrations measured over a certain distance, e.g., several hundred meters to several kilometers. Differential optical absorption spectroscopy (DOAS) in the visible and near-UV region is more suitable to monitor horizontally averaged concentrations of pollutants (Edner *et al.*, 1993, Evangelist *et al.*, 1995, Stutz *et al.*, 2000).

In the conventional long-path DOAS method, a continuously emitting light source is employed, and the source (or occasionally a retroreflector) is placed at a certain distance from the observation site. The use of aviation obstruction lights makes it possible to employ a simple detection system that consists of a telescope and a compact CCD spectrometer. Our group in Center for Environmental Remote Sensing, Chiba University (CEReS) reported a novel DOAS method that is based on a white flashlight source and a compact CCD spectrometer (Yoshii *et al.*, 2003, Si *et al.*, 2005). In Japan, it is mandatory for tall constructions (higher than 60 m) to operate highly illuminant (more than 2×10^6 cd) white flashlights during the daytime that are detectable in every direction from several kilometers away.

In this paper we report on the extension of the technique in terms of the spectral range toward the near UV and near infrared. In the UV range, we have constructed a specially designed telescope, with which molecular species such as O_3 and SO_2 that exhibit absorption features in the near UV range can be measured using the UV light beam generated with a Xe arc lamp. In the case of near-infrared measurement around 1 μm wavelength, an InGaAs photodiode is employed to measure

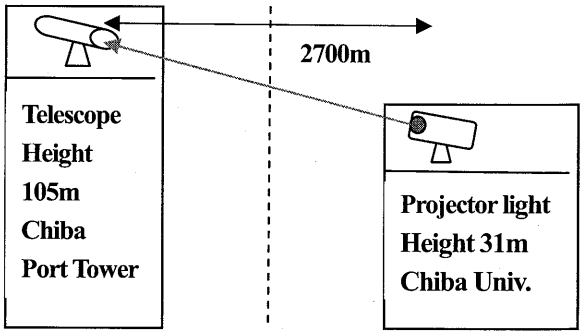

Fig. 1 An example of experiment setup for measuring NO_2 and SPM

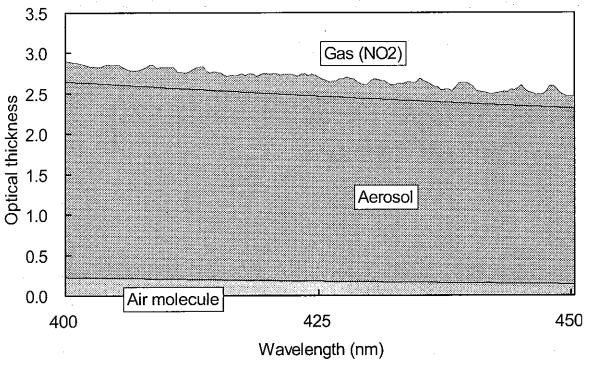

Fig. 2 Optical thickness of each component detected by the DOAS spectrometer

absorption of CO_2 and aromatic/non-aromatic air-pollution molecules. In this infrared wavelength range, laboratory measurements are required to obtain standard absorption spectra, since the region is outside the standard infrared absorption measurements.

2. Experiment Methods

2.1 Aviation obstruction lamp DOAS system

Figure 1 shows a schematic of the experiment setup. In this experiment, a projector flashlight was used as a light source and the distance of the light source and observation was 2.7 km. The projector flashlight was set up at about 30 m height in Chiba University. Power consumption of the projector is 220 W, and the emission covers the visible wavelength. The observation of the transmitted light was made near the top of the Chiba port tower, about 90 m in height.

Here we give a brief outline of the DOAS detection system. An astronomical telescope (Meade, DS-115), with an aperture diameter of 115 mm and a focal length of 910 mm, is employed to focus the image of a point light source located at a far distance. The image is formed near the eyepiece location (the eyepiece itself is removed from the telescope) where the entrance slit (1 mm high and 5 μm wide) of a CCD spectrometer (Ocean Optics, USB2000) is placed. The CCD consists of 2048 elements and is sensitive in a wavelength range of 200-800 nm, resulting in an average resolution of 0.3 nm/pixel. This CCD spectrometer is composed of a fixed grating and a linear CCD array with a mechanically stable, crossed Czerny-Turner design. No moving parts are incorporated, resulting in high reliability and compactness (89 mm wide × 63 mm deep × 34 mm high). The CCD gate duration is set at 300 ms in the experiment. Between successive gate periods, there exists a time lag of 7 ms, in which each spectral data is sent to a personal computer (PC) through the universal serial bus. The data acquisition can be attained successfully even when no trigger (synchronous with the flashlight) is applied to the CCD spectrometer, though this relatively long gate time as compared with the flashlight duration causes somewhat increased amount of the background skylight.

The discrimination of data with and without the flash event is automatically achieved by comparing the light intensity integrated over a wavelength region of 400-450 nm, used for the NO_2 detection. The spectral difference between the flash and the no-flash events exhibits the net strobe intensity after the long-path transmission in the urban atmosphere. Figure 2 shows optical thickness of each component detected by the DOAS spectrometer. The absorption of NO_2 gas species gives a structure in the optical thickness of the order of 0.2. In order to extract the NO_2 concentration, contributions from molecules and aerosol particles can be subtracted by simply applying a linear fit to the back-ground. Another important aspect from this figure is that, by measuring the light intensity, it becomes feasible to evaluate the aerosol contribution in the DOAS signal itself.

2.2 NO_2 and aerosol retrieval

The analysis of the DOAS spectra is based on the Beer–Lambert's law expressed as

$$I(\lambda) = kI_0(\lambda)e^{-L\sigma(\lambda)n} \qquad (1)$$

where $I(\lambda)$ is the measured intensity, k is the system constant, $I_0(\lambda)$ the unattenuated reference intensity, L the path length, $\sigma(\lambda)$ the wavelength-dependent absorption cross section, and n the number density of the species averaged over the path length. The dimensionless quantity $L\sigma(\lambda)n$ represents the optical thickness, denoted as τ .

Here we describe the algorithm developed for the retrieval of both the NO_2 concentration and the aerosol optical thickness. After the background subtraction, the observed light intensity $I_{obs}(\lambda)$ can be expressed as

$$I_{obs}(\lambda) = kI_0(\lambda)T_m(\lambda)T_a(\lambda)T_{NO_2}(\lambda) \qquad (2)$$

Here k is an empirically determined coefficient, $I_0(\lambda)$ is the spectrum of the light source observed at a location close to the light source, $T_m(\lambda) = \exp[-\tau_m(\lambda)]$ is the transmittance of air molecules (Rayleigh scattering) [$\tau_m(\lambda)$ is the molecular optical thickness], $T_a(\lambda) = \exp[-\tau_a(\lambda)]$ is the transmittance of air molecules (Mie scattering) [$\tau_a(\lambda)$ is the aerosol optical thickness], and $T_{NO2}(\lambda)$ is the transmittance representing the NO_2 absorption. In the present algorithm involving both the NO_2 and the aerosol retrieval, we first correct the observed

spectrum $I_{obs}(\lambda)$ for the first three factors on the right-hand side of Eq. (2):

$$I_{obs}'(\lambda) = \frac{I_{obs}(\lambda)}{kI_0(\lambda)T_m(\lambda)} \qquad (3)$$

Combining Eqs. (2) and (3), we obtain

$$I_{obs}'(\lambda) = \exp[-\tau_a(\lambda) - \sigma(\lambda)C] \qquad (4)$$

where $C = Nl$ is the column amount of NO_2. Moreover, if it is assumed that the aerosol optical thickness exhibits wavelength dependence as given by the Angstrom exponent, we obtain

$$-\ln I_{obs}'(\lambda) = B\lambda^{-A} + \sigma(\lambda)C \qquad (5)$$

Removing the slowly varying contribution from Eq. (5), and applying the spectral matching to the rapidly varying part with the laboratory cross-sectional data, we obtain the value of C. Then, substituting C into Eq. (5) leads to the value of $B\lambda^{-A}$. In the actual data analysis, this process has to be operated in an iterative way.

2.3 Near-UV DOAS system

Measurement of UV absorbing molecules such as O_3 and SO_2 is also feasible using the DOAS method. Since the projector lamp does not emit in the UV wavelengths, here we employ a 300 W Xe lamp (Cermax, PE300BFM). The setup of the UV light source is given in Fig. 3. A collimated beam is generated by means of a lens and mirror system, and subsequently rotation and tilt stages are employed to couple the light beam to the telescope. For the detector part, since the ordinary astronomical telescope cannot be used for wavelengths shorter than 350 nm, we have constructed a homemade UV telescope system. An aluminum tube of 1 m in length and 100 mm in inner diameter is employed for the telescope body. The object lens has a diameter of 100 mm and a focal length of 1000 mm, while the ocular lens has a diameter of 20 mm and a focal length of 25 mm, both being a plano-convex lens made of quartz.

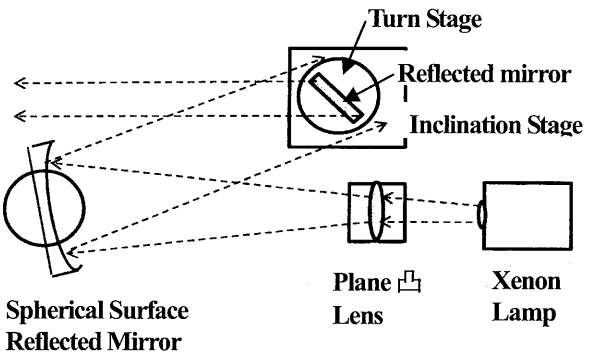

Fig. 3 Xe lamp and the collimator

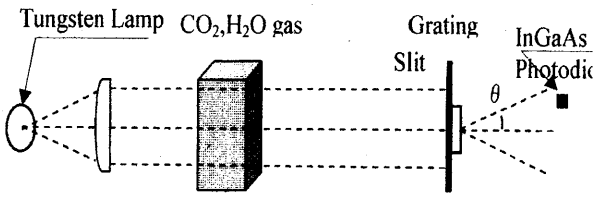

Fig. 4 Schematic of near-infrared DOAS measurement

2.4 Near-infrared absorption measurement

Figure 4 shows the schematic for measuring the near-infrared absorption of molecules such as CO_2 and H_2O. The light emitted from a 1000 W tungsten lamp (Fuji Denkyu, FP12) is collimated. After passing through a quartz cell, the light is directed toward a diffraction grating (830 grooves/mm) with a 0.5 mm slit for wavelength measurement. The diffracted light is detected with an InGaAs photodiode, which has a detection range of 0.9 – 2.1 μm.

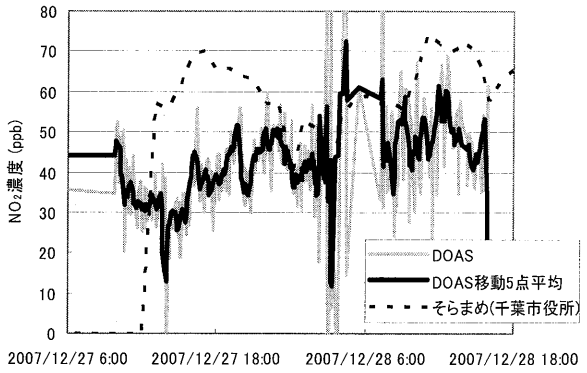

Fig. 5 DOAS measurement in comparison with the ground sampling data

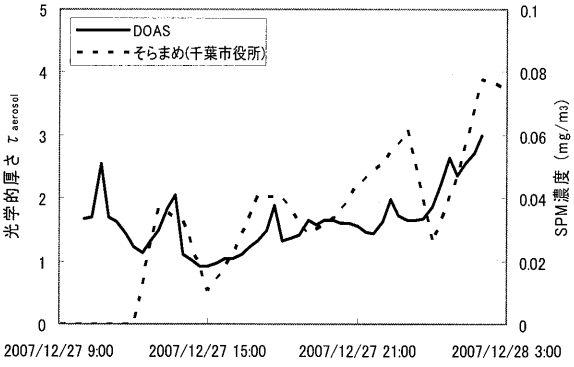

Fig. 6 Comparison between aerosol optical thickness and SPM concentration

3. Results and discussion

3.1 DOAS measurement with a projector flashlight in the restoration zone

The DOAS method acquires a data point every five minutes, much more frequent than the data (every one hour) provided from the Ministry of the Environment Atmospheric Environmental Regional Observation System (AEROS). Also it is noted that there is a difference of the observation height between the DOAS and ground sampling measurements. Nevertheless, a reasonable temporal correlation was found between the result of the long-path measurement using DOAS method and the data of NO_2 concentration from a ground station near each optical path in Chiba city (Fig. 5). Moreover, a reasonable correlation was found between the aerosol optical thickness using DOAS method and the data of SPM concentration from a nearby ground station (Fig. 6).

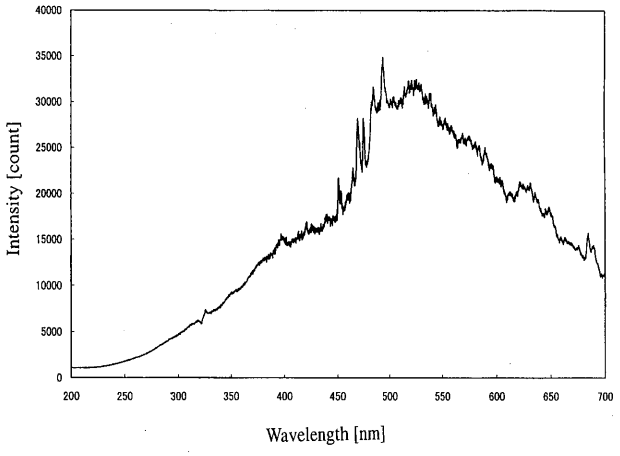

Fig. 7 Spectrum of the xenon lamp

3.2 Near UV DOAS measurement

Figure 7 shows a spectrum obtained by detecting the UV light from the Xe lamp with a compact spectrometer (Ocean Optics, USB4000). The UV light in the wavelength range of 280-300 nm can be used for the DOAS measurement. This will be used for the measurement of O_3 and SO_2 in the polluted atmosphere. The detection of SO_2 is also of importance for the volcano emission monitoring.

3.3 Near infrared absorption measurement

The tungsten lamp was used to generate a near-infrared light beam having wavelength of 0.9-2.1 μm. The detection was made using an InGaAs photodiode (or alternatively, an infrared photodiode array). The difference absorption between the gas-filled and evacuated cell is measured to obtain the near infrared absorption strength of a sample gas. The results of this measurement will be shown in the presentation.

4. Conclusions

A continuous day-night DOAS measurement was demonstrated using a PC projector light source, giving information on the concentration on the NO_2 and aerosols in the urban atmosphere. By extending the method to the near UV spectral range, important pollutants such as O_3 and SO_2 can be measure using the DOAS technique. Although these gases are of secondary importance in the usual air pollution in the urban atmosphere in Japan, such measurements are still required in occasional events of photo-chemical smog and volcanic eruption. In the near infrared range, the method can be utilized to measure concentrations of CO_2 and a variety of organic gas species. Since the region of 1-2 μm is outside the conventional infrared spectroscopy (longer than 2.5 μm), we have started from measuring the standard absorption data using a homemade near-infrared spectrometer.

References

Edner, H., Ragnarson, P., Spannare, S., and Svanberg, S. (1993): Differential optical absorption spectroscopy (DOAS) system for urban atmospheric pollution monitoring, Applied, Optics, 32, 327-333.

Evangelisti, F., Baronecelli, A., Bonasoni, P., Givanelli, G., Ravegnani, F.(1995): Differential optical absorption pectrometer for measurement of tropospheric pollutants. Applied Optics 34, 2737–2744

Stutz, J., Kim, E.S., Platt, U., Bruno, P., Perrino, C., Febo, A. (2000): UV–VIS absorption cross-section of nitrous acid. Journal of Geophysical Research 105 (D11), 14585–14592.

Si, F., Kuze, H., Yoshii, Y., Nemoto, M., Takeuchi, N., Kimura, T., Umekawa, T., Yoshida, T., Hioki, T., Tsutsui, T., and Kawasaki, M. (2005): Measurement of regional distribution of atmospheric NO_2 and aerosol particles with flashlight long-path optical monitoring, Atmospheric Environment, 39, 4959-4968.

Yoshii, Y., Kuze, H., Takeuchi, N. (2003): Long-path measurement of atmospheric NO_2 with an obstruction flashlight and a charge coupled device spectrometer, Applied Optics, 42, 4362-4368.

Observing SO_2 emissions at Japanese volcanoes using an ultraviolet imaging camera

Thomas Bouquet[1]*, Kisei Kinoshita[2], Matthew Watson[3]

[1]*Faculty of Science, Kagoshima University, 1-21-35 Korimoto, Kagoshima, 890-0065, Japan*

[2]*Faculty of Education, Kagoshima University, 1-20-6 Korimoto, Kagoshima, 890-0065, Japan*

[3]*Department of Earth Sciences, University of Bristol, Queen's Road, Bristol, BS2 9RQ, UK*

**t.bouquet@ms.kagoshima-u.ac.jp*

Abstract

A newly developed ultraviolet (UV) imaging camera offers a new approach to the ground-based surveillance of volcanic sulphur dioxide (SO_2). Using highly sensitive 2-dimensional CCD technology and a bandpass filter centred in the UV region where SO_2 selectively absorbs UV light, the camera is able to quantify SO_2 within a gas plume in great detail. This study presents results from Sakurajima and Satsuma-Iojima volcanoes, where image sequences were obtained at an unprecedented temporal resolution and revealed interesting variations in SO_2 emission rate. The SO_2 retrieval technique is also discussed with respect to atmospheric scattering and the use of different UV wavelength filters.

Keywords: gas monitoring, sulphur dioxide, UV camera, Sakurajima, Satsuma-Iojima

1. Introduction

The measurement of volcanic gas emissions is an ongoing objective of volcano hazard monitoring. Of the most abundant gases, sulphur dioxide (SO_2) has been mainly measured remotely: firstly for its high concentration in contrast to low atmospheric levels, and secondly for its specific absorption in the ultraviolet (UV) spectrum (300-315 nm). Utilising this characteristic, the correlation spectrometer (COSPEC) has been in use since the 1970s,[1] but has been replaced more recently by low-cost and lightweight miniature UV spectrometers, adopting the differential absorption (DOAS) technique.[2] Both instruments traverse or pan a gas plume and scale UV absorption to SO_2 concentration in accordance with the Beer-Lambert Law. However, calculations of emission rates are often dependent upon crude estimations of plume geometry and wind speed. An unrepresentative wind speed can contribute up to 40% of the overall error,[1] whilst the time resolution is limited to the duration of individual measurements.

The UV camera therefore offers an improved alternative, adopting the same principles of remote sensing, but also making use of 2-dimensional CCD technology.[3),4)] A synoptic view of a whole gas plume is provided, as well as benefiting from the portability and low detection limit of ground-based technology. A sequence of digitised images allows for improved measurement of plume geometry and velocity, and the delay between individual images can be set to as little as one second thus offering an unprecedented frequency for gas monitoring. This study uses the camera described in 3) and presents the latest images obtained from fieldwork during April 2008, concentrating on results retrieved at Sakurajima and Satsuma-Iojima volcanoes in southern Japan.

2. Methods

2.1. Instrumentation

Instrumentation consists of an Apogee Instruments E6 Alta digital camera with a Kodak KAF-1001E-2 1024×1024 CCD array with 16-bit quantisation level per pixel, a 105 mm lens from Coastal Optics, and a bandpass filter from Andover Optics centred at 307 nm with a 12 nm full width at half maximum. The system is cooled with a thermoelectric cooler and is controlled by the imaging software MaxIm DL (Diffraction Ltd.). In the field the camera is mounted on a standard tripod (fig. 1) and takes around 10 minutes to set up, allowing time for manual adjustment of focus and exposure time. The lens is used with an F number of 4.5, producing a field-of-view (FOV) of approximately 13°.

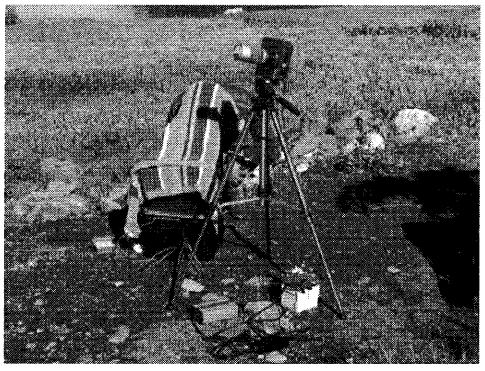

Fig. 1: Field set-up of UV camera and components.

2.2. SO_2 retrieval

Using sunlight as the source of UV light, the apparent absorbance (A) of SO_2 in plume images at i-th row and j-th column pixel is calculated as follows:

$$A(i,j) = log_{10}[I_o(i,j)/I(i,j)] \quad (1)$$

where I_o = light intensity before passing through SO_2 (background sky), and I = light intensity after passing through SO_2. The plume absorbances are then scaled using measured absorbance values from two calibration cells composed of 115 and 270 ppm.m, to derive the SO_2 slant column concentration. Essentially a "map" of SO_2 column concentration is created and cross-sectional plume profiles can then be extracted to compute SO_2 emission rate.

2.3. Field measurements at volcanoes

The data discussed in this study are based on results from the UV camera deployment at Sakurajima on April 24, 2008, and at Satsuma-Iojima on April 26, 2008. On both occasions a clear blue sky provided a background for measurements (see discussion for specific conditions) and the wind speed was 14.4 ms^{-1} and 8.1 ms^{-1} respectively, calculated from the time difference between integrated vertical SO_2 column profile amounts for the 700th and 900th pixels.

Sakurajima is one of the most active volcanoes in Japan and at the time of imaging, activity consisted of high SO_2 flux (exceeding 1000 tonnes/day (td^{-1}); K. Yamamoto, pers. comm.) and intermittent explosions. A sequence of images was obtained between 15:41 and 16:02 local time at a distance of 4.5 km south-west from the vent, resulting in a pixel resolution of 1.51 m. One image was collected every 5 seconds with an exposure time of 0.6 seconds for each.

In contrast, Satsuma-Iojima is characterised by intensive degassing (SO_2 flux is typically 300-1100 td^{-1}), but no historical eruptions have been recorded.[5] Images were obtained every 5 seconds between 13:31 and 13:43, with an exposure time of 0.8 seconds. The imaging location was 3.15 km WSW from the vent, resulting in a pixel resolution of 0.85 m.

3. Results

Fig. 2 depicts a typical image of SO_2 column concentration, taken at Sakurajima volcano and processed to show heterogeneities within the plume. The plume was moving across the image from left to right, and gas emissions from two craters can distinguished: the first, from Minami-dake to the left of the image, and the second rising from the Showa crater behind the flank in the centre of the image. This is even more apparent when analysing sequential images as one is able to track individual gas "puffs" or pulses in SO_2 emission. Similar features, albeit less dramatic, were also observed at Satsuma-Iojima.

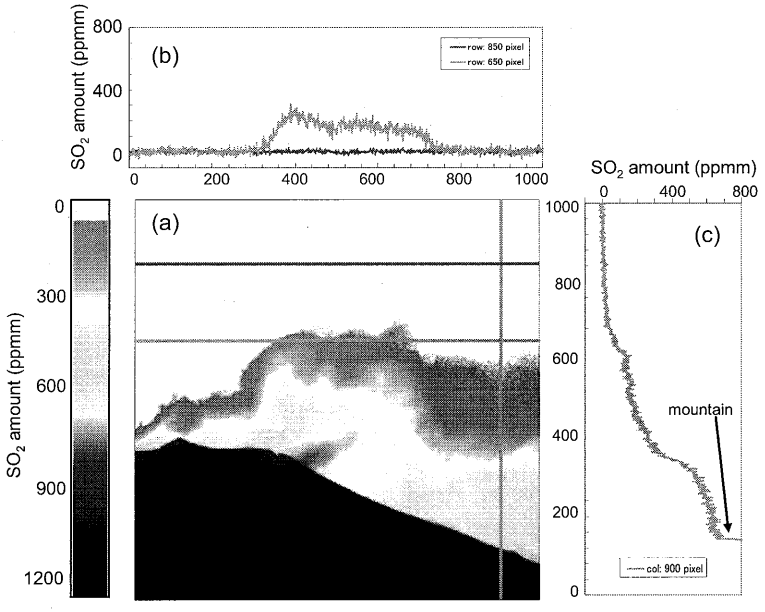

Fig. 2: (a) False-colour image of SO_2 column concentration for a Sakurajima plume at 15:47:58. The scale on the left is of calibrated SO_2 column concentration in ppm.m. (b) Horizontal profiles of the SO_2 column amount at the 850th (dark line) and 650th (light grey line) row pixels. (c) Vertical SO_2 column amount at the 900th (light grey line) column pixels.

SO_2 emission rate was calculated for both volcanoes using integrated vertical SO_2 column profile amounts extracted from the 900th pixel location, multiplied by the pixel resolution and computed wind speed. An angular correction is also applied to account for the deviation from a horizontal plane in the camera's FOV. From each image sequence, average SO_2 flux was approximately 1090 td^{-1} (12.6 kgs^{-1}) and 96 td^{-1} (1.1 kgs^{-1}) for Sakurajima and Satsuma-Iojima, respectively. Temporal variation of SO_2 flux also greatly differs for the two volcanoes (fig. 3): although for Satsuma-Iojima flux remains constant at about 1 kgs^{-1}, the emission rate at Sakurajima ranged from around 10 kgs^{-1} to 18 kgs^{-1}. Peaks in flux can be related to gas "puffs" and two small explosions were observed (indicated in fig. 3), which occur after 392 seconds and towards the end of the sequence after 1070 seconds.

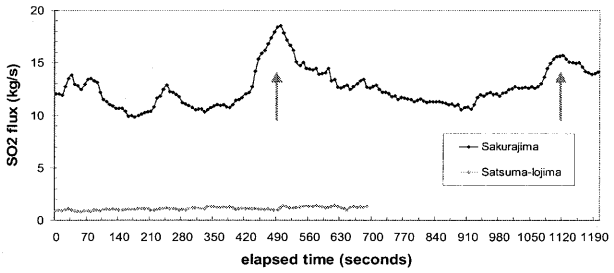

Fig. 3: Temporal variations of SO_2 flux for Sakurajima (dark) and Satsuma-Iojima (light grey) obtained from integrated vertical profiles of the 900th pixel. Arrows indicate peaks caused by explosions.

4. Discussion

4.1. Imaging conditions

Flux calculations derived from Sakurajima imagery appear to agree with regular UV spectrometer (DOAS) measurements (K. Yamamoto, pers. comm.). However, due to recent explosive activity there was a high amount of volcanic ash particles in the air and it is possible that this may influence the SO_2 absorbance signal. Ash particles block UV light, thus indicating artificially enhanced absorbances,[6] but as wind speed was sufficiently high (14.4 ms^{-1}) to transport explosion clouds away during 24 April, it is suspected that ash did not linger above the vent as in other cases. Further investigation using images from other imaging days is necessary to analyse this phenomenon.

No such difficulty exists at Satsuma-Iojima, but clearly camera SO_2 flux values underestimate emission rate by at least a third compared to typical measurements.[5] One reason may be that the whole gas plume was not imaged as it was partially transported behind the flank of the volcano. A second may be due to increased atmospheric turbidity during 26 April, as aerosol scattering between the camera and target would have diluted the SO_2 signal. This was a major issue during the field campaign as such conditions are characteristic of spring in southern Japan. The problem can be modelled by simple atmospheric modelling, whereby signal degradation is dependant upon distance and relative humidity.[7] With this in mind, the camera was deployed at a power station in the UK and images were obtained from successive distances up to 5.3km away from the plume and a clear decrease in absorbance was established (fig. 4).[8] Subsequent extrapolation to a true "zero-distance" value can then be performed, thus providing a simple atmospheric correction for absorbance values. Attenuation factors derived from this method (36%) show reasonable agreement with other studies, approximating 35-50% for short wavelengths (309 nm and 313 nm) over a distance of 2.6 km.[9]

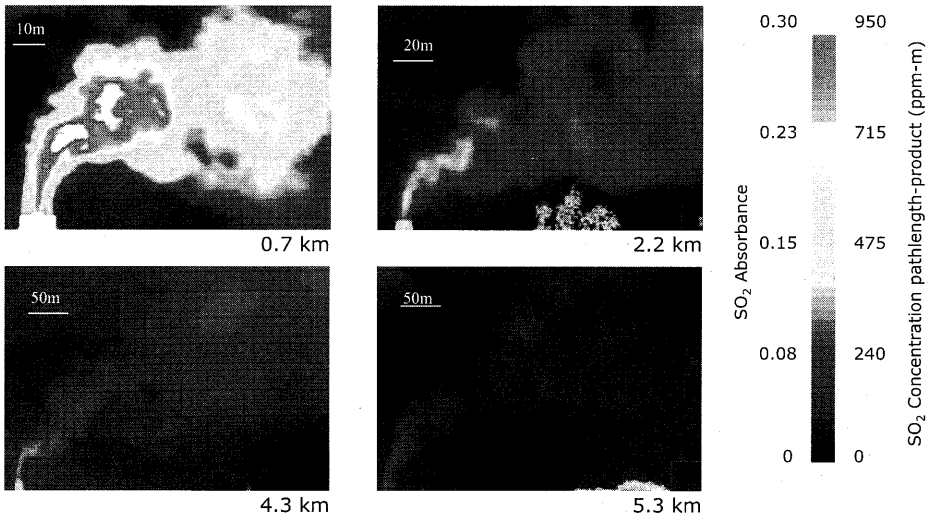

Fig. 4: False-colour power station SO_2 plume images, showing SO_2 absorbance degradation with distance.

4.2. UV bandpass filters

This research was conducted using only a single bandpass filter centred at 307 nm. Ideally the camera system should incorporate a second filter outside the SO_2 absorption signature (i.e. >315 nm), as the difference in transmittance between two filters would increase sensitivity to the SO_2 signal and help to eliminate interference from other gas species.[4] However, with the current system set-up it is difficult to capture an image with two filters as the target plume is constantly moving. In the absence of a secondary imaging system, future study will incorporate the use of a filter wheel enabling quick changes between bandpass filters of different wavelengths. In addition, it is also hoped that filters with a narrower band wavelength will be available to further improve the SO_2 retrieval routine.

5. Conclusion

A UV imaging camera was deployed at Sakurajima volcano and for the first time at Satsuma-Iojima volcano. SO_2 flux was successfully calculated for Sakurajima, averaging 12.6 kgs^{-1} for the 20-minute sequence, and also showed interesting temporal variability due to pulses in gas emissions or explosions. SO_2 flux at Satsuma-Iojima, however, was greatly underestimated due to atmospheric scattering between the camera and target, diluting the SO_2 absorbance signal. It is also expected that use of a single bandpass filter rather than two limits the accuracy of SO_2 detection. In conclusion, it is hoped that, with further development and increased automation, the UV imaging camera could become a useful tool in the remote sensing of gas emissions.

Acknowledgements

The authors are grateful to T. Mori of GSJ (AIST) for use of a portable battery, and to K. Yamamoto of SVO (DPRI, Kyoto University) for field assistance at Sakurajima volcano.

References

1) Stoiber, R.E., Malinconico Jr., L.L., Williams, S.N., 1983: Use of the correlation spectrometer at volcanoes, in Tazieff, H., Sabroux, J.C. (Eds.), *Forecasting Volcanic Events*, pp. 425-444. Amsterdam-New York.
2) Galle, B., Oppenheimer, C., Geyer, A., McGonigle, J.S., Edmonds, M., Horrocks, L.A., 2003: A miniaturised UV spectrometer for remote sensing of SO_2 fluxes: a new tool for volcano surveillance, J. Volc. Geo. Res. 119:241-254.
3) Bluth, G.J.S., Shannon, J.M., Watson, I.M., Prata, A.J., Realmuto, V.J., 2007: Development of an ultra-violet digital camera for volcanic SO_2 imaging, J. Volc. Geo. Res., 161: 47-56, doi:10.1016/j.jvolgeores.2006.11.004.
4) Mori, T., and Burton, M., 2006: The SO_2 camera: A simple, fast and cheap method for ground-based imaging of SO_2 in volcanic plumes, Geophys. Res. Ltrs, 33, L24804, doi:10.1029/2006GL027916.
5) Kazahaya, K., Shinohara, H., Saito, G. 2002: Degassing process of Satsuma- Iwojima volcano, Japan: Supply of volatile components from a deep magma chamber, Earth Planets Space 54:327-335.
6) Andres, R.J., and Schmid, J.W., 2001: The effects of volcanic ash on COSPEC measurements, J. Volc. Geo. Res. 108:237-244.
7) Shettle, E.P., and Fenn, R.W., 1979: Models for the aerosols of the lower atmosphere and the effects of humidity variations on their optical properties, AFGL-TR790214, Optical Physics division, Air Force Geophysics Laboratory, Hanscom Air Force Base, MA, US.
8) Bouquet, T., 2007, Measuring volcanic sulphur dioxide emissions using an ultraviolet imaging camera, MSc thesis University of Bristol, UK.
9) Mori, T., Mori, T., Kazahaya, K., Ohwada, M., Hirabayashi, J., Yoshikawa, S., 2006: Effect of UV scattering on SO_2 emission rate measurements, Geophys. Res. Ltrs, 33, L17315, doi:10.1029/2006GL026285.

Crop area classification using satellite data
Case study: Selenge region, Mongolia

B.Erdenee[1], Md. Mijanur Rahman[2], C.Sujatahamma[3], Ryutaro Tateishi[4]

[1,2,3,4] *Center for Environmental Remote Sensing (CEReS), Chiba University, 1-33 Yayoi-cho, Inage-ku, Chiba 263-8522, Japan,*

[1]*E-mail: erdenee@graduate.chiba-u.jp*

[2]*E-mail: Mijan@graduate.chiba-u.jp*

[3]*E-mail : sujatha.krishnaiah@yahoo.com*

[4]*E-mail: tateishi@faculty.chiba-u.jp*

Abstract

Satellite image classification involves designing and developing efficient image classifiers. A particularly important application of remote sensing is the generation of land use/ land-cover maps from satellite imagery. Land-use mapping using satellite imagery has the advantages of low cost, large area coverage, repetitively, and computability. Consequently, land-use information products obtained from satellite imagery such as land-use maps, data and GIS layers have become an essential tool in many operational programs involving land resource management.

Remote sensed images can be used to identify nutrient deficiencies, diseases, water deficiency of surplus, weed infestations, insect damage, hail damage, herbicide damage and plant populations, land use and land cover change mapping and classifications. Information from remote sensing can be used as base maps in variable rate applications of fertilizers and pesticides. The other common using of remote sensing data in yield prediction is crop simulation models, which require high amount of detailed soil and climatic data and full information about agricultural practices. Coupled with GPS and GIS, remote sensing offers potential for improving farm management practices.

Agriculture is one of the major sour economic of Mongolia and the country's economy highest dependent on the development of agricultural production.

The situation of cropland use in Mongolia is very complicated. In many areas, the cropland is used in multi-cropped ways.

In this study, maximum likelihood supervised classification were applied to Landsat TM and ETM images acquired in 1989 and 2000, respectively, to map cropland cover changes in the Tsagaannuur of Mongolia. A supervised classification was carried out on the six reflective bands for the two images individually with the aid of ground based agricultural monitoring data.

These changes in land cover led to cropping land use change in part of the study area.

Key words: Land use, Land cover; remote sensing; GIS

1. Introduction

Using satellite imagery to extract and represent land-use/land cover information is a key application of remote sensing technology. Remotely sensed data have great potential to help solve many environmental problems (Swain & Davis 1978; Lillesand & Kiefer 2000): 1) management and conservation of natural resources, 2) urban and regional planning, 3) controlling and mitigating of environmental pollution, and 4) meteorological phenomena. In analysis of remotely sensed data, there are numerous techniques developed to derive useful information from remotely sensed data to address these problems. Among them the computer-assisted digital imaging processing of remotely sensed data is the most popular technique used by most remote sensing researchers and scientists (Swain & Davis 1978). In recent decades, with the rapid emergence of many kinds of remotely sensed data, remote sensing has been widely used in Land-Use/Land-Cover (LU/LC) classification applications, such as urban planning, agricultural crop characterization, forest ecosystem

classification, and flood monitoring (Jerson, 1996). The resulted land use and land cover mapping is one of the important sources for governments to manage and plan the natural resources at local and regional scales.

In recent decades a variety of classification techniques have been developed to perform multispectral classification (Jensen 1996; Serpico & Roli 1995; Jain 1989; Schowengerdt 1983; Swain & Davis 1978; Duda & Hart 1973).

Basically, they are fit into two general classification categories: supervised and unsupervised. In a supervised classification, a priori knowledge of the scene with respect to the identity and location of desired land categories is used to collect training data through field work and analysis of very high resolution remotely sensed data maps in interesting area (Mausel et al. 1990). Unsupervised classification is known as "clustering" which is "a generic labeling procedure designed to find natural groupings, or clusters, in multidimensional data based on measured or perceived similarities among patterns" (Jain 1989).

2. Study area

Mongolia is located in the Asia between the latitudes of 41°35'N and 52°09'N and the longitudes of 87°44'E and 119°56'E covering an area of 1.564 thousands square kilometers. The total land area used for agriculture is 1,301,704km2. Almost all land is for livestock grazing. Only 757.5 km2 is used for crop production.

Ecologically, Mongolia consists of great Siberian taiga forest, central Asian steppe, high mountains and the Gobi desert. All natural zones such as taiga, forest, steppe, High Mountain, desert steppe and desert zones are combined.

Economically, Mongolia divided into 21 administrative territorial units, named aimags (provinces) each with a provincial capital and a local government.

The agricultural sector is the core economic sector in the country and accounts for 35 percent of GDP and one/fourth of total exports. 49 percent of the Mongolian labor force is involved in this sector.

The selected study area Tsagaannuur is located to the north of the Mongolia, which is situated on the Selenge aimag and sub area measuring approximately 3814.72 sq. km (figure 1).

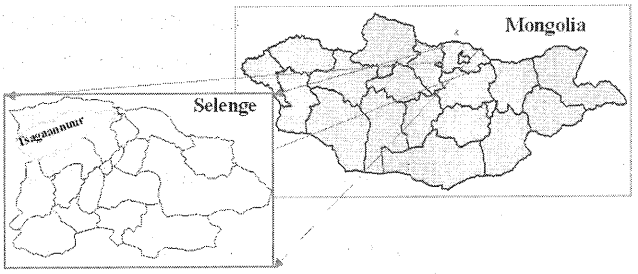

Figure 1. Study area

Selenge aimag is produces 60 percent of grain of the country. Selenge aimag coordinate is 49° 45′ 0″ N, 106° 30′ 0″ E and measuring approximetaly 41,152.6 sq.km. The climate of the region is semi-arid and arid; and the mean annual precipitation is 250-301 mm.

The main crops grown in the region wheat, fodder crops, potato, and some vegetables. Except for wheat, all other crops are rain fed. The planting dates of wheat and fodder crops are mostly planted in from mid of May to October period. For vegetables planting starts in end of May and continues until the end of August and mid-September, respectively. Almost crops present an important vegetative development in the June–August period. The wheat is harvested between late September and early October. Vegetables are harvested gradually from late July to September.

3. Materials

Landsat Thematic Mapper (TM) and Enhanced Thematic Mapper (ETM+) images (with path/row132/25, 133/25) acquired on 11 September 2000 and 21 August 1989, respectively. The satellites orbit at an altitude of 705km and provide a 16-day. These satellites also were designed and operated to collect data over a 185-km swath. The TM sensor primarily detect reflected radiation from the Earth's surface in the visible and near-infrared (IR) wavelengths, the TM sensor have seven spectral bands. The wavelength range for the TM sensor is from the visible, through the mid-IR, into the thermal-IR portion of the electronic spectrum. Finally, ground information was collected 2006-2008 years for the purpose of supervised classification and classification accuracy assessment.

4. Methodology

Supervised classification was done using ground checkpoints of the study area. The area was classified into four main classes: active cropland, unused area in that year, open space area and water body.

. In order to increase the accuracy of land cover mapping of the two images, reference data and the classification result using GIS in order to improve the classification accuracy of the classified image. The flow chart of detail methodology is given below.

5. Flow chart of crop mapping

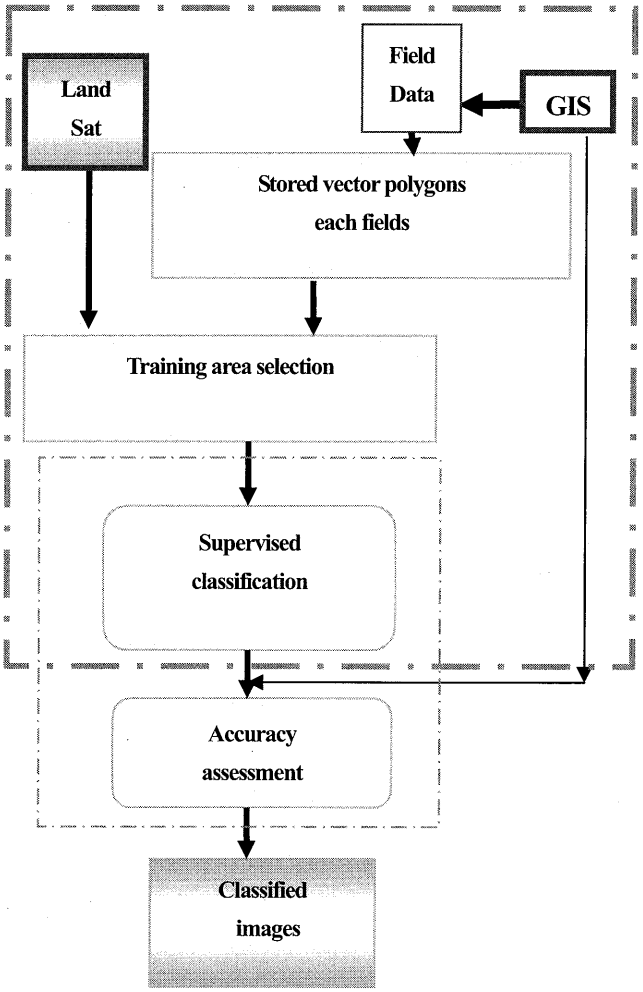

6. Results and discussion

Supervised classification using all reflective bands of the images acquired on 21 August 1989 and on 11 September 2000, respectively was carried out using maximum likelihood classifier. Figs. 2 and 3 show the result of the classification.

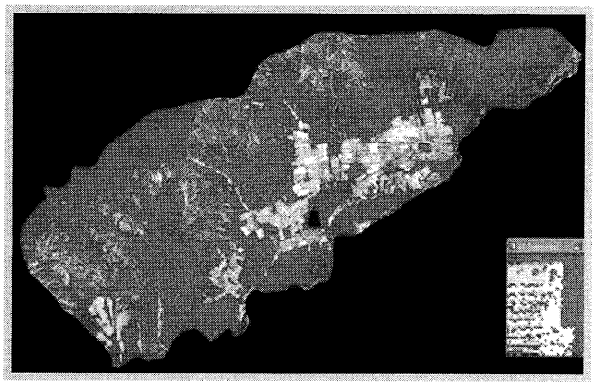

Fig.2. Land use/cover classification map in Tsagaannuur of Mongolia, using Landsat TM 1989.

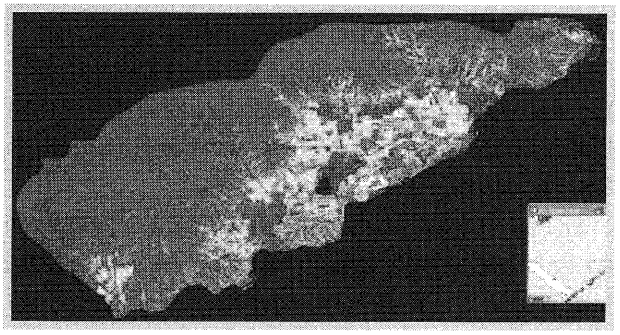

Fig.3. Land use/cover classification map in Tsagaannuur of Mongolia,, using Landsat ETM+ 2000

It was very hardly to make the crop classification for the Tsagaannuur of Mongolia. Two images of cropland area had different months and cropland area sizes, which makes them difficult to differentiate.

The accuracy assessment is an important part of this study. This part is not yet been finished but It is under processing. I hope that that it will be finished very soon.

Acknowledgements

I would like to thank Dr. Javzandulam particularly for spending lots of time helping me clarify many technical issues in my research work. She is input has greatly improved the completeness of my work.

I want to express my sincere gratefulness to Mr Badarch officer of Selenge aimag, for his technical supports and help to my fieldwork.

References

1) Aboel Ghar, M., Shalaby, A., & Tateishi, R. (2004). Agricultural land monitoring in the Egyptian Nile Delta using Landsat data. The International Journal of environmental studies, 61(6), 651–657.

2) Anderson, J. R., Hardy, E. E., Roach, J. T., & Witmer, R. E. (1976). A land-use and land-cover classification system for use with remote sensor data. US Geological Survey Professional Paper 964, Washington, DC.

3) Khorram, S., Biging, G. S., Chrisman, N. R., Congalton, R. G, Dobson, J. E., Ferguson, R. L., et al. (1999). Accuracy assessment of remote sensing-derived change detection. Bethesda: American Society of Photogrammetry and Remote Sensing.

4) Lins, K. S., & Kleckner, R. L. (1996). Land cover mapping: An overview and history of the concepts. In J. M. Scott, T. H. Tear, & F. Davis (Eds.), Gap analysis: A landscape approach to biodiversity planning (pp. 57–65). Bethesda, MD: American Society for Photogrammetry and Remote Sensing.

5) Ram, B., & Kolarkar, A. S. (1993). Remote sensing application in monitoring land-use changes in arid Rajasthan. International Journal of Remote Sensing, 14(17), 3191–3220.

6) Shalaby, A., Aboel Ghar, M., & Tateishi, R. (2004). Desertification impact assessment in Egypt using low-resolution satellite data and GIS. The International Journal of Environmental Studies, 61(4), 375–384.

7) Thomas, I.L., Benning, V.M., & Ching, N. P. (1987). Classification of remotely sensed images. Bristol: Adam Hilger.

8) Yuan, D., Elvidge, C. D., & Lunetta, R. S. (1999). Survey of multi-spectral methods for land cover change analysis. In R. S. Lunetta, & C. D. Elvidge (Eds.), Remote sensing change detection: Environmental monitoring methods and applications (pp. 21–39). London: Taylor & Francis.

Assessment of land use/cover change and urban expansion of the central part of Jordan using remote sensing

Bayan Alsaaideh, Ahmad Al-Hanbali, Ryutaro Tateishi

Center for Environmental Remote Sensing (CERes), Chiba University, 1-33Yayoi-cho, Inage-ku, Chiba 263-8522, Japan.

Telephone: +81-43-290-2964; Fax: +81-43-290-3857; E-mail: bayan@graduate.chiba-u.jp

Abstract

This paper presents the temporal and spatial characteristics of land use/cover changes and identifies the process of urbanization for the major cities at the central part of Jordan. Specifically, the study area covers the capital Amman, Zarqa and Al-salt cities. In this study, subsets of Landsat Thematic Mapper (TM), Landsat Enhanced Thematic Mapper (ETM+) and ASTER visible and near infrared radiometer (VNIR) images acquired in August 1987, 1999 and 2005 respectively, were used for mapping land use/cover changes. The color composites for the three images were selected using the filtered Landsat (TM and ETM+) bands 2, 4, 7 and ASTER VNIR bands 3, 2, 1. A supervised classification system using Maximum likelihood classifier was used to create land use/cover maps, that composed of six classes: Urban/ built up areas, Water, Bare land, Natural vegetation, Agricultural land, and Forestland. The overall accuracy generated from Landsat TM, Landsat ETM+ and ASTER VNIR ranging from 90 % to 95 %. The trends in land use/cover changes indicated signeficant changes in urban, agricultural land and bare land classes. The output land use/cover maps showed that urban expansion has been associated with loss of agricultural land and urban sprawl. Land use/cover statistics revealed that urban/built up areas have increased by 220 Km^2 , while agriculture land have decreased by 99 Km^2 and bare land have decreased by 101 Km^2 over the study period. These results can provide city planners and decision makers who can use this information to give an essential consideration for monitoring the rapid urbanization trend by predicting the amount of changes and the location of future built-up areas, as well as evaluating the existing urban strategies.

Keywords: Urban expansion, Land use/cover changes, Remote sensing, Jordan

1. Introduction

land use/cover change is a major factor for global change, because it can affect ecosystem processes, biodiversity, climate, biogeochemical cycles as they directly affect human activities (Xiao et al. 2005).

The process of urbanization is a major trend in recent years all over the world (Weber and Puissant 2002) . Recently urban planners frequently make use of remotely sensed

imagery, which they can then superimpose on other demographic or geographic information to provide a more detailed and insightful picture of the human landscape (Toby 2003).

Jordanian cities have experienced rapid urbanization over the last two decade, mainly resulted from high natural growth rate, and equally important the continuous migration flows from Gulf countries after the first and second wars in 1991 and 2003, respectively. Urbanization in Jordan is significantly high: in 1998, about 78% of the kingdom's population were living in urban areas and it is projected to increase in the future which may probably reach more than 85% of the total population by the year 2010 (Jaber and Probert 2001) .

The objective of this study is to allow the urban planners to know the changing conditions in the study area in order to develop urban in presence of adequate planning and instructions and to protect the local environment. To perform the objective this study presents a three time series analysis using remote sensed data (Landsat and ASTER images) in combination with Geographical Information System (GIS) to identify a land use/cover classification schem for the major cities at the central part of Jordan and determine urban expansion trend and rate.

Study area

The study area, as shown in figure 1 is located at the central part of Jordan between the range of 35° 46′E- 36° 13′E and 31° 46′N- 32° 13′N, and is composed of the capital Amman, Zarqa and Al-Salt cities. The study area is covers about 13,459 km^2 representing a bout 15% of the total area of Jordan (DOS 2008). The climate of the study area, in summer it is hot and dry and temperature ranges from (27-36) °C, while in winter it is cold, and temperature ranges from (1.4-10) °C. The amount of rainfall is low, ranges between (250-350) mm/year.

2. Methodology

Landsat Thematic Mapper (TM) 1987 , Landsat Enhanced Thematic Mapper (ETM+) 1999 and ASTER visible and near infrared radiometer (VNIR) 2005 were used to extract land use/cover information and to map the physical extent of urban areas for the central part of Jordan at the same season (August). In addition, topographic map with a scale of 1:50,000 was used as a reference for land cover/use types.

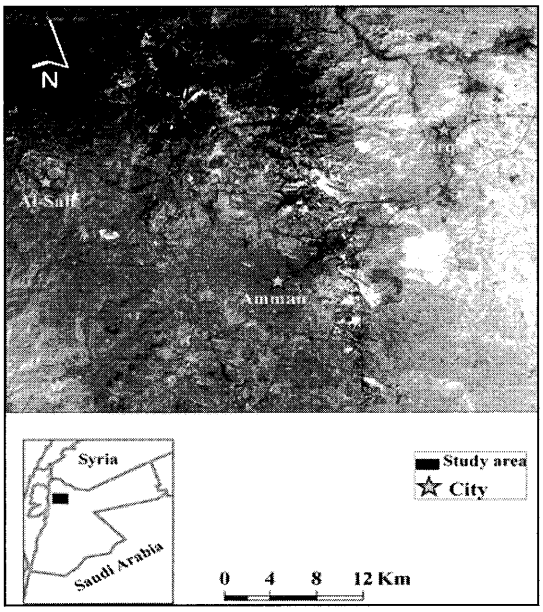

Figure 1. Location map of the study area

The Landsat TM and ETM+ images were in UTM projection (Zone 36) on WGS84. The

Landsat TM image was used as a reference to register ASTER (VNIR) image. The nearest neighbor method was used to a void altering the original pixel values. The resultant root mean square error (RMSE) was less than 0.5 pixels using 15 ground control points (GCPs).

A supervised classification system using maximum likelihood algorithm was consequently applied to the three images. In total, six separable land use/cover classes were recognized which are: Urban/ built up areas, Water, Bare land, Natural vegetation, Agricultural land, and Forestland. A median convolution filter, Kernel size 3×3 was used to smoothen the images. Visual interpretation was performed to solve the difficulty of misclassification error. The accuracy of each of Landsat TM, Landsat ETM+ and ASTER VNIR were 90%, 92% and 95%, respectively.

3. Results

The static land use/cover distribution for the three time series (1987, 1999 and 2005) as derived from the maps showed that there are three main classes of interest in the study area: urban/built-up areas, agriculture land and bare land, because of their significant records in the last 18 years of the study period. The spatial distributions of the six classes were extracted from each land use/cover maps of 1987, 1999 and 2005 as shown in Figures 2.

The trends in the last three land use/cover change indicated that the urban/built up areas have increased from 174 Km^2 in 1987 to 260 Km^2 in 1999, and then to 394 Km^2 in 2005, showing an expansion of urban/built up areas by 220 Km^2 from 1987 to 2005. In contrast, agriculture land occupied a bout 205 Km^2 in 1987, decreased to 115 Km^2 in 1999 and then to 105 Km^2 in 2005, indicating a decrease by 99 Km^2 from 1987 to 2005. On the other hand, bare land have slightly increased from 1394 Km^2 in 1987 to 1411 Km^2 in 1999 and then have decreased to 1292 Km^2 in 2005, a record loss of 101 Km^2 in the 18 years of the study period.

Rapid urban sprawl have occurred a round Amman, Zarqa and Al-Salt cities, since the sprawl normally takes place in radial direction around the city center or in linear direction along the highways (Sudhira et al. 2003). In addition, these changes have pointed toward that the spatial pattern of urban expansion; has not occurred evenly in all direction but has taken place much faster and further in certain directions. Therefore urban planning studies should be applied to determine the magnitude of encroachment resulting from expanding urban areas centered mostly in the central part of Jordan.

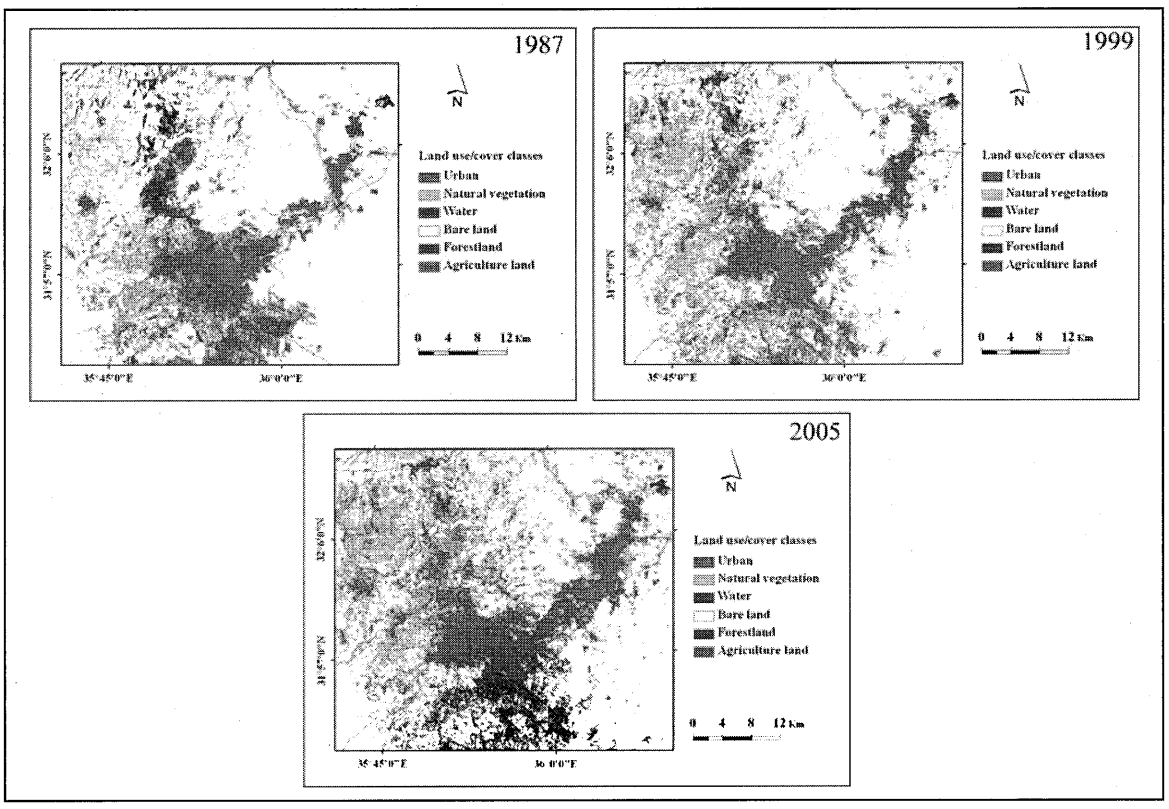

Figure 2. Classified land use/cover maps of the central part of Jordan in 1987, 1999, 2005

References

1. Xiao, J., Shen, Y., Ge, J., Tateishi,R., Tang, C., Liang, Y., Huang, Z. (2006). Evaluating urban expansion and land use change in Shijiazhuang, China, by using GIS and remote sensing. Landscape and urban planning, 75 (2006) 69–80
2. Sudhira, H.S., Ramachandra, T.V., Jagadish K.S (2005). Urban sprawl: metrics, dynamics and modelling using GIS. International Journal of Applied Earth Observation and Geoinformation, 5 (2004) 29–39
3. Weber, C., Puissant, A. (2003). Urbanization pressure and modeling of urban growth: example of the Tunis Metropolitan Area. Remote Sensing of Environment 86 (2003) 341–352
4. Jaber, J.O., Probert, S.D. (2001). Energy demand, poverty and the urban environment in Jordan. Applied Energy 68(2001) 119-134.
5. Carlson, T. (2003). Preface Applications of remote sensing to urban problems. Remote Sensing of Environment 86 (2003) 273–274.
6. Department of Statistics (DOS), Jordan, (http://www.dos.gov.jo/)

Semi-real time media contents on haze hazard in Ganges River Basin

Kithsiri PERERA[1], Ryutaro TATEISHI[2]

[1]*Terranean Mapping, PO Box.729, Fortitude Valley, QLD, Australia, 4006, kithsiri.perera@terranean.com.au*

[2]*CEReS, Chiba University, 1-33 Yayoi-cho, Inage-ku, Chiba-shi, Japan, tateishi@faculty.chiba-u.jp*

Abstract: The world most populated river basin, Ganges river basin, which runs from the central Himalayas to the Bay of Bengal, faces numerous natural and manmade environmental disasters. With the increase of population and industrial activities in resent decades in the basin, a hazardous haze layer in winter months are forming annually over the basin, causing many deaths and other health complications. The thick haze in winter months further increases cold temperature while hazardously decreasing the visibility for road and air traffic. Due to the gravity of this hazard, it's important to bring haze cover information to public to enhance the understanding and to get the appropriate attention to the situation. Here, production of semi-real time media contents on the hazard plays a vital role. Moderate resolution daily MODIS satellite data are highly suitable to monitor the haze for such content production. This research uses freely accessible MODIS data to monitor haze development and movements over Ganges basin to produce semi-real time mass media contents. The content making is emphasized on academically sound image processing and production of easy to understand graphic products.

1. The hazard

The region affected by haze cover (figure 01), addressed in this study is related to the increase of cloud cover over Indian Sub-Continent in recent decades.

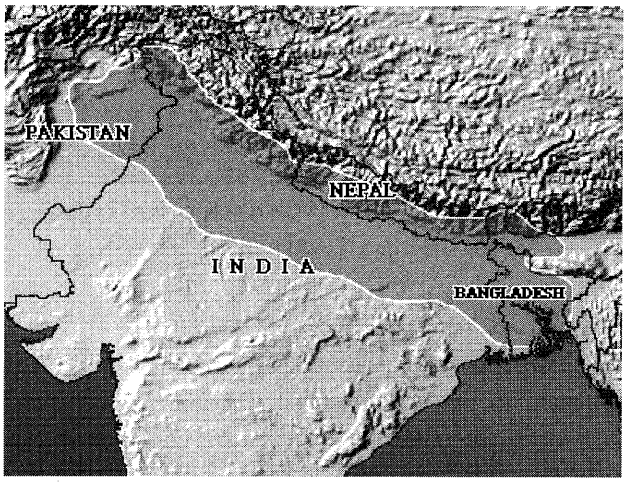

Figure 01. Approximate area (in pink color) affected by haze over Ganges River Basin.

The increase of cloud cover over northern Indian sky attracted the attention of scientists from early 1990s. In a 2001 study, Noriis explains the clear increase (from about 13.3% of sky to 14.5%) of low-level cloud cover over Indian sub-continent from 19950 to 1990 (Norris, 2001). Scientists suspect this increase is related to the increase of aerosol over Indian Ocean, which increased by the population and industrial growth of the region (Alles, 2008). In another study, author's preliminary estimation suggested an increase of 5% in cloud cover due to the aerosols increase (Kaufman and Koren, 2006). The smog conditions associate with the increase of these clouds, named as "Asian Brown Cloud (ABC)", first came to wide attention after UN sponsored a detailed study (INDOEX, the Indian Ocean Experiment), which concluded in year 2002 by a panel of about 200 scientists. INDOEX measurements indicated cloud droplet concentrations are greater over the polluted northern Indian Ocean than the relatively clean southern Indian Ocean (Norris, 2001). The study found the amazing extent and threat of the cloud, which contains unusual amounts of 'heavy' pollutants such as soot, ash and other black carbon aerosols.

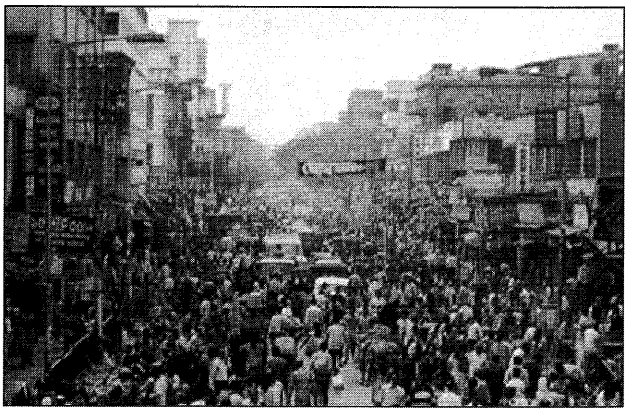

Figure 02. Bentinck Street, Calcutta (source: Musleah R., 2008)

Another study found the biofuel combustion is the largest source of black carbon emissions in India (Venkataraman, et al., C, 2005) India's air pollution, because it is also rich in black carbon, has reached the point where scientists

fear it may have already altered the seasonal climate cycle of the monsoons (Alles, 2008), and many direct and indirect deaths and health hazards. Figure 02 shows a typical busy Indian city scene (Bentinck Street, Calcutta), which has all micro levels of air-pollution that considers as one of the major reasons for the formation of hazardous haze. According to the UN, this Asian smog cloud (the huge haze layer), affects millions of people of the region. The present study concentrates on bringing satellite data related to these research findings in a simple graphical form to general public to enlighten the public interest of this newly formed natural hazard.

2. Data

Delivering scientific information to general public has a genuine need, although the lack of freely available suitable data plays as a barrier for that. In order to observe the haze layer over Ganges River basin, it's important to obtain suitable satellite data at daily interval. The geometrically corrected true-color MODIS products (by NASA) on daily basis are one of the highly suitable data sets for this purpose. At 250m resolution, these automatically generated near-real-time images give substantial amount of information to observe haze cover. Figure 03 shows the daily image scene layout over Ganges River Basin (pink area shows the area of interest of this study).

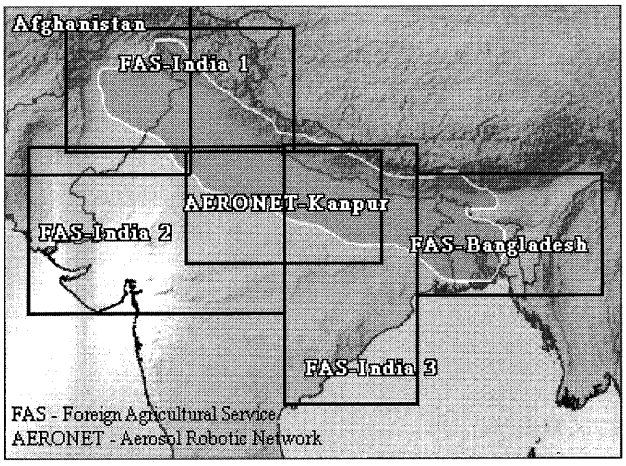

Figure 03. MODIS image subset layout.

For each of this geographic area, the archive imagery is available online (MODIS 2008).

Production of contents from these images needs two major background environments,

I. Information about the haze hazard occurrence

Most of MODIS data sets including aerosol and cloud data collected by AQUA and TERRA satellites can be freely download from the WEB. MODIS Aerosol imageries (with 2 days of time lap) can be used to track down haze conditions, by entering fixed searching parameters for Ganges river basin region. Figure 04 shows 2 images of high aerosol (JD: 2008022) and low aerosols existence (JD: 2008289) over lower river basin region (LAADS WEB 2008). Also, searching these images must be combined with local weather reports and news sources about haze or fog conditions.

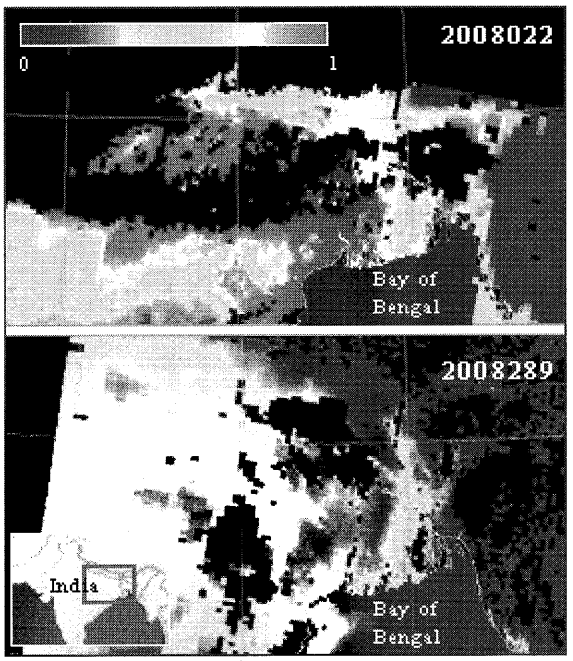

Figure 04. High and low concentrations of aerosol optical thickness data (LAADS WEB 2008).

II. A GIS data set

The GIS (geographic information systems) data set is impotent to produce contents with a consistence and better accuracy. Here, a basic data environment is sufficient with raster map layers, which can be re-directed to edit in Photoshop environment. The entire area under Ganges river Basin can be found under geometrically corrected (Plate Carree projection with WGS_1984 coordinate system) MODIS subset products, and other data must be corrected to match with same coordinate system. But, final images are producing at low resolution for visualization purpose, and no operational use must be encouraged. Data layers like, political boundaries, major cities, major roads, rivers, and elevation data are sufficient at initial stage to merge with MODIS images. But the use of data types like distribution of rainfall and temperature, population, and air pollution, are highly productive, if

combined into the system.

3. Methodology

For proposed near-real-time haze hazard content production, basic knowledge and skills in; GIS, remote sensing data handling, and graphic production, are needed. This is for the maintenance of accuracy of contents, speedup of the content production, and to achieve a high quality in data visualization.

3.1. Accuracy

Since contents bringing first hand information to general public, the geographical and informative accuracy must be maintained at a high level. Simply, it's easy to maintain a substantial accuracy of the product, if the GIS database is registered with MODIS subset collection of the Ganges River Basin. When data layers are ready to be imported from any remote sensing software environment into base graphic templates in Photoshop environment, rest of the works will be more graphic oriented than conventional image processing.

3.2. Speed

Speed can be maximized at two different levels. The first is data mining, downloading, and converting into GIS database. Once the Ganges River Basin region is well studied, relevant subsets can be identified (figure 03). The second level is graphic production process, which mainly maintains by a large database template in Photoshop. The template helps to focus on any sub region of the river basin and also to produce smaller size contents for respective media need. Here, graphic skills in Photoshop will be helpful to minimize times.

3.3. Quality

The use of colors, fonts, and symbols in contents must be carefully selected to meet the technical requirements of the respective media, and target viewers including age groups. For web media, graphics must have small file size (JPG/GIF file formats) to support fast download of the content. For TV media, full color heavy TIF graphic products can be created, but easy to read and less complicated graphics must be the produced. Font sizes must be large enough to read easily, and priorities of words must be maintained to balance the informative quality. All graphic products in original TIF format with all image layers must be systematically archived.

4. Sample contents

Figure 05 and 06 shows two samples produced to demonstrate the use of MODIS data to capture haze and smog conditions over northeast Ganges River Basin, India.

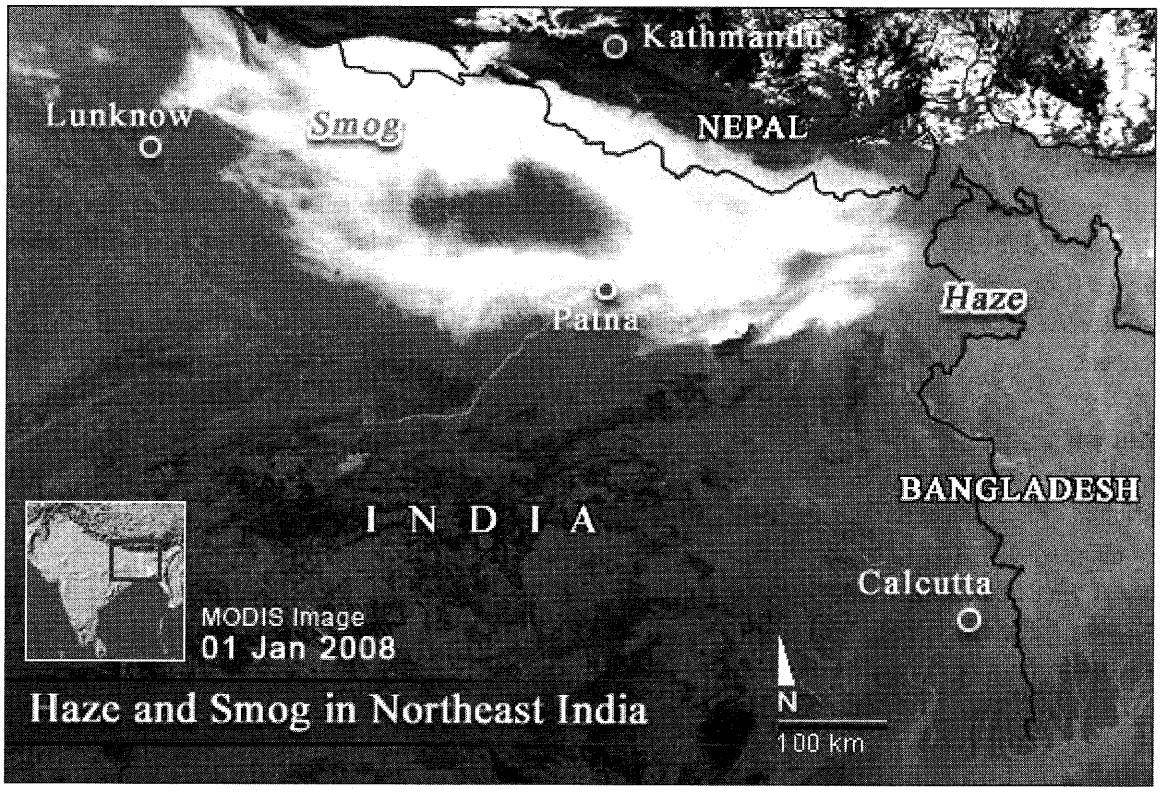

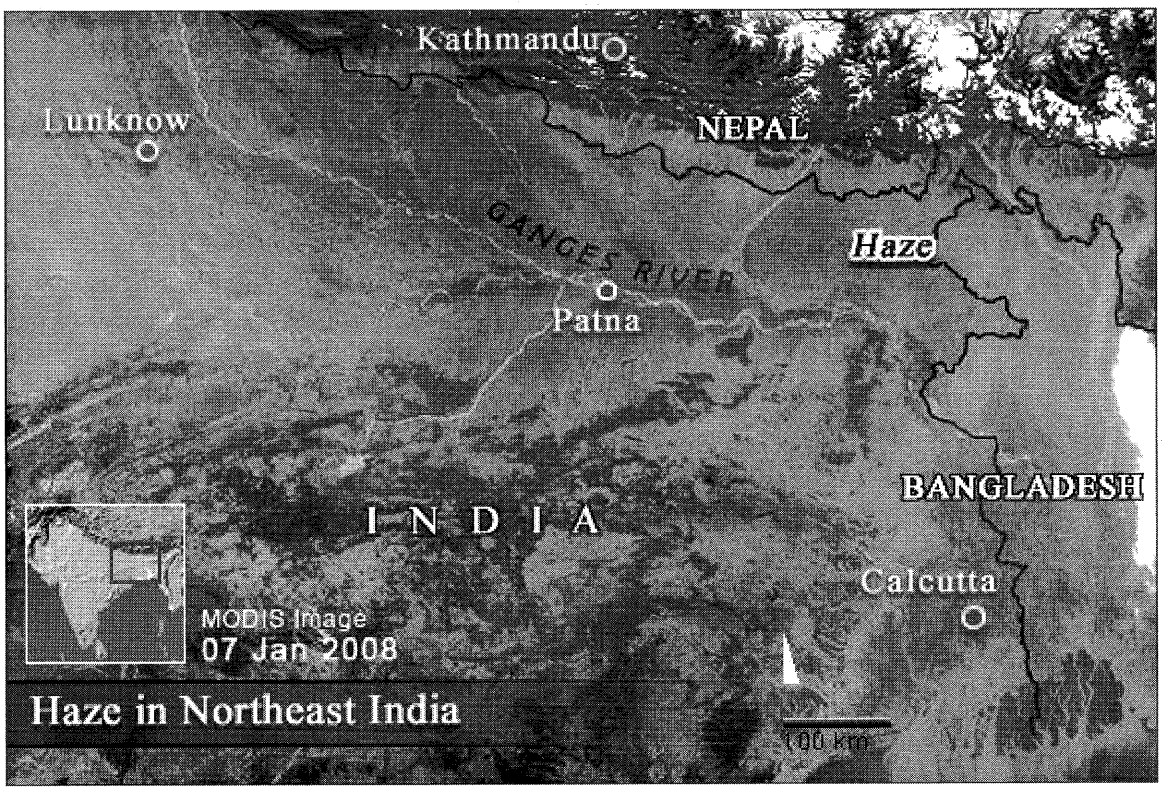

Figure 05 (top) and 06. Changes occurred in haze and smog conditions over northeast India within seven days. It's clear that bout 700 km long huge smog concentration has moved away by Jan 07.

These samples only show changes of smog and haze conditions within 7 days with major cities of the region. These images can be used in TV, printed, or in WEB media, and each JPG file has only less than 85K of data. A smaller version can be produced to obtain a JPG file with just 35k of data volume by just reducing the size (e.g. 70%), without loosing information. Also updating same series of images will cost less time, once the initial template produced for Jan 01 Image. When data stored in an archive, comparisons can be conducted with next hazard seasons as well as with other regions of the Indian sub-continent.

5. Conclusion

The development of the link between "general public understanding" and scientific achievements in "haze hazard monitoring" over Ganges River Basin is emphasized in this study. Using freely available near-real-time MODIS satellite imagery products, an affective production procedure is proposed to create contents suitable for TV, prints, or WEB media. Integrating weather data into the system will enhance the practical use of these contents greatly.

Acknowledgements

Thankful to CEReS, Chiba University for partly funding this project (P2008-1) and a special gratitude is due to Dr. Massy Hara, VisionTech Inc, Tsukuba, Japan, for facilities and encouragements given for the joint research.

References

1. Alles D. L., 2008, Asian Air Pollution, Western Washington, University, http://fire.biol.wwu.edu/trent/alles/AirPollution.pdf

2. LAADS WEB 2008, Level 1 Atmospheric Archive and Distribution System, http://ladsweb.nascom.nasa.gov/data/search.html

3. MODIS 2008, http://rapidfire.sci.gsfc.nasa.gov/subsets/

4. Musleah R., 2008, http://www.rahelsjewishindia.com/india/articles.htm#Calcutta

5. Norris, J. R., 2001: Has Northern Indian Ocean cloud cover changed due to increasing anthropogenic aerosol?, *Geophys. Res. Lett.*, 28, 3271-3274

6. Venkataraman C., Habib G., Eiguren-Fernandez A., Miguel A. H., Friedlander S. K.,(2005). Residential Biofuels in South Asia: Carbonaceous Aerosol Emissions and Climate Impacts. *Science*, 307(March 4), 1454-1456.

7. Yoram J. Kaufman and Ilan Koren, 2006, Smoke and Pollution Aerosol Effect on Cloud Cover, Science 4 August 2006 313: 655-658; published online 12 July 2006

A Research of Calculation Method of Daily Solar Radiation in Ningxia Region

YANG Qin[1]

[1] Weather Station of Meteorological bureau of Ningxia, Yinchuan City

E-mail:ya20060421@yahoo.com.cn

Abstract

Through observation data of daily solar radiation of Yinchuan station of Ningxia, using linear relationship between observation values of solar radiation and extraterrestrial radiation and relative sunshine duration and daylength, we obtained regional coefficients a_s =0.18, b_s =0.62 by their linear correlation of past five years(1981-1985). Using the same method, coefficients of Guyuan region were confirmed too. Applying regional coefficients to be gotten and calculation formula of solar radiation, we validated daily solar radiation of two years(1986-1987) of Yinchuan station and four years(1991-1994) of Guyuan station through comparison with observation data, the results showed there were higher relationship because of the high square error R^2=0.94 in Yinchuan and R^2=0.85 in Guyuan. Simulation effect was evaluated through those methods called mean bias error, mean absolute bias error, root mean square error, mean absolute percentage error on solar radiation of Yinchuan(1973-2006) and Guyuan(1986-2006) stations. Results showed the root mean square error was large slightly, mean absolute bias error was not up to 13% and 17% in Yinchuan station and Guyuan station respectively. We estimated daily solar radiation of Yongning station using the related formula of solar radiation and regional coefficients and comparing with daily solar radiation of observation of Yinchuan of the past twelve years(1989-2000). The results showed there were good linear relationships in the twelve years, the minimum of correlation coefficient R^2 equaled 0.88 in twelve years.

Key words: Local coefficient Daily solar radiation Extraterrestrial radiation Relative sunshine duration

1.Introduction

In order to develop and apply climate source, the method that local solar energy is evaluated becomes a kind of exigent need. Most of paper on solar energy assessment method is to resolve a application of daily solar radiation as the basic input variables in crop modeling[1-4]. But the method how to confirm local coefficients in calculation formula is not introduced detailedly. In Ningxia region there are 26 weather stations, but at only two stations daily solar radiation was observed. In this paper, by classical simulation calculation method, different local coefficients were obtained for calculating daily solar radiation of north and south in.Ningxia region, and then simulated daily solar radiation of Yongning station in Ningxia for past twelve years(1989-2000). This simulation method is expected to be able to apply in other stations.

2. Method and Data

Though calculation formula of daily solar radiation in DeBoer et. al (2005)'s paper was quoted, as form (1) below.

$$Rs = (as + bs\frac{n}{N})Ra \qquad (1)$$

Where R_s: solar or shortwave radiation [MJ m^{-2} day^{-1}]; n: actual duration of sunshine [hour], is duration of bright sunshine observed by weather station as a normal meteorological factor; N : maximum possible duration of sunshine or daylight hours [hour], is daylength and need to calculate; n/N : relative sunshine duration. R_a : extraterrestrial radiation [MJ m^{-2} day^{-1}], is available through calculation; a_s : Regression constant, expressing the fraction of extraterrestrial radiation reaching the earth on overcast days (n = 0); $a_s + b_s$: fraction of extraterrestrial radiation reaching the earth on clear days ($n = N$). How to calculate N and Ra detailedly, please refer DeBoer et. al (2005)'s paper.

All relative meteorological data in calculation are from observation value of weather stations of Ningxia. Local coefficients a_s and b_s in this formula were confirmed and validated through applying observation data of daily solar radiation of Yinchuan and Guyuan stations in Ningxia. In order to decide coefficient a_s and b_s of local regions, we applied daily data of five years' solar radiation observed from 1981 to 1985 in Yinchuan using a linear relationship relating solar radiation to extraterrestrial radiation and sunshine hours. Fig.2-1 shows a linear relation between solar radiation (R_s) and the formula relating to extraterrestrial radiation (R_a) and sunshine hours(n) and daylength(N) in Yinchuan after deleting one or two extreme values.Through this relationship we were able to obtain values of a_s =0.18 and b_s =0.62 and use them to calculate solar radiation for other counties near Yingchuan in Ningxia.

From above relationship by iterating test local coefficients a_s =0.18 and b_s =0.62 were obtained and validated for two-year's results in 1986 and 1987 by comparing with measured radiation. Fig.2-2 showed there was a good agreement between calculated and measured values and approached 1:1 line, so we can consider using a_s and b_s values to calculate solar radiation of other regions near Yinchuan station in Ningxia.

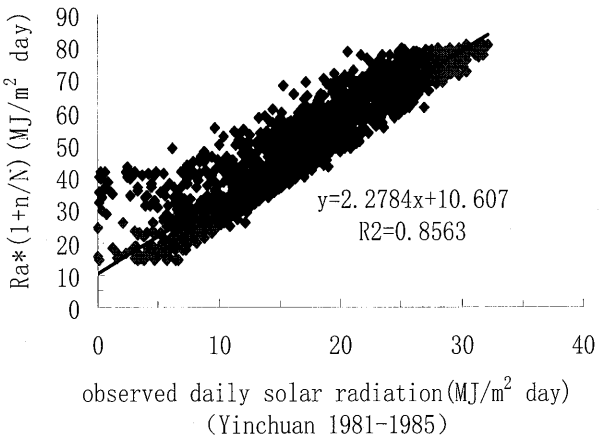

Fig.2-1 Relationship between solar radiation observed and formula

Using the same method, the local coefficients of Guyan station, a_s=0.16 and b_s=.58 were confirmed and validated with observation data of daily solar radiation for four years(1991～1994). Results were showed in Fig.2-3.

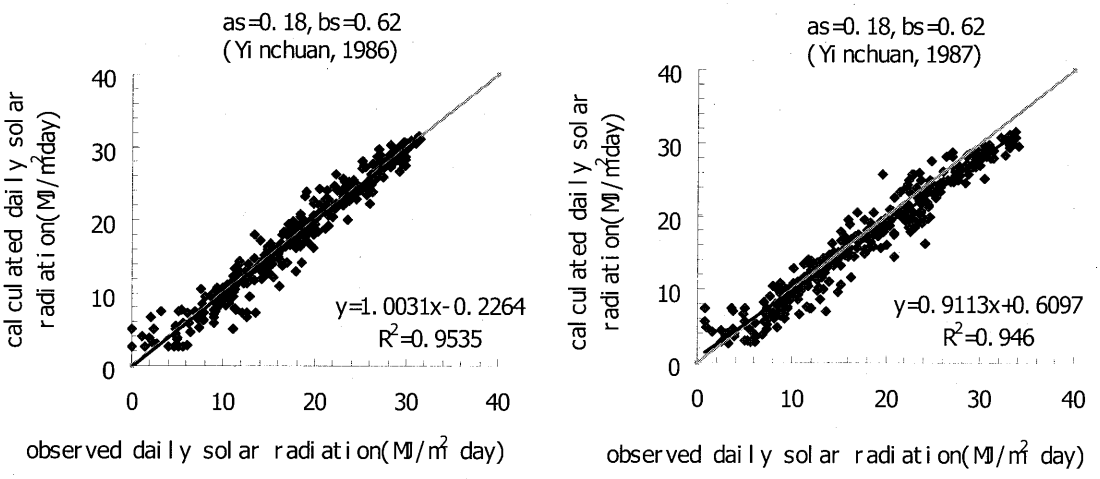

Fig.2-2 Validation of observed and calculated dialy solar radiation in 1986 and 1987 in Yinchuan

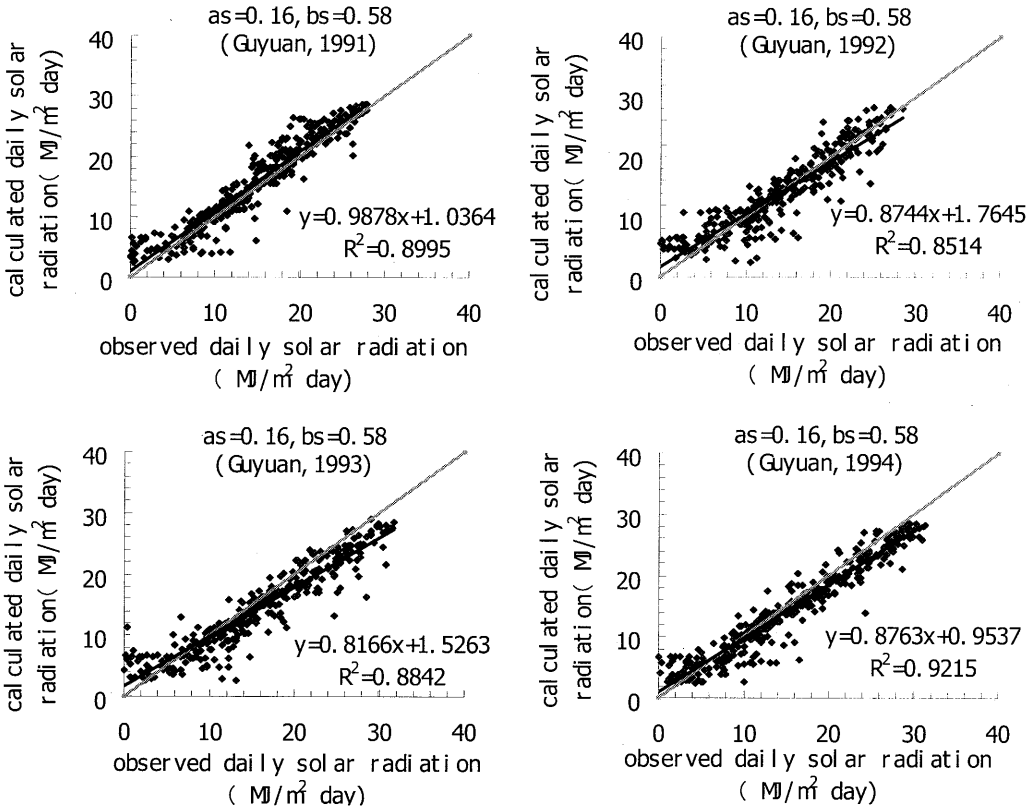

Fig.2-3 Comparison of observation and simulation value of daily solar radiation for four sample years on Guyuan station(1991～1994).

3. Error and Confidence level analysis

3.1 Error analysis

Through validation and error analysis local region coefficients were confirmed and considered that they are available, so two formulas for calculating daily solar radiation were gotten for different climate region of Ningxia below.

$$R_S = (0.18 + 0.62\frac{n}{N})R_a \quad (2)$$

$$R_S = (0.16 + 0.58\frac{n}{N})R_a \quad (3)$$

Where, form (2) is appropriate north and middle regions of Ningxia, form (3) is appropriate south Guyuan region of Ningxia. Applying above two formulas, we simulated historic value of daily solar radiation of Yinchuan(1973-2006) and Guyuan(1986-2006) and analyzed mean bias error(MBE MJ m^{-2} d^{-1}), mean absolute bias error(MABE MJ $m^{-2}d^{-1}$), root mean square error(RMSE MJ m^{-2} d^{-1}), mean absolute percentage error(MAPE %).Error analysis results showed in table 3.1-(1) below.

$$MBE = \frac{1}{n}\sum_{i=1}^{n}(R_{sim} - R_{obs})$$

$$MABE = \frac{1}{n}\sum_{i=1}^{n}|(R_{sim} - R_{obs})|$$

$$RMSE = \sqrt{\frac{1}{n}\sum_{i=1}^{n}(R_{sim} - R_{obs})^2}$$

$$MAPE = \frac{100}{n}\sum_{i=1}^{n}|R_{sim} - R_{obs}| \Big/ \frac{1}{n}\sum_{i=1}^{n}R_{obs}$$

Because Guyuan station was set up in 1986, so data showed from this year.

Where, Rsim and Robs are simulation and observation value, n is the number of sample years.

Error analysis descried MBE、MSBE、RMSE are more approach for two stations, MBE in most years in Yinchuan station is positive, in Guyuan station is negative. It shows simulation value is higher than observation value in Yinchuan, is lower in Guyuan station. MAPE of Yinchuan is lower than Guyuan, the maximize is up to 13% and 17% in Yinchuan station and

3.2 Confidence Level test

Confidence level T-test was done on simulation and observation value of daily solar radiation for five years(1986-1990) in Guyuan station, as table 3.2-(1) below. According to this T-test table, when confidence level was set at α=0.05, T value is 1.96. For the five years absolute value T is lower than 1.96, so they have obvious correlation between simulation and observation value. Simulation results are better.

Table 3-(1) Various error test of daily solar radiation in

Yinchuan(1973～2006) and Guyuan(1986～2006) stations

Yinchuan station	MBE	MABE	RMSE	MAPE(%)	Guyuan station	MBE	MABE	RMSE	MAPE(%)
1973	1.4	1.8	2.5	10.7					
1974	1.4	1.7	2.3	9.9					
1975	0.7	1.4	1.9	8.6					
1976	0.5	1.4	2.3	8.4					
1977	0.3	1.3	1.8	7.7					
1978	0.8	1.3	1.9	7.8					
1979	0.2	1.4	1.9	8.2					
1980	1.5	1.9	2.8	11.9					
1981	1.3	1.8	2.5	11.5					
1982	0.7	1.5	2.1	9.1					
1983	0.8	1.5	2.2	9.6					
1984	0.3	1.3	1.8	7.6					
1985	-0.2	1.7	2.2	8.3					
1986	-0.3	1.2	1.7	7.2	1986	-0.2	2.5	3.9	16.5
1987	-1.0	1.7	2.2	9.9	1987	-0.4	1.9	2.4	11.9
1988	-0.1	1.6	2.1	9.5	1988	0.3	1.9	2.5	13.5
1989	0.6	1.4	1.9	9.1	1989	0.2	2.0	2.6	14.2
1990	1.6	1.9	2.6	12.1	1990	0.0	1.7	2.4	11.5
1991	0.3	1.4	2.0	8.4	1991	1.0	1.8	2.4	12.4
1992	0.4	1.8	3.1	11.6	1992	0.3	2.0	2.8	14.5
1993	-0.1	1.4	2.3	8.5	1993	-1.0	2.3	3.3	15.1
1994	1.4	1.8	2.5	10.7	1994	-0.8	1.8	2.4	11.8
1995	1.3	1.7	2.3	9.9	1995	-0.3	1.4	1.7	8.6
1996	0.7	1.4	1.9	8.5	1996	-0.4	1.4	1.8	8.8
1997	0.5	1.4	2.3	8.5	1997	-0.8	1.5	1.9	9.5
1998	0.4	1.3	1.8	7.7	1998	-0.9	1.8	2.0	9.1
1999	0.8	1.3	1.9	7.8	1999	-0.5	1.5	2.0	9.7
2000	0.1	1.4	1.9	8.2	2000	-0.9	1.6	2.2	10.3
2001	1.5	2.0	2.8	12.1	2001	-0.6	1.6	2.3	10.6
2002	1.3	1.8	2.5	11.3	2002	-0.3	1.3	1.8	8.6
2003	0.7	1.5	2.1	9.3	2003	-0.4	1.6	2.1	11.0
2004	0.8	1.5	2.1	9.5	2004	-0.4	1.6	2.1	10.4
2005	0.2	1.3	1.8	7.6	2005	-0.9	1.7	2.1	11.0
2006	-0.2	1.7	2.3	8.3	2006	-1.0	1.5	2.2	11.7

Table 3.1-(1) T-tests value of daily solar radiation for five years

in Guyuan station (1986～1990)

	1986	1987	1988	1989	1990(year)
freedom	728	728	730	728	728
sample size	365	365	366	365	365
T-tests vaule	0.335	0.683	-0.624	-0.328	0.014

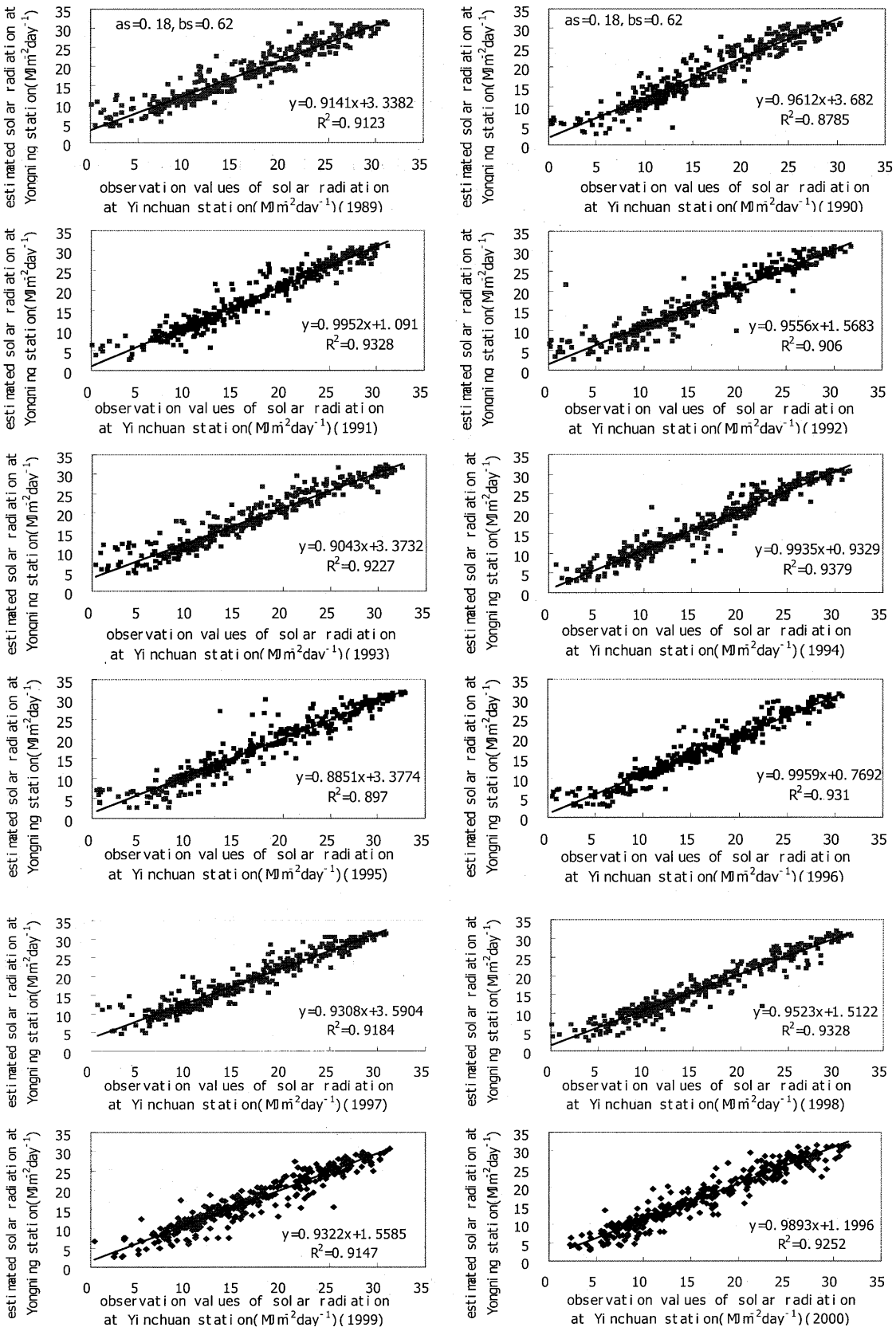

Fig. 4-1 Comparison of estimated solar radiation of Yongning station with observation values of solar radiation of Yinchuan for twelve years(1989-2000)

4. Conclusion

Application calculation formula obtained from Yinchuan station, daily solar radiation of Yongning station was estimated for twelve years(1989-2000). Results were compared with the same time series observation value of Yinchuan as reference in order to avoid extreme value. Results were showed in Fig. 4-1. There is a better line relationship between estimation results of Yongning station and observation of Yinchuan station because minimum square error R^2 reached 0.88, maximum R^2 reached 0.93. It is considered this method is available to estimated daily solar radiation of other regions of Ningxia similar climate condition of Yinchuan.

5. Discussion

There are many methods to calculate daily solar radiation for different regions. On a certain region, a general suggestion is to confirm and validate region coefficients. From two weather stations of Ningxia region, two group better appropriate region coefficients were gotten. A year(1991) was selected random as sample for analysis. Observation value of Yinchuan station was defined as reference standard, relative error of Yongning station was calculated. In 55 days of 365 days relative error was over 20%, in other days, was down 20% except few extreme value. A reason that large difference occurred is thought the quality of observation data, another one is considered observation data suddenly jump to low value range when its change is more stable up or down trend in continuous days. Maybe in initial liner correlation that local coefficients were sought, effect of cloudy or raining days should be eliminated. Obtained relative formula should be applied in a region where there is a similar climate condition so as to insure higher accuracy.

Reference

[1] Hoogenboom G.. Contribution of agrometeorology to the simulation of crop production and its applications[J]. Agriculture an Forest Meteorology, 2000,103, 137-157.

[2] Htmt L A,Knehar L,Swanton C J. Estimation of solar radiation for use in crop modeling[J]. Agriculture and Forest Meteorology, 1998, 9, 91(3-4): 293-300.

[3] DeBoer D W, Olson D I, Skonard C J. Evaluation of solar radiation estimation procedures for eastern south DAKOTA[J]. Proceedings of the South Dakota Academy of Science, 2005, Vol. 84: 265-275.

[4] Rivington M, Matthews K B, Buchan K. A Comparison of Methods for Providing Solar Radiation Data to Crop Models and Decision Support Systems[J]. Integrated Assessment and Decision Support: Proceedings of the 1st biennial meeting of the International Environmental Modelling and Software Society, University of Lugano, Switzerland, 2002, Vol. 3: 193-198.

Frequently used monsoon circulation indices of the Asian summer monsoon

D. Rajan , VS. Prasad, AK. Mitra and AK. Bohra
Ministry of Earth Sciences
National Center for Medium Range Weather Forecasting
email: drajan@ncmrwf.gov.in
A-50, Sector 62, Noida 201307, India

Abstract

Asian monsoon is one of the major components of the earth climate system. The arrival of the Indian summer monsoon over the Kerala coast is found to be reasonably punctual either towards the end of May or beginning of June. A delay in the onset of the monsoon by a few weeks would affect agricultural activity while an early onset might not be utilized to its full advantage without accurate prediction in advance. The traditional methods of defining onset guarantee a marked increase in rainfall over this Kerala coast. So far there exists no widely accepted definitions of these monsoon transitions. The monsoon onset occurs due to large-scale interactions between surface heating and atmospheric dynamical, thermal and hydrological process. Given the relatively small scale of Kerala that is less than 200 km in breath, sensitivity of the declaration of onset based solely on the district's rainfall to spatial area in the monsoon transitions is also likely to be large. The IMD, which is run by the Ministry of Earth Sciences, has been using the qualitative method over a long period using rainfall to declare the onset date. IMD declared the observed onset date of the southwest monsoon 2008 over the Kerala on 31 May, which is a day before the normal date. In the normal course it takes about one and half months time to cover the whole of India.

In India the NCMRWF, a Center of Excellence in modeling, has generated vast experience in global and regional modeling. Currently NCMRWF is running the global spectral model T254/L64 operationally. This spectral model is being used to for this study to monitor the onset phase of the monsoon 2008 with the following various circulation indices. (1) In 1996 Ramesh et al. gave the following characteristics for the evolution of the onset over the Arabian Sea covering the area of 0° - 19.5° N and 55.5 °E - 75 °E: (a) the net tropospheric moisture build-up, (b) the mean tropospheric temperature increase, (c) sharp rise of the kinetic energy at 850 hPa. (2) In 2002 Fasullo gave the hydrological definition (HOWI). (3) In 1992 Webster and Yang (4) In 1999 Goswami et al (5) 1999 Wang and Fan (6) 2000 Lau et al (7) In 2002 Syroka and Toumi

The Analysis of Grassland Dynamic and Its Driving Forces in Northern-Tibet Plateau of China Based on Remotely Sensed Data and Climate Information

Jiahua Zhang[1,2], Fengmei Yao[3,4]

[1]*LRSCIS, Chinese Academy of Meteorological Sciences, No.46, Zhongguancun South Street, Beijing, 100081, China*

[2]*Key Laboratory of Land use, Ministry of Land and Resource, Beijing, 100035;China*

E-mail: zhangjh@cams.cma.gov.cn

[3] *College of Earth Sciences, the Graduated Uuniversity of Chinese Academy of Sciences, Beijing, 100049, China*

[4] *Institute of Remote Sensing and Geomatics, Shanghai University, Shanghai, 200072, China*

E-mail:yaofm@gucas.ac.cn

Abstract

A ten-day interval of satellite data (NOAA/AVHRR) between 1981 and 2001 were used to investigate the vegetation dynamic in Northern-Tibet Plateau (NTP), China. The relationships between NDVI and climatic parameters were analyzed in six counties of NTP. And the human activities factors such as population also tested in this study. The result shown that the prominent increase and decrease of NDVI occurred in middle eastern and eastern NTP with low altitude. Correspondingly, the linear trends of VP-NDVI were weak and no change in western part of the NTP with high altitude. The strong negative relationship between NDVI and evapotranspiration (*PE*) occurred in sub-frigid semi-arid and frigid arid regions, e.g., Nakchu, Shantsa, Palgon and Amdo counties, which indicated that the *PE* was main effecting factor on vegetation degradation in these areas. But in temperate-humid and sub-frigid semi-humid regions, significantly negative correlations imply that human activities had primary influenced on vegetation degradation like Chali and Soksa counties.

Keywords: Northern-Tibet Plateau of China, NOAA/AVHRR, Climate change vegetation dynamic

1. Introduction

The NTP is the sources of ancient and modern glaciers as well as many rivers such as the Yangtze, the Nujiang and the Lancang in China[1].The NTP grassland is the third largest grassland in China and one part of the important land ecosystem in the NTP, it has the function of windproof, solid sand, self-control water source, prevent soil erosion, adjustment microclimate and purification air so on [2]. In recently years, a large expanse of grassland in NTP has seriously degradation. It is generally believed that the occurrence and development of land degradation over the NTP is closely related to the eco-environment conditions, climatic changes and human activities [3].

The satellite remote sensing has become import tool for ecological, geographical, meteorological and environmental studies [4-8]. The Advanced Very High Resolution Radiometer (AVHRR) on board the NOAA series of satellites has been widely used for monitoring the terrestrial environment in regional and global scales [9-12].

In this study, we used a 19-year series of the Normalized Difference Vegetation Index (NDVI) derived from NOAA-AVHRR PAL (Pathfinder AVHRR Land) images and *in-situ* meteorological data, mainly studies the dynamic change of grassland in the NTP (Nakchu Prefecture) based on multi-annual NDVI data, to study the spatial distribution of grassland cover change, and to analyze the effect factor of dynamic change of NDVI in the NTP.

2. Study Area

The NTP is lies between 29°55' and 36°30'N, and 83°55' and 95°5'E. It accounts for 32.82% of the total area of Tibet Autonomous Region (TAR), and the grassland covers 41.65% of total grassland of TAR. The average altitude in the northwest exceeds 5000 m and descends to 4000 m in the east. In NTP region, the annual mean temperature is between -2.9 °C and 3.4°C and annual precipitation between 298.6 mm and 708.4 mm. The overall precipitation declines from east to west and from south to north. The annual evaporation (measured by evaporating dish) is 1500~2300 mm, rising from southeast to northwest [2,13].

Geographically, four climatic zones are delimited in the NTP: temperate-humid, sub-frigid semi-humid, sub-frigid semi-arid, and frigid arid zones[14]. Following these climatic zones, four major native pasture landscapes can be identified from the southeast to the northwest: bush-meadow, alpine meadow, alpine grassland, and desert grassland. The composition of pastures in the east and central part of the region is complex due to the wet climate and variable terrain. The grassland becomes less complex botanically towards the northwest where the altitude is higher and the climate is harsher. The population in Nakchu is about 37 6800 (2003 census). Farmers in this region are

primarily engaged in animal husbandry, except for a few who produce grain crops in the eastern counties. Tibetan sheep, goats, and yak are dominant livestock enterprises, supported by horses and cattle.

3. Data and methodology

The NOAA- AVHRR PAL data set is available with a spatial resolution of 8×8 km^2 at temporal resolution of 10-day interval maximum composites [15]. This data set originated from NOAA-7, -9, -11 and 14 satellite images that were radiometrically and spatially corrected [16]. The time series data between 1981-2001 (except for 1994) are used to study the NDVI of grassland in the NTP and obtain the spatial distribution characteristic of the vegetation cover.

The NDVI has been widely used to estimate green biomass, leaf area index and patterns of productivity [4,5]. The NDVI provides essential information of land degradation status through vegetative change in temporal and spatial scales. The formula is following:

$$NDVI = \frac{NIR - \mathrm{Re}d}{NIR + \mathrm{Re}d} \qquad (1)$$

Where NIR (AVHRR Channel2: 0.725-1.1μm) and Red (AVHRR Channel1: 0.58-0.68μm) are the amounts of near-infrared and red light respectively, reflected by the vegetation and captured by the sensor of the satellite.

NDVI values are in the range from -1.0 to 1.0, where in growth season, generally increasing 0.1 values indicate increasing green vegetation and less 0.1 values indicate non-vegetated features such as water, barren areas, ice, snow or clouds. The upper boundary above 0.8 basically is taken for pure vegetation. The NDVI exists the saturation in land vegetation's application. In this paper, the NDVI third generation product was used for solving NDVI saturation problem in a certain extent and stretched NDVI value (range from 0 to 254).

The PAL AVHRR NDVI 10-day maximum value composites (MVC) were used to investigate trends in vegetation degradation. In the study area, the annual NDVI maximum occurs in July, August or September. In each 64km^2 pixel, the 10-day values were used to calculate a vegetation peak (VP) seasonal value as the average of the 9 NDVI-values in July, August and September. Calculating an averaged annual vegetation peak value would also filter out extreme values. The VP-NDVI slope of the linear trend of best fit through the 19-year was calculated using the least square method It counts the regression coefficients of all pixels in the NTP in Fig.1. The gain coefficient values were classed into 5 classes that describe the NDVI change over the 20 years as derived from linear trends: High increase: > 0.41 NDVI unites over the 20 years. Slight increase: between 0.15 and 0.41 NDVI unites. No change: ±0.15 NDVI unites. Slight decrease: between -0.15 and -0.41 NDVI unites. High decrease: < - 0.41 NDVI unites.

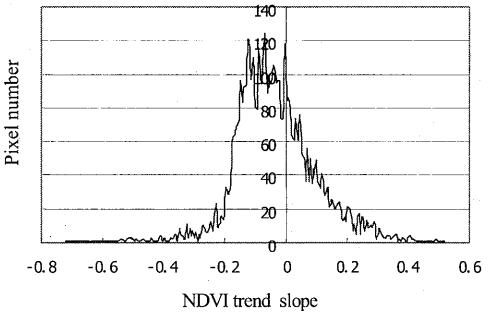

Fig.1 Statistic of NDVI change in the NTP region from 1981 to 2001a

4. Results and discussion

4.1 Vegetation covers spatial pattern and variations in inter-annual scale

The average of VP-NDVI values showed that there are the obvious spatial differences of vegetation cover in the NTP. The east part is high and west part is low, the largest VP-NDVI values appear in farmland and forest regions, and second is bush-meadow and alpine meadow. The farmland, forest area, and bush-meadow, alpine meadow are mainly located in eastern NTP regions. Compared with others regions, this region have maximum vegetation coverage with low altitude. In the middle regions of the NTP, the maximal value of VP-NDVI was from 160-180.In the western region; the maximal value of VP-NDVI was from 140-160. The main vegetation types include alpine steppe and desert steppe; the vegetation coverage is lower with high altitude. The results of pixels number of VP-NDVI value trend described that the no-change area is accounting for 77.27% of pixels number in the NTP, high increase and slight increase account for 0.27% and 8.71%, and high decrease and slight decrease account for account for 0.69% and 13.06% respectively.

Fig.2 showed that the linear trends of VP-NDVI between 1981 and 2001 for each 64km^2 pixel of the NTP. The grain coefficients of the slops were re-classed into 5 classes ranging from high increase to high decrease of VP-NDVI. The prominently increasing and decreasing of NDVI occurred in eastern NTP with low altitude. Correspondingly, the linear trends of VP-NDVI were weak and no change in 20 years in western part of the NTP with high altitude.

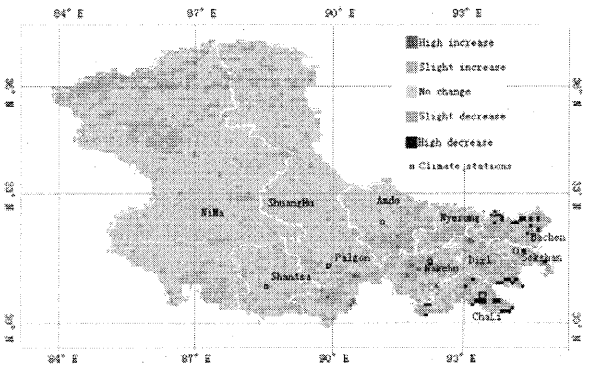

Fig.2 The linear trends of VP-NDVI in the NTP between 1981 and 2001a

4.2 Climatic and anthropogenic driving forces

The six climatic stations were selected to study the relationship between climatic factors and NDVI. The correlation coefficient between monthly VP-NDVI and monthly precipitation were calculated between 1981 and 2001. The obviously positive correlation occurs in six counties in seasonal cycle (n=237, significant at the 99% confidence level) (see Table 1). It revealed that precipitation is dominant factor controlling the seasonal variation of vegetation growth in the NTP.

Table 1 The correlation coefficient (R) between monthly VP-NDVI and monthly precipitation

County	Nakchu	Shantsa	Palgon	Amdo	Soksa	Chali
Altit.(m)	4508	4674	4701	4801	4024	4489
R	0.81	0.67	0.86	0.74	0.77	0.71

The Fig.2 showed the linear trends of VP-NDVI between 1981 and 2001 are different form southern to middle and to Western of the NTP. The reason is uncertain. We calculated the relationships between NDVI and climatic factors such as temperature, precipitation, *PE*, relative variability of annual precipitation during grass growth, wind velocity etc. The NDVI of Nakchu station increases almost linearly with the increase of precipitation. The Table 2 showed that the VP-NDVI trend slope and annual precipitation trend increase in Nakchu from 1981-2001.

The correlation coefficient between minimum temperature (T_{min}) of Nakchu area and NDVI are 0.51. It is recognized that T_{min} is main limited factor effecting over-wintered perennial grass growth. Thus, increases of precipitation and T_{min} are benefit for the vegetation growth of Nakchu County. The relationship between NDVI and evapotranspration show high negative in Nakchu County （R = -0.63） .The *PE* can describe vegetation response to climate factors (i.e. radiation, temperature, precipitation and wind) synthetically. With the decrease of *PE* in Nakchu County, the vegetation drought stress will decrease, which benefits the vegetation growth. Thus, from 1981 to 2001, the NDVI in Nakchu County show a high increase (see Fig.2). Chali station is located in the sub-frigid semi-humid zone, the relation between NDVI and annual precipitation is negative, which indicated that the more rainfall inhibit the vegetation growths. However, The coefficient between NDVI and T_{max} is positive, the T_{max} might be a dominant factor influencing the grass growths in Chali station.

Table 2 VP-NDVI trend and annual precipitation trend slopes in six counties from 1981 to 2001

County	Nakchu	Shantsa	Palgon	Amdo	Soksa	Chali
VP-NDVI trend slope	0.41	0.24	0.06	-0.02	-0.07	-0.16
Precip. trend slope	4.35	5.88	0.07	1.68	0.43	4.80

The correlation coefficient between T_{min} of Nakchu area and NDVI are 0.51. It is recognized that T_{min} is main limited factor effecting over-wintered perennial grass growth. Thus, increases of precipitation and T_{min} are benefit for the vegetation growth of Nakchu County. The relationship between NDVI and evapotranspration show high negative in Nakchu County （R = -0.63） .The *PE* can synthetically describe vegetation response to climate factors (i.e. radiation, temperature, precipitation and wind). With the decrease of the PE in Nakchu County, the vegetation drought stress will decrease, which benefits the vegetation growth. Thus, from 1981 to 2001, the NDVI in Nakchu County show a high increase (see Fig.2). Chali station is located in the sub-frigid semi-humid zone, the relation between NDVI and annual precipitation is negative, which indicated that the more rainfall inhibit the vegetation growths. However, The coefficient between NDVI and T_{max} is positive, the T_{max} might be a dominant factor influencing the grass growths in Chali station.

The positive correlation between *PE* and NDVI indicated that *PE* decrease owing to decreases of wind velocity; sunshine duration in Chali County was disadvantageous factor for the grass growth in semi-humid area of the NTP from1981 to 2001. Considering anthropogenic factor, there is negative correlation between NDVI *vs.* population (R=-0.45), means that human activates become dominant factor influencing the grassland degradation [2]. In that case, the NDVI shows decreasing trend in Chali County in recently (see Fig.2). Climatically, Soksa County also located at sub-frigid semi-wet zone, but the annual precipitation is less

than that of Chali station. In this region, the obviously positive correlation (R=0.53) occurred between NDVI and the precipitation at growth period (from July to September); But the relationship between NDVI and the annual precipitation seems weak, which indicates that the moisture condition is main dominant factor impacting vegetation development in grass growth period in Soksa region. The relationship between accumulated temperature and NDVI is relative high, which show that the temperature is also an important factor impacting on the grass growth. The other important effecting factor is human activates. The population increased from end of 1989 year (19371 person) to 2000 year the (23694 person), whereas, the NDVI decreased in Soksa region in recently (see Fig.2). The negative correlation between the NDVI and population (R=-0.40) could imply that human activates also act as a dominant factor influencing the grassland degradation in Soksa region. Statistical result presents that the highest population density is Soksa County, and fastest growing of population rate is Chali. In the eastern NTP, grassland animal husbandry is an important component of the regional economy [3].

It is generally believed that the main factor of grassland degradation is man's improper economic activities. The main factor leading to grassland degradation is over grazing. At the end of 2003, the total number of livestock on hand was 7.682 million, equal to 14.867 million sheep units, being nearly a two-fold increase over 1958 [13].

At the middle-western NTP, Shantsa, Palgon and Amdo counties belong to sub-frigid semi-arid and frigid arid zone. The characteristics of cold, drought, windy, and strong transpiration affect the grass growth in these regions. The correlation coefficient between *PE* and NDVI showed obviously negative for Shantsa (-0.51), Palgon (-0.63) and Amdo(-0.54) areas. In these regions, with the increase of the *PE*, the vegetation drought stress will increase, whereas inhibit the vegetation growth. With the rise in temperature and the falling in humidity, the evaporation increases in sub-frigid semi-arid and frigid arid zone of the NTP, all these lead to the further degradation of the grassland and promote the occurrence and development of desertification in these area. Moreover, at the Shantsa County, the annual mean wind velocity exceeds 4.5 m/s, the correlation coefficient between annual mean wind velocity and NDVI is negative (R=-0.40). It is soon conceivable that NDVI is affected not only by the *PE* but also by factors such as annual mean wind velocity and transpiration rate. Normally, land degradation and desertification include a series of wind sand activity processes, such as soil wind erosion, wind sand stream, shifting sand accumulation and sand dune migration.

A positive relationship between NDVI and precipitation occurs in Palgon County (R=0.39), and presumably precipitation is the dominating variable responsible for the measured NDVI fluctuations. The Table 3 also found that the trend was weak for both NDVI (trend slope equals to 0.06) and rainfall (trend slope is 0.07) in Palgon County between 1981 and 2001. The precipitation increases almost weakly linearly with the decrease of NDVI for Amdo County (NDVI trend slope equals to -0.02, annual precipitation trend slope is 1.68). However, the coefficient between total number of the dry spells (defined as those with longer than 10 days without rainfall) and NDVI is negative (R= -0.40). It means that the temporal distribution of precipitation is also main factor corresponding to the NDVI changes in Amdo County. However, the human activates seem not the main effecting factor to grassland degradation owing to the weak relationship between NDVI and human population occurred in these three counties.

5. Conclusion

In past 20years, significantly increase of grassland vegetation occurred in middle eastern and eastern NTP, and high decrease in Eastern parts. The *PE* has a negative response to increased vegetation cover changes in summer season. The high T_{min} and precipitation are benefit for the grass growth in the NTP regions. Global warming and unreasonable human activities such as over-grazed has caused grassland degradation in the eastern counties of the temperate humid zone of the NTP. The dynamical mechanisms responsible for the feedback of vegetation cover changes and degradation need further study.

Acknowledgments

This work was supported jointly by the Foundation of Key Laboratory of Land use, M.L.R of China (07-01), the Open Research Program of LRCE-IAP, CAS; NSFC (No.40641003, 40771147), the MOST Project (No. 2003DIB4J144, 2006BAD04B04, 2006AA10Z213, 2006GB24160430).

References ***(Omitted)***

Preliminary Result of Aerosol Optical Properties from the Observatory for Atmospheric Research at Phimai, Nakhon Ratchasima, Thailand

Boossarasiri Thana, Akkaneewut Chabangborn, Thawatchai Sudjai

Earth Sciences Programe, Department of Geology, Faculty of Science, Chulalongkorn University, Thailand

Abstract

Aerosol is an atmospheric constituent that is high temporal and spatial variation. The aerosol effects have not yet cleared due to lack of data and complex behaviors in the atmosphere. The observatory for atmospheric research at Phimai, Nakhon Ratchasima was established in 2005 in order to observe aerosol variation and related parameters. It is only one observatory that located in Southeast Asia. The objective of this study is to investigate the variation of aerosol optical properties from the observatory from May 2005 to April 2006. The properties consist of aerosol optical depth (AOD), Angstrom exponent and single scattering albedo (SSA).

According to aerosol optical properties, we can divide aerosol at the observatory for atmospheric research at Phimai, Nakhon Ratchasima into 4 groups as below;

The first group consists of coarse mode aerosol with high absorption aerosols. They suspend in the atmosphere during August to September which is rainy season. It may be local dust that is compound of iron oxide or hematite. Resulting is low SSA aerosol distributed during this period. SSA are 0.77±0.15, 0.79±0.15 and 0.86±0.17 in channel 0.4, 0.5 and 0.87 μm, in respectively.

The second group is major by coarse mode aerosol and low absorption. It is possibly consisted of rock salt (halite) that exposes near the study area or the other soluble aerosol. This group of aerosol is found in during October to December. The second group of aerosol is coarser than the first group because of the lower Ångstrom exponent.

For the third and forth group of aerosol, they are fine mode aerosol which Ångstrom exponent are 1.13±0.25 for the third group and 1.15±0.40 for the forth group. The different between these two groups is SSA that is lower for the third group. SSA of the third group of aerosol is 0.78±0.11, 0.76±0.13 and 0.77±0.12 for the different wavelength that express absorbing aerosol characteristic. Therefore, they may be the aerosol from biomass burning under long flaming stage that suppose with low humidity during January and February. The forth group appear during March to April which is the crop preparation period.

ADEOS-II/GLI Water Vapour Channel and Quality Assessment of Upper Tropospheric Humidity retrievals

J. R. Dim[1], H. Murakami[1], M. Hori[1]

1. Earth Observation Research Center / JAXA
2-1-1 Sengen, Tsukuba, Ibaraki 305-8505 Japan
E-mail: dimjules.rostand@jaxa.jp

Abstract.

The quality of radiative transfer models can be evaluated by studying the impact of these models on atmospheric parameters retrievals. For the present study, the water vapour channel (6.7 μm) of the Global Imager (GLI) onboard ADEOS-II satellite is used to examine the influence of a radiative transfer simulation model (RSTAR6b) on the retrieval of the clear-sky upper tropospheric relative humidity (UTRH) as observed by the ADEOS II/GLI satellite and the interaction between this humidity and the surrounding clouds.

Lidar Network Observations of Tropospheric Aerosols

Nobuo Sugimoto(1), Ichiro Matsui(1), Atsushi Shimizu(1), Tomoaki Nishizawa(1), Yukari Hara(1), Chenbo Xie(1,2), Jun Zhou(2), Itsushi Uno(3), Keiya Yumimoto(3), Zifa Wang(4), Jixia Zhou(5), Soon-Chang Yoon(6), Tamio Takamura(7)

(1) National Institute for Environmental Studies, Tsukuba 305-8506 Japan,
E-mail:nsugimot@nies.go.jp
(2) Anhui Institute of Optics and Fine Mechanics, Hehei, China
(3) Research Institute for Applied Mechanics, Kyushu University, Fukuoka, Japan
(4) Institute of Atmospheric Physics, Beijing, China
(5) Cold and Arid Regions Environmental and Engineering Research Institute, Lanzhou, China
(6) School of Earth and Environmental Sciences, Seoul National University, Seoul, Korea
(7) Center for Environmental Remote Sensing(CEReS), Chiba University

ABSTRACT

In the East Asian region, various kinds of aerosols such as mineral dust, air-pollution aerosols, biomass burning smoke, coexist, and it is important to understand the effects of these aerosols on climate and the environment. Continuous observations of the three-dimensional distribution and optical characteristics of aerosols with a network of lidars provide useful information for studying emission, transport, change of characteristics during transport, deposition, etc.

We started continuous observation with a compact automatic Mie scattering lidar in 1996 at NIES in Tsukuba in a research project on the effect aerosols in the global warming. In 2001, we constructed lidars in Beijing and Nagasaki and started network observations with the lidars at the three locations. The network has been expanded in the research programs and international cooperation. Currently, we are operating the lidars at 23 locations in Japan, Korea, Mongolia, and Thailand. Most of the lidars are operated in the research program on Asian dust. The lidars in Toyama, Nagasaki, Matsue, Niigata, and Tokyo were constructed by Ministry of the Environment of Japan in the Asian dust monitoring program. Some of the lidars are allocated in the radiation observation network GEOSS/SKYNET. All of the lidars in the NIES lidar network, except for some stations in China, participate in the GAW Aerosol Lidar Observation Network (GALION).

The lidar used in the network is two wavelength (1064nm, 532nm) Mie-scattering lidar having a depolarization ratio measurement function (532 nm). The lidar uses a commercial flash lamp pumped Nd:YAG laser as a light source. The output power at 1064 nm (532 nm) is 20 mJ (20 mJ). The receiver telescope diameter is 20 cm. Polarization components of received light at 532 nm are separated with a polarization prism and detected with two photomultiplier tubes (PMTs). Received light at 1064 nm is detected with an avalanche photodiode (APD). Signals from the PMTs and APD are digitized with 12-bit analogue-to-digital converters and recorded on a hard disk of the data acquisition PC.

The lidars are operated continuously regardless of weather. In the continuous observation, 5-min averaged lidar profiles are measured every 15 minutes. Consequently, 96 sets of profiles are obtained per day. The data from the on-line stations are transferred to NIES and processed in real time to derive the attenuated backscatter coefficients and the extinction coefficients for non-spherical and spherical aerosols. The data are used in the real-time monitoring of Asian dust as well as in the studies of regional air pollution and climate change.

Skyradiometer POM-01L

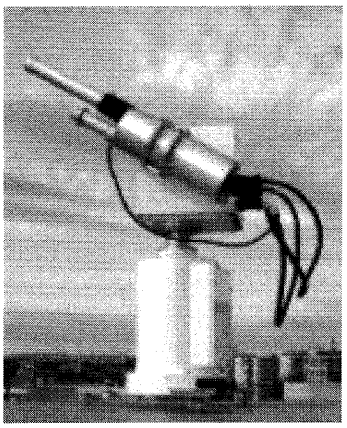

Half field of view	0.5°
Minimum scattering angle	3°
Wavelength	315,400,500,675,870,940,1020 nm
Wavelength selection	Filter wheel method
Detector	Silicon photodiode
Measurement range	2.5mA,250μA,25μA,250nA,25nA,2.5nA
Motor	Stepping Motor (0.0036degree : 2 axis)
Sun Tracking	Calculation with latitude, longitude and local time (Sun sensor can compensate the position)
Measurement cycle	Time mode , Airmass mode
Scan direction	Combination of horizontal and vertical direction
The number of scattering angle	Maximum 50points
Sun sensor	4silicon sensor
PC interface	RS-232C
Operating temperature	-10∽45℃
Power consumption	200W (100V/2A)
Required Power	AC100-240V/2A
Weight	Skyradiometer ; 19kg
	Cable etc ; 4kg

Features

A sky radiometer for the routine automated measurement of direct and scattered sun radiation with seven wavelengths from 315 to 1020nm.

It is easy to install, set up and use. The adjustable base platform has a built-in bubble level. The integrated sun sensor provides active sun tracking.

It comes with Windows control and data logging software supplied. The instrument must be connected to the RS232 port to a computer (not included) running the supplied software in order to operate.

SKY VIEW PSV-100

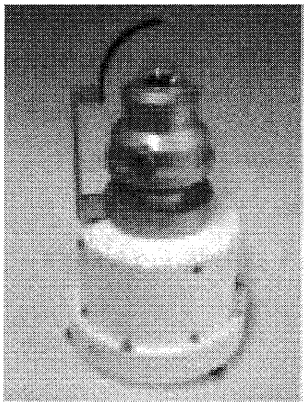

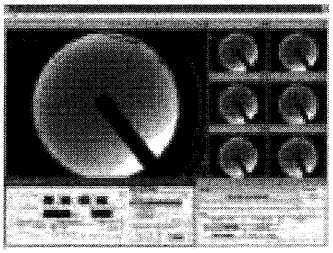

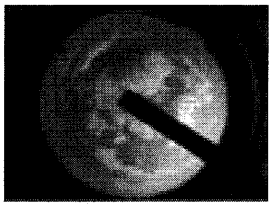

Features

This instrument is monitoring of the sky.

It can record sky image with CCD camera.

Sky image is automatically saved as JPEG format into daily folder in computer.

Sun shading blade traces sun position to protect CCD from direct sun.

Maintenance free

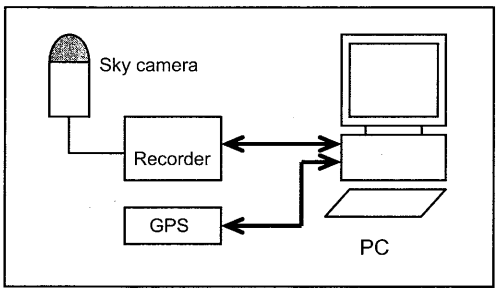

Camera	1/3CCD, 400 thousand pixels
Lens	160° field of view (Standard) 180° (PSV-100H)
Tracking System	CPU automatic calculation
Capture mode	Time mode/Sun Mode
Minimum capture interval	1min
Communication	RS-232C
Temperature	− 10∽50℃
Power consumption	100W (100V/1A)
Input power Required	AC100-220V, 2A, 50/60Hz
Cable length	10m
Size	φ432×160mm
Weight	10kg

PREDE **PREDE CO.,LTD.**

Research Center: Sasamoto Building, 26-8 Kamidaira 1-Chome, Fussa-shi, Tokyo 197-0012 Japan

TEL:+81-(0)42-539-3755 FAX:+81-(0)42-539-3757

URL: http://www.prede.com/ E-mail: sales@prede.com

Radiometrics (USA), Advanced Microwave Profilers

連続　温度、湿度、水分量測定

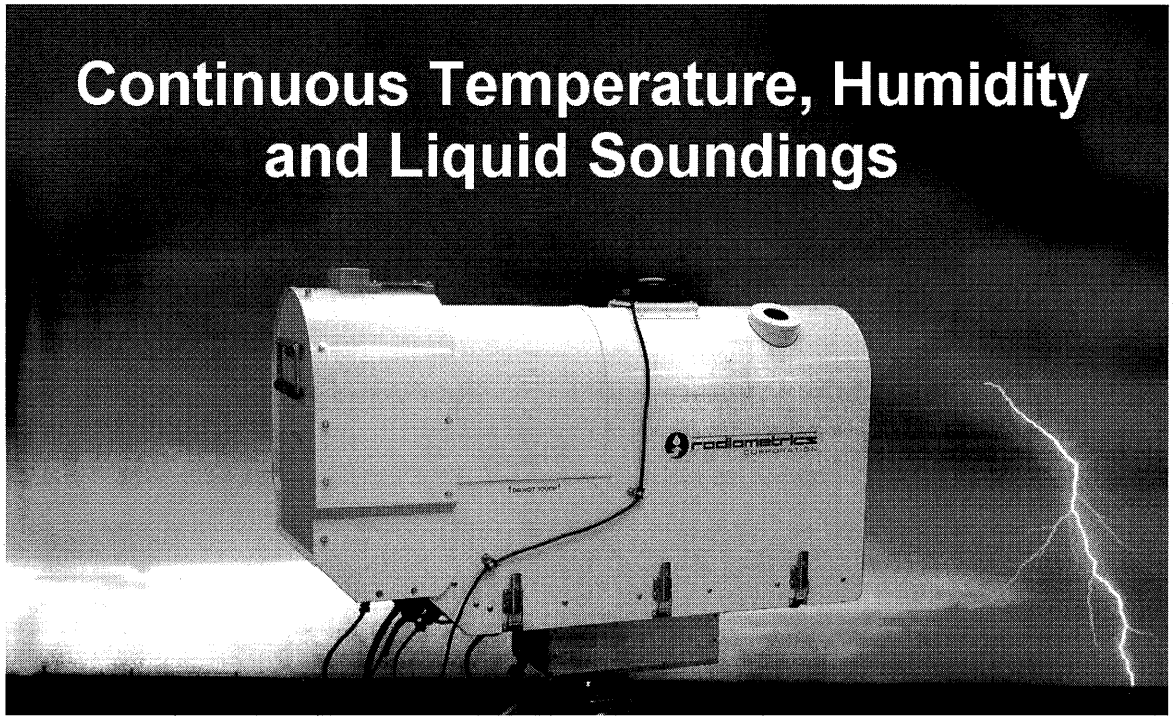

- ***Continuous temperature and humidity profiles essential for accurate short-term weather forecasting***

天気の短時間変化を正確に予報するための、連続温度、湿度プロファイル

- ***Liquid profiles – not available by other methods – key to accurate precipitation forecasting***

*水分量プロファイル　－　**Precipitation** を正確に予報　－　他の技術では不可能*

- ***Patented design delivers optimum performance and flexibility in a compact, portable package***

特許デザインによる最適なパフォーマンス、コンパクト、ポータブルで順応性を持つ

- ***Proven in long-term polar, tropical and mid-latitude operations***

南北極、熱帯地、中緯度の長期間オペレーションにて立証済み

- ***Internal infrared cloud-base sensor for reliable operation in harsh conditions***

厳しい条件でも信頼できるオペレーションが可能な赤外線クラウドベースセンサー内蔵

- ***All-Sky observations with optional Azimuth Positioner***

オプションによるアジマスポジショナーにて全方位観測可能

- ***GPS time and position***　*GPS 内蔵による時間と方位*

Agent in Japan

Nihon SiberHegner k.k.

Industrial Tools & Supply

3-4-19, Mita, Minato-ku, Tokyo
TEL：０３－５７３０－７６２０
FAX：０３－５７３０－７６００

www.dksh.com/japan

Radiometer Physics GmbH

Dual Polarisation Rain Radiometer

Dual Polarisation rain Radiometer(DP-RR) for thick cloud and rain LWP

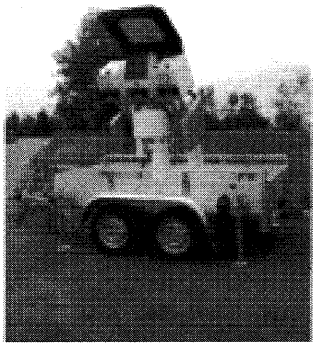

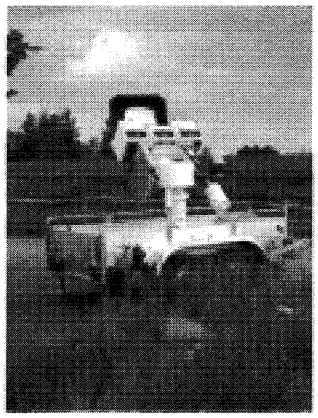

This instrument observers at 3 or 4 frequencies with 2 orthogonal polarisations(6 or 8 channels in total).

Technical Specifications

- Optical resolution
- Radiometric resolution : 0.2 K RMS at 1.0 s integration time
- Absolut system stability : <1.0 K
- Receiver and antenna thermal stabilization :
- Environmental temperature range for operation : -30℃ to +45℃
- Integrated PC on-board
- Stand alone operation
- Data storage and backup on-board, power-failure safe-guard
- Low maintenance(3 months intervall for absolute calibration using LN)
- Power supply : 85 to 265 V AC(at 47 to 63 Hz), or 120 to 330 V DC
- Power consumption : 350 W turn-on power, 150 W under stabilized conditions

Please access "Radiometer Physics GmbH" on Sogo Electronics, Inc.'s website(http://www.sogoel.co.jp/maker.html) for their various products and technical information.

SOGO ELECTRONICS, INC.

6-22-7, Nagayama, Tama-shi, Tokyo, 206-0025, Japan
TEL 042-337-4411 FAX 042-373-1919
E-mail sogo@sogoel.co.jp
URL http://www.sogoel.co.jp

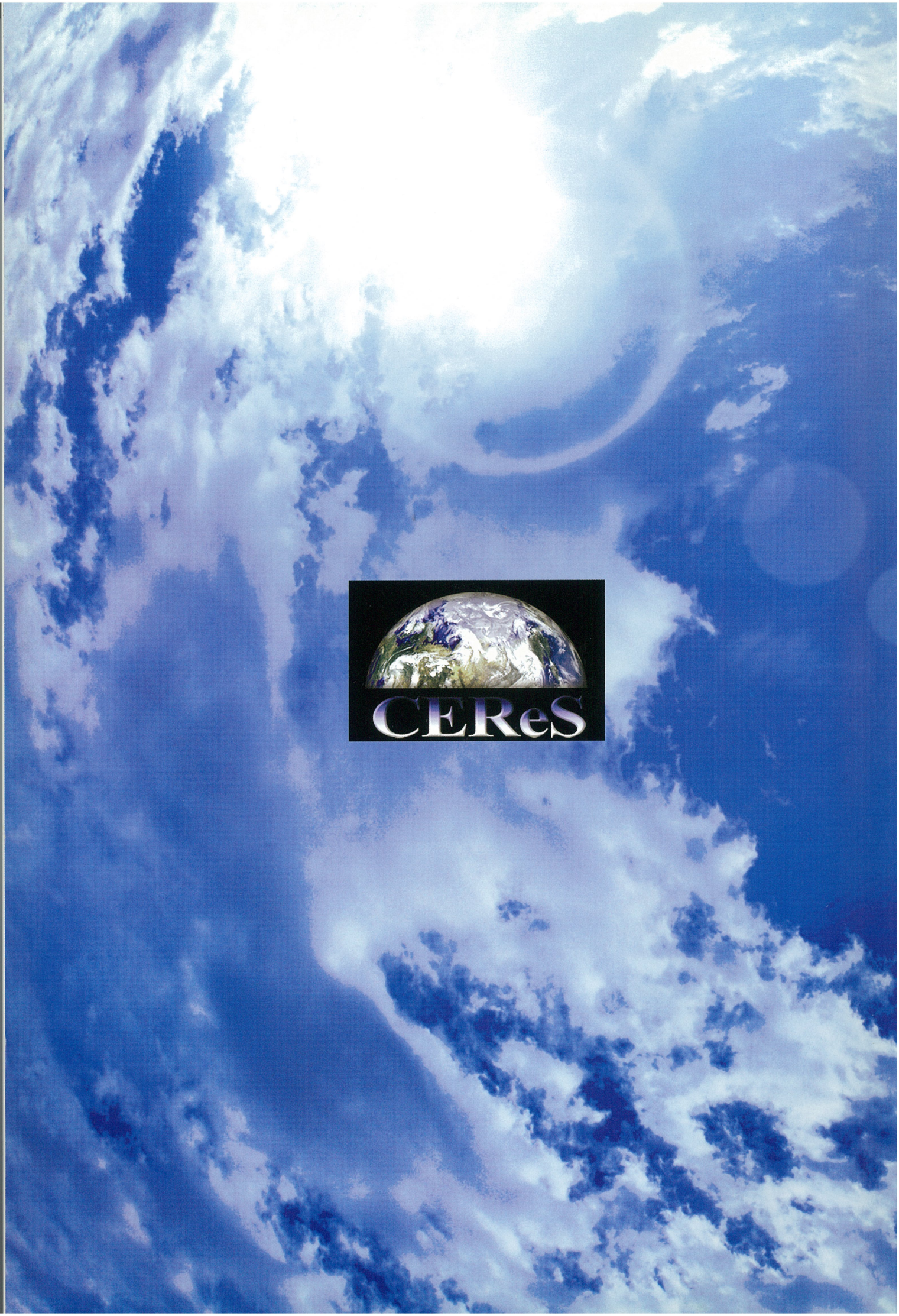
CEReS